PROPELLER TIME-DEPENDENT FORCES DUE TO NONUNIFORM FLOW

PENNSYLVANIA STATE UNIVERSITY

PREPARED FOR
NAVAL SEA SYSTEMS COMMAND

9 MARCH 1976

194073

PROPELLER TIME-DEPENDENT FORCES DUE TO NONUNIFORM FLOW

Donald E. Thompson

Technical Memorandum
TM No. 76-48
March 9, 1976
Contract No. N00017-73-C-1418

Copy No. 16

The Pennsylvania State University
Institute for Science and Engineering
APPLIED RESEARCH LABORATORY
Post Office Box 30
State College, PA 16801

NAVY DEPARTMENT

NAVAL SEA SYSTEMS COMMAND

UNCLASSIFIED
SECURITY CLASSIFICATION OF THIS PAGE (When Data Entered)

REPORT DOCUMENTATION PAGE

READ INSTRUCTIONS BEFORE COMPLETING FORM

1. REPORT NUMBER: TM 76-48
2. GOVT ACCESSION NO.:
3. RECIPIENT'S CATALOG NUMBER:

4. TITLE (and Subtitle): PROPELLER TIME-DEPENDENT FORCES DUE TO NONUNIFORM FLOW

5. TYPE OF REPORT & PERIOD COVERED: Ph.D. Thesis, May 1976

6. PERFORMING ORG. REPORT NUMBER: TM 76-48

7. AUTHOR(s): Donald E. Thompson

8. CONTRACT OR GRANT NUMBER(s): N00017-73-C-1418

9. PERFORMING ORGANIZATION NAME AND ADDRESS:
The Pennsylvania State University
Applied Research Laboratory
P. O. Box 30, State College, PA 16801

10. PROGRAM ELEMENT, PROJECT, TASK AREA & WORK UNIT NUMBERS:

11. CONTROLLING OFFICE NAME AND ADDRESS:
Naval Sea Systems Command
Department of the Navy
Washington, D. C. 20362

12. REPORT DATE: March 9, 1976

13. NUMBER OF PAGES: 225 pages & figures

14. MONITORING AGENCY NAME & ADDRESS(if different from Controlling Office):

15. SECURITY CLASS. (of this report): Unclassified, Unlimited

15a. DECLASSIFICATION/DOWNGRADING SCHEDULE:

16. DISTRIBUTION STATEMENT (of this Report)

Approved for public release, distribution unlimited,
per NSSC (Naval Sea Systems Command), 3/24/76

17. DISTRIBUTION STATEMENT (of the abstract entered in Block 20, if different from Report)

18. SUPPLEMENTARY NOTES

19. KEY WORDS (Continue on reverse side if necessary and identify by block number)

NON-UNIFORM FLOW
PREDICTION
PROPELLER
PROPULSOR BLADES
RADIATED NOISE
SPACE VARYING FLOW
THRUST RESPONSE
TIME DEPENDENT FORCES AND MOMENTS
TIME VARYING FLOW
TURBULENT INFLOW
VIBRATION

20. ABSTRACT (Continue on reverse side if necessary and identify by block number)

The ability to accurately predict the magnitude and phase of the time-dependent forces and moments generated by the blades of a propulsor is important due to the possible resulting vibrations and/or radiated sound. The present thesis considers the time-dependent thrust response of an open propeller due to operating in both spatially and temporally varying flows.

The experimental investigation consisted of measuring, in a water tunnel, the time-dependent thrust generated by a series of propellers operating

DD FORM 1 JAN 73 1473 EDITION OF 1 NOV 65 IS OBSOLETE

UNCLASSIFIED
SECURITY CLASSIFICATION OF THIS PAGE (When Data Entered)

20. ABSTRACT (continued)

first in various spatially nonuniform inflows and then in various turbulent inflows. The spatial variations were generated by an upstream strut, and the turbulence was generated by square mesh grids placed upstream of the propeller. Three propellers were considered. Measurements were made with each propeller operating over a range of advance ratios for each nonuniform inflow condition considered.

The analytical investigation considered several different methods for predicting both the propeller response to spatial and to temporal variations in the inflow. With respect to spatial variations, both an unsteady, two-dimensional airfoil theory and an unsteady, three-dimensional lifting surface theory are considered. With respect to temporal variations, two different unsteady, two-dimensional theories were employed, one considering blade-to-blade correlations, one which does not.

A correlation of the experimental and analytical results indicates several things. The unsteady, two-dimensional theory, with proper corrections, predicts the propeller time-dependent thrust more accurately than the unsteady, three-dimensional, lifting surface theory for response to spatial variations. For response to temporal variations in the inflow, the analytical method which considers blade-to-blade correlations predicts the propeller time-dependent thrust response more accurately than the method without the blade-to-blade correlations.

THESIS ABSTRACT

The objective of the investigation reported in this thesis is to study, both analytically and experimentally, various aspects of the time-dependent forces and moments generated by marine propellers due to operating in a nonuniform velocity field. The response of a propeller to both a spatially and temporally nonuniform flow field is considered. The propeller time-dependent response to each type of nonuniform flow is treated analytically and predictions are made which are compared to experimentally determined values of unsteady propeller thrust.

Two fundamentally different analytical approaches are considered for predicting response to spatial variations in the inflow. One approach employs a modified unsteady, two-dimensional airfoil theory. Included in this application are the response of the propeller to sinusoidal velocity variations which are both normal and parallel to the propeller blade section chordlines. A quasi-steady correction for blade-to-blade induction effects is included. The second approach employs a lifting surface theory developed at the Stevens Institute of Technology.

An experimental program was conducted in which measurements of the time-dependent thrust generated by a series of propellers operating in a strut wake were made. Variables in the experiment included the advance ratio of the propeller and the spatial separation between the propeller and strut. These measured values are compared to predictions made with the different analytical methods. Conclusions are then drawn with respect to the merits of the different analytical methods.

An existing analytical approach to the propeller time-dependent thrust response to turbulent inflows has been extended. The original approach did not include blade-to-blade correlations of the time-dependent lift. This blade-to-blade correlation was included.

An experiment was conducted in which measurements of the time-dependent thrust generated by a series of propellers operating in various turbulent inflows were made. Variables in the experiment were turbulence intensity and length scale. These measured values are compared to predictions made with the analysis which does not include blade-to-blade correlations and the analysis which includes blade-to-blade correlations. Conclusions are then drawn with respect to the merits of the different analytical methods.

It is shown that the contribution to propeller time-dependent thrust due to velocity variations parallel to the blade chordlines can be significant at certain propeller advance ratios. In addition, the quasi-steady correction for induced effects to the two-dimensional analytical method produces results which agree well with those from the lifting surface theory. The analytical method for propeller response to a turbulent inflow which includes blade-to-blade correlation of time-dependent lift predicts the level and shape of the time-dependent thrust spectra more accurately than the analysis which does not include blade-to-blade correlation.

ic

ACKNOWLEDGMENTS

The author gratefully acknowledges the many people associated with the Applied Research Laboratory at The Pennsylvania State University who have helped in the successful completion of this dissertation. Professor Robert E. Henderson, thesis advisor, provided many helpful suggestions and guidance throughout the course of the research as well as the other members of the doctoral committee, Professor Joseph Eisenhuth, B. Lakshminarayana, Gerhard Reethof and Allan Krall. Mr. Wilden Nuss provided invaluable assistance in setting up the data acquisition system, acquiring the data, and in data analysis.

The author wishes to thank Dr. Blaine R. Parkin, Director of the Garfield Thomas Water Tunnel, for granting permission to work on this dissertation. Appreciation is expressed to Dr. Maurice Sevik of the David Taylor Naval Ship Research and Development Center, and formerly Director of the Garfield Thomas Water Tunnel, for suggesting the thesis topic.

This research was supported by the Applied Research Laboratory of The Pennsylvania State University under contract with the U. S. Naval Sea Systems Command.

TABLE OF CONTENTS

TABLE OF CONTENTS (Cont.)

TABLE OF CONTENTS (Cont.)

LIST OF TABLES

LIST OF FIGURES

LIST OF FIGURES (Cont.)

LIST OF FIGURES (Cont.)

LIST OF FIGURES (Cont.)

LIST OF FIGURES (Cont.)

LIST OF FIGURES (Cont.)

NOMENCLATURE

a	Ω/U
a_o	zeroth order Fourier coefficient
a_n	n^{th} order Fourier coefficient
B	number of propeller blades
b	airfoil semi-chord
b_j	semi-chord of propeller blade at the j^{th} spanwise element
b_n	n^{th} order Fourier coefficient
C_L	lift coefficient of propeller blade section in steady flow
c_{nj}	n^{th} order complex Fourier coefficient of the inflow to the propeller at the j^{th} spanwise element
$C(k)$	Theodorsen's function
D_p	propeller diameter
$\tilde{F}_x$	time-dependent transverse force in the x-direction (Figure 14) generated by the propeller
$\tilde{F}_y$	time-dependent transverse force in the y-direction (Figure 14) generated by the propeller
$\tilde{F}_z$	time-dependent transverse force in the z-direction (Figure 14) generated by the propeller
$(\tilde{F}_x)_m$	time-dependent transverse force in the x-direction generated by the propeller at blade rate frequency and harmonics ($mB\Omega$)
$(\tilde{F}_y)_m$	time-dependent transverse force in the y-direction generated by the propeller at blade rate frequency and harmonics ($mB\Omega$)
$(\tilde{F}_z)_m$	time-dependent transverse force in the z-direction generated by the propeller at blade rate frequency and harmonics ($mB\Omega$)

NOMENCLATURE (Cont.)

$(\tilde{F}_x)_{jn}$	time-dependent transverse force in the x-direction generated by the j^{th} element of a propeller blade due to the n^{th} harmonic component of the propeller inflow
$(\tilde{F}_y)_{jn}$	time-dependent transverse force in the y-direction generated by the j^{th} element of a propeller blade due to the n^{th} harmonic component of the propeller inflow
$(\tilde{F}_z)_{jn}$	time-dependent transverse force in the z-direction generated by the j^{th} element of a propeller blade due to the n^{th} harmonic component of the propeller inflow
$f_m(q,\phi_\alpha)$	function which results from separating ϕ_α from the Kernel function
J	advance ratio, U/ND_p
$\bar{K}_t$	thrust coefficient based upon steady component of thrust, $\bar{T}/\rho_f n^2 D_p^4$
$\tilde{K}_t$	time-dependent thrust coefficient based upon amplitude of harmonic of thrust, $T/\rho_f n^2 D_p^4$
k	reduced frequency, $\omega b/U$
k_{nj}	reduced frequency at the j^{th} blade element due to the n^{th} harmonic component of propeller inflow, nNb_j/U_{rj}
$K(k)$	Sears' function
$K(r,\phi_o;\rho,\theta_o;q)$	Kernel of integral equation
$\bar{K}(\quad)$	Kernel after θ_α-integration and ϕ_α-integration
L_u	time-dependent lift per unit span on an airfoil operating in a sinusoidally varying velocity field parallel to the airfoil's chordline
L_v	time-dependent lift per unit span on an airfoil operating in a sinusoidally varying velocity field normal to the airfoil's chordline
$\tilde{L}_{jn}$	time-dependent lift on the j^{th} element of a propeller blade due to the n^{th} harmonic component of the propeller inflow
$\tilde{L}_{\ell jn}$	time-dependent lift on the j^{th} element of the ℓ^{th} propeller blade due to the n^{th} harmonic component of the propeller inflow

NOMENCLATURE (Cont.)

$\tilde{L}^{(\bar{n})}(\rho)$	spanwise loading components (coefficients of Birnbaum distribution)
$\tilde{M}_{jn}$	time-dependent moment on the j^{th} element of a propeller blade due to the n^{th} harmonic component of the propeller inflow
$\tilde{M}_{\ell jn}$	time-dependent moment on the j^{th} element of the ℓ^{th} propeller blade due to the n^{th} harmonic component of the propeller inflow
m	order of harmonic of propeller time-dependent forces and moments
N	propeller rotational frequency in revolutions per second
n	order of the harmonic content of the propeller inflow
P	number of spanwise elements per blade
$\Delta P(\xi,\rho,\theta_o)$	perturbation pressure at the loading point
$Q_{m-1/2}(\quad)$	Legendre spherical function of half odd-integer order
q	order of blade harmonic, ω/Ω
R	Descartes distance
R_{TIP}	propeller tip radius
r	radial coordinate in cylindrical polar coordinate system
r_j	radial location of the j^{th} spanwise blade element
Δr_j	spanwise extent of the j^{th} spanwise blade element
S	lifting surface
$S(\rho,\theta_o)$	blade loading distribution
$\tilde{T}_x$	time-dependent moment about the x-axis generated by the propeller
$\tilde{T}_y$	time-dependent moment about the y-axis generated by the propeller

NOMENCLATURE (Cont.)

$\tilde{T}_z$	time-dependent moment about the z-axis generated by the propeller
$(\tilde{T}_x)_m$	time-dependent moment about the x-axis generated by the propeller at blade rate frequency and harmonics ($mB\Omega$)
$(\tilde{T}_y)_m$	time-dependent moment about the y-axis generated by the propeller at blade rate frequency and harmonics ($mB\Omega$)
$(\tilde{T}_z)_m$	time-dependent moment about the z-axis generated by the propeller at blade rate frequency and harmonics ($mB\Omega$)
$(\tilde{T}_x)_{jn}$	time-dependent moment about the x-axis generated by the j^{th} element of a propeller blade due to the n^{th} harmonic component of the propeller inflow
$(\tilde{T}_y)_{jn}$	time-dependent moment about the y-axis generated by the j^{th} element of a propeller blade due to the n^{th} harmonic component of the propeller inflow
$(\tilde{T}_z)_{jn}$	time-dependent moment about the z-axis generated by the j^{th} element of a propeller blade due to the n^{th} harmonic component of the propeller inflow
$T(k)$	Horlock's function
t	time
U	free stream velocity
U_j	induced velocity at the j^{th} blade element
U_L	local steady velocity in the axial direction
U_{Rj}	resultant steady velocity at the j^{th} section of a propeller blade
u_o	amplitude of time-dependent velocity parallel to airfoil's surface
u_{nj}	n^{th} harmonic component of the time-dependent velocity parallel to the j^{th} section of a propeller blade
$u(x,t)$	time-dependent velocity parallel to airfoil's surface
$u(r,\theta)$	axial velocity component at polar position (r,θ)

NOMENCLATURE (Cont.)

V_a	speed of advance
$V_N^n(r)$	known amplitude of velocity normal to helicoidal surface
v_{nj}	n^{th} harmonic component of the time-dependent velocity normal to the j^{th} section of a propeller blade
$v(x,t)$	time-dependent velocity normal to airfoil's chordline
W	amplitude of time-dependent velocity normal to airfoil's chordline
X	distance from strut trailing edge to propeller leading edge plane
α	steady angle of attack measured from zero lift line
α_j	steady angle of attack at the j^{th} element of a propeller blade measured from the zero lift line of that section
β	one-half of the spanwise extent of a typical spanwise element
β_j	angle between resultant velocity vector and rotational velocity vector at the j^{th} element
η_ℓ	phase angle due to blade separation
Θ	$\overline{\theta}_n+\theta_o-\phi_0-a(\tau-\chi+\xi)$
θ	angular coordinate in the cylindrical polar coordinate system
θ_o	initial angular position of loading point in propeller plane
θ_α	angular chordwise location of loading point
θ_b	projected propeller semi-chord length, in radians
$\overline{\theta}_n$	$2\pi(n-1)/N$; $n=1,2,\ldots,N$
ξ	axial coordinate of loading point in the cylindrical polar coordinate system
ρ	radial coordinate of loading point in the cylindrical polar coordinate system

NOMENCLATURE (Cont.)

ρ_f	density of fluid
τ,τ'	variables of integration
ϕ	angular coordinate of the control point in the cylindrical polar coordinate system
ϕ_o	initial angular position of the control point in the propeller plane
ϕ_j	phase angle of the j^{th} blade element
$\phi_{\ell j}$	$\psi_j + \eta_\ell$
ϕ_α	angular chordwise location of control point
χ	$[\Theta-\theta_n+\phi_o-\theta_o]/a-(x-\xi)$
ψ_j	phase angle of the j^{th} blade element due to blade skew
Ω	angular velocity of the propeller, RPM
ω	frequency

CHAPTER I

INTRODUCTION AND SCOPE

Propeller-induced ship vibrations have become increasingly important in recent years due to the increased size and horsepower per shaft of new ships. Ship vibrations are caused by the vector sums of several time-dependent forces and moments which are due to the operation of the propeller in the wake of the ship. The components of the vector sums of the time-dependent forces and moments may be thought of as (1) those transmitted by the bearings of the propeller shaft which are due to time-dependent propeller loads, and (2) those transmitted by the hull near the propeller, by bossings, and by appendages near the propeller which are due to the near-field pressures induced by the propeller.

The time-dependent forces and moments generated by a propeller operating in the wake of a ship are due to variations in the propeller inflow velocity field. These velocity variations can be thought of as composed of temporal variations due to turbulence and time-dependent motions of the ship and of spatial variations of the steady velocity field.

Various aspects of propeller time-dependent forces and moments have been investigated. Several analytical methods exist for the prediction of propeller time-dependent forces and moments due to operation in either a spatially or temporally varying velocity field. In addition, the time-dependent forces and moments generated by various propellers operating over a range of conditions due to

operating in a variety of spatially and temporally varying velocity fields have been measured. In some instances, the predicted and measured values have been correlated.

The result of these previous investigations is that certain inadequacies in the existing analytical methods results in unacceptable differences between predicted and measured values. The intent of the present investigation is to either modify existing methods or generate new methods for predicting propeller time-dependent forces and moments which result in improved predictions. The results of each new analytical method is to be compared to experimental results from tests which are designed to investigate each particular propeller or flow variable of interest.

The limitations of the current investigation are with respect to both the flow and the propeller configuration. The flow is restricted to one that is incompressible and inviscid. In addition, the experimental investigation was conducted in the forty eight inch diameter water tunnel of the Applied Research Laboratory at The Pennsylvania State University and the flow regime with respect to the propeller was noncavitating. The propeller blades employed in the experiments had a nonskewed, rectangular planform and an aspect ratio of three.

The approach taken is as follows. An extensive literature survey was conducted, the results of which are described in Chapter II. The nonuniform inflow velocity field at the propeller is considered. The resulting propeller time-dependent forces and moments from both an experimental and analytical viewpoint are considered. And finally, the previous correlations between analysis and experiment are considered.

Chapter III discusses the theories for propeller time-dependent forces and moments due to operation in spatially nonuniform flow. The two-dimensional, unsteady airfoil theory and its application to propellers is discussed. The three-dimensional, unsteady lifting surface theory is also presented.

The experimental investigation of the propeller response to spatially nonuniform inflows is considered in Chapters IV and V. The generation and measurement of a spatially nonuniform inflow is discussed in Chapter IV. The measurement of the time-dependent thrust response to the spatially nonuniform inflow is considered in Chapter V.

The results of the experiments to measure propeller time-dependent thrust and correlation with the results of various analyses is presented in Chapter VI.

The development of a new method for predicting propeller time-dependent thrust response to turbulent inflows is presented in Chapter VII. Chapter VIII discusses the methods for generating particular turbulent inflows and the measurement of propeller time-dependent thrust response due to operation in those turbulent flows. The following chapter presents correlations of the experimental results with the results from analysis.

Based on the results of the investigation, conclusions are drawn and recommendations for future research are made.

CHAPTER II

STATE OF THE ART OF PROPELLER TIME-DEPENDENT FORCES

2.1 Introduction

Propeller-induced ship vibrations have become increasingly important in recent years due to the increased size and horsepower per shaft of new ships. Ship vibrations are caused by the vector sums of several time-dependent forces and moments which are due to the operation of the propeller in the wake of the ship. The components of the vector sums of the time-dependent forces and moments may be thought of as (1) those transmitted by the bearings of the propeller shaft which are due to time-dependent propeller loads, and (2) those transmitted by the hull near the propeller, by bossings and by appendages near the propeller which are due to the near-field pressures induced by the propeller.

The time-dependent forces and moments which are transmitted by the bearings of the propeller shaft will be considered in this investigation. The existing theoretical approaches for predicting propeller-induced bearing forces and moments are discussed. Also considered are correlations between experimental results and the various existing theoretical approaches. Since the inflow to the propeller plays such an important part in the generation of time-dependent forces and moments, a discussion of the propeller flow environment is also given.

2.2 Propeller Inflow Environment

A ship propeller operates in a spatially and temporally varying velocity field. The temporal variations are due to turbulence in the flow, wave-induced effects and to motions of the ship. The spatial variations are due to the potential and viscous effects of the flow around the hull of the ship. The spatial variation is periodic along a trajectory described by the motion of an element of a propeller blade, while the temporal variations are random. The velocity field also varies along the propeller radius.

Let us consider the manner in which the spatially varying propeller inflow is generated. For the sake of simplicity, consider first the flow over a symmetric body of revolution, as shown in Figure 1a. Of particular interest is the flow field in a plane perpendicular to the axis of symmetry at a point just downstream of the body of revolution. A potential flow solution to this problem would yield the effects on the axial component of the velocity field due to the geometrical properties of the body. A radial component of velocity would exist, but this component is unimportant as far as time-dependent forces and moments are concerned, since it lies parallel to the blade surface. Due to the axisymmetry of the body, no component of velocity in the tangential direction would exist.

If viscous effects are considered, the boundary layer on the surface of the body will result in a radial variation of the axial component of the velocity field apart from that due to the potential flow. Figure 1b is a polar plot of the circumferential distribution of axial velocity at various radii in a plane perpendicular to the axis of symmetry located just aft of the body.

Consider, now, the velocity field just aft of an axisymmetric body of revolution upon which has been mounted a protuberance, such as a strut, normal to the surface. Due to the viscous flow over the strut, the axial component of the velocity downstream of the strut will be reduced except in the region where the strut and body intersect. Hawthorne [1] has shown that when a strut exists in an approaching velocity field that varies along the span of the airfoil, streamwise vorticity is generated. The boundary layer on the body considered here, interacting with the strut will produce such streamwise vorticity. The effects are twofold: the secondary vorticity introduces a component of velocity in the tangential direction, and high-energy fluid is entrained into the region downstream of the intersection of the strut and body. Figure 2 is a polar plot of the axial velocity distributions just aft of a body of revolution on which a strut has been mounted.

The spatially varying velocity field in the propeller plane of a ship is caused by the same physical phenomena described above. Real flow effects due to the boundary layer on the ship's hull and potential-flow effects combine to produce the spatial variations in the axial and tangential components of the velocity field in the propeller plane. The distributions of the axial and tangential components of the velocity in the propeller plane of one particular ship are shown in Figure 3. The distributions of the various velocity components in the propeller plane on a large variety of ships have been measured [2, 3].

In the design and analysis of propellers, it is convenient to represent the axial and tangential velocity distributions in terms of Fourier series. This representation is possible because the velocity

distributions are periodic and continuous, as shown in Figure 3. For example, the axial component of the velocity at a position (r,θ) can be expressed as

$$u(r,\theta) = 1/2\ a_o(r) + \sum_{n=1}^{\infty} (a_n(r) \cos n\theta + b_n(r) \sin n\theta) \quad ,$$

where $a_o(r)$, $a_n(r)$, and $b_n(r)$ are the Fourier coefficients defined in the usual manner. The harmonic content of the axial velocity in the propeller plane of a typical ship is shown in Figure 4. The important feature to notice in Figure 4 is the rapid decrease in amplitude of the harmonic constituents as the order of the harmonic increases.

The axial, tangential, and radial velocity distributions must be obtained experimentally. The harmonic content of the velocity distributions is then determined from the experimentally obtained velocity distributions. Both the data acquisition and analysis techniques are well known and will not be discussed here. Three items will be discussed that relate to the experimental determination of velocity distributions: (1) scale effect for model tests, (2) the effect of the propeller on the velocity distribution, and (3) the repeatability of wake-survey data.

Tjoenneland [4] has investigated the repeatability of experimental velocity distributions and the Fourier coefficients calculated from the velocity distributions. It is shown that the measurement of local velocity is repeatable to within ± 2 to 3 percent. The repeatability of the Fourier coefficients varies with the order of the coefficient as shown in Figure 5. It is seen that, as the order of the

coefficient increases, the percentage deviation from the mean increases. After the sixth harmonic, the deviation is from ± 30 to ± 100 percent of the mean.

Most wake surveys have been made in the absence of the propeller. The effect of the propeller on the inflow velocity field has been studied by Burstein [5]. The harmonic content of the axial component of the propeller inflow velocity has been determined for a body of revolution with fins both with and without propeller. The results of this study are shown in Figure 6. The propeller is shown to have a substantial effect on certain harmonics of the propeller inflow. This effect can be attributed to both a change in the potential flow around the body and a change in the boundary layer due to the presence of the propeller.

Most wake surveys performed on ship models are conducted at Froude numbers corresponding to the full-size ship; however, if Froude number scaling is achieved, then Reynolds number scaling will not be achieved. As discussed before, the spatially varying velocity field in the propeller plane is formed, in part, by the boundary layer on the ship's hull, which is Reynolds number dependent. Several studies have considered the Reynolds number dependency of the velocity distributions on the harmonic content of the wake.

The velocity distributions in the propeller plane of seven models of Victory ships ranging in scale from 18 to 50 were made by van Manen and Lap [3]. The results show that the difference between maxima and minima of the velocity distributions is independent of Reynolds number. It is also shown that, with an increase in Reynolds number, the width of the wake decreases due to the thinner boundary

layer. Hadler and Cheng [2], in determining the harmonic content of the wakes measured by van Manen and Lap [3], found the variation of the relative amplitude of the harmonics with Reynolds number to be unimportant. Boyle [6] reached the same conclusion based on wake surveys made on a body of revolution with fins.

The measurement of the important flow quantities, intensities and length scales, for the turbulent flow at the propeller leading edge planes for typical marine vessels is currently in progress. Previous measurements of intensities and cross-power spectral densities have been made by Burstein [5] in the propeller plane of an axisymmetric body with fins.

2.3 Time-Dependent Propeller Forces

2.3.1 Theory. As just discussed, a ship propeller operates in a rather complex spatially varying velocity field. As also discussed, this spatially varying velocity field can be represented as a sum of sinusoidally varying components with various amplitudes and frequencies. A propeller blade operating in such a sinusoidally varying velocity field will experience a sinusoidal change in angle of attack at any blade element and, hence, a sinusoidal variation in blade loading will occur. The analogous situations of a two-dimensional airfoil moving through a sinusoidally varying velocity field normal to and parallel to the airfoil have been studied by Sears [7] and Horlock [8], respectively. These time-dependent forces on the propeller blades are transmitted as vibratory forces and moments through the propeller shaft and bearing to the ship's structure.

The fundamentally different theories for predicting the time-dependent vibratory forces and moments caused by a propeller operating in a given spatially varying velocity field can be divided into the following catagories: (1) quasi-steady using uniform flow tests, (2) quasi-steady using steady-state lifting-line theory (3) two-dimensional unsteady, (4) combination quasi-steady and two-dimensional, and (5) three-dimensional unsteady lifting surface. A good review of the assumptions made in and the results obtained by using each of these theories for a particular propeller operating in a given spatially varying inflow has been given by Boswell [9]. Figure 7 shows the nondimensional blade frequency thrust and torque, respectively, versus the expanded area ratio of the propeller blade as calculated by each theoretical method and as obtained experimentally. This figure shows that the three-dimensional unsteady lifting surface theory yields unsteady thrust and torque values that are in close agreement with the experimental values. The other theories, being essentially two-dimensional, ignore the three-dimensional induction effects inherent in the low-aspect ratio blades encountered in marine propulsion. In addition, the phase of the unsteady propeller forces and moments is not predicted correctly by two-dimensional theory.

The two-dimensional theory, however, does predict the proper trend of time-dependent thrust magnitude with expanded area ratio.

Both the three-dimensional lifting surface theory and the two-dimensional strip theory employed by Boswell [9] ignore the previously mentioned effects of chordwise velocity variations on the propeller time-dependent forces and moments. One objective of the present thesis is to investigate the effects of chordwise velocity

variations, using the two-dimensional theory, on propeller time-dependent thrust.

A more detailed discussion of the three-dimensional unsteady lifting surface theory and the two-dimensional unsteady theory will be given in a subsequent chapter.

Henderson [10] and Whitehead [11] have developed response functions which account for blade-to-blade interaction. In Henderson's calculations, the subject blade is represented by continuous vortex distribution along the blade chord and the other blades in the cascade are represented by a single vortex located at the quarter-chord of each blade. The vorticity in the wake of each blade is represented by a continuous vortex distribution. Parameters taken into account by Henderson's analysis are the reduced frequency, the space-to-chord ratio, the phase angle between adjacent blades and the stagger angle. In Whitehead's analysis, all blades are represented by a finite number of vortices and a vortex distribution represents the vorticity in the wake of each blade. The parameters taken into account by Whitehead's analysis are reduced frequency, space-to-chord ratio, stagger angle, and phase angle between adjacent blades. Henderson's analysis is for cambered airfoils while Whitehead's analysis is for flat plate airfoils.

Henderson [10] has made comparisons of results of his analysis and Whitehead's [11] analysis for a stagger angle of 45°, with space-to-chord ratios of $s/c = 1.0$ and 2.0, for reduced frequencies from 0 to 2.4. Figures 8 and 9 show the comparisons for $s/c = 2.0$ and $s/c = 1.0$, respectively. Figure 8 also includes the results of Sears' [7] analysis which corresponds to $s/c = \infty$. The figures show

both the magnitude of the unsteady lift coefficient and the phase angle referenced to the blade leading edge versus reduced frequency. Good agreement between both the magnitude and phase as predicted by the methods of Henderson and Whitehead is obtained except at certain resonance conditions in Henderson's analysis. The resonance conditions occur when the circumferential wavelength of the sinusoidal velocity disturbance in the inflow to the blade row is equal to the blade spacing or some multiple.

Included in Figure 8 is the response as predicted by Sears' [7] analysis. Good agreement is obtained in the magnitude of the unsteady lift coefficient and phase above reduced frequencies of about 0.4.

Let us consider the analytical treatment of the time-dependent shaft forces developed by a propeller operating in a turbulent inflow. Until very recently, all analyses considered the propeller response to homogeneous, isotropic turbulence only, e.g., Sevik [12], [13], Mani [14], Mugridge [15], and Robbins and Lakshminarayana [16]. The turbulence is assumed to be stationary and the longitudinal velocity correlation is of the type exp(-r/L).

The response function used in most analyses is that due to Sears [7], which is described in detail in Section 3.2. It is assumed that the fluid in which the propulsor operates is incompressible and inviscid. Further, the propulsor blades are assumed to be two-dimensional, isolated airfoils with small camber (i.e., lightly loaded). The unsteady lift on the airfoil is determined for a sinusoidal type gust acting normal to the airfoil.

The Sears function has been employed by Sevik [12] who considers the time-dependent thrust response of a propulsor due to operating in

a turbulent inflow. A problem of considerable practical importance at the present is radiated sound from propulsors due to fluctuating blade lift which results from fluctuations in the inlet velocity. In considering this problem, Sevik [13], Mani [14], Mugridge [15], and Robbins and Lakshminarayana [16] have employed Sears' function to determine the fluctuating blade lift for a given configuration.

In addition, Robbins and Lakshminarayana [16] have employed response functions which account for blade-to-blade interaction as developed by Henderson [10] and Whitehead [11].

Barlow [17, 18] has considered the response of the propulsors of VSTOL aircraft to atmospheric turbulence. The assumptions made in the analysis are the following. The propeller is represented by a set of rotating lines. The propeller centerline is not coincident with the free stream velocity vector, i.e., yaw or pitch is taken into account. The time-dependent lift and drag terms are based on quasi-steady theory. The assumptions used in obtaining, and the results due to, the quasi-steady theory are discussed by Boswell [9].

2.3.2 Experimental Apparatus. Systems for measuring time-dependent forces and moments have been developed at several facilities. Miller [19] and Brandau [20] describe the design of the six-component balance in use at the David W. Taylor Naval Ship Research and Development Center (DTNSRDC). This balance utilizes semiconductor strain gages as sensing elements. Calibration methods and data acquisition and analysis techniques employed at DTNSRDC are also discussed. A six-component balance described by Wereldsma [21] for measuring time-dependent forces and moments generated by a propeller

is in use at the Netherlands Ship Model Basin (NSMB). A system utilizing a piezoelectric crystal as a sensing element has been developed at the Applied Research Laboratory of The Pennsylvania State University for measuring time-dependent propeller thrust [22]. A more detailed discussion of this device is presented in Section 5.2.

2.3.3 Correlation of Theoretical and Experimental Propeller Time-Dependent Forces. Several studies have been made of the correlation between theoretical and experimental time-dependent forces and moments generated by propellers operating in a spatially nonuniform inflow. In the earliest study, made by Lewis [23], the vibratory force due to a propeller operating on a ship model was measured by using a null technique. The experimentally determined propeller forces were correlated with a quasi-steady theory.

Wereldsma [24 - 26] measured the time-dependent thrust and torque on a series of three- and five-bladed model propellers operating in the wake shed from a three-bladed or five-bladed "cross-plate" wake generator. The effect on time-dependent propeller thrust and torque of variations in blade area ratio, advance ratio, skew, Reynolds number, and blade gap (or number of blades) was studied experimentally. These results are compared to time-dependent propeller thrust and torque as predicted by a method based on two-dimensional unsteady airfoil theory. The trends of the measured values are in accordance with the theory for variations in blade number and advance ratio. But the two-dimensional theory yields trends that are opposite to experimental results when variation in blade area ratio is considered.

Jacobs and Tsakonas [27] correlated the experimental values of time-dependent propeller thrust and torque obtained by Wereldsma [25, 26] with values predicted by the three-dimensional, unsteady lifting-surface theory discussed previously. The results show that the trends of vibratory thrust and torque with change in blade area ratio, blade number, blade skew, and wake-generator vane length are accurately predicted, but that large discrepancies in magnitude are present. These discrepancies are attributed to the presence of the open-water boat boundary, insufficiencies of wake data, and the omission of the effects of viscosity and blade thickness from the theory. Another possibility is the effect of chordwise velocity variations.

As discussed previously, Boswell [9] measured the time-dependent forces and moments generated by a series of three-bladed propellers operating in a spatially nonuniform velocity field generated by a wake screen. The measured values were correlated with values predicted by several theoretical approaches. As shown in Figure 7, the three-dimensional, unsteady lifting-surface theory correlates quite well with experimental values. Boswell found that the trends and amplitudes of time-dependent propeller thrust, torque, side forces, and bending moments with variations in propeller expanded area ratio are predicted accurately by the unsteady lifting-surface theory.

Experimental and unsteady lifting-surface theoretical values of single-amplitude time-dependent thrust for five- and seven-bladed propellers operating in the wake shed from a model have been correlated by Tsakonas et al. [18]. The comparison between experimental and theoretical values is good.

2.4 Summary

It has been shown that, of all existing theories, the three-dimensional, unsteady lifting surface theory provides the best prediction of propeller time-dependent forces and moments due to operation in a spatially varying inflow velocity field when compared to experimental values. It has also been shown that the two-dimensional, unsteady theory predicts the proper trends of propeller time-dependent thrust with variations in important geometrical and operating parameters of the propeller. However, the magnitude of the predicted values is higher than experimental values.

The computer analysis required in applying the three-dimensional, unsteady lifting surface theory is much more time consuming, and hence expensive, than that required in applying the two-dimensional, unsteady theory. It would be advantageous to apply a simple correction to the two-dimensional, unsteady theory to account for the induced effects which are inherent in the three-dimensional, unsteady lifting surface theory.

Neither the three-dimensional, unsteady lifting surface theory nor the two-dimensional, unsteady theory for propeller time-dependent forces and moments include the effects of chordwise velocity variations. As discussed by Horlock [8], the time-dependent lift due to chordwise velocity variations can be, for certain pitch angles, an appreciable part of the total time-dependent lift generated by an airfoil operating in a mean flow with superposed sinusoidally varying velocity field. The inclusion of the effects of chordwise velocity variations into the two-dimensional, unsteady theory would therefore be advantageous. This is one objective of the present thesis.

CHAPTER III

THEORY OF PROPELLER TIME-DEPENDENT THRUST DUE TO OPERATION IN SPATIALLY NONUNIFORM INFLOW

3.1 Introduction

The present thesis considers two analytical approaches and compares the results of each approach with experimental results. As discussed in the preceding chapter, it has been shown by Boswell [9] that the three-dimensional, unsteady lifting surface theory and the two-dimensional, unsteady theory predicted propeller time-dependent thrust most accurately. As a consequence, these two theoretical approaches will be employed here.

The three-dimensional, unsteady lifting surface theory as developed by Tsakonas et al. [29] will be employed. No attempts to improve upon the existing analysis have been made.

The two-dimensional, unsteady theory has been improved in two ways from that used by Boswell [9]. A correction for the effects of blade-to-blade induction has been made. In addition, the contribution to propeller time-dependent forces and moments due to velocity variations parallel to the chordline of the blades has been incorporated in the theory. Development of the improved two-dimensional, unsteady theory follows.

3.2 Two-Dimensional, Unsteady Airfoil Theory

Since one theory used in this investigation is based on two-dimensional, unsteady airfoil theory, a brief description of the assumptions and conclusions which apply to this theory may be helpful.

The fluid in which the propeller operates is assumed to be incompressible and inviscid. Furthermore, the propeller blades are assumed to be two-dimensional, isolated airfoils with small camber (i.e., lightly loaded). The airfoil is assumed to be replaced by a vortex distribution as is the wake shed by the airfoil. The unsteady lift on the airfoil is then determined for a sinusoidal-type gust acting normal to the airfoil. This is done by equating the velocity normal to the airfoil surface due to the gust to the normal velocity on the airfoil induced by the distributed vortices. An integral equation results with the unknown being the distributed vorticity.

The resulting integral equation can be inverted by using the Söhngen inversion equation. This inversion places the unknown vortex distribution outside of the integral and the known velocity distribution inside of the integral; hence, the unknown vortex distribution can be found. Knowing the vortex distribution, the pressure difference across the blade surface can be found and, therefore, the unsteady lift on the blade can be found.

Sears [7] has determined the unsteady lift on an airfoil which operates in a free-stream velocity with a superposed sinusoidal gust velocity which is normal to the airfoil surface, see Figure 10. If the coordinate axes are fixed to the airfoil with x=0 at the mid-chord, the vertical gust velocity is given by the expression

$$v(x,t) = W\, e^{i\omega(t - x/U)} \quad . \tag{1}$$

This equation expresses the fact that the sinusoidal gust with maximum single amplitude equal to W moves past the airfoil with the speed U.

Sears has shown that for an airfoil of semichord b, the unsteady lift due to a velocity distribution given by Equation (1) is

$$L_v = 2\pi \rho_f b U W e^{i\omega t} \{[J_o(k) - i J_1(k)] C(k) + i J_1(k)\} \quad , \qquad (2)$$

where

L_v ≡ lift per unit span,

κ ≡ reduced frequency = $\omega b/U$

and

$C(k)$ ≡ Theordorsen's function = $K_1(ik)/[K_o(ik) + K_1(ik)]$.

In Figure 11, the nondimensional lift, $L/\pi\rho_f 2b U W e^{i\omega t}$, is presented in the form of a vector diagram.

In addition to velocity variations normal to the airfoil surface, velocity variations parallel to the airfoil chord may exist. Horlock [8] has determined the unsteady lift on an uncambered airfoil operating in such a velocity field, which is given by

$$u(x,t) = u_o e^{i\omega(t - x/U)} \quad . \qquad (3)$$

Using a technique similar to that described above, Horlock has shown that the unsteady lift on an airfoil operating in a velocity field given by Equation (3) is

$$L_u = 2\pi U u_o b \alpha \rho_f e^{i\omega t} T(k) \quad , \qquad (4)$$

where

$$T(k) = (2 - a)\, J_o(k) - b\, J_1(k) + i\,[(a + 1)\, J_1(k) - b\, J_o(k)] \quad , \quad (5)$$

$$a + ib = \frac{K_o(ik)}{K_o(ik) + K_1(ik)} \quad (6)$$

and

$\alpha \equiv$ angle of attack measured from zero lift line.

The function T(k), known as the Horlock function, is plotted in Figure 12.

Holmes [30] and Naumann and Yeh [31] have developed functions which include the effects of camber on the unsteady lift generated by an isolated airfoil due to operating in a sinusoidally varying velocity parallel to the airfoil chordline.

Naumann and Yeh have considered a thin airfoil having a parabolic mean camber line. Using a vortex distribution to replace the airfoil and wake, an approach and method of solution like that of Sears [7] and Horlock [8] was taken. The result of Naumann and Yeh is an aerodynamic response function which varies with reduced frequency and, in addition to the effects considered by Sears [7] and Horlock [8], includes the effects of camber.

Holmes [30] has taken an approach similar to that of Naumann and Yeh [31] for airfoils having a camber line defined by

$$y = y_{max}\left(\frac{1 - \cos 2\theta}{2}\right) \quad .$$

His result is an aerodynamic response function which varies with reduced frequency.

The blades considered in the present investigation have no camber; therefore, the effects of camber are not to be included in the subsequent analysis.

3.3 Application of Two-Dimensional, Unsteady Airfoil Theory to Propellers

Let us consider first the inflow to the propeller in light of what has been discussed in the previous section. A typical circumferential distribution of axial velocity in the leading edge plane of a propeller is shown in Figure 3. The local velocity ratio U_L/U at any point of the wake is a function of the radial distance from the center of the hub, of angular position and of time, i.e.,

$$U_L/U = g\left(\frac{r}{R_{TIP}}, \theta, t\right) \quad . \tag{7}$$

Considering the time-mean of the wake pattern, U_L/U is not a function of time, therefore, at any given value of r/R_{TIP} = constant,

$$\left(U_L/U\right)_j = f_j(\theta) \quad . \tag{8}$$

Now, $f_j(\theta)$ is a continuous and periodic function and may, therefore, be approximated by a Fourier series, i.e.,

$$\left(U_L/U\right)_j = f_j(\theta) = \sum_{n=-\infty}^{\infty} c_{nj}\, e^{in\theta} \quad , \tag{9}$$

where

$$c_{nj} = \frac{1}{2\pi} \int_0^{2\pi} f_j(\theta)\, e^{-in\theta}\, d\theta \quad .$$

One can see by comparing Equations (9), propeller inflow velocity, and (1) or (3), nonuniform velocity used by Sears [7] and Horlock [8], that the circumferential distribution of axial, propeller inflow velocity at some value of radius along the propeller can be put in the form necessary to calculate the unsteady lift on the propeller blades.

Consider a typical propeller blade as shown in Figure 13a. The harmonic content of the axial component of the propeller inflow velocity at the j^{th} section of the blade can be determined. The j^{th} blade element is also subjected to a mean velocity, $U\, c_{oj}$, a circumferential velocity $r_j\Omega$ and an induced velocity U_j. A velocity triangle appropriate to the j^{th} blade element is shown in Figure 13b.

Let U_{Rj} be the resultant local velocity and α_j be the local steady angle of attack. The axial velocity fluctuations, given by Equation (9), must be resolved into components along and normal to the resultant velocity. The normal velocity component corresponding to the n^{th} Fourier component may be written as

$$v_{nj} = -U\, c_{nj} \cos \beta_j\, e^{in(\Omega t + \phi_j)} \quad . \tag{10}$$

The component in the direction of the resultant velocity is given by

$$u_{nj} = U\, c_{nj} \sin \beta_j\, e^{in(\Omega t + \phi_j)} \quad . \tag{11}$$

However, due to the motion of the blade through the wake and with the coordinate system fixed to the blade, Equations (10) and (11) become

$$v_{nj} = U\, c_{nj} \cos \beta_j e^{in \left(\Omega t - \frac{\Omega x_b}{U_{Rj}} + \phi_j \right)} \tag{12}$$

and

$$u_{nj} = c_{nj} \sin \beta_j\, e^{in \left(\Omega t - \frac{\Omega x_b}{U_{Rj}} + \phi_j \right)} \quad , \tag{13}$$

where x_b is measured along the blade chord.

Equation (12), for the normal velocity component corresponding to the n^{th} Fourier component, has the same form as Equation (1); therefore, the lift on the j^{th} blade element, by using Equation (2), can be written as

$$L_v = -2\pi \rho_j b_j\, U_{Rj}\, U\, c_{nj} \cos \beta_j\, e^{in(\Omega t + \phi_j)} \{ [J_o(k_{nj}) - i\, J_1(k_{nj})]\, C(k_{nj}) + i\, J_1(k_{nj}) \}\, \Delta r_j \quad . \tag{14}$$

Equation (13), for the velocity fluctuations in the direction of the resultant velocity corresponding to the n^{th} Fourier component, has the same form as Equation (3); therefore, the lift on the j^{th} blade element, by using Equation (4), can be written as

$$L_u = 2\pi\rho_f\, b_j\, U_{Rj}\, U\, c_{nj}\, \alpha_j \sin\beta_j\, e^{in(\Omega t + \phi_j)}\, \{T(k_{nj})\}\, \Delta r_j \quad . \quad (15)$$

The total unsteady lift on the j^{th} blade segment due to the n^{th} Fourier component of the propeller inflow is found by adding Equations (14) and (15), i.e.,

$$\tilde{L}_{jn} = -2\pi\rho_f\, b_j\, U_{Rj}\, U\, c_{nj}\, e^{in(\Omega t + \phi_j)}\, \{K(k_{nj}) \cos\beta_j - \alpha_j\, (T(k_{nj}) \sin\beta_j)\}\, \Delta r_j \quad , \quad (16)$$

where

$$K(k_{nj}) = C(k_{nj})\, [J_o(k_{nj}) - i\, J_1(k_{nj})] + i\, J_1(k_{nj})$$

and

$$k_{nj} = \frac{n\Omega\, b_j}{U_{Rj}} \quad .$$

The moment on the j^{th} blade segment, about the center of the propeller hub, due to the n^{th} Fourier component of the propeller inflow is given by

$$\tilde{M}_{jn} = 2\pi\rho_f\, b_j\, r_j\, U_{Rj}\, U\, c_{nj}\, e^{in(\Omega t + \phi_j)}\, \{K(k_{nj}) \cos\beta_j - \alpha_j\, (T(k_{nj}) \sin\beta_j)\}\, \Delta r_j \quad . \quad (17)$$

Equations (16) and (17) were derived from the equations for unsteady lift on an isolated airfoil operating in sinusoidal velocity disturbances normal to the airfoil's surface and along the airfoil's surface. Equations (16) and (17), however, are to be applied to a propeller where, for a large number of blades, the isolated airfoil concept will be invalid. The 2π component of Equations (16) and (17) may be thought of as the lift curve slope $(\partial C_L/\partial\alpha)$ for the two-dimensional isolated airfoil. To include the effects of adjacent blades on unsteady forces and moments, let us substitute the value of $(\partial C_L/\partial\alpha)$ for 2π at each blade segment considered, i.e., replace 2π at each blade segment considered, in Equations (16) and (17) by $(\partial C_L/\partial\alpha)_j$. Hence,

$$\tilde{L}_{jn} = \left(\frac{\partial C_L}{\partial \alpha}\right)_j \rho_f\, b_j\, U_{Rj}\, U_\infty\, c_{nj}\, e^{in(\Omega t + \phi_j)} \{K(k_{nj}) \cos\beta_j - \alpha_j\, T(k_{nj}) \sin\beta_j\}\, \Delta r_j \qquad (18)$$

and

$$\tilde{M}_{jn} = \left(\frac{\partial C_L}{\partial \alpha}\right)_j \rho_f\, b_j\, r_j\, U_{Rj}\, U_\infty\, c_{nj}\, e^{in(\Omega t + \phi_j)} \{K(k_{nj}) \cos\beta_j - \alpha_j\, T(k_{nj}) \sin\beta_j\}\, \Delta r_j \quad . \qquad (19)$$

The $(\partial C_L/\partial\alpha)_j$ term should then be determined from experimental data which reflects the cascade effects and airfoil section characteristics at each blade segment.

This correction is based on steady state experimental information and, therefore, will not reflect any variation with reduced frequency. The reduced frequency range considered in this investigation is relatively small, from about 0.3 to about 1.5. Analytical approaches, such as those due to Whitehead [11] and to Henderson and Daneshyar [32], could also be used to obtain a correction factor for unsteady blade-to-blade interaction effects.

3.4 Components of Force and Moment on a Propeller

Adopting the coordinate system shown in Figure 14, the following unsteady forces and moments due to the n^{th} harmonic component of the inflow act on the j^{th} blade element:

$$\left.\begin{aligned}
(\tilde{F}_z)_{jn} &= \tilde{L}_{jn} \cos \beta_j \\
(\tilde{F}_x)_{jn} &= \tilde{L}_{jn} \sin \beta_j \sin (\theta + \phi_j) \\
(\tilde{F}_y)_{jn} &= \tilde{L}_{jn} \sin \beta_j \cos (\theta + \phi_j) \\
(\tilde{T}_z)_{jn} &= \tilde{M}_{jn} \sin \beta_j \\
(\tilde{T}_x)_{jn} &= -\tilde{M}_{jn} \cos \beta_j \sin (\theta + \phi_j) \\
(\tilde{T}_y)_{jn} &= -\tilde{M}_{jn} \sin \beta_j \cos (\theta + \phi_j)
\end{aligned}\right\} . \qquad (20)$$

The unsteady forces and moments acting on a propeller are determined by summing the unsteady forces and moments for each blade element over all Fourier components corresponding to positive propeller rotation and then summing over all blade elements, i.e.,

$$
\left.
\begin{aligned}
\tilde{F}_z &= \sum_{j=1}^{p} \sum_{\ell=1}^{B} \sum_{n=1}^{\infty} \tilde{L}_{\ell jn} \cos \beta_j \\
\tilde{F}_x &= \sum_{j=1}^{p} \sum_{\ell=1}^{B} \sum_{n=1}^{\infty} \tilde{L}_{\ell jn} \sin \beta_j \sin (\theta + \phi_{\ell j}) \\
\tilde{F}_y &= \sum_{j=1}^{p} \sum_{\ell=1}^{B} \sum_{n=1}^{\infty} \tilde{L}_{\ell jn} \sin \beta_j \cos (\theta + \phi_{\ell j}) \\
\tilde{T}_z &= \sum_{j=1}^{p} \sum_{\ell=1}^{B} \sum_{n=1}^{\infty} \tilde{M}_{\ell jn} \sin \beta_j \\
\tilde{T}_x &= \sum_{j=1}^{p} \sum_{\ell=1}^{B} \sum_{n=1}^{\infty} -\tilde{M}_{\ell jn} \cos \beta_j \sin (\theta + \phi_{\ell j}) \\
\tilde{T}_y &= \sum_{j=1}^{p} \sum_{\ell=1}^{B} \sum_{n=1}^{\infty} -\tilde{M}_{\ell jn} \sin \beta_j \cos (\theta + \phi_{\ell j})
\end{aligned}
\right\} . \qquad (21)
$$

In Equations (21), the sum over the blade elements has been separated into a sum over P elements per blade and a sum over B blades. The quantity $\phi_{\ell j} = \Psi_j + \eta_\ell$, where Ψ_j is the phase angle due to blade skew and η_ℓ is the phase angle due to blade separation. The quantities $\tilde{L}_{\ell jn}$ and $\tilde{M}_{\ell jn}$ are the same as given in Equations (18) and (19) except that ϕ_j is replaced by $\phi_{\ell j}$.

It is shown in Appendix A that only certain harmonics of the propeller inflow contribute to the unsteady forces and moments on the propeller. Only those harmonics of the inflow which are integer multiples of the number of propeller blades (mB) contribute to the unsteady thrust $\tilde{F}_z$ and torque $\tilde{T}_z$. Only those harmonics of the inflow which are adjacent to the multiples of the number of propeller blades (mB±1) contribute to the unsteady side forces, $\tilde{F}_x$ and $\tilde{F}_y$, and bending

moments, $\tilde{T}_x$ and $\tilde{T}_y$. A summary of the sensitivity of various propellers to the harmonic components of the propeller inflow is given in Table 1.

From Appendix A, Equations (21) reduce to

$$\left.\begin{aligned}
(\tilde{F}_z)_m &= B \sum_{j=1}^{P} \{ | \tilde{L}_{j(mB)} |_1 \, e^{imB(\Omega t + \Psi_j)} \} \\
(\tilde{F}_x)_m &= \frac{B}{2} \sum_{j=1}^{P} \{ i \, [- | \tilde{L}_{j(mB-1)} |_2 + | \tilde{L}_{j(mB+1)} |_2] \times \\
&\qquad e^{imB(\Omega t + \Psi_j)} \} \\
(\tilde{F}_y)_m &= \frac{B}{2} \sum_{j=1}^{P} \{ [| \tilde{L}_{j(mB-1)} |_2 + | \tilde{L}_{j(mB+1)} |_2] \times \\
&\qquad e^{imB(\Omega t + \Psi_j)} \} \\
(\tilde{T}_z)_m &= B \sum_{j=1}^{P} \{ | \tilde{M}_{j(mB)} |_1 \, e^{imB(\Omega t + \Psi_j)} \} \\
(\tilde{T}_x)_m &= - \frac{B}{2} \sum_{j=1}^{P} \{ i \, [- | \tilde{M}_{j(mB-1)} |_2 + | \tilde{M}_{j(mB+1)} |_2] \times \\
&\qquad e^{imB(\Omega t + \Psi_j)} \} \\
(\tilde{T}_y)_m &= - \frac{B}{2} \sum_{j=1}^{P} \{ [| \tilde{M}_{j(mB-1)} |_2 + | \tilde{M}_{j(mB+1)} |_2] \times \\
&\qquad e^{imB(\Omega t + \Psi_j)} \}
\end{aligned}\right\} , \qquad (22)$$

where B is the number of blades on the propeller, m=0, 1, 2, ..., and where

$$
\left.
\begin{aligned}
|\,\tilde{L}_{jn}\,|_1 &= \left(\frac{\partial C_L}{\partial \alpha}\right)\ \rho_f b_j\ \Delta r_j\ U_{Rj}\ U_\infty\ c_{nj}\ \{K(k_{nj})\cos\beta_j - \\
&\qquad \alpha_j\ T(k_{nj})\ \sin\beta_j\}\cos\beta_j \\
|\,\tilde{L}_{jn}\,|_2 &= \left(\frac{\partial C_L}{\partial \alpha}\right)\ \rho_f b_j\ \Delta r_j\ U_{Rj}\ U_\infty\ c_{nj}\ \{K(k_{nj})\cos\beta_j - \\
&\qquad \alpha_j\ T(k_{nj})\ \sin\beta_j\}\sin\beta_j \\
|\,\tilde{M}_{jn}\,|_1 &= \left(\frac{\partial C_L}{\partial \alpha}\right)\ \rho_f b_j\ r_j\ \Delta r_j\ U_{Rj}\ U_\infty\ c_{nj}\ \{K(k_{nj})\cos\beta_j - \\
&\qquad \alpha_j\ T(k_{nj})\ \sin\beta_j\}\sin\beta_j \\
|\,\tilde{M}_{jn}\,|_2 &= \left(\frac{\partial C_L}{\partial \alpha}\right)\ \rho_f b_j\ r_j\ \Delta r_j\ U_{Rj}\ U_\infty\ c_{nj}\ \{K(k_{nj})\cos\beta_j - \\
&\qquad \alpha_j\ T(k_{nj})\ \sin\beta_j\}\cos\beta_j
\end{aligned}
\right\} \quad . \qquad (23)
$$

The quantity n in Equation (23) takes on the values mB, mB+1, or mB-1 according to their use in Equation (22). Also, since the values of c_{nj} are for positive values of n only, c_{nj} may be written in terms of the real and imaginary components of the Fourier coefficient as

$$c_{nj} = \frac{1}{2}\,(a_{nj} - i\,b_{nj})$$

for the purpose of computation.

Equation (22) along with Equation (23) constitute the final equations describing the unsteady forces and moments experienced by a

propeller operating in a spatially nonuniform inflow. A computer program, contained in Appendix B, has been written to allow rapid computation of the unsteady forces and moments.

3.5 Three-Dimensional, Unsteady Lifting Surface Theory

Hanaoka [33] developed a linearized unsteady lifting surface theory for the unsteady loading on a propeller operating in incompressible, potential flow. The theory is applicable to unsteady phenomena caused by rigid body vibrations of the propeller, vibrations of the propeller blades, and a circumferentially varying steady velocity field. The following integral equation was derived which relates the known unsteady downwash distribution on the blades to the unknown unsteady loading distribution:

$$V_N^n(r)\, e^{in(\Omega t - \phi_o)} = \sum_{n=1}^{B} \frac{e^{iq\Omega t}}{r\pi\rho_f V_a} \int\int_S \Delta p(\xi,\rho,\theta_o)\, \frac{\partial}{\partial n'} \times \int_{-\infty}^{x} e^{iq[a(\tau'-x)-\bar{\theta}_n]}\, \frac{\partial}{\partial n}\left(\frac{1}{R}\right) d\tau' dS \quad , \tag{24}$$

where

$$R = \{(\tau' - \xi)^2 + r^2 + \rho^2 - 2r\rho \cos\,[\theta_o - \phi_o + \bar{\theta}_n - a(\tau'-x)]\}^{1/2} \quad .$$

Both the lifting surface and trailing vorticity are assumed to lie on a given helicoidal surface of constant pitch. Any deviation from this surface by either the flow or the lifting surface is considered as a small perturbation.

The problem considered here is the unsteady response of a rigid, nonvibrating propeller operating in a known circumferentially varying steady inflow velocity. In a series of investigations conducted at Stevens Institute of Technology [34], [35], [36], [29], the unsteady lifting surface Equation (24) has been numerically evaluated under successively less restrictive assumptions regarding the propeller geometry and the chordwise loading distribution for this problem. The techniques of evaluation used in the most recent investigation [29] are reviewed here, since this method of analysis has been employed to predict unsteady propeller response in the present investigation.

In Equation (24), $\partial/\partial n$ and $\partial/\partial n'$ are the directional derivatives normal to the helicoidal surface at the loading point and at the control point, respectively. They are given as:

$$\frac{\partial}{\partial n} = \frac{\rho}{\sqrt{1 + a^2\rho^2}} \left(a \frac{\partial}{\partial \xi} - \frac{1}{\rho^2} \frac{\partial}{\partial \theta_o} \right)$$

and

$$\frac{\partial}{\partial n'} = \frac{r}{\sqrt{1 + a^2 r^2}} \left(a \frac{\partial}{\partial x} - \frac{1}{r^2} \frac{\partial}{\partial \phi_o} \right) .$$

A high order singularity exists in the kernel function of the integral Equation (24). In order to circumvent this problem, the integral is evaluated over the projection of the blade in the propeller plane instead of over the actual blade surface. After the mathematical manipulations have been performed on the slightly shifted surface, the projected surface is trought back into coincidence with the actual surface.

The unknown loading function is approximated in the following manner. Equation (24) can be written as

$$\frac{V(r)}{U} e^{iq(\Omega t-\phi_o)} = \int_o^{\pi} \int_{\rho} S(\rho,\theta_o)\, K(r,\phi_o;\rho,\theta_o;q) \sin\theta_\alpha \, d\theta_\alpha \, d\rho \quad ,$$

where

$$S(\rho,\theta_o) = \Delta p(\rho,\theta_o)\, \rho\, \theta_b^{\rho} \quad ,$$

$$K(r,\phi_o;\rho,\theta_o;q) = -\frac{e^{iq\Omega t}}{4\pi\rho_f U^2} \left[\frac{\sqrt{1+a^2\rho^2}}{a\rho}\right] \lim_{\delta \to o} \sum_{n=1}^{N} e^{-iq\bar{\theta}_n} \frac{\partial}{\partial n'} \times$$

$$\int_{-\infty}^{x} e^{iqa(\tau'-x)} \frac{\partial}{\partial n} \left(\frac{1}{R}\right) d\tau' \quad ,$$

and the transformation $\theta_o = \theta_b^{\rho} \cos\theta_\alpha$ has been used.

The unknown loading function $S(\rho,\theta_o)$ is approximated by a Birnbaum series:

$$S(\rho,\theta_o) = \frac{1}{\pi} \left\{ L^{(1)}(\rho) \cot\frac{\theta_\alpha}{2} + \sum_{\bar{n}=2}^{\infty} L^{(\bar{n})}(\rho) \frac{\sin(\bar{n}-1)\theta_\alpha}{\bar{n}-1} \right\} \quad ,$$

where $L^{(\bar{n})}(\rho)$ are the spanwise loading components. This series reproduces the proper leading edge singularity and fulfills the Kutta condition along the trailing edge.

The inverse Descartes distance 1/R is expanded in terms of Lengendre functions of the second kind:

$$\frac{1}{[\chi^2 + r^2 + \rho^2 - 2r\rho \cos\theta]^{1/2}} = \sum_{m=0}^{\infty} \varepsilon_m \cos m\theta \frac{1}{\pi\sqrt{r\rho}} \times Q_{m-1/2}\left(\frac{\chi^2 + r^2 + \rho^2}{2r\rho}\right) ,$$

where

$$\varepsilon_m = \begin{cases} 1, & m=0 \\ 2, & m\neq 0 \end{cases} .$$

The kernel is now in separable form, so that the chordwise integration can be performed, whereby, the surface integral equation is reduced to a line integral equation

$$\frac{V(r)}{U} e^{iq(\Omega t-\phi_o)} = \int_\rho L^{(1)}(\rho)\, \bar{K}^{(1)}(r,\rho,\phi_o;q)d\rho + \int_\rho \sum_{\bar{n}=2}^{\infty} L^{(\bar{n})}(\rho)\bar{K}^{(\bar{n})}(r,\rho,\phi_o;q)d\rho \quad .$$

The new kernels $\bar{K}^{(\bar{n})}$ are the result of the θ_α - integration.

The transformation $\theta_o = -\theta_b^r \cos\phi_\alpha$ is made and the integral equation becomes

$$\frac{V(r)}{U} e^{iq\theta_b^r \cos\phi_\alpha} = \int_\rho \sum_{\bar{n}=1}^{\infty} L^{(\bar{n})}(\rho) \sum_{m=-\infty}^{\infty} f_m(q,\phi_\alpha)\, \bar{K}_m^{(\bar{n})}(r,\rho;q)d\rho \quad . \quad (25)$$

The chordwise boundary conditions are satisfied for each of the chordwise loading modes by use of the series of "generalized lift operators":

$$m=1,\ \frac{1}{\pi}\int_0^{\pi}\{\ \}\ (1-\cos\phi_\alpha)\,d\phi_\alpha\quad,$$

$$m=2,\ \frac{1}{\pi}\int_0^{\pi}\{\ \}\ (1+2\cos\phi_\alpha)\,d\phi_\alpha \tag{26}$$

and

$$m>2,\ \frac{1}{\pi}\int_0^{\pi}\{\ \}\ \frac{\cos\,(m-1)\phi_\alpha}{m-1}\,d\phi_\alpha\quad.$$

Application of the lift operators to both sides of Equation (25) results in

$$\frac{V(r)}{U}\,I^{(\bar{m})}\,(q\theta_b^r) = \int_\rho L^{(1)}(\rho)\bar{K}^{(\bar{m},1)}(r,\rho,q)\,d\rho + \sum_{\bar{n}=2}^{\infty}\int_\rho L^{(\bar{n})}(\rho)\bar{K}^{(\bar{m},\bar{n})}(r,\rho;q)\,d\rho\quad,$$

where $I^{(\bar{m})}(q\theta_b^r)$ is of the form given in Equation (26), and $\bar{K}^{(\bar{m},\bar{n})}$ are the kernels after both the θ_α and ϕ_α integrations.

The number of resulting integral equations is $\bar{m} = \bar{n}$. The solution of these integral equations is obtained by the collocation method. The blade is divided into i-strips, of length 2β along the span, which reduces the $\bar{m}$ integral equations to a set of algebraic equations,

$$\frac{V(r_i)}{U}\,I^{(\bar{m})}(q\theta_b^{r_i}) = \sum_{\bar{n}=1}^{\bar{n}_{max}}\sum_{j=1}^{p} L^{(\bar{n})}(\rho_j)K_{ij}^{(\bar{m},\bar{n})}\,(r_i,\rho_i)\quad. \tag{27}$$

This set of equations is solved for the spanwise loading components $L^{(\bar{n})}(\rho_j)$ by the use of a digital computer.

The resulting spanwise loading distribution is approximated by

$$L(r) = L^{(1)}(\rho_j) + \frac{1}{2} L^{(2)}(\rho_j) \quad .$$

The time-dependent thrust at blade rate frequency is then given by

$$\tilde{F}_z = - \mathrm{Re} \left[B \int_{R_{hub}}^{R_{TIP}} L(r) \frac{ar}{\sqrt{1 + a^2 r^2}} dr \right] e^{iq\Omega t} \quad . \qquad (28)$$

The particular computer program used in this investigation for solving the set of algebraic Equations (27) approximates the directional derivatives normal to the helicoidal surface by directional derivatives in the axial direction, i.e.,

$$\frac{\rho}{\sqrt{1 + a^2 \rho^2}} \left(a \frac{\partial}{\partial \xi} - \frac{1}{\rho^2} \frac{\partial}{\partial \theta_o} \right) \rightarrow \frac{\partial}{\partial \xi}$$

and

$$\frac{r}{\sqrt{1 + a^2 r^2}} \left(a \frac{\partial}{\partial x} - \frac{1}{r^2} \frac{\partial}{\partial \phi_o} \right) \rightarrow \frac{\partial}{\partial x} \quad .$$

In addition, the helicoidal surface of integration, both on the blades and in the downstream wakes, is approximated in a staircase manner. The calculations made for this investigation used five chordwise modes.

This analysis considers only the effect of velocity disturbances normal to the blade chord, i.e., the effect of velocity disturbances parallel to the blade chord are not considered.

CHAPTER IV

EXPERIMENTAL DETERMINATION OF SPATIAL VELOCITY DISTRIBUTIONS

4.1 Introduction

As shown in Equations (18) and (19), the theoretical value of the time-dependent thrust generated by a propeller operating in a spatially varying velocity field is proportional to the radial distribution of the harmonic content of the circumferential variation of the axial velocity. These quantities must be determined from experimentally determined velocity distributions. The first part of the experimental program discussed here involves measuring the circumferential distribution of axial velocity in the propeller leading edge plane for each of the test conditions at which propeller time-dependent thrust was measured.

4.2 Test Apparatus

The spatial variations in the propeller inflow were generated by a strut with a symmetrical airfoil cross-section having an eight-inch chord and a one-inch maximum thickness at the mid-chord. In order to permit measurements of the time-dependent propeller thrust in velocity fields having different spatial variations, the strut-to-propeller spacing was adjustable from four inches to thirty-two inches. The strut was placed at zero angle of attack and, therefore, the wake width was proportional to $X^{1/2}$ and the maximum velocity deficit was proportional to X^{-1}, where X is the distance from the strut trailing edge, Reference [37]. A typical velocity distribution behind the strut is shown in Figure 15 for various nondimensional radii.

In order to determine the harmonic content of the propeller inflow, the circumferential distributions of axial velocity at a number of radii were measured. A wake rake, i.e., a series of radially distributed pitot total and static tubes, Figure 16, was employed for these measurements. The wake rake is shown schematically in Figure 17.

4.3 Data Acquisition and Reduction

The wake rake was rotated about its centerline through 180° and, since the rake was symmetric about the centerline, a survey over 360° was made. Measurements were made at each of the following angular increments, where zero is perpendicular to the strut:

θ	$\Delta\theta$
0° - 70°	5°
70° - 110°	1°
110° - 180°	5°

The value $\Delta\theta$ was varied so that a good definition of the velocity field could be obtained while minimizing data acquisition.

The data acquisition and reduction system used to measure the velocity distributions is shown in the block diagram of Figure 18. At each angular position considered, the values of total and static pressures measured by the wake rake pitot tubes were recorded on paper tape. In addition, the free-stream total and static pressures were recorded. Based on these data, the free stream velocity and the radial distribution of axial velocity at each angular position considered were calculated. Thereby, the circumferential distribution of nondimensional axial velocity at various radii were determined.

The velocity distributions were determined for a free-stream velocity of 18 ft/sec at each of the following nondimensional distances,

based on strut chord, downstream of the strut trailing edge: 1.0, 1.25, 1.5, 2.0, 3.0 and 4.0.

4.4 Data Analysis

For each free-stream velocity and strut position considered, the harmonic content of the circumferential distribution of axial velocity at each radius considered was determined. Standard Fourier analysis techniques were used with numerical integration being performed by the trapezoidal rule. The resulting real and imaginary parts of the Fourier coefficients are listed in Table 2. Since the time-dependent thrust on a two-, five- and ten-bladed propeller were to be considered, only harmonics of order 0, 2, 5 and 10 are listed in the table.

As previously indicated, the objective of positioning the strut at a number of upstream distances was to alter the spatial variation of the inflow at the propeller leading edge. Figures 19, 20 and 21 show the second, fifth and tenth complex Fourier coefficient, nondimensionalized by the free-stream velocity, versus the radial position, nondimensionalized by the propeller tip radius, for two values of nondimensional strut position. It is seen in these figures that the Fourier coefficients do vary with strut position.

Since the harmonic content of the propeller inflow is calculated from experimentally determined velocity distributions, there will be some experimental error involved, Tjoenneland [4]. In order to determine the repeatability of the Fourier coefficients, a series of eight wake surveys were performed with a free-stream velocity of 15 ft/sec and a nondimensional distance $X/D_p = 0.625$ between the strut

trailing edge and the wake rake. The Fourier coefficients were calculated for each of the tests at each radius considered. The mean and standard deviation of each set of Fourier coefficients was calculated. Figures 22 through 28 show the mean and standard deviation of the zeroth, second, fifth, and tenth Fourier coefficient versus the nondimensional radius.

The mean values are as expected. That is, a two-cycle wake has a high second harmonic. The fifth harmonic, being odd, will be low in amplitude. The tenth harmonic, being a multiple of two, will be higher than the fifth harmonic but lower than the second.

The standard deviations of the fifth and tenth harmonics are quite high compared to the mean values. This is due to the velocity variations inherent in the data acquisition system.

CHAPTER V

EXPERIMENTAL DETERMINATION OF TIME-DEPENDENT PROPELLER THRUST

5.1 Introduction

The time-dependent thrust generated by three different propellers operating in the wake of a strut was measured. Measurements were made for each propeller operating at various advance ratios, for a range of strut-to-propeller distances and for various free-stream velocities.

5.2 Test Apparatus

Two of the propellers used in the test are shown in Figure 29. The same blades were used for each of the propellers, the blade number differences being achieved by using different sized spacers on a common hub. Each blade has a constant chord of one inch, and a span of three inches with a hub-to-tip ratio of 0.25. The design advance ratio of each propeller is $J = 1.17$.

The propellers were driven by a dynamometer located downstream as shown in Figure 30. As seen, the forward part of the dynamometer shell was made as small in diameter as possible in order to minimize its effect on the propeller. By placing the propeller drive mechanism downstream, the presence of a boundary layer inflow, with its radial variation in velocity, was avoided. Thus, the generation of time-dependent propeller thrust due only to operation in the strut wake could be studied.

The time-dependent thrust generated by the propeller was measured with a dynamic thrust balance which utilizes a piezoelectric crystal as a sensing element. The balance is located in the propeller drive

shaft and is placed as close to the propeller as possible, Figure 31. The crystal generates an electrical signal due to the deformation caused by the time-dependent propeller forces and moments. The time-dependent forces and moments are transmitted to the crystal by a hemispherical ball which is aligned with the drive shaft centerline. The piezoelectric crystal is also aligned with the centerline of the drive shaft, see Figure 32. By positioning the hemispherical ball and crystal in this way, the sensitivity of the balance to a bending moment is low when compared to the sensitivity to an axial force.

A mass was placed on the drive shaft between the balance and the drive motor. This mass is large when compared to the combined mass of the propeller and short section of drive shaft forward of the balance. Thus, the system is considered to be a lumped mass-spring system with the compliance provided by a thin-walled section on the shaft, see Figure 32. A trade-off was made in the design of the compliant section since it is desired to have a high natural frequency of the system, i.e., large stiffness, and a high balance sensitivity, i.e., small stiffness.

5.3 Data Acquisition and Reduction

A block diagram of the data acquisition and reduction system is shown in Figure 33. An electric signal is generated by the piezoelectric crystal due to the deformation caused by the propeller time-dependent forces and moments. Since the balance rotates along with the shaft, the signal is passed through a set of slip-rings. Since slip-rings are a source of noise, the signal is amplified before

passing through the slip-rings in order to have a good signal-to-noise ratio.

The signal from the slip-rings was then passed through a set of variable filters, two high pass and one low pass. The low pass filter was set at 1 kHz for all tests since the balance was flat with frequency up to about 800 Hz and the cut-off frequency of the two high pass filters was set at 50 percent above the shaft rate frequency for each particular test.

The spectrum of the time-dependent thrust was obtained by passing the filtered signal through a wave analyzer. A typical spectrum is shown in Figure 34. The time-dependent thrust of interest here is that occurring at blade-rate frequency, i.e., number of blades times shaft RPS. To measure this, the center frequency of the wave analyzer was set at the blade-rate frequency of the particular test and the level at this frequency was recorded. A typical level of time-dependent thrust at blade-rate frequency is shown in Figure 34.

5.4 Calibration

The time-dependent thrust balance was calibrated by applying a known sinusoidal axial force to the propeller shaft and recording the output of the balance. Figure 35 shows a block diagram of the calibration test set-up. The sinusoidal axial force was applied with a fifty-pound electromagnetic shaker. The amplitude of the force was measured with a force cube located between the shaker and the propeller drive shaft. The balance output was recorded both on the wave analyzer level recorder and on a voltmeter in terms of peak voltage for various known values of applied axial force. Figure 36 shows

applied force versus balance output for a range of applied force. It is seen that the balance output is linear with force.

Since the calibration was performed at a frequency of 500 Hz and the blade-rate frequencies of interest ranged from 35 Hz to 298 Hz, the frequency response of the balance for a constant amplitude applied force was determined. The electromagnetic shaker was driven with a white noise generator and the spectrum of the balance output was obtained with the wave analyzer. The frequency response of the balance is shown in Figure 37. As seen, the response is flat with frequency in the range of interest.

The calibration was performed with no steady axial force applied to the shaft. However, during the measurement of the time-dependent thrust generated by a propeller, a steady axial force is applied to the shaft due to the steady thrust generated by the propeller. Tests were performed where the balance output due to a time-dependent axial force was measured when various levels of steady axial force were applied to the shaft. A sketch of the test set-up is shown in Figure 38. The test results are shown in Table 3. The steady thrusts expected during the measurement of time-dependent thrust are shown in Table 4 as determined from previous tests. It is seen that the steady thrust has only a small effect on the measured values of time-dependent thrust; however, these corrections were made to the data.

5.5 Tests Conducted

The time-dependent thrust at blade-rate frequency generated by a series of propellers operating in the wake of a strut was measured.

For the two-, five- and ten-bladed propellers, measurements were made with the strut at the following strut nondimensional trailing edge-to-propeller spacings: 1.0, 1.25, 1.5, 2.0, 3.0, and 4.0. For the ten-bladed propeller, additional measurements were made with the strut at 7 inches.

For each of the strut positions considered, measurements were made for each propeller operating at its design advance ratio, at design advance ratio plus ten percent, and at design advance ratio minus ten percent. Table 5 shows the propeller operating conditions at which measurements were made.

The time-dependent thrust at blade-rate frequency is a multiple of shaft-rate frequency. Due to the presence of rotating parts and their supports, the balance will generate signals at shaft-rate frequency and its multiples. The signal generated by the rotating components of the propeller drive system should be lower than the signal generated due to the time-dependent propeller thrust. To obtain the signal level due to the rotating parts, tests were conducted to measure the spectrum of the signal level due to the propellers operating in a spatially uniform inflow, i.e., with no strut mounted in the test section. Spectrum levels were obtained for the two- and ten-bladed propellers operating at various advance ratios and free-stream velocities. In all cases, the signal-to-noise ratio was sufficiently high.

CHAPTER VI

RESULTS OF EXPERIMENTS WITH SPATIALLY VARYING INFLOWS AND COMPARISON WITH THEORY

6.1 Introduction

The experimentally obtained data have inherent errors associated with them due to the usual sources of experimental error. The values predicted by the theoretical methods also have errors associated with them, since the theories employ the experimentally determined harmonic content of the propeller inflow velocity field.

In order to be able to compare the magnitudes and trends of the experimental and theoretical values, a least squares polynomial technique was used to fit curves to the data points. The data points comprising any one of the curves has a given shape due to the trend of the data, but also has scatter about the true trend line. The problem is ther to select the "correct" degree of the polynomial to fit the data points such that a "true" representation of the curve is obtained while minimizing the effects of the random scatter of the data points. A method of accomplishing this has been developed by Dylewski [38]. The general approach taken is to accept that type of curve for representation of the data for which residual deviations show the least bias, where bias is defined to be systematic discrepancy between the true and the assumed curve types. This minimum bias criterion has been used to choose the degree of the polynomial curve fits for the time-dependent thrust coefficient versus nondimensional strut position curves.

6.2 Comparison of Unsteady Lifting Surface Theory and Two-Dimensional Unsteady Theory

Let us consider a comparison of the results of the unsteady lifting surface theory and the two-dimensional unsteady theory. The two-dimensional unsteady theory employed here considers only the effects of velocity variations normal to the blade surfaces since this is the only component considered in the unsteady lifting surface theory. The effects on velocity variations parallel to the blade surfaces will be considered in a later section. The comparison of the results of these two theories will show the merits of approximating the unsteady induced effects with $(\partial C_L/\partial\alpha)_j$ as discussed in Section 3.3.

Predictions of the time-dependent thrust coefficients based on the two-dimensional unsteady airfoil theory have been made for the ten-bladed propeller operating at an advance ratio of 1.29 in a free-stream velocity of 18 ft/sec for all of the strut positions considered. Predictions of the time-dependent thrust coefficients based on the unsteady lifting surface theory have been made for the same propeller operating at the same conditions. A comparison of the results is shown in Figure 39, where the curves shown are faired by hand in order to accentuate the comparison.

It is seen that the predictions based on two-dimensional theory which employs a $\partial C_L/\partial\alpha = 2\pi$ results in consistently higher values than both the unsteady lifting surface theory (this corresponds with the findings of Boswell [9]) and the two-dimensional theory which employs corrected values of $\partial C_L/\partial\alpha$. The agreement between the predictions based on two-dimensional theory with corrected values of $\partial C_L/\partial\alpha$ and on the unsteady lifting surface theory is excellent. The same results are

obtained for advance ratios of 1.05 and 1.17. Consequently, it is seen that, at least for this particular propeller configuration, approximating the unsteady cascade effect with values of $\partial C_L/\partial\alpha$ based on steady state cascade tests in the two-dimensional unsteady theory produces results in good agreement with predictions based on unsteady lifting surface theory. It is expected that for blades having small aspect ratios, a further correction for three-dimensional effects would be needed in the two-dimensional theory.

Table 6 shows the values of $\partial C_L/\partial\alpha$ for each propeller at a number of nondimensional radii. These values have been calculated from steady state cascade test results, Emery et al. [39]. Subsequent calculations of time-dependent thrust employ the values of $\partial C_L/\partial\alpha$ shown in Table 6.

6.3 Comparison of Results of Two-Dimensional Theory and Experiment

The two-dimensional theory with corrected values of $\partial C_L/\partial\alpha$ was used to predict time-dependent thrust coefficients. Predictions were made for the condition where only gusts normal to the chord of the blades were considered and for the condition where gusts normal to the chord and along the chord of the blades were considered. Comparisons of these predicted values with experimentally determined values are made.

The two-, five- and ten-bladed propellers were considered. The propeller operating conditions considered were advance ratios of 1.05, 1.17 and 1.29 for a free-stream velocity of 18 ft/sec. At the Reynolds numbers existing for these operating conditions, the blade boundary layers on the blade surfaces are turbulent. Predictions of

the time-dependent thrust coefficients were also made for an advance ratio of 1.34. The results are shown in Figures 40 through 51.

As expected, the trends of the results of the two prediction techniques with advance ratio are the same. The predictions which consider both normal and chordwise gusts are consistently lower in magnitude than those which consider only the effects of the gusts normal to the blade chord. In general, the trends of the experimental data agree with those of predicted values. The difference in the magnitudes of the experimental and predicted values seems to be a function of the propeller advance ratio.

In order to investigate the variation of time-dependent thrust coefficient with advance ratio, the time-dependent thrust coefficient versus nondimensional strut distance curves were crossplotted at constant values of nondimensional strut distance for each propeller. These plots of time-dependent thrust coefficient versus advance ratio are shown in Figures 52, 53 and 54.

It is seen that as the advance ratio decreases, the effect of the chordwise velocity variations on the predicted values of time-dependent thrust coefficient increases. This is due to the angle of incidence increasing as the advance ratio decreases, Figures 55, 56 and 57. These data were obtained from an unpublished propeller design report. As seen in Equation (19), the effect of chordwise velocity variations is directly proportional to the angle of incidence, α, therefore, advance ratio.

The trends of the predicted and experimental time-dependent thrust coefficients with advance ratio are essentially the same. However, as blade number increases, the experimental results decrease

more rapidly with advance ratio than either analytical approach. The results of the analytical method which includes the chordwise gust effects follow the trends of the experimental data better than the results of the analytical method which does not include the chordwise gust effects.

CHAPTER VII

THEORETICAL RESPONSE OF PROPELLERS TO TURBULENT INFLOW

7.1 Introduction

The objective of this section is to derive a theory for the prediction of the time-dependent thrust generated by a propeller due to operating in a known turbulent inflow. The desire is to obtain a relationship which includes the important characteristics of the propeller, both geometrical and operational, and the important turbulent inflow parameters, but yet is relatively simple to apply to a practical problem.

An assumption of homogeneity and isotropy for the turbulent inflow is made. In addition, Taylor's hypothesis is used for the turbulent flow through the blade row. The response function selected is that due to Sears [7]. The analysis due to Sevik [12] will be followed except that blade-to-blade summation of the time-dependent thrust will be made, in addition to spanwise summation. The frequency spectrum of the propeller time-dependent thrust results from the analysis.

7.2 General Theory

The quantities involved in the development of the theory are expressed as tensors; consequently, the index notation is used. Coordinate directions and elements of the propeller blades involved are denoted by subscripts. For example, $u_{k\beta}(\tau')$ denotes the component of the fluctuating velocity u at time τ' in the direction β of the rotating reference frame, Figure 58, at the blade element k. Also,

$F_{ik\alpha\beta}(t,\tau')$ denotes the aerodynamic force acting on the i^{th} blade element in the direction α at the instant of time t caused by a velocity fluctuation of unit magnitude in the direction β to which the k^{th} element was subjected at the instant of time τ'.

Consider the propeller blades to be subdivided into an arbitrarily large number of spanwise elements and consider a typical element located at r_i as shown in Figure 58. The fluctuating aerodynamic forces acting on the various surface elements are interdependent by virtue of induction effects, as well as by virtue of spatial and temporal correlation of the turbulent velocity fluctuations. Neglecting higher order terms, the lift force, $\ell_{i\alpha}(t)$, on the i^{th} element at time t in the direction α is given by

$$\ell_{i\alpha}(t) = \int_0^\infty F_{ik\alpha\beta}(\tau)\, u_{k\beta}(t-\tau)d\tau \quad , \tag{29}$$

where

$$\alpha,\beta=1,2,3;$$

$$i,k=1,2,\ldots,m;$$

and

$$\tau \leq t \quad .$$

The total force acting on the propeller is obtained by summing the forces acting on each individual blade element,

$$L_\alpha(t) = \sum_{i=1}^{m} \ell_{i\alpha}(t) \quad . \tag{30}$$

Since $L_\alpha(t)$ is a random function of time, a statistical approach must be employed. The statistical methods employed here are discussed in detail by Bendat and Piersol [40]. In this particular application, the correlation tensor $\langle L_\alpha(t)L_\beta(t+\tau)\rangle$ and its Fourier transform are of importance. The random processes are assumed to be stationary and ergodic in forming average values of the forces and fluid velocities.

Consider the lift correlation tensor and its Fourier transform

$$[\ell_{i\alpha}(t)\ell_{j\beta}(t+\tau)] = \lim_{T\to\infty}\frac{1}{T}\int_0^T \ell_{i\alpha}(t)\ell_{j\beta}(t+\tau)dt = \Phi'_{ij\alpha\beta}(\tau) \quad . \tag{31}$$

In terms of the aerodynamic force functions and the velocity fluctuations, i.e., Equation (29), the lift correlation tensor becomes

$$\Phi'_{ij\alpha\beta}(\tau) = \lim_{T\to\infty}\frac{1}{T}\int_0^T \left\{\int_0^\infty F_{ik\alpha\gamma}(\tau_1)u_{k\gamma}(t-\tau_1)d\tau_1\right\} \left\{\int_0^\infty F_{jr\beta\delta}(\tau_2)u_{r\delta}(t-\tau_2+\tau)d\tau_2\right\} dt \quad . \tag{32}$$

Rearranging terms, Equation (32) becomes

$$\Phi'_{ij\alpha\beta}(\tau) = \lim_{T\to\infty}\frac{1}{T}\int_0^T \left\{\int_0^\infty\int_0^\infty F_{ik\alpha\gamma}(\tau_1)F_{jr\beta\delta}(\tau_2)u_{k\gamma}(t-\tau_1)\times u_{r\delta}(t-\tau_2+\tau)d\tau_1 d\tau_2\right\} dt \quad . \tag{33}$$

Changing the order of integration does not affect the result, so Equation (33) becomes

$$\Phi'_{ij\alpha\beta}(\tau) = \int_0^\infty \int_0^\infty F_{ik\alpha\gamma}(\tau_1) F_{jr\beta\delta}(\tau_2) \left\{ \lim_{T\to\infty} \frac{1}{T} \int_0^T u_{k\gamma}(t-\tau_1) \times \right.$$

$$\left. u_{r\delta}(t-\tau_2+\tau)dt \right\} d\tau_1 d\tau_2 \quad . \tag{34}$$

The integral inside the brackets of Equation (34) is the velocity correlation tensor $R_{kr\gamma\delta}(\tau-\tau_2+\tau_1)$, so that Equation (34) can be written as

$$\Phi'_{ij\alpha\beta}(\tau) = \int_0^\infty \int_0^\infty F_{ik\alpha\gamma}(\tau_1) F_{jr\beta\delta}(\tau_2) R_{kr\gamma\delta}(\tau-\tau_2+\tau_1) d\tau_1 d\tau_2 \quad . \tag{35}$$

The spectrum tensor of the force fluctuations, $G'_{ij\alpha\beta}(\omega)$, is then obtained as the Fourier transform of the cross-correlation tensor of the forces, $\Phi'_{ij\alpha\beta}(\tau)$, i.e., Equation (35),

$$G'_{ij\alpha\beta}(\omega) = \frac{1}{\pi} \int_{-\infty}^{\infty} \left\{ \int_0^\infty \int_0^\infty F_{ik\alpha\gamma}(\tau_1) F_{jr\beta\delta}(\tau_2)\, R_{kr\gamma\delta}(\tau-\tau_2+\tau_1) \times \right.$$

$$\left. d\tau_1 d\tau_2 \right\} e^{-i\omega\tau} d\tau$$

or

$$G'_{ij\alpha\beta}(\omega) = \int_0^\infty \int_0^\infty F_{ik\alpha\gamma}(\tau_1) F_{jr\beta\delta}(\tau_2) \left\{ \frac{1}{\pi} \int_{-\infty}^{\infty} R_{kr\gamma\delta}(\tau-\tau_2+\tau_1) e^{-i\omega\tau} d\tau \right\} \times$$

$$d\tau_1 d\tau_2 \quad . \tag{36}$$

Multiplying and dividing the right-hand side of Equation (36) by $\exp\{i\omega\tau_2 - i\omega\tau_1\}$,

$$G'_{ij\alpha\beta}(\omega) = \int_0^\infty \int_0^\infty F_{ik\alpha\gamma}(\tau_1) e^{i\omega\tau_1} F_{jr\beta\delta}(\tau_2) e^{-i\omega\tau_2} \times$$

$$\left\{ \frac{1}{\pi} \int_{-\infty}^{\infty} R_{kr\gamma\delta}(\tau-\tau_2+\tau_1) e^{-i\omega(\tau-\tau_2+\tau_1)} d\tau \right\} d\tau_1 d\tau_2 \quad . \tag{37}$$

The term in brackets is the spectrum tensor of the velocity fluctuations

$$G_{kr\gamma\delta}(\omega) = \frac{1}{\pi} \int_{-\infty}^{\infty} R_{kr\gamma\delta}(\tau-\tau_2+\tau_1) e^{-i\omega(\tau-\tau_2+\tau_1)} d\tau \quad .$$

Equation (37) can then be written as

$$G'_{ij\alpha\beta}(\omega) = \int_0^\infty F_{ik\alpha\gamma}(\tau_1) e^{i\omega\tau_1} d\tau_1 \int_0^\infty F_{jr\beta\delta}(\tau_2) e^{-i\omega\tau_2} d\tau_2 G_{kr\gamma\delta}(\omega) \quad . \tag{38}$$

The integrals in Equation (38) are aerodynamic frequency response functions which are denoted by $H(\omega)$, making Equation (38):

$$G'_{ij\alpha\beta}(\omega) = \{H_{ik\alpha\delta}(\omega)\}^* \{H_{jr\beta\delta}(\omega)\} G_{kr\gamma\delta}(\omega) \quad , \tag{39}$$

where the asterisk denotes the complex conjugate of the aerodynamic frequency response function.

Equation (39) is the spectrum tensor of the force fluctuations in terms of the aerodynamic frequency response function and the spectrum tensor of the velocity fluctuations as derived by Sevik [12]. The application of this equation requires choosing an appropriate aerodynamic frequency response function which is consistent with the given propulsor and velocity fluctuations. In addition, the spectrum tensor of the velocity fluctuations must be determined.

7.3 Application of Theory to a Propeller

A brief description of the approach taken by Sevik [12] will be given. This description is provided because Sevik considers only the response of a single blade to the velocity fluctuations and then multiplies by the blade number, while a theory developed later in Section 7.4 includes blade-to-blade correlation effects. Following the description of the theory due to Sevik, a new approach will be taken.

Sevik [12] considered the specific case of a propeller of low solidity with blades of high aspect ratio operating in a homogeneous. isotropic flow. For this type of flow, the velocity correlation tensor can be expressed in terms of the distance $\underline{r}$ between two points in the flow field and the mean square value of the velocity fluctuations $\overline{u^2}$ as follows, Batchelor [41]:

$$R_{kr\alpha\beta}(\underline{r}) = \overline{u^2} \left\{ -\frac{1}{2\underline{r}} \frac{r_\alpha r_\beta}{\underline{r}} \frac{\partial f(\underline{r})}{\partial \underline{r}} + [f(\underline{r}) + \frac{1}{2} \underline{r} \frac{\partial f(\underline{r})}{\partial \underline{r}}]\delta_{\alpha\beta} \right\} \quad , \qquad (40)$$

where $\delta_{\alpha\beta}$ is the Kronecker delta and $f(\underline{r})$ is the coefficient of longitudinal correlation. The coefficient of longitudinal correlation as measured by Stewart and Townsend [42] is shown in Figure 59. An approximate expression for the coefficient of longitudinal correlation

$$f(r) = e^{-\underline{r}/\Lambda} \quad , \qquad (41)$$

where Λ is the integral scale of the turbulence, has been used by Sevik [12]. This approximation is also shown in Figure 59.

The aerodynamic frequency response function employed is that derived by Sears [7] as follows:

$$H_j(\omega) = 2\pi\rho V_j b_j \{C(k_j)[J_o(k_j) - i\, J_1(k_j)] + i\, J_1(k_j)\}\, \delta R_j \quad , \qquad (42)$$

where V_j is the resultant velocity at the j^{th} element of the propeller, J_o and J_1 are Bessel functions, C(k) is the Theodorsen function, and $k_j = \omega b_j / V_j$ is the reduced frequency. All of the assumptions used in deriving Equation (42) have been discussed in Section 3.2.

Substituting the relationships given by Equations (40), (41) and (42) into Equation (39) permits the calculation of the response of a propulsor to turbulence by numerical means. Sevik [12], however, by making certain approximations and assumptions, was able to obtain relatively simple expressions for the RMS thrust coefficient and the

spectrum tensor of the thrust fluctuations. These approximations and assumptions are as follows:

1. The axis of rotation of the propeller is colinear with the free stream velocity vector.
2. The resultant velocity and chord of the various propeller elements may be represented by those of a single "typical section" located at some fraction of the blade span, i.e., changes are small over the blade span.
3. The velocity correlation tensor is approximated by

$$R_{kr\alpha\beta}(\underline{r}) = e^{-q/\Lambda} R_{kk\alpha\beta}(C_x\tau) \quad , \tag{43}$$

where q is the distance between the elements k and r of the propeller, see Figure 59.

Substituting Equations (40) through (43) into Equation (39), Sevik [12] has derived an expression for the spectrum tensor of the fluctuating thrust:

$$G'_{11}(\omega) = \sum_i \sum_j \{H_i^*(\omega)\, H_j(\omega) \cos^2\beta_i \cos^2\beta_j\, G_{ij11}(\omega) +$$

$$\frac{1}{4} H_i^*(\omega)\, H_j(\omega) \sin^2\beta_i \sin^2\beta_j\, G_{ij22}(\omega)\} \quad , \tag{44}$$

where

$$G_{ij11}(\omega) = \frac{\overline{2u^2}}{\pi} \left\{ \frac{C_x/\Lambda}{(C_x/\Lambda)^2 + \omega^2} \right\} e^{-q/\Lambda}$$

and

$$G_{ij22}(\omega) = \frac{2\overline{u^2}}{\pi} \left\{ \frac{C_x/\Lambda}{(C_x/\Lambda)^2 + \omega^2} \right\} \left\{ 1 + \frac{1}{2} \left[\frac{(C_x/\Lambda)^2 - \omega^2}{(C_x/\Lambda)^2 + \omega^2} \right] \right\} e^{-q/\Lambda} \quad .$$

The angle β between the resultant velocity vector and the direction of propeller blade rotation is given by

$$\tan \beta = \frac{V}{R\Omega} \quad .$$

The "typical section" concept mentioned in the second assumption above is now employed with respect to the aerodynamic frequency response functions

$$H_i^*(\omega)\, H_j(\omega) \cong H_T^*(\omega)\, H_T(\omega) = |\, H_T(\omega)\, |^2 =$$

$$(2\pi\rho V_T b_T)^2 \left[\frac{1}{1 + 2\pi \frac{\omega b_T}{V_T}} \right] \delta R_i \delta R_j \quad , \tag{45}$$

where an approximation to Sears' function, Fung [43], has been used for mathematical expediency.

Substituting Equation (45) into Equation (44), the spectrum of the thrust fluctuations is expressed as

$$G(\Gamma) = \pi(\rho C_x^2 R^2)^2 \left[\frac{2bB}{R} \frac{u}{C_x} \right] \left[\frac{1}{1 + \phi^2} \right] f(\Gamma) S(\tfrac{R}{\Lambda}) \quad , \tag{46}$$

where

$\phi = \frac{C_x}{V}$, flow coefficient,

B = number of rotor blades

and

$\frac{u}{C_x}$ = turbulence level in the approach stream.

The function $S(R/\Lambda)$ represents a "correlation area" and is given by

$$S(R/\Lambda) = \frac{1}{B^2R^2} \int\int e^{-q/\Lambda}\, dr_i dr_j \quad ; \quad q = |r_i - r_j| \quad . \tag{47}$$

The integration is performed from the hub radius r_h to the tip radius R_{TIP}. This function, as computed by Sevik [12] for propellers having various numbers of blades and hub-to-tip ratios, is shown plotted in Figure 60. The variation of the total thrust driving the rotor with frequency, Γ, is given by $f(\Gamma)$ as

$$f(\Gamma) = \left[\frac{1}{1 + e\Gamma}\right]\left[\frac{1}{1 + \Gamma^2}\right]\left[c + \frac{1 - \Gamma^2}{1 + \Gamma^2}\right] \quad , \tag{48}$$

where

$\Gamma = \omega\Lambda/C_x$,

$e = \pi\frac{2b}{\Lambda}\cos\beta$

and

$c = 2(1 + \frac{1}{\phi^2})$.

Equation (46) represents the results obtained by Sevik [12]. He proceeded to describe an experiment in which a propeller was operated in a turbulent inflow generated by a square mesh grid designed to

generate homogeneous, isotropic turbulence. The spectrum of the resulting fluctuating thrust was measured and compared to that resulting from Equation (46). The same experimental apparatus and procedure is employed in the present paper, so that details will be presented later. A typical result due to Sevik [12] is shown in Figure 61. It is noted that the experimentally determined spectrum exhibits a peak whereas the computed spectrum does not.

It has been shown, Mani [14], that the radiated sound spectrum from propulsors operating in a turbulent inflow exhibits peaks centered at blade passing frequency and integer multiples. Mani [14] has shown that the width of the peaks is related to the ratio of the turbulence length scale to the blade spacing. At small values of this ratio, no peaks appear. As the value of the ratio is increased, peaks appear and become sharper. This peaking of the spectra for large values of length scale to blade spacing is due to blade-to-blade correlation of time-dependent lift as a result of the fluctuating velocity being correlated.

7.4 A Theory to Include Blade-to-Blade Correlation Effects

An attempt to incorporate blade-to-blade correlation of time-dependent lift into Sevik's theory is presented in the following. Consider the aerodynamic frequency response functions of Equation (44). The subscript on this function refers to a particular spanwise element of a propeller blade and the summation is over all spanwise elements. There is a blade-to-blade phasing associated with the aerodynamic response functions which can be written as

$$H_h(\omega)^* \, H_\ell(\omega) \, e^{i\omega\frac{2\pi}{B\Omega}(n-m)} \quad ,$$

where the h and the ℓ subscripts now refer to radial locations of elements only and the n and m indices refer to circumferential locations of the blades. Also, B is the total number of blades and Ω is the rotational speed of the propeller. In Equation (44) a double summation is used, however, with the new aerodynamic frequency response functions a quadruple summation is needed, i.e., over the h, ℓ, m and n. Using the new response functions, Equation (44) for the spectrum tensor of the fluctuating thrust becomes:

$$G'_{11}(\omega) = \sum_{h}\sum_{\ell}\sum_{m}\sum_{n} \left\{ H_h^*(\omega) \, H_\ell(\omega) \cos^2\beta_h \cos^2\beta_\ell \, G_{h\ell 11}(\omega) \, e^{i\omega\frac{2\pi}{B\Omega}(n-m)} + \right.$$

$$\left. \frac{1}{4} H_h^*(\omega) \, H_\ell(\omega) \sin^2\beta_h \sin^2\beta_\ell \, G_{h\ell 22} \, e^{i\omega\frac{2\pi}{B\Omega}(n-m)} \right\} \quad . \qquad (49)$$

Let us now employ the "typical section" concept, expressed by Equation (45) in Equation (49). Hence,

$$G'_{11}(\omega) = (2\pi\rho V_T b_T)^2 \left[\frac{1}{1 + 2\frac{b_r}{V_r}}\right] \sum_{h}\sum_{\ell}\sum_{m}\sum_{n} \left\{ [\cos^2\beta_T \cos^2\beta_T \times \right.$$

$$\left. G_{h\ell 11}(\omega) + \frac{1}{4} \sin^2\beta_T \sin^2\beta_T \, G_{h\ell 22}] \, e^{i\omega\frac{2\pi}{B\Omega}(n-m)} \right\} \quad . \qquad (50)$$

The functions $G_{h\ell 11}(\omega)$ and $G_{h\ell 22}(\omega)$ are defined in Equation (44). Substituting these expressions for $G_{h\ell 11}(\omega)$ and $G_{h\ell 22}(\omega)$ into Equation (50) results in

$$G'_{11}(\omega) = (2\pi\rho V_T b_T)^2 \left[\frac{1}{1 + 2\frac{b_T}{V_T}}\right] \sum_h \sum_\ell \sum_m \sum_n \left\{ \left\{ \cos^4\beta_T \left[\frac{2\overline{u^2}}{\pi} \times \left\{\frac{C_x/\Lambda}{(C_x/\Lambda)^2 + \omega^2}\right\}\right] + \frac{1}{4}\sin^2\beta_T \left[\frac{2\overline{u^2}}{\pi}\left\{\frac{C_x/\Lambda}{(C_x/\Lambda)^2 + \omega^2}\right\} \times \left\{1 + \frac{1}{2}\left[\frac{(C_x/\Lambda)^2 - \omega^2}{(C_x/\Lambda)^2 + \omega^2}\right]\right\}\right]\right\} e^{-q/\Lambda} e^{i\frac{2\pi\omega}{B\Omega}(n-m)} \right\} \quad . \quad (51)$$

It is seen that this equation is the same as that derived by Sevik [12] except for the additional exponential term, $\exp\{i\frac{2\pi\omega}{B\Omega}(n-m)\}$. Consequently, Equation (51) reduces to

$$G_{11}(\Gamma) = \pi(\rho C_x^2 R^2)^2 \left[\frac{2bB}{R}\frac{u}{C_x}\right] \left[\frac{1}{1+\phi^2}\right] f(\Gamma)\, S_T\left(\frac{R}{\Lambda}, \frac{2\pi\omega}{B\Omega}\right) \quad , \quad (52)$$

where

$$S_T\left(\frac{R}{\Lambda}, \frac{2\pi\omega}{B\Omega}\right) = \frac{1}{B^2R^2} \sum_{n=1}^{B} \sum_{m=1}^{B} \sum_{\ell=1}^{P} \sum_{h=1}^{P} \exp\left\{ i\frac{\omega}{\Omega}\frac{2\pi}{B}(n-m) - \frac{R}{\Lambda}\left[r_\ell^2 + r_h^2 - 2r_\ell r_h \cos\left[\frac{2\pi}{B}(m-n)\right]\right]^{1/2}\right\} \delta r_\ell \, \delta r_h \quad . \tag{53}$$

The function $S_T\left(\frac{R}{\Lambda}, \frac{2\pi\omega}{B\Omega}\right)$ is similar to Sevik's function $S(\frac{R}{\Lambda})$ except that the new function includes the effects of blade spacing and is frequency dependent. Figures 62 through 67 show the important features of the function S_T. Figures 62, 63, 64, 65 and 66 are plots of S_T versus $\omega/B\Omega$ for various values of Λ/R or $\Lambda/S_{0.75}$ for two-, five- and ten-bladed propellers, respectively. The value $S_{0.75}$ is the blade spacing at 0.75 of the propeller radius which was chosen as a representative spacing. It is seen for the two- and five-bladed propellers that for the smallest values of $\Lambda/S_{0.75}$ chosen $\Lambda/S_{0.75} \simeq 0.143$, no peaking of the thrust spectrum will occur. For all the propellers considered, the thrust spectrum will exhibit narrower peaks with larger magnitude as the value of $\Lambda/S_{0.75}$ increases. The peaks occur at values of $\omega/B\Omega = N$, where $N = 0,1,2,3,\ldots,\infty$, i.e., at blade passing frequency and its multiples.

Figure 67 is a plot of S_T versus $\omega/B\Omega$ for the two-, five- and ten-bladed propellers for a Λ/R value of 0.286. For propellers having the same radius, the turbulence length scale remains the same for each curve. Then, as the blade number is increased, the peaks become sharper since the turbulence length scale-to-blade spacing ratio is increasing. Not surprisingly, this is the same phenomenon as observed by Mani [14] for the spectrum of the radiated sound, both

in the width of the peaks and the frequencies at which the peaks occur.

The parameters chosen for display of the pertinent trends of the function $S_T\left(\frac{R}{\Lambda}, \frac{2\pi\omega}{B\Omega}\right)$ were those associated with the particular propellers used in the experimental phase of this investigation. The propeller radius is 4 inches and the hub-to-tip ratio is 0.25. As mentioned, the number of blades is 2, 5, and 10, making the blade spacings at 0.75R equal to 9.40, 3.77, and 1.88 in., respectively. The turbulence length scales, Λ, used are those generated by a set of square mesh grids used in the experiments.

CHAPTER VIII

EXPERIMENTAL INVESTIGATION OF TIME-DEPENDENT THRUST RESPONSE OF PROPELLERS TO TURBULENT INFLOW

8.1 Introduction

The response of typical marine propellers to typical turbulent inflows has not been considered experimentally. Sevik [22] has measured the response of a free stream propeller operating in a homogeneous, isotropic turbulent flow, and compared the results to theory.

It was felt that a more comprehensive experimental investigation should be performed with a free stream propeller operating in homogeneous, isotropic turbulence. Three propellers were chosen, two-, five-, and ten-bladed, so that the effects of blade spacing-to-turbulence length scale could be investigated. A range of turbulence length scales and intensities was chosen so that the effects of these variables could be investigated.

A comparison of the time-dependent thrust spectra obtained experimentally are to be compared to spectra generated by two different analytical methods.

8.2 Propellers and Drive System

In order to investigate the time-dependent thrust response of propellers due to operation in various turbulent inflows, a series of experiments were conducted in the 48-inch diameter water tunnel at the Applied Research Laboratory.

The time-dependent thrust as generated by a two-, five-, and ten-bladed propeller due to its operation in various turbulent inflows was measured. The system used to measure the propeller time-dependent thrust and the propellers themselves, are the same as described previously in Sections 5.2, 5.3 and 5.4.

8.3 Generation of Turbulence

The propellers were operated in turbulent inflows having different turbulent length scales and intensities. Three square mesh grids were used to generate the different turbulent inflows. Since, in the theoretical approach, the assumption of homogeneous, isotropic turbulence has been made, an attempt to generate this type of turbulence was made by maintaining the ratio of rod diameter to mesh size at 0.2 and by always operating with the grid-to-propeller spacing greater than 15 mesh sizes. Three grids were used, having mesh sizes of 2, 4 and 6 inches. Figure 68 shows a typical grid installation in the test section of the water tunnel.

The length scales and intensities of the turbulence generated by square mesh grids have been investigated by Naudascher [44] in which he correlates measurements made by a large number of investigators. Naudascher's results which are used in this investigation are reproduced in Figures 69 through 75. The Reynolds' numbers based on rod diameter appropriate to this particular experiment are given in Table 7. The positions of the grid locations upstream of the propeller are given in Table 8.

The virtual origin of the turbulence, nondimensionalized by the mesh size of the grid, is plotted versus Reynolds number in Figure 69.

The virtual origin is that axial location where the turbulent length scale tends to zero. From this figure, the virtual origin was determined for each of the grids employed, and these are listed in Table 9. Using the virtual origins and Reynolds numbers of Tables 8 and 9, nondimensional distances for use with Figure 70 were computed. The two curves for each set of data on Figure 70 are generated by using Equation (12) of Naudascher [44] which is

$$\frac{L}{b} = \frac{L_\infty - L_o}{\lambda_\infty} \left\{ \sqrt{10} \left[\frac{x - x_o}{bR_b} \right]^{1/2} \right\} + \frac{L_o}{b} \quad , \tag{54}$$

where Equation (13) due to Naudascher [44] has been used. Naudascher [44] found that Equation (54) above fits the upper and lower limits of the data by using values of $L_o/b = 1.25$, $\lambda_\infty/L_o = 19.2$, $L_\infty/\lambda_\infty = 3.0$ and $L_\infty/\lambda_\infty = 1.25$ for the upper and lower limits, respectively.

It was found that the nondimensional distances, $(x-x_o)/bR_b$, for the present experiment were lower than those given in Figure 70. Consequently, Equation (54) above was used to generate two curves, representing the upper and lower limits, which would be in the range of interest of the present investigation. The results are shown in Figure 71. Using this figure, the values of turbulence integral length scale were determined for the nondimensional distances of this investigation, see Table 10. The average values of the length scales given in Table 10 are used in predicting the spectra of propeller time-dependent thrust.

The turbulence intensities for the present experiments were calculated from information contained in Naudascher's [44] paper. He has correlated the results of a number of experiments and presented

the data as plots of uR_b/UC versus $(x-x_o)/bR_b$ which are reproduced here as Figure 72. The values of nondimensional distance encountered in the present investigation are smaller than those used in the correlation by Naudascher. The equation

$$\frac{u}{U}\frac{R_b}{C} = 5\left[\frac{1}{\lambda/b} - \frac{1}{\lambda_\infty/b}\right] \quad , \tag{55}$$

where

$$\lambda/b \cong \sqrt{10}\left[\frac{x-x_o}{bR_b}\right]^{1/2} \quad \text{and} \quad \frac{\lambda_\infty}{b} = 24 \quad ,$$

was shown to fit the data of Figure 72. Thus, Equation (55) above was used to generate turbulence intensities, $(u/U)(R_b/C)$, for values of nondimensional distance, $(x-x_o)/bR_b$, in the range of interest for the present investigation. The results are presented in Figure 73.

The constant C is a function of drag coefficient and solidity of the grid. Naudascher [44] has correlated a large number of experimental results to generate the curve reproduced in Figure 74. This figure was used to obtain values of $C/\sqrt{C_D R_b}$ for solidities appropriate to the grids used in the present experiment. The drag coefficient, C_D, plotted versus grid solidity in Figure 75 was obtained from Table 1, Naudascher [44]. The constants C were then computed for all values of solidity and Reynolds numbers encountered in the present experiment.

Knowing appropriate values of C and the other important parameters, Equation (55) was used to compute the turbulence intensities, u/U, occurring at the propeller due to a particular

grid upstream of the propeller. Table 11 lists these computed values of turbulence intensity.

The values of turbulence integral length scale and intensity listed in Table 10 and 11, respectively, were used in the computation of propeller time-dependent thrust spectra for the two theories considered in this investigation.

8.4 Data Acquisition and Analysis for Time-Dependent Thrust

A block diagram of the data acquisition and analysis system is shown in Figure 76. For a particular propeller operating in the turbulence field due to a particular grid, the piezoelectric crystal in the time-dependent thrust balance responds with a signal. The signal is high pass filtered, with Krohn-Hite variable filters, to remove the strong shaft rate frequency component from the signal. The filtered signal was then narrowband, 10 Hz, analyzed with a General Radio Wave Analyzer and Level Recorder on site in order to monitor the output. The signal was also recorded on magnetic tape for later analysis on a real time analyzer, Federal Scientific Ubiquitous Analyzer. The spectra from the real time analyses are those presented here. The experimental data has been corrected to a 1 Hz bandwidth spectra. The frequency range analyzed was 0-150 Hz. Permanent records of the spectra were obtained with an x-y plotter.

A typical spectrum as produced by the Federal Scientific Ubiquitous Analyzer is shown in Figure 77. As seen, the time-dependent thrust levels fluctuate erratically with small changes in frequency. The amplitudes of these fluctuations in level are a function of the bandwidth and averaging time of the analyzer. They are irrelevant as

far as comparing experimental and analytical results. Hence, a dB averaging of the levels of time-dependent thrust at a number of discrete frequencies was performed. The large dots in Figure 77 are the result of dB averaging. A smooth line connecting the large dots then represents an averaged spectrum of the single amplitude time-dependent thrust. These averaged spectra were used for comparison with analytical results.

8.5 Experiments Conducted

Measurement of the time-dependent thrust generated by the propeller due to operation in turbulent inflows having various length scales and intensities were made. For each test condition considered, the propeller was operated at its design advance ratio of J = 1.17 in a free stream mean velocity of 18 ft/sec. Three propellers were considered, having 2, 5, and 10 blades. Figure 29 shows the two- and ten-bladed propellers. The blades of each of these propellers had a constant chord of one inch and a span of three inches. The propellers tested in this phase of the investigation are the same as discussed previously in Section 5.2, and hence, will not be discussed further here.

Each propeller was operated in each of several turbulent inflows. The propellers were driven by the downstream dynamometer and the turbulence was generated by the upstream square mesh grids. The propeller operating conditions and turbulent inflow characteristics considered in the present experiment are listed in Table 12. The turbulence length scales listed in Table 12 are the average of the maximum and minimum length scales listed in Table 10. These average

turbulence length scales as well as the turbulence intensities listed in Table 12 were used in each analytical method considered.

For each of the propeller operating conditions and turbulent inflow conditions considered, the spectrum of the single amplitude time-dependent thrust was measured with the system shown in Figure 76. Permanent records of the spectra were produced with an x-y plotter. The averaged spectra are used for correlation with the results of analytical methods.

The single amplitude time-dependent thrust developed by each propeller operating with no grid installed upstream was measured and constitutes background levels. Each propeller was operated at an advance ratio of J = 1.17 in a free stream velocity of 18 ft/sec and the spectrum obtained. In all cases, the background level is well below the level obtained with any grid installed.

CHAPTER IX

RESULTS OF EXPERIMENTS WITH TURBULENT INFLOWS AND COMPARISON WITH THEORY

The results of the experiments are presented in the form of spectra of the single amplitude time-dependent thrust. The frequency range considered is always large enough to include the blade passing frequency of the propeller considered. The spectra are presented in Figures 78 through 88. Each figure includes the experimental results, the predicted spectra due to Sevik's [12] analysis and the analysis developed in the present thesis, and measurements of the propeller response to the turbulence present in the test section without a turbulence generating grid, i.e., background.

In general, the measurements of the response of each propeller to the turbulence in the flow with no turbulence generating grid in the water tunnel showed sufficiently lower levels than the propeller response with grids present in the water tunnel. For the two-bladed propeller, Figures 78 to 80, the broadband level due to background is at least 14 dB lower than with a grid installed. The blade passing frequency tone due to the background is at least 2 dB lower than with a grid installed. The large tone in the spectra of the background is due to imbalance in the propeller drive system.

For the five-bladed propeller, Figures 81 to 83, the broadband level due to background is at least 3 dB lower than with a grid installed. The blade passing frequency tone due to the background is about the same as the broadband level with a grid installed. However, there is a "hump" in the broadband level of the spectra with a grid

installed which is not present in the background spectra. This broadband hump is attributed to the response of the propeller to the turbulent flows generated by the grids.

For the ten-bladed propeller, Figures 85 to 88, the broadband level due to background is at least 11 dB lower than with a grid installed. There is no pure tone blade passing frequency for the propeller operating in the background turbulence level. There is a broadband hump in the spectra with a grid installed which is not present in the background spectra. This broadband hump is attributed to the response of the propeller to the turbulent flows generated by the grids.

The two analytical approaches yield essentially the same spectra for the two-bladed propeller operating in the turbulent inflows chosen. The analysis which employs blade-to-blade correlation of time-dependent lift due to correlation of velocity fluctuations does not show large amplitude broadband "humps" in the spectra. The experimental spectra do not exhibit "humps" at blade passing frequency and multiples. This is because the length scale of the turbulence is small compared to the spacing of the blades. The analysis which does not include blade-to-blade correlation does not predict "humps" in the spectra, as expected.

The levels of the predicted and measured spectra for the two-bladed propeller correlate quite well for frequencies below blade passing frequency. For frequencies above blade passing frequency, the levels of the predicted and measured spectra diverge, the measured values falling off faster with frequency than the predictions. The rate of divergence decreases with increasing turbulence length scale,

however. This is due almost entirely to the experimental results whose slope with increasing frequency decreases with increasing turbulence length scale. This can be seen by comparing Figures 77 and 80. The slope of the spectra, i.e., change in level with frequency with change in turbulence intensity for the experiments, is about the same as seen by comparing Figures 78 and 79.

For the five-bladed and ten-bladed propellers, the two analytical methods yield dissimilar spectra. The method which includes blade-to-blade correlation yields results lower in level than the method not including blade-to-blade correlation. In addition, the method which includes blade-to-blade correlation yields peaks in the spectra at blade passing frequency, where the method not including blade-to-blade correlation does not.

A comparison of spectra from the analytical methods with those from experiment reveals good correlation with the analytical method including blade-to-blade correlation. The levels are predicted quite accurately when comparing experimental results to the analysis which includes blade-to-blade correlation. In addition, the "humps" centered at blade passing frequency are shown in both the experimental spectra and the analysis including blade-to-blade correlation, but not in the analysis excluding blade-to-blade correlation. The "hump" of the experimental spectra is consistently lower in amplitude than that due to the analysis. This is in part due to using average values of length scales computed from Table 10.

There is, however, as seen in Figures 81 through 88, a much better agreement between experimental spectra and the spectra predicted by the analytical method which includes blade-to-blade

correlation than between the experimental spectra and the spectra predicted by the analytical method which does not include blade-to-blade correlation. This better agreement is in both shape and level of the spectra.

CHAPTER X

CONCLUSIONS AND RECOMMENDATIONS FOR FUTURE RESEARCH

With respect to blade passing frequency time-dependent thrust due to a propeller operating in a spatially varying inflow, the following conclusions can, in general, be made:

1. The comparison made in Section 6.2 shows that using $\partial C_L/\partial\alpha$ from steady state cascade data to approximate the unsteady blade-to-blade induced effects in a two-dimensional theory produces good agreement with unsteady lifting surface theory for the particular propeller considered in this investigation, i.e., the aspect ratio of the blades is high when compared to most marine propellers. In addition, the two-dimensional theory, and, hence, the lifting surface theory, including approximations for blade-to-blade induced effects, correlates well with experimental results for all strut-to-propeller spacings, as shown in Section 6.3.

2. As also shown in Section 6.3, a further improvement in correlation between two-dimensional theory and experimental results is provided when effects of chordwise velocity variations are included in the theory. The improvement is greatest at lower advance ratios, i.e., higher blade incidence angles, where the effect of chordwise velocity variations is greatest.

3. The effects of both chordwise velocity variations and blade-to-blade induction should be included in predicting time-dependent forces and moments when employing the two-dimensional theory.

With respect to broadband time-dependent thrust, as shown in Chapter IX, due to a propeller operating in a turbulent inflow, the following conclusions can in general, be made:

1. The analytical treatment which incorporates blade-to-blade correlation of time-dependent lift predicts the level of the time-dependent thrust spectra as compared to experiment better than the analysis which does not include blade-to-blade correlation.

2. The analytical treatment which incorporated blade-to-blade correlation of time-dependent lift predicts the "humps" which occur in the time-dependent thrust spectra at blade passing frequency while that which does not include blade-to-blade correlation does not predict the "humps".

Recommendations for future research are as follows:

1. The effects of camber on the propeller time-dependent forces due to operation in a spatially nonuniform velocity field should be incorporated into the analytical method. Experiments should be performed with cambered bladed propellers and correlations with predictions made.

2. The effects of blade thickness on the propeller time-dependent forces due to operation in a spatially nonuniform velocity field should be incorporated into the analytical method. Experiments should be performed with several propellers having various thicknesses and correlations with predictions made.

3. The effects of blade aspect ratio should be investigated experimentally with a series of propellers having different aspect ratios and correlations with predictions made.

4. The effects of unsteady potential interaction can become important on a marine vessel due to the close proximity of the propeller and nearby surfaces such as rudders, shaft support struts, etc. An experimental and analytical investigation of the effects of potential interaction on propeller time-dependent forces should be done.

5. Once a determination of the importance of the various possible contributors to propeller time-dependent forces has been made, an incorporation of time-dependent force considerations intc the design aspect of propellers should be made. One could then design a propeller to meet steady state requirements while minimizing its unsteady response.

6. An investigation of methods to reduce the scatter of the Fourier coefficients determined from wake surveys should be made. This is important since the coefficients are used in the prediction of propeller time-dependent forces.

7. The length scales and intensitites of the turbulence at the propeller leading edge should be determined experimentally for typical marine vessels. Using this information, a parametric investigation of the propeller unsteady response to turbulence should be done.

REFERENCES

1. Hawthorne, W. R., "The Secondary Flow about Struts and Airfoils," J. Aero. Sci., Vol. 21, September 1954.

2. Hadler, J. B. and H. M. Cheng, "Analysis of Experimental Wake Data in Way of Propeller Plane of Single and Twin-Screw Ship Models," Trans. SNAME, Vol. 73, 1965.

3. van Manen, J. D. and A. J. W. Lap, "Scale-Effect Experiments on Victory Ships and Models, Part II," Trans. Inst. Nav. Arch., 1958.

4. Tjoenneland, J. P., "An Investigation into the Repeatability of Wake Velocities," MIT, Dept. of Naval Architecture and Marine Engineers, Report No. 67-5, January 1967.

5. Burstein, N. M., "Boundary-Layer Investigation on a Body of Revolution with Fins," M. S. Thesis, The Pennsylvania State University, 1965.

6. Boyle, A. L., "An Investigation of the Effect on Reynolds Number of Velocity Surveys Conducted in the Subsonic Wind Tunnel," NSRDC Report No. 3408, September 1970.

7. Sears, W. R., "Some Aspects of Non-Stationary Airfoil Theory and Its Practical Application," J. Aero. Sci., 1941.

8. Horlock, J. H., "Fluctuating Lift Forces on Aerofoils Moving Through Transverse and Chordwise Gusts," Trans. ASME, J. Basic Eng., Paper No. 68-FE-28, 1968.

9. Boswell, R. J., "Measurement, Correlation with Theory and Parametric Investigation of Unsteady Propeller Forces and Moments," M. S. Thesis, The Pennsylvania State University, August 1967.

10. Henderson, R. E., "Unsteady Response of an Axial Flow Turbomachine to an Upstream Disturbance," Ph. D. Thesis, Cambridge Univeristy, 1972.

11. Whitehead, D. S., "Force and Moment Coefficients for Vibrating Airfoils in Cascade," Aeronautical Research Council R and M 3254, February 1960.

12. Sevik, M. M., "The Response of a Propulsor to Random Velocity Fluctuations," ORL, Serial No. N00017-70-C-1407-2, April 30, 1970.

13. Sevik, M. M., "Sound Radiation from a Subsonic Rotor Subjected to Turbulence," NASA SP 304, Part II, p. 493, The Pennsylvania State University, 1970.

REFERENCES (CONT.)

14. Mani, R., "Noise Due to Interaction of Inlet Turbulence with Isolated Stators and Rotors," J. Sound Vib., Vol. 17, (2), 1971, p. 251-260.

15. Mugridge, B. D., "Broadband Noise Generation by Aerofoils and Axial Flow Fans," AIAA Aero-Acoustics Conf., Paper No. 73-1018, 1973.

16. Robbins, B. and B. Lakshminarayana, "Effect of Inlet Turbulence on Compressor Noise," J. Aircraft, Vol. 11, No. 5, May 1974, pp. 273-281.

17. Barlow, J. B. "Theory of Propeller Forces in a Turbulent Atmosphere," University of Toronto, UTIAS Report No. 155, Sept. 1970.

18. Barlow, J. B., "On the Forces and Moments on a Propeller Moving Axially Through Homogeneous Turbulence," AIAA Paper No. 70-549, AIAA Atmospheric Flight Mechanics Conf., May 13-15, 1970.

19. Miller, M. L., "Experimental Determination of Unsteady Propeller Forces," Seventh ONR Symposium of Naval Hydrodynamics, Rome, Italy, August, 1968.

20. Brandau, J. H., "Static and Dynamic Calibration of Propeller Model Fluctuating Force Balances," Naval Ship Research and Development Center Report No. 2350, August 1967; and "Calibration of Propeller Model Fluctuating Force Balances," Technologia Naval, January 1968.

21. Wereldsma, R., "Dynamic Behavior of Ship Propellers," Netherlands Ship Model Basin Publication No. 255, 1962.

22. Sevik, M., "The Response of Propulsors of Turbulence," Proc. of Seventh Symposium on Naval Hydrodynamics, DR-148, 1968.

23. Lewis, F. M., "Propeller Vibration," Trans. SNAME, 1935 and 1936.

24. Wereldsma, R., "Experiments on Vibrating Propeller Models," Netherlands Ship Model Basin Publication No. 252, 1960.

25. Wereldsma, R., "Further Research on Propeller Vibratory Forces," Report No. 66-172-AS, Netherlands Ship Model Basin, Wageningen, The Netherlands, 1966.

26. Wereldsma, R., "Research on Propeller Vibratory Forces, Final Report," Netherlands Ship Model Basin, Report 193, Wageningen, The Netherlands, 1964.

REFERENCES (CONT.)

27. Jacobs, W. R., and S. Tsakonas, "Correlation of Vibratory Thrust and Torque Calculations with Experimental Values for the Netherlands Ship Model Basin Propellers, Parts I and II," Stevens Institute of Technology, DL Report 1237, September 1967, and DL Report 1288, April 1968.

28. Tsakonas, S., J. P. Breslin, and M. Miller, "Correlation and Application of an Unsteady Flow Theory for Propeller Forces," Trans. SNAME, Vol. 75, 1967.

29. Tsakonas, S., W. R. Jacobs, and P. H. Rank, "Unsteady Propeller Lifting Surface Theory with Finite Number of Chordwise Modes," Stevens Institute of Technology, Davidson Laboratory Report 1133, December 1966.

30. Holmes, D. W., "Lift Fluctuations on Airfoils in Transverse and Chordwise Gusts," Ph. D. Thesis, Cambridge University, 1972.

31. Naumann, H. and H. Yeh, "Lift and Pressure Fluctuations of a Cambered Airfoil Under Periodic Gusts and Applications in Turbomachinery," Trans. ASME, J. Engr. Power, January 1973.

32. Henderson, R. E., and H. Daneshyar, "Theoretical Analysis of Fluctuating Lift on the Rotor of an Axial Turbomachine," Aeronautical Research Council R and M 3684, 1972.

33. Hanaoka, T., "Hydrodynamics of an Oscillating Screw Propeller," Fourth Symposium on Naval Hydrodynamics, Office Naval Research, Dept. of Navy, ACR-92, 1962.

34. Shiroi, J. and S. Tsakonas, "Three-Dimensional Approach to the Gust Problem for a Screw Propeller," Stevens Institute of Technology, Davidson Laboratory Report 940, March 1963; J. Ship Res., Vol. 7, No. 4, April 1964.

35. Tsakonas, S., and W. R. Jacobs, "Unsteady Lifting Surface Theory for a Marine Propeller at Low Pitch Angle with Chordwise Loading Distribution," Stevens Institute of Technology, Davidson Laboratory Report 994, January 1964; J. Ship Res., Vol. 9, No. 2, September 1965.

36. Tsakonas, S., C. Y. Chen, and W. R. Jacobs, "Exact Treatment of the Helicoidal Wake in the Propeller Lifting Surface Theory," Stevens Institute of Technology, Davidson Laboratory Report 1117, August 1966.

37. Silverstein, A., S. Katzoff, and W. K. Bullivant, "Downwash and Wake Behind Plain and Flapped Airfoils," NACA TR-651, 1939.

REFERENCES (CONT.)

38. Dylewski, T. J., "Criteria for Selecting Curves for Fitting to Data," AIAA J., Vol. 8, No. 8, August 1970.

39. Emery, J. C., L. J. Herrig, J. R. Erwin, and A. R. Felix, "Systematic Two-Dimensional Cascade Tests of NACA 65-Series Compressor Blades at Low Speeds," NACA TN-1368.

40. Bendat, J. S., and A. G. Piersol, Random Data: Analysis and Measurement Procedures, Wiley-Interscience, 1971.

41. Batchelor, G. K., The Theory of Homogeneous Turbulence, Cambridge University Press, 1970.

42. Stewart, R. W., and A. A. Townsend, "Similarity and Self-Preservation in Isotropic Turbulence," Trans. Roy. Soc., Vol. 243, pp. 359-386, 1951.

43. Fung, Y. C., An Introduction to the Theory of Aeroelasticity, Dover, 1969.

44. Naudascher, E., and C. Farell, "Unified Analysis of Grid Turbulence," J. Eng. Mch. Div., Proc. ASCE, pp. 121-141, April 1970.

45. Thompson, D. E., "State-of-the-Art Report on Propeller-Induced Time-Dependent Forces," Trans. of 16th American Towing Tank Conference, Institute De Pesquisas Technologicas Marinha Do Brasil, Sao Paulo, Brasil, August 9-13, 1971.

46. Thompson, D. E., "Time-Dependent Thrust Generated by a Propeller Operating in a Turbulent Inflow," 2nd Interagency Symposium on University Research in Transportation Noise, North Carolina State University, June 5-7, 1974.

47. Thompson, D. E., "Effects of Chordwise Velocity Variations on Propeller Time-Dependent Thrust," Submitted to J. Hydronaut., 1976.

48. Stewart, R. W., and A. A. Townsend, "Similarity and Self-Preservation in Isotropic Turbulence," Phil. Trans., Series A, Vol. 243, 1951, p. 359.

49. Van der Hegge-Zijnen, B. G., "Measurements of the Intensity, Integral Scale and Microscale of Turbulence Downstream of Three Grids in a Stream of Air," Appl. Sci. Res., Section A, Vol. 7, 1958, p. 149.

50. Batchelor, G. K., and A. A. Townsend, "Decay of Istropic Turbulence in the Initial Period," Proc. Roy. Soc., Series A, Vol. 193, 1948, p. 539.

REFERENCES (CONT.)

51. Dryden. H. L., G. B. Schubauer, W. C. Mock, and H. K. Skramstad, "Measurements of the Intensity and Scale of Wind Tunnel Turbulence and Their Relation to the Critical Reynolds Number of Spheres," National Advisory Committee for Aeronautics, Reprint No. 581, 1937.

52. Von Kármán, T., "Some Remarks on the Statistical Theory of Turbulence," Proceedings, 5th International Congress of Applied Mechanics, 1938, p. 347.

53. Uberoi, M. S., "Energy Transfer in Isotropic Turbulence," Physics of Fluids, Vol. 6, 1963, p. 1048.

54. Wyatt, L. A., "Energy and Spectra in Decaying Homogeneous Turbulence," Thesis presented to the University of Manchester, at Manchester, England, in 1955, in partial fulfillment of the requirements for the degree of Doctor of Philosophy.

55. Batchelor, G. K., and A. A. Townsend, "Decay of Turbulence in the Final Period," Proc. Roy. Soc., Series A, Vol. 194, 1948, p. 527.

56. Baines, W. D., and E. G. Peterson, "An Investigation of Flow Through Screens," Trans. ASME, Vol. 6, 1948, p. 97.

57. Comte-Bellot, G., and S. Corrsin, "The Use of a Contraction to Improve the Isotropy of Grid-Generated Turbulence," Proc. Roy. Soc., Vol. 25, 1966, p. 657.

APPENDIX A

DETAILED CALCULATIONS OF UNSTEADY FORCES AND MOMENTS

The objective of this appendix is to show that only certain harmonics of the inflow to the propeller result in unsteady forces and moments. Consider the unsteady axial force or thrust $\tilde{F}_z$ as given in Equation (21). The phase angle between blade segments, ϕ_j, can be due to two things; namely, the separation between blades and the phase difference between segments on each blade due to blade skew:

$$\tilde{F}_z = \sum_{j=1}^{P} \sum_{\ell=1}^{B} \sum_{n=1}^{\infty} \tilde{L}_{\ell jn} \cos\beta_j \quad . \tag{A1}$$

Write this equation as

$$\tilde{F}_z = \sum_{j=1}^{P} \sum_{\ell=1}^{B} \sum_{n=1}^{\infty} |\tilde{L}_{jn}|_1 \; e^{in(\Omega t + \psi_j + \eta_\ell)} \quad , \tag{A2}$$

where

$\psi_j \equiv$ phase angle due to blade skew,

$\eta_\ell \equiv$ phase angle due to blade separation

and

$$|\tilde{L}_{jn}|_1 = \left(\frac{\partial C_L}{\partial \alpha}\right)_j \rho_f b_j \Delta r_j U_{Rj} Uc_{nj} \{K(k_{nj}) \cos\beta_j - \alpha_j T(k_{nj}) \sin\beta_j\} \times \cos\beta_j \quad . \tag{A3}$$

Here, it has been assumed that at a constant radius, i.e., a particular value of j, the blade geometry and steady flow characteristics are constant at each blade.

Equation (A2) can be written as

$$\tilde{F}_z = \sum_{j=1}^{P} \sum_{\ell=1}^{B} \sum_{n=1}^{\infty} \left|\tilde{L}_{jn}\right|_1 e^{in(\zeta_j + \eta_\ell)} \quad , \tag{A4}$$

where, for simplicity, $\zeta_j = \Omega t + \psi_j$. The phase angle η_ℓ can be written as

$$\eta_\ell = \ell \frac{2\pi}{B} \quad ,$$

where $\ell = 1, 2, \ldots, B$.

Then, Equation (A4) becomes

$$\tilde{F}_z = \sum_{j=1}^{P} \sum_{\ell=1}^{B} \sum_{n=1}^{\infty} \left|\tilde{L}_{jn}\right|_1 e^{i(n\zeta_j + \ell\frac{2\pi n}{B})} \quad . \tag{A5}$$

Using the relationship

$$\sum_{\ell=1}^{B} e^{i\ell\frac{2\pi n}{B}} = \begin{cases} B & \text{if } n = mB \\ 0 & \text{if } n \neq mB \end{cases} \quad , \tag{A6}$$

Equation (A5) becomes

$$(\tilde{F}_z)_m = B \sum_{j=1}^{P} \{\left|L_{j(mB)}\right|_1 e^{imB\zeta_j}\} \tag{A7}$$

or

$$(\tilde{F}_z)_m = B \sum_{j=1}^{P} \{|\tilde{L}_{j(mB)}|_1 \, e^{imB(\Omega t + \psi_j)}\} \quad . \tag{A8}$$

Equation (A8) indicates that an unsteady thrust exists on a propeller which operates in a nonuniform inflow. The unsteady thrusts exist at integer multiples of blade rate frequency, $mB\Omega$.

Consider now the unsteady side force, $\tilde{F}_x$, as given in Equation (21).

$$\tilde{F}_x = \sum_{j=1}^{P} \sum_{\ell=1}^{B} \sum_{n=1}^{\infty} \tilde{L}_{\ell jn} \sin\beta_j \sin(\Omega t + \psi_j + \eta_\ell) \quad . \tag{A9}$$

Write this equation as

$$\tilde{F}_x = \sum_{j=1}^{P} \sum_{\ell=1}^{B} \sum_{n=1}^{\infty} |\tilde{L}_{jn}|_2 \sin(\Omega t + \psi_j + \eta_\ell) \times$$

$$e^{in(\Omega t + \psi_j + \eta_\ell)} \quad , \tag{A10}$$

where

$$|\tilde{L}_{jn}|_2 = \left(\frac{\partial C_L}{\partial \alpha}\right)_j \rho_f b_j U_{Rj} U c_{nj} \{K(k_{nj}) \cos\beta_j -$$

$$\alpha_j T(k_{nj}) \sin\beta_j\} \Delta r_j \sin\beta_j \quad . \tag{A11}$$

Expanding the exponential in Equation (A10),

$$\tilde{F}_x = \sum_{j=1}^{P} \sum_{\ell=1}^{B} \sum_{n=1}^{\infty} \{|\tilde{L}_{jn}|_2 \sin(\zeta_j + \eta_\ell) [\cos n(\zeta_j + \eta_\ell) +$$

$$i \sin n(\zeta_j + \eta_\ell)]\} \quad , \tag{A12}$$

where $\zeta_j = \Omega t + \psi_j$. The phase angle η_ℓ can be written as

$$\eta_\ell = \ell \frac{2\pi}{B} \quad ,$$

where $\ell = 1, 2, \ldots B$.

Equation (A12) then becomes:

$$\tilde{F}_x = \sum_{j=1}^{P} \sum_{\ell=1}^{B} \sum_{n=1}^{\infty} \{|\tilde{L}_{jn}|_2 \sin(\zeta_j + \frac{2\pi}{B}) [\cos(n\zeta_j + \ell\frac{2\pi n}{B}) +$$

$$i \sin(n\zeta_j + \ell\frac{2\pi n}{B})]\} \quad . \tag{A13}$$

Using standard trigonometric identities, Equation (A13) can be written as

$$\tilde{F}_x = \sum_{j=1}^{P} \sum_{\ell=1}^{B} \sum_{n=1}^{\infty} \left(|\tilde{L}_{jn}|_2 \left\{ \frac{1}{2} \left[\sin\left((n+1)\zeta_j + \ell\frac{2\pi(n+1)}{B} \right) - \right. \right. \right.$$

$$\left. \sin\left((n-1)\zeta_j + \ell\frac{2\pi(n-1)}{B} \right) \right] + \frac{1}{2} i \left[\cos\left((n-1)\zeta_j + \ell\frac{2\pi(n-1)}{B} \right) -$$

$$\left. \left. \left. \cos\left((n+1)\zeta_j + \frac{2\pi(n+1)}{B} \right) \right] \right\} \right)$$

or

$$\tilde{F}_x = \sum_{j=1}^{P} \sum_{\ell=1}^{B} \sum_{n=1}^{\infty} \left[|\tilde{L}_{jn}|_2 \frac{1}{2} \left\{ [\sin(n+1)\zeta_j \cos\ell \frac{2\pi(n+1)}{B} + \right.\right.$$

$$\cos(n+1)\zeta_j \sin\ell \frac{2\pi(n+1)}{B} - \sin(n-1)\zeta_j \cos\ell \frac{2\pi(n-1)}{B} -$$

$$\cos(n-1)\zeta_j \sin\ell \frac{2\pi(n-1)}{B}] + i[\cos(n-1)\zeta_j \cos\ell \frac{2\pi(n-1)}{B} -$$

$$\sin(n-1)\zeta_j \sin\ell \frac{2\pi(n-1)}{B} - \cos(n+1)\zeta_j \cos\ell \frac{2\pi(n+1)}{B} +$$

$$\left.\left. \sin(n+1)\zeta_j \sin\ell \frac{2\pi(n+1)}{B}] \right\} \right] \quad . \tag{A14}$$

It is well known that

$$\sum_{\ell=1}^{B} \cos\ell \frac{2\pi(n\pm1)}{B} = \begin{cases} 0 & \text{if } n \pm 1 \neq mB \\ B & \text{if } n \pm 1 = mB \end{cases} \tag{A15}$$

and

$$\sum_{\ell=1}^{B} \sin\ell \frac{2\pi(n\pm1)}{B} = 0 \quad \text{for all values of } n \pm 1 \quad . \tag{A16}$$

Using Equations (A15) and (A16) in Equation (A14), we obtain

$$(\tilde{F}_x)_m = \sum_{j=1}^{P} \frac{B}{2} |\tilde{L}_{j(mB-1)}|_2 [\sin mB\zeta_j - i \cos mB\zeta_j] +$$

$$\sum_{j=1}^{P} \frac{B}{2} |\tilde{L}_{j(mB+1)}|_2 [-\sin mB\zeta_j + i \cos mB\zeta_j]$$

or

$$(\tilde{F}_x)_m = \sum_{j=1}^{P} i \frac{B}{2} \{- |\tilde{L}_{j(mB-1)}|_2 e^{imB\zeta_j} + |\tilde{L}_{j(mB+1)}|_2 e^{imB\zeta_j}\} \quad . \quad (A17)$$

Letting $\zeta_j = \Omega t + \psi_j$, the total unsteady force $\tilde{F}_x$ occurs at blade rate and multiples, $mB\Omega$, and is given by

$$(\tilde{F}_x)_m = \frac{B}{2} \{ \sum_{j=1}^{P} i [- |\tilde{L}_{j(mB-1)}|_2 + |\tilde{L}_{j(mB+1)}|_2] e^{imB(\Omega t + \psi_j)}\} \quad . \quad (A18)$$

Consider now the unsteady side force, $\tilde{F}_y$, as given in Equation (21)

$$\tilde{F}_y = \sum_{j=1}^{P} \sum_{\ell=1}^{B} \sum_{n=1}^{\infty} \tilde{L}_{\ell jn} \sin \beta_j \cos (\Omega t + \psi_j + \eta_\ell) \quad . \quad (A19)$$

Using Equation (A11), $\tilde{F}_y$ may be written as

$$\tilde{F}_y = \sum_{j=1}^{P} \sum_{\ell=1}^{B} \sum_{n=1}^{\infty} |\tilde{L}_{jn}|_2 \cos (\zeta_j + \eta_\ell) \quad [\cos n (\zeta_j + \eta_\ell) + i \sin (\zeta_j + \eta_\ell)] \quad , \quad (A20)$$

where ζ_j and η_ℓ are defined as before. Equation (A20) becomes

$$\tilde{F}_y = \sum_{j=1}^{P} \sum_{\ell=1}^{B} \sum_{n=1}^{\infty} \{|\tilde{L}_{jn}|_2 \cos (\zeta_j + \ell\tfrac{2\pi}{B}) [\cos (n\zeta_j + \ell\tfrac{2\pi n}{B}) + i \sin (n\zeta_j + \ell\tfrac{2\pi n}{B})]\} \quad . \quad (A21)$$

Using standard trigonometric identities, Equation (A21) can be written as

$$\tilde{F}_y = \sum_{j=1}^{P} \sum_{\ell=1}^{B} \sum_{n=1}^{\infty} \left(|\tilde{L}_{jn}|_2 \left\{ \frac{1}{2} \left[\cos\left((n+1)\zeta_j + \ell\frac{2\pi(n+1)}{B} \right) + \cos\left((n-1)\zeta_j + \ell\frac{2\pi(n-1)}{B} \right) \right] + i\,\frac{1}{2} \left[\sin\left((n+1)\zeta_j + \ell\frac{2\pi(n+1)}{B} \right) + \sin\left((n-1)\zeta_j + \ell\frac{2\pi(n-1)}{B} \right) \right] \right\} \right)$$

or

$$\tilde{F}_y = \sum_{j=1}^{P} \sum_{\ell=1}^{B} \sum_{n=1}^{\infty} \left(|L_{jn}|_2 \frac{1}{2} \{ [\cos (n+1)\zeta_j \cos \ell\frac{2\pi(n+1)}{B} - \sin (n+1)\zeta_j \sin \ell\frac{2\pi(n+1)}{B} + \cos (n-1)\zeta_j \cos \ell\frac{2\pi(n-1)}{B} - \sin (n-1)\zeta_j \sin \ell\frac{2\pi(n-1)}{B}] + i\,[\sin (n+1)\zeta_j \cos \ell\frac{2\pi(n+1)}{B} + \cos (n+1)\zeta_j \sin \ell\frac{2\pi(n+1)}{B} + \sin (n-1)\zeta_j \cos \ell\frac{2\pi(n-1)}{B} + \cos (n-1)\zeta_j \sin \ell\frac{2\pi(n-1)}{B}] \} \right) . \quad \text{(A22)}$$

Using Equations (A15) and (A16) in Equation (A22), we obtain

$$(\tilde{F}_y)_m = \sum_{j=1}^{P} \{|\tilde{L}_{j(mB-1)}|_2 \frac{B}{2} [\cos mB\zeta_j + i \sin mB\zeta_j] +$$

$$\sum_{j=1}^{P} |\tilde{L}_{j(mB+1)}|_2 \frac{B}{2} [\cos mB\zeta_j + i \sin mB\zeta_j]\}$$

or

$$(\tilde{F}_y)_m = \sum_{j=1}^{P} \frac{B}{2} \{[|\tilde{L}_{j(mB-1)}|_2 + |\tilde{L}_{j(mB+1)}|_2] e^{imB\zeta_j}\} \quad . \tag{A23}$$

Letting $\zeta_j = mB\Omega t + \psi_j$, we obtain the unsteady force $\tilde{F}_y$ which occurs at blade rate and multiplies, $mB\Omega$:

$$(\tilde{F}_y)_m = \frac{B}{2} \sum_{j=1}^{P} \{[|\tilde{L}_{j(mB-1)}|_2 + |\tilde{L}_{j(mB+1)}|_2] e^{imB(\Omega t + \psi_j)}\} \quad . \tag{A24}$$

From Equation (21), it is seen that the unsteady torque is given by

$$\tilde{T}_z = \sum_{j=1}^{P} \sum_{\ell=1}^{B} \sum_{n=1}^{\infty} \tilde{M}_{\ell jn} \sin \beta_j$$

and may be written as

$$\tilde{T}_z = \sum_{j=1}^{P} \sum_{\ell=1}^{B} \sum_{n=1}^{\infty} |\tilde{M}_{jn}|_1 e^{in(\Omega t + \psi_j + \eta_\ell)} \quad , \tag{A25}$$

where

$$|\tilde{M}_{jn}|_1 = \left(\frac{\partial C_L}{\partial \alpha}\right)_j \rho_f b_j r_j U_{Rj} U c_{nj} \{K(k_{nj}) \cos \beta_j - \alpha_j T(k_{nj}) \sin \beta_j\} \Delta r_j \sin \beta_j \quad . \tag{A26}$$

Equation (A25) is of the same form as Equation (A2), so that it reduces to

$$(\tilde{T}_z)_m = B \sum_{j=1}^{P} \{|\tilde{M}_{j(mB)}|_1 e^{imB\psi_j}\} e^{imB\Omega t} \quad . \tag{A27}$$

From Equation (21), it is seen that the unsteady bending moment, $\tilde{T}_x$ is given by

$$\tilde{T}_x = - \sum_{j=1}^{P} \sum_{\ell=1}^{B} \sum_{n=1}^{\infty} \tilde{M}_{\ell jn} \cos\beta_j \sin(\Omega t + \psi_j + \eta_\ell) \quad .$$

This may be written as

$$\tilde{T}_x = - \sum_{j=1}^{P} \sum_{\ell=1}^{B} \sum_{n=1}^{\infty} |\tilde{M}_{jn}|_2 \sin(\Omega t + \psi_j + \eta_\ell) \times e^{in(\Omega t + \psi_j + \eta_\ell)} \quad , \tag{A28}$$

where

$$|\tilde{M}_{jn}|_2 = \left(\frac{\partial C_L}{\partial \alpha}\right)_j \rho_f b_j r_j U_{Rj} U c_{nj} \{K(k_{nj}) \cos \beta_j - \alpha_j T(k_{nj}) \sin\beta_j\} \Delta r_j \cos \beta_j \quad . \tag{A29}$$

Equation (A28) is of the same form as Equation (A10), so that it reduces to

$$(\tilde{T}_x)_m = -\frac{B}{2}\left\{\sum_{j=1}^{P} i\left[-\left|\tilde{M}_{j(mB-1)}\right|_2 + \left|\tilde{M}_{j(mB+1)}\right|_2\right] \times e^{imB(\Omega t + \psi_j)}\right\} \quad . \tag{A30}$$

From Equation (21), it is seen that the unsteady bending moment, $\tilde{T}_y$, is given by

$$\tilde{T}_y = -\sum_{j=1}^{P}\sum_{\ell=1}^{B}\sum_{n=1}^{\infty} \tilde{M}_{\ell jn} \sin\beta_j \cos(\Omega t + \psi_j + \eta_\ell) \quad .$$

This may be written as

$$\tilde{T}_y = -\sum_{j=1}^{P}\sum_{\ell=1}^{B}\sum_{n=1}^{\infty} \left|\tilde{M}_{jn}\right|_1 \cos(\Omega t + \psi_j + \eta_\ell) \times e^{in(\Omega t + \psi_j + \eta_\ell)} \quad , \tag{A31}$$

where $\left|\tilde{M}_{jn}\right|_1$ is given by Equation (A26).

Equation (A31) is of the same form as Equation (A20), so that it reduces to

$$(\tilde{T}_y)_m = -\frac{B}{2}\left\{\sum_{j=1}^{P}\left[\left|\tilde{M}_{j(mB-1)}\right|_2 + \left|\tilde{M}_{j(mB+1)}\right|_2\right] \times e^{imB(\Omega t + \psi_j)}\right\} \quad . \tag{A32}$$

APPENDIX B

COMPUTER PROGRAM FOR UNSTEADY FORCES AND MOMENTS

```
**  UNSTEADY FORCES AND MOMENTS ON PROPULSORS
    REAL M,KMBJ(20),KMBA1(20),KMBS1(20),MOM(2,20),MOMA1(2,20)
    REAL MOMS1(2,20)
    REAL K(2,20),KA1(2,20),KS1(2,20),LIFT(2,20),LIFA1(2,20)
    REAL LIFS1(2,20)
    DIMENSION RJ(20),SCOSI(20),BSJ(20),URJ(20),CMB(2,20),TMB(2,20)
    DIMENSION BLJ(20),XJ(20),CMBA1(2,20),TMBA1(2,20),CMBS1(2,20)
    DIMENSION TMBS1(2,20),DJ(20),EJ(20),DRJ(20),AL(2),ALA1(2),ALS1(2)
    DIMENSION ALIF1(2,20),ALIA1(2,20),ALIS1(2,20),ALIF2(2,20),SUM(2)
    DIMENSIONALIA2(2,20),ALIS2(2,20),AM1(2,20),AMA11(2,20),AMS11(2,20)
    DIMENSION AM2(2,20),AMA12(2,20),AMS12(2,20),DMB(2),ALSM(2),FZM(2)
    DIMENSION FXM(2),FYM(2),TZ(2),TXM(2),TYM(2),PROPT(20),PSI(20)
101 FORMAT (8F10.5)
    READ (2,102) PROPT
C   PROPT=TITLE
102 FORMAT (20A4)
100 FORMAT (15,7F10.5)
    READ (2,100) NVALJ,RHO,OMEGA,BETA,UI,M
C   NVALJ=NUMBER OF BLADE ELEMENTS
C   RHO=DENSITY OF FLUID
C   OMEGA=PROPELLER RPM
C   BETA=NUMBER OF PROPELLER BLADES
C   M=ORDER OF BLADE FREQUENCY FORCE CLACULATED
```

```
C    UI=VELOCITY OF THE FREE STREAM
     WRITE (3,100) NVALJ,RHO,OMEGA,BETA,M,UI
     READ (2,101) (RJ(I),SCOSI(I),BSJ(I),URJ(I),CMB(1,I),CMB(2,I),BLJ(I
    1),XJ(I),I=1,NVALJ)
C    RJ(I)=RADIUS OF EACH BLADE ELEMENT
C    SCOSI(I)=LIFT CURVE SLOPE FOR EACH BLADE ELEMENT
C    BSJ(I)=BLADE SEMI-CHORD OF EACH BLADE ELEMENT
C    URJ(I)=RESULTANT VELOCITY AT EACH BLADE ELEMENT
C
C    CMB(1,I)=REAL PART OF FOURIER COEFFICIENT OF ORDER (MB)
C    OF INFLOW AT EACH BLADE ELEMENT
C    CMB(2,I)=IMAGINARY PART OF FOURIER COEFFICIENT OF ORDER (MB)
C    OF INFLOW AT EACH BLADE ELEMENT
C    BLJ(I)=ANGLE BETWEEN CIRCUMFERENTIAL VELOCITY COMPONENT AND
C    RESULTANT VELOCITY AT EACH BLADE ELEMENT
C    XJ(I)=STEADY ANGLE OF ATTACK AT EACH BLADE ELEMENT
     WRITE (3,101)(RJ(I),SCOSI(I),BSJ(I),URJ(I)CMB(1,I),CMB(2,I),BLJ(I
    1),XJ(I),I=1,NVALJ)
     DO 14  I=1,NVALJ
  14 CMB(2,I)=-CMB(2,I)
 130 FORMAT (6F10.5)
     READ (2,130) (DRJ(I),PSI(I),CMBA1(1,I),CMBA1(2,I),CMBS1(1,I),CMBS1
    1(2,I),I=1,NVALJ)
C    DRJ(I)=SPANWISE DIMENSION OF EACH BLADE ELEMENT
C    PSI(I)=ANGLE OF BLADE SKEW AT EACH BLADE ELEMENT
C    CMBA1(1,I)=REAL PART OF FOURIER COEFFICIENT OF ORDER
C    (MB+1) OF INFLOW AT EACH BLADE ELEMENT
```

```
C   CMBA1(2,I)=IMAGINARY PART OF FOURIER COEFFICIENT OF ORDER
C   (MB+1) OF INFLOW AT EACH BLADE ELEMENT
C   CMBS1(1,I)=REAL PART OF FOURIER COEFFICIENT OF ORDER
C   (MB-1) OF INFLOW AT EACH BLADE ELEMENT
C   CMB(2,I)=IMAGINARY PART OF FOURIER COEFFICIENT OF ORDER
C   (MB-1) OF INFLOW AT EACH BLADE ELEMENT
    WRITE (3,130)(DRJ(I),PSI(I),CMBA1(1,I),CMBA1(2,I),CMBS1(1,I),CMBS
   1(2,I),I=1,NVALJ)
    DO 1 I=1,NVALJ
C   CALCULATE REDUCED FREQUENCIES
    KMBJ(I)=2.0*3.14159278*M*BETA*OMEGA*BSJ(I)/(URJ(I)*60.0*UI)
    KMBA1(I)=(M*BETA+1.0)*2.0*3.14159278*OMEGA*BSJ(I)/(URJ(I)*60.0)
    KMBS1(I)=(M*BETA-1.0)*2.0*3.14159278*OMEGA*BSJ(I)/(URJ(I)*60.0)
C   CALCULATE CONSTANTS
    DJ(I)=SCOSI(I)*RHO*BSJ(I)*DRJ(I)*URJ(I)*UI*UI
   1 EJ(I)=SCOSI(I)*RHO*BSJ(I)*RJ(I)*DRJ(I)*URJ(I)*UI*UI
C   CALCULATE BESSEL FCTNS FROM IBM SUBROUTINES
    DO 2 I=1,NVALJ
    CALL BESJ(KMBJ(I),0,AJ0,0.0001,IER)
    CALL BESJ(KMBJ(I),1,AJ1,0.0001,IER)
    CALL BESY(KMBJ(I),0,AY0,IER)
    CALL BESY(KMBJ(I),1,AY1,IER)
C   CALCULATION OF SEARS FUNCTION FOR THRUST AND TORQUE
    K(1,I)=(AJ0*(AJ1*AY0+AJ1*AJ1-AJ0*AY1+AY1*AY1)-AJ1*(AJ0*AJ1
   1+AY0*AY1))/((AY0+AJ1)**2+(AJ0-AY1)**2)
    K(2,I)=(AJ0*(AJ0*AJ1+AY0*AY1)+AJ1*(AJ1*AY0+AJ1*AJ1-AJ0*AY1+
   1AY1*AY1))/((AY0+AJ1)**2+(AJ0-AY1)**2)-AJ1
```

```
      K(2,I)=-K(2,I)
C     CALCULATION OF HORLOCK FUNCTION FOR THRUST AND TORQUE
      AC=(AJ1*AY0+AY0*AY0+AJ0*AJ0-AJ0*AY1)/((AJ1+AJ0)**2+(AJ0-AY1)**2)
      BC=(AJ0*AJ1+AY0*AY1)/((AJ1+AY0)**2+(AJ0-AY1)**2)
      TMB(1,I)=(2.0-AC)*AJ0-BC*AJ1
      TMB(2,I)=(AC+1.0)*AJ1-BC*AJ0
      CALL BESJ(KMBA1(I),0,AJ0,0.0001,IER)
      CALL BESJ(KMBA1(I),1,AJ1,0.0001,IER)
      CALL BESY(KMBA1(I),0,AY0,IER)
      CALL BESY(KMBA1(I),1,AY1,IER)
C     CALCULATION OF SEARS FUNCTION FOR BENDING MOMENT AND SIDE FORCES
      KA1(1,I)=(AJ0*(AJ1*AY0+AJ1*AJ1-AJ0*AY1+AY1*AY1)-AJ1*(AJ0*AJ1
     1+AY0*AY1))/((AY0+AJ1)**2+(AJ0-AY1)**2)
      KA1(2,I)=(AJ0*(AJ0*AJ1+AY0*AY1)+AJ1*(AJ1*AY0+AJ1*AJ1-AJ0*AY1+
     1AY1*AY1))/((AY0+AJ1)**2+(AJ0-AY1)**2)-AJ1
      KA1(2,I)=-KA1(2,I)
C     CALCULATION OF HORLOCK FUNCTION FOR BENDING MOMENT AND SIDE FORCES
      AC=(AJ1*AY0+AY0*AY0+AJ0*AJ0-AJ0*AY1)/((AJ1+AY0)**2+(AJ0-AY1)**2)
      BC=(AJ0*AJ1+AY0*AY1)/((AJ1+AY0)**2+(AJ0-AY1)**2)
      TMBA1(1,I)=(2.0-AC)*AJ0-BC*AJ1
      TMBA1(2,I)=(AC+1.0)*AJ1-BC*AJ0
      CALL BESJ(KMBS1(I),0,AJ0,0.0001,IER)
      CALL BESJ(KMBS1(I),1,AJ1,0.0001,IER)
      CALL BESY(KMBS1(I),0,AY0,IER)
      CALL BESY(KMBS1(I),1,AY1,IER)
C     CALCULATION OF SEARS FUNCTION FOR BENDING MOMENT AND SIDE FORCES
      KS1(1,I)=(AJ0*(AJ1*AY0+AJ1*AJ1-AJ0*AY1+AY1*AY1)-AJ1*(AJ0*AJ1
```

```
     1+AYO*AY1))/((AYO+AJ1)**2+(AJO-AY1)**2)
      KS1(2,I)=(AJO*(AJO*AJ1+AYO*AY1)+AJ1*(AJ1*AYO+AJ1*AJ1-AJO*AY1+
     1AY1*AY1))/((AYO+AJ1)**2+(AJO-AY1)**2)-AJ1
      KS1(2,I)=-KS1(2,I)
C     CALCULATION OF HORLOCK FUNCTION FOR BENDING MOMENT AND SIDE FORCES
      AC=(AJ1*AYO+AYO*AYO+AJO*AJO-AJO*AY1)/((AJ1+AYO)**2+(AJO-AY1)**2)
      BC=(AJO*AJ1+AYO*AY1)/((AJ1+AYO)**2+(AJO-AY1)**2)
      TMBS1(1,I)=(2.0-AC)*AJO-BC*AJ1
      TMBS1(2,I)=(AC+1.0)*AJ1-BC*AJO
C     MULTIPLY REAL AND IMAGINARY FOURIER COEFFICIENTS BY 0.5 DJ
      DO 7 JJ=1,2
      CMB(JJ,I)=CMB(JJ,I)*0.5*DJ(I)
      CMBA1(JJ,I)=CMBA1(JJ,I)*0.5*DJ(I)
    7 CMBS1(JJ,I)=CMBS1(JJ,I)*0.5*DJ(I)
C     MULTIPLY REAL AND IMAGINARY PARTS OF SEARS FUNCTION BY COS(BJ)
      DO 3 JJ=1,2
      K(JJ,I)=K(JJ,I)*COS(BLJ(I))
      KA1(JJ,I)=KA1(JJ,I)*COS(BLJ(I))
    3 KS1(JJ,I)=KS1(JJ,I)*COS(BLJ(I))
C     MULTIPLY REAL AND IMAGINARY PARTS OF HORLOCKS FUNCTION BY XJ SIN(BJ)
      DO 4 JJ=1,2
      TMB(JJ,I)=TMB(JJ,I)*XJ(I)*SIN(BLJ(I))
      TMBA1(JJ,I)=TMBA1(JJ,I)*XJ(I)*SIN(BLJ(I))
    4 TMBS1(JJ,I)=TMBS1(JJ,I)*XJ(I)*SIN(BLJ(I))
C     CALCULATION OF LIFT AT EACH BLADE SECTION USING IBM SUBROUTINES
      CALL CXSUB(K(1,I),TMB(1,I),AL(1))
      CALL CXSUB(KA1(1,I),TMBA1(1,I),ALA1(1))
```

```
      CALL CXSUB(KS1(1,I),TMBS1(1,I),ALS1(1))
      CALL CXMPY(AL(1),CMB(1,I),LIFT(1,I))
      CALL CXMPY(ALA1(1),CMBA1(1,I),LIFA1(1,2))
      CALL CXMPY(ALS1(1),CMBS1(1,I),LIFS1(1,2))
C     CALCULATE VECTOR COMPONENTS OF LIFT AT EACH BLADE SECTION
      DO 5 JJ=1.2
      ALIF1(JJ,I)=LIFT(JJ,I)*COS(BLJ(I))
      ALIA1(JJ,I)=LIFA1(JJ,I)*COS(BLJ(I))
      ALIS1(JJ,I)=LIFS1(JJ,I)*COS(BLJ(I))
      ALIF2(JJ,I)=LIFT(JJ,I)*SIN(BLJ(I))
      ALIA2(JJ,I)=LIFA1(JJ,I)*SIN(BLJ(I))
    5 ALIS2(JJ,I)=LIFS1(JJ,I)*SIN(BLJ(I))
C     CALCULATION OF MOMENT AT EACH BLADE SECTION
      DO 6 JJ=1,2
      MOM(JJ,I)=LIFT(JJ,I)*RJ(I)
      MOMA1(JJ,I)=LIFA1(JJ,I)*RJ(I)
      MOMS1(JJ,I)=LIFS1(JJ,I)*RJ(I)
C     CALCULATE VECTOR COMPONENTS OF MOMENT AT EACH BLADE SECTION
      AM1(JJ,I)=MOM(JJ,I)*SIN(BLJ(I))
      AMA11(JJ,I)=MOMA1(JJ,I)*SIN(BLJ(I))
      AMS11(JJ,I)=MOMS1(JJ,I)*SIN(BLJ(I))
      AM2(JJ,I)=MOM(JJ,I)*COS(BLJ(I))
      AMA12(JJ,I)=MOMA1(JJ,I)*COS(BLJ(I))
    6 AMS12(JJ,I)=MOMS1(JJ,I)*COS(BLJ(I))
    2 CONTINUE
C     CALCULATION OF THRUST FZM
      FZM(1)=0.0
```

```
      FZM(2)=0.0
      DO 8 JJ=1,NVALJ
      DMB(1)=COS(M*BETA*PSI(JJ))
      DMB(2)=SIN(M*BETA*PSI(JJ))
      CALL CXMPY (DMB(1),ALIF1(1,JJ),SUM(1))
      FZM(1)=FZM(1)+SUM(1)
    8 FZM(2)=FZM(2)+SUM(2)
      FZM(1)=FZM(1)*BETA
      FZM(2)=FZM(2)*BETA
C     MODULUS OF THRUST
      AFZM=SQRT(FZM(1)**2+FZM(2)**2)
C     CALCULATION OF PHASE ANGLE OF THRUST IN DEGREES
      AAFZM=ATAN(FZM(2)/FZM(1))/57.29578
C     CALCULATION OF SIDE FORCE FXM
      FXM(1)=0.0
      FXM(2)=0.0
      DO 9 JJ=1,NVALJ
      DMB(1)=-SIN(M*BETA*PSI(JJ))
      DMB(2)=COS(M*BETA*PSI(JJ))
      ALSM(1)=ALIA2(1,JJ)-ALIS2(1,JJ)
      ALSM(2)=ALIA2(2,JJ)-ALIS2(2,JJ)
      CALL CXMPY(DMB(1),ALSM(1),SUM(1))
      FXM(1)=FXM(1)+SUM(1)
    9 FXM(2)=FXM(2)+SUM(2)
      FXM(1)=FXM(1)*BETA/2.0
      FXM(2)=FXM(2)*BETA/2.0
C     CALCULATION OF ABSOLUTE VALUE OF SIDE FORCE FXM
```

```
      AFXM=SQRT(FXM(1)**2+FXM(2)**2)
C     CALCULATION OF THE PHASE ANGLE FOR THE SIDE FORCE FXM
      AAFXM=ATAN(FXM(2)/FXM(1))/57.29578
C     CALCULATION OF THE SIDE FORCE FYM
      FYM(1)=0.0
      FYM(2)=0.0
      DO 10  JJ=1,NVALJ
      DMB(1)=COS(M*BETA*PSI(JJ))
      DMB(2)=SIN(M*BETA*PSI(JJ))
      ALSM(1)=ALIA2(1,JJ)+ALIS2(1,JJ)
      ALSM(2)=ALIA2(2,JJ)+ALIS2(2,JJ)
      CALL CXMPY (DMB(1),ALSM(1),SUM(1))
      FYM(1)=FYM(1)+SUM(1)
   10 FYM(2)=FYM(2)+SUM(2)
      FYM(1)=FYM(1)*BETA/2.0
      FYM(2)=FYM(2)*BETA/2.0
C     CALCULATE ABSOLUTE VALUE OF THE FORCE FYM
      AFYM=SQRT(FYM(1)**2+FYM(2)**2)
C     CALCULATION OF PHASE ANGLE OF FORCE FYM
      AAFYM=ATAN(FYM(2)/FYM(1))/57.29578
C     CALCULATION OF TORQUE TZM
      TZ(1)=0.0
      TZ(2)=0.0
      DO 11  JJ=1,NVALJ
      DMB(1)=COS(M*BETA*PSI(JJ))
      DMB(2)=SIN(M*BETA*PSI(JJ))
      CALL CXYMPY (AM1(1,JJ),DMB(1),SUM(1))
```

```
      TZ(1)=TZ(1)+SUM(1)
   11 TZ(2)=TZ(2)+SUM(2)
      TZ(1)=TZ(1)*BETA
      TZ(2)=TZ(2)*BETA
C     CALCULATION OF THE MODULUS OF TORQUE
      ATZ=SQRT(TZ(1)**2+TZ(2)**2)
C     CALCULATION OF THE PHASE ANGLE FOR TORQUE
      AATZ=ATAN(TZ(2)/TZ(1))/57.29578
C     CALCULATION OF BENDING MOMENT TXM
      TXM(1)=0.0
      TXM(2)=0.0
      DO 12 JJ=1,NVALJ
      DMB(1)=-SIN(M*BETA*PSI(JJ))
      DMB(2)=COS(M*BETA*PSI(JJ))
      ALSM(1)=AMS12(1,JJ)-AMA12(1,JJ)
      ALSM(2)=AMS12(2,JJ)-AMA12(2,JJ)
      CALL CXMPY(DMB(1),ALSM(1),SUM(1))
      TXM(1)=TXM(1)+SUM(1)
   12 TXM(2)=TXM(2)+SUM(2)
      TXM(1)=TXM(1)*BETA/2.0
      TXM(2)=TXM(2)*BETA/2.0
C     CALCULATION OF THE MODULUS OF THE BENDING MOMENT TXM
      ATXM=SQRT(TXM(1)**2+TXM(2)**2)
C     CALCULATION OF THE PHASE ANGLE OF TXM
      AATXM=ATAN(TXM(2)/TXM(1))/57.29578
C     CALCULATION OF THE BENDING MOMENT TYM
      TYM(1)=0.0
```

```
      TYM(2)=0.0
      DO 13 JJ=1,NVALJ
      DMB(1)=COS(M*BETA*PSI(JJ))
      DMB(2)=SIN(M*BETA*PSI(JJ))
      ALSM(1)=AMS12(1,JJ)+AMA12(1,JJ)
      ALSM(2)=AMS12(2,JJ)+AMA12(2,JJ)
      CALL CXMPY (DMB(1),ALSM(1),SUM(1))
      TYM(1)=TYM(1)+SUM(1)
   13 TYM(2)=TYM(2)+SUM(2)
      TYM(1)=-TYM(1)*BETA/2.0
      TYM(2)=-TYM(1)*BETA/2.0
C     CALCULATION OF THE MODULUS OF BENDING MOMENT TYM
      ATYM=SQRT(TYM(1)**2+TYM(2)**2)
C     CALCULATION OF THE PHASE ANGLE FOR THE BENDING MOMENT TYM
      AATYM=ATAN(TYM(2)/TYM(1))/57.29578
  110 FORMAT ('1COMPLEX THRUST (FZM)        '2E15.7)
      WRITE (3,110) FZM(1),FZM(2)
  111 FORMAT ('OCOMPLEX SIDE FORCE (FXM)    '2E15.7)
      WRITE (3,111) FXM(1),FXM(2)
  112 FORMAT ('OCOMPLEX SIDE FORCE (FYM)    '2E15.7)
      WRITE (3,112) FYM(1),FYM(2)
  113 FORMAT ('OCOMPLEX TORQUE (TZ)         '2E15.7)
      WRITE (3,113) TZ(1),TZ(2)             '2E15.7)
  114 FORMAT ('OCOMPLEX BENDING MOMENT (TXM)'2E15.7)
      WRITE (3,114) TXM(1), TXM(2)
  115 FORMAT ('OCOMPLEX BENDING MOMENT (TYM)'2E15.7)
      WRITE (3,115) TYM(1),TYM(2)
```

```
120 FORMAT ('OTHRUST AMPLITUDE (AFZM)        'E15.7'   THRUST PHASE
   1 ANGLE         'F10.5)
    WRITE (3,120) AFZM,AAFZM
121 FORMAT ('OSIDE FORCE AMPLITUDE (AFXM)    'E15.7'   SIDE FORCE P
   1HASE ANGLE     'F10.5)
    WRITE (3,121) AFXM,AAFMX
122 FORMAT ('OSIDE FORCE AMPLITUDE (AFYM)    'E15.7'   SIDE FORCE P
   1HASE ANGLE     'F10.5)
    WRITE (3,122) AFYM,AAFYM
123 FORMAT ('OTORQUE AMPLITUDE (ATZ)         'E15.7'   TORQUE PHASE
   1 ANGLE         'F10.5)
    WRITE (3,123) ATZ,AATZ
124 FORMAT ('OBENDING MOMENT AMPLITUDE (ATXM)'E15.7,'  BENDING MOME
   1NT PHASE ANGLE'F10.5)
    WRITE (3,124) ATXM,AATXM
125 FORMAT ('OBENDING MOMENT AMPLITUDE (ATYM)'E15.7,'  BENDING MOME
   1NT PHASE ANGLE'F10.5
    WRITE (3,125)ATYM,AATYM
    CALL EXIT
    END
```

TABLE I

SENSITIVITY OF VARIOUS PROPELLER TYPES TO THE HARMONIC COMPONENTS OF THE WAKE

$T_Z F_Z$	B	HARMONIC COMPONENTS																				
	3	X			X			X			X			X			X			X		
	4	X				X				X				X				X				X
	5	X					X					X					X					X
	6	X						X						X						X		

$T_X F_X T_Y F_Y$	3		X	X		X	X		X	X		X	X		X	X		X	X		X	X
	4		X		X		X		X		X		X		X		X		X		X	
	5		X			X		X			X		X			X		X			X	
	6		X				X		X				X		X				X		X	
		0	1	2	3	4	5	6	7	8	9	10	11	12	13	14	15	16	17	18	19	20

TABLE 2

HARMONIC CONTENT OF PROPELLER INFLOW

U = 18 fps

X/D_p = 1.0

R/R_{TIP}	a_o	a_2	b_2	a_5	b_5	a_{10}	b_{10}
0.2	0.972	0.0126	-0.0138	-0.0005	0.0020	0.0010	0.0026
0.3	0.973	0.0184	-0.0020	-0.0079	-0.0035	0.0008	0.0027
0.4	0.974	0.0154	0.0028	0.0063	-0.0059	0.0027	0.0035
0.5	0.975	0.0117	0.0026	-0.0044	-0.0022	0.0047	0.0033
0.6	0.975	0.0105	0.0010	-0.0025	-0.0001	0.0058	0.0015
0.7	0.976	0.0058	-0.0004	-0.0003	-0.0026	0.0060	-0.0012
0.8	0.976	0.0064	0.0002	0.0017	-0.0015	0.0081	-0.0005
0.9	0.976	0.0049	0.0015	0.0007	-0.0005	0.0080	0.0038
1.0	0.976	0.0030	0.0021	-0.0012	-0.0007	0.0074	0.0048

U = 18 fps

X/D_p = 1.25

R/R_{TIP}	a_o	a_2	b_2	a_5	b_5	a_{10}	b_{10}
0.2	0.967	0.0246	-0.0015	-0.0006	0.0018	0.0024	0.0001
0.3	0.974	0.0204	0.0017	0.0013	0.0007	0.0036	-0.0001
0.4	0.975	0.0165	0.0026	0.0018	-0.0008	0.0050	0.0021
0.5	0.975	0.0128	0.0018	0.0003	-0.0005	0.0066	0.0018
0.6	0.976	0.0098	0.0012	-0.0008	0.0002	0.0079	0.0012
0.7	0.976	0.0086	0.0012	0	-0.0002	0.0090	0.0013
0.8	0.976	0.0075	0.0013	0.0013	-0.0015	0.0091	0.0022
0.9	0.976	0.0064	0.0012	0.0017	-0.0023	0.0092	0.0017
1.0	0.976	0.0064	0.0011	0.0017	-0.0014	0.0094	0.0009

TABLE 2 (Cont.)

U = 18 fps

X/D_p = 1.50

R/R_{TIP}	a_o	a_2	b_2	a_5	b_5	a_{10}	b_{10}
0.2	0.954	0.0214	-0.0007	-0.0041	-0.0009	0.0034	-0.0021
0.3	0.960	0.0189	0.0003	0.0001	-0.0003	0.0038	-0.0020
0.4	0.961	0.0150	0.0001	0.0017	-0.0010	0.0045	-0.0003
0.5	0.961	0.0111	0.0010	0.0002	-0.0013	0.0057	-0.0006
0.6	0.962	0.0083	-0.0022	-0.0013	-0.0008	0.0075	-0.0012
0.7	0.963	0.0070	-0.0026	-0.0005	-0.0007	0.0083	-0.0012
0.8	0.963	0.0074	-0.0022	0.0004	-0.0012	0.0083	0.0008
0.9	0.964	0.0072	-0.0023	0.0007	-0.0017	0.0086	0.0011
1.0	0.964	0.0067	-0.0025	0.0002	-0.0010	0.0085	-0.0003

U = 18 fps

X/D_p = 2.00

R/R_{TIP}	a_o	a_2	b_2	a_5	b_5	a_{10}	b_{10}
0.2	0.972	0.0033	-0.0006	-0.0022	0.0007	0.0036	-0.0006
0.3	0.977	0.0145	-0.0006	0.0020	0.0036	0.0032	-0.0003
0.4	0.980	0.0135	0.0025	0.0048	0.0065	0.0033	-0.0005
0.5	0.982	0.0117	0.0006	0.0037	0.0035	0.0031	-0.0016
0.6	0.983	0.0091	-0.0012	0.0018	0.0013	0.0029	-0.0024
0.7	0.984	0.0055	-0.0017	0.0002	0.0032	0.0034	-0.0017
0.8	0.985	0.0071	-0.0012	-0.0017	0.0003	0.0055	-0.0007
0.9	0.985	0.0056	0.0003	-0.0008	-0.0006	0.0052	0.0022
1.0	0.985	0.0044	0.0012	0.0014	0.0008	0.0045	0.0028

TABLE 2 (Cont.)

U = 18 fps

X/D_p = 3.00

R/R_{TIP}	a_o	a_2	b_2	a_5	b_5	a_{10}	b_{10}
0.2	0.979	0.0060	-0.0042	0.0013	-0.0026	0.0036	0.0006
0.3	0.983	0.0106	-0.0011	0.0022	0.0002	0.0030	0.0003
0.4	0.985	0.0109	0.0017	0.0031	0.0041	0.0026	0
0.5	0.986	0.0118	0.0007	0.0027	0.0035	0.0020	-0.0013
0.6	0.987	0.0101	-0.0012	0.0013	0.0016	0.0023	-0.0019
0.7	0.987	0.0056	-0.0018	-0.0002	0.0031	0.0038	-0.0017
0.8	0.988	0.0080	-0.0013	-0.0019	0.0023	0.0051	-0.0014
0.9	0.988	0.0061	0.0005	-0.0011	0.0004	0.0047	0.0010
1.0	0.988	0.0041	0.0015	0.0009	0.0002	0.0041	0.0023

U = 18 fps

X/D_p = 4.00

R/R_{TIP}	a_o	a_2	b_2	a_5	b_5	a_{10}	b_{10}
0.2	0.978	0.0098	-0.0032	-0.0005	-0.0010	0.0033	0.0001
0.3	0.982	0.0124	-0.0012	-0.0014	-0.0015	0.0035	0.0003
0.4	0.985	0.0131	0.0028	-0.0015	-0.0013	0.0027	0.0005
0.5	0.987	0.0121	0.0015	-0.0016	-0.0002	0.0032	0.0003
0.6	0.989	0.0091	-0.0008	-0.0016	0.0013	0.0041	0.0002
0.7	0.990	0.0077	-0.0021	-0.0015	0.0021	0.0045	0.0003
0.8	0.990	0.0075	-0.0015	-0.0021	0.0014	0.0044	0.0011
0.9	0.990	0.0063	-0.0009	-0.0014	0.0005	0.0044	0.0025
1.0	0.990	0.0057	-0.0004	-0.0013	0.0006	0.0043	0.0026

TABLE 3

RESULTS OF CALIBRATION WITH STEADY AXIAL FORCE APPLIED TO THE SHAFT

Steady Load (lb)	Dynamic Load (peak lb)	Balance Output (peak volt)
0	10	1.000
33	10	0.920
65	10	0.930
104	10	0.885
126	10	0.865

TABLE 4

STEADY THRUST OF FREE-STREAM PROPELLERS

2 Blades

J	C_T	Thrust (lb)
1.05	0.190	20.8
1.17	0.105	11.5
1.29	0.030	3.28

5 Blades

J	C_T	Thrust (lb)
1.05	0.360	39.4
1.17	0.185	20.2
1.29	0.055	6.01

10 Blades

J	C_T	Thrust (lb)
1.05	0.48	52.5
1.17	0.22	24.1
1.29	0.04	4.38

TABLE 5

CONDITIONS FOR WHICH EXPERIMENTS AND THEORETICAL PREDICTIONS WERE MADE

Free Stream Velocity = 18 fps

TWO-BLADED PROPELLER

Advance Ratio	Experiment	Two-Dimensional Theory
1.29	X	X
1.17	X	X
1.05	X	X

FIVE-BLADED PROPELLER

Advance Ratio	Experiment	Two-Dimensional Theory	Lifting Surface Theory
1.29	X	X	X
1.17	X	X	X
1.05	X	X	X

TEN-BLADED PROPELLER

Advance Ratio	Experiment	Two-Dimensional Theory	Lifting Surface Theory
1.29	X	X	X
1.17	X	X	X
1.05	X	X	X

TABLE 6

RADIAL VARIATIONS OF $\partial C_L/\partial\alpha$ AS CALCULATED FROM EXPERIMENTAL CASCADE DATA

Two-Bladed Propeller		Five-Bladed Propeller		Ten-Bladed Propeller	
r/R_{TIP}	$\partial C_L/\partial\alpha$	r/R_{TIP}	$\partial C_L/\partial\alpha$	r/R_{TIP}	$\partial C_L/\partial\alpha$
0.3	2π	0.3	3.10	0.3	1.69
0.4	2π	0.4	4.20	0.4	2.18
0.5	2π	0.5	5.19	0.5	2.95
0.6	2π	0.6	5.96	0.6	3.71
0.7	2π	0.7	2π	0.7	4.10
0.8	2π	0.8	2π	0.8	4.77
0.9	2π	0.9	2π	0.9	5.76
1.0	2π	1.0	2π	1.0	6.20

TABLE 7

REYNOLDS NUMBERS FOR TURBULENCE GENERATING GRIDS

Rod Diameter (in)	Re U=18 fps	Re U=9 fps
0.375	52000	26000
0.750	104000	52000
0.875	121400	60700

TABLE 8

TURBULENCE GENERATING GRID LOCATIONS IN WATER TUNNEL

Grid Mesh Size (in)	Grid Location (in)
2	32
4	64
6	96

TABLE 9

TURBULENCE VIRTUAL ORIGINS FOR TURBULENCE GENERATING GRIDS

Grid Mesh Size (in)	Virtual Origin (in)
2	6
4	12
6	18

TABLE 10

TURBULENCE LENGTH SCALES FOR EXPERIMENTS CONDUCTED

Velocity (fps)	Mesh Size (in)	Location Upstream of Propeller (in)	X_o (in) Table 9	Rod Diameter (in)	$\frac{x-x_o}{bR_b}$	Maximum Λ/b	Maximum Λ(in)	Minimum Λ/b	Minimum Λ(in)
18	2	32	6	0.375	0.0013	1.589	0.600	1.392	0.522
	4	64	12	0.750	0.00067	1.482	1.11	1.348	1.011
	4	134	12	0.750	0.0016	1.626	1.22	1.406	1.055
	6	96	18	0.875	0.00073	1.485	1.31	1.352	1.183
9	2	32	6	0.375	0.0027	1.730	0.649	1.448	0.543
	4	64	12	0.750	0.0013	1.589	1.19	1.391	1.043
	4	134	12	0.750	0.0031	1.757	1.32	1.459	1.094
	6	96	18	0.875	0.0015	1.615	1.41	1.402	1.227

TABLE 11

TURBULENCE INTENSITIES FOR EXPERIMENTS CONDUCTED

Mesh Size (in)	Location Upstream from Propeller (in)	$\frac{x-x_o}{bR_b}$	$\frac{u}{U}$
2	32	0.0013	0.0295
4	64	0.00067	0.0292
4	134	0.0016	0.0190
6	96	0.00073	0.0250

TABLE 12

TURBULENCE INTENSITIES FOR EXPERIMENTS CONDUCTED

Number of Blades	Velocity (fps)	Grid Size (in)	Grid Location (in)	Length Scale (in)	Turbulence Intensity
2	18	4	64	1.06	0.029
		4	134	1.137	0.019
		6	96	1.25	0.025
		2	32	0.562	0.0295
5	18	4	64	1.06	0.029
		4	134	1.137	0.019
		6	96	1.25	0.025
		2	32	0.59	0.0291
10	9	4	64	1.12	0.0295
		4	134	1.21	0.0193
		6	96	1.32	0.0246

Figure 1a - Axisymmetric Body in Flow

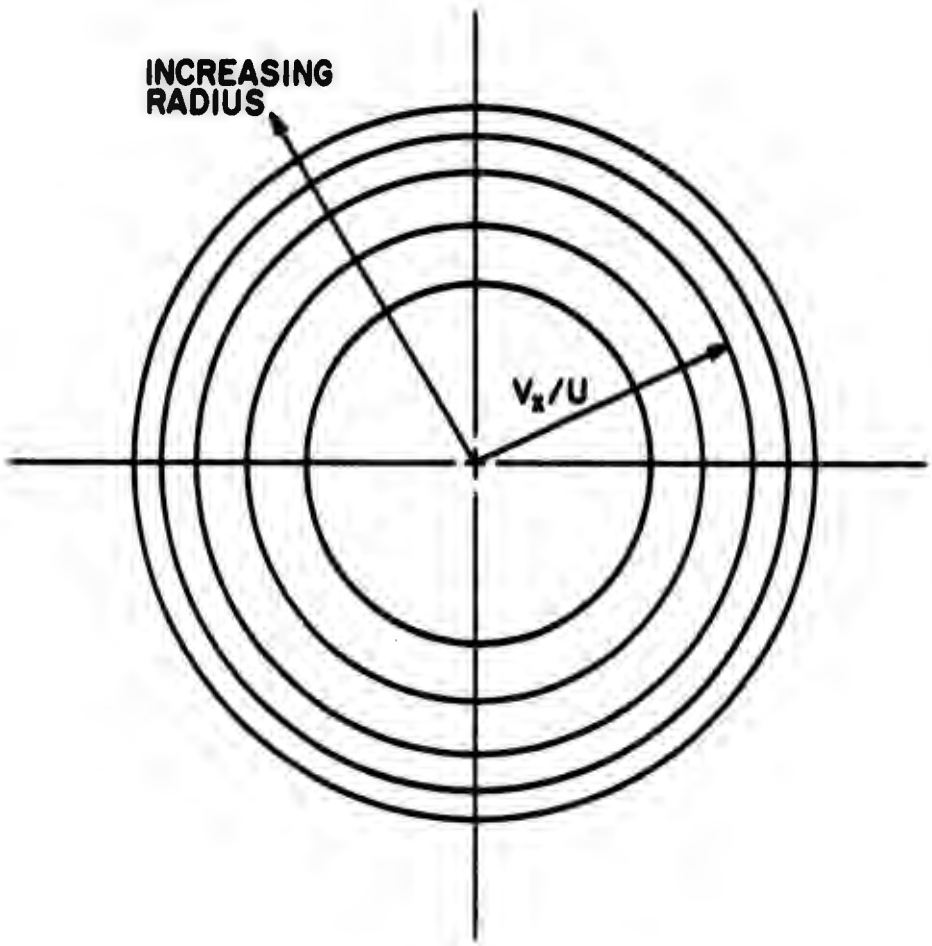

Figure 1b - Circumferential Distribution of Axial Velocity Just Downstream of an Axisymmetric Body

Figure 2a - Axisymmetric Body with Strut in Flow

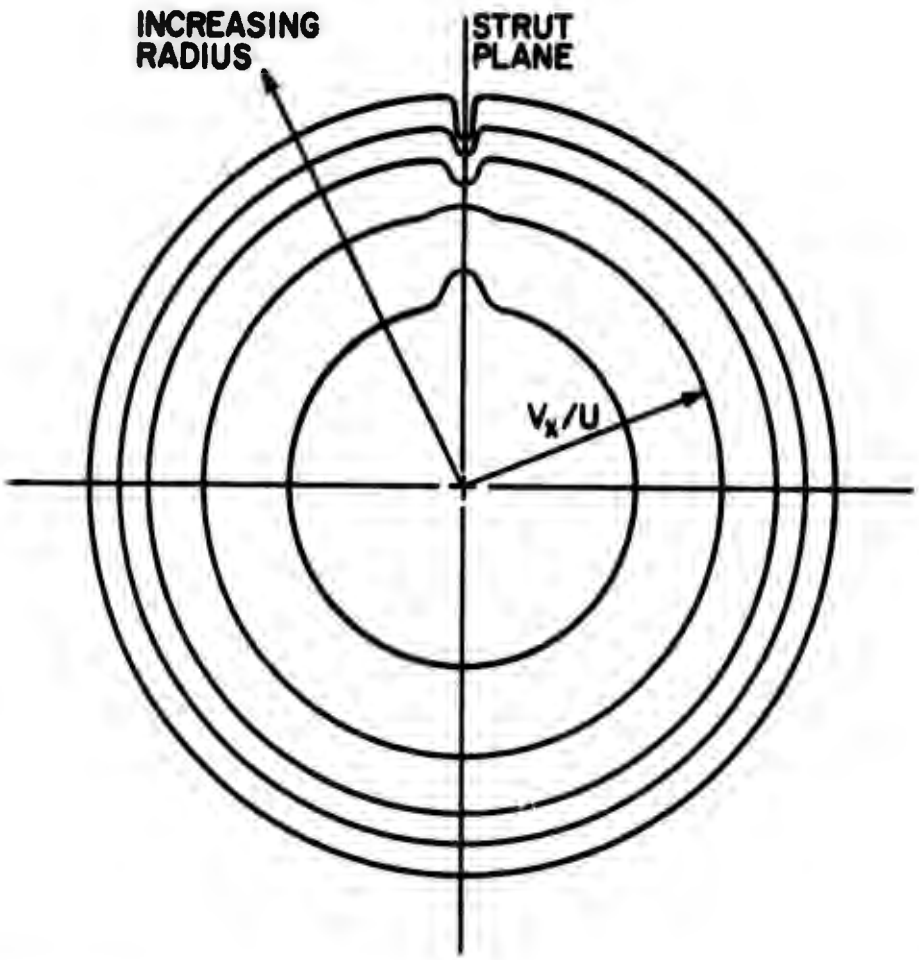

Figure 2b - Circumferential Distribution of Axial Velocity Just Downstream of an Axisymmetric Body with Strut

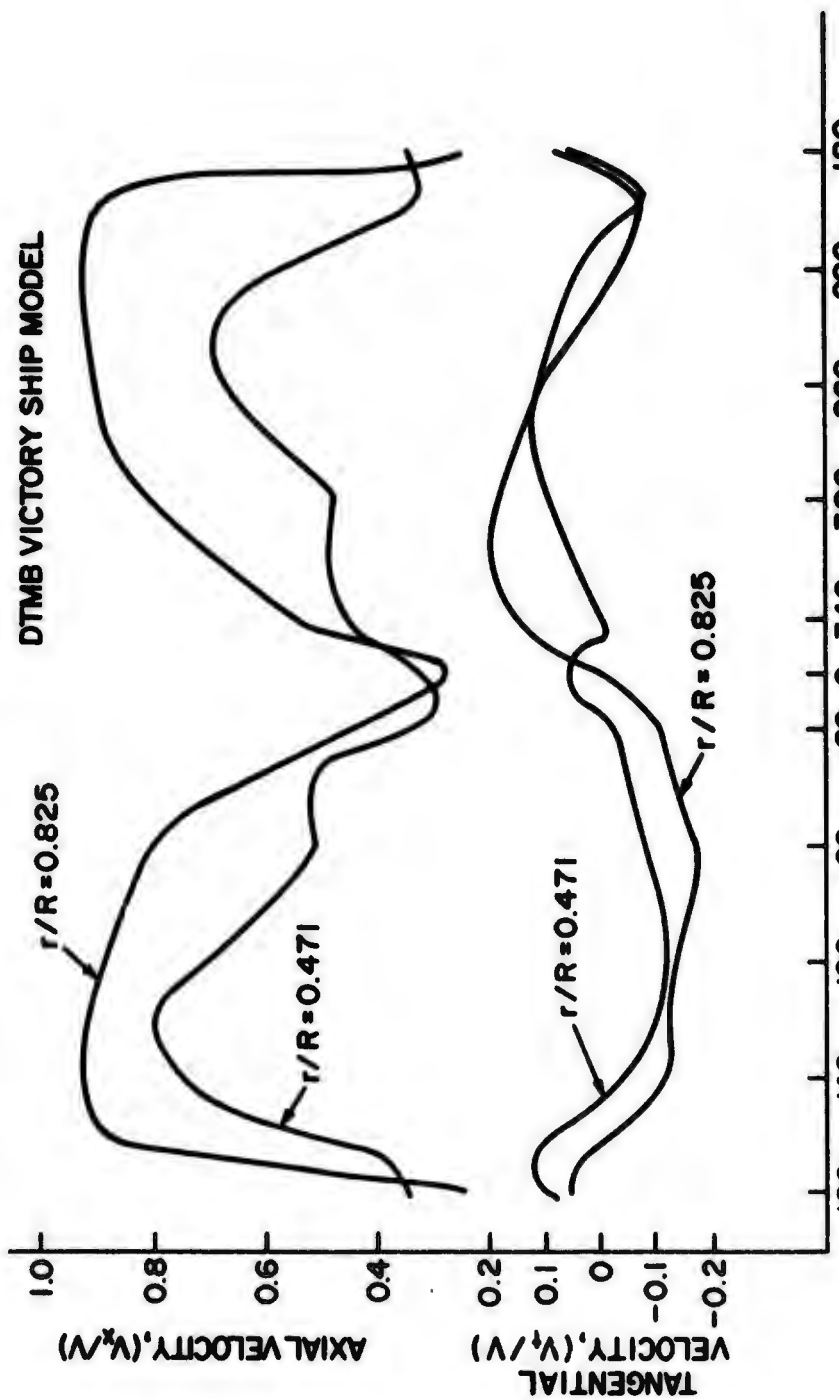

Figure 3 - Distribution of Axial and Tangential Velocity Components as Measured in the Propeller Plane of a Single Screw Ship

Source: van Manen, J. D. and A. J. W. Lap, "Scale-Effect Experiments on Victory Ships and Models, Part II," Trans. Inst. Nav. Arch., 1958.

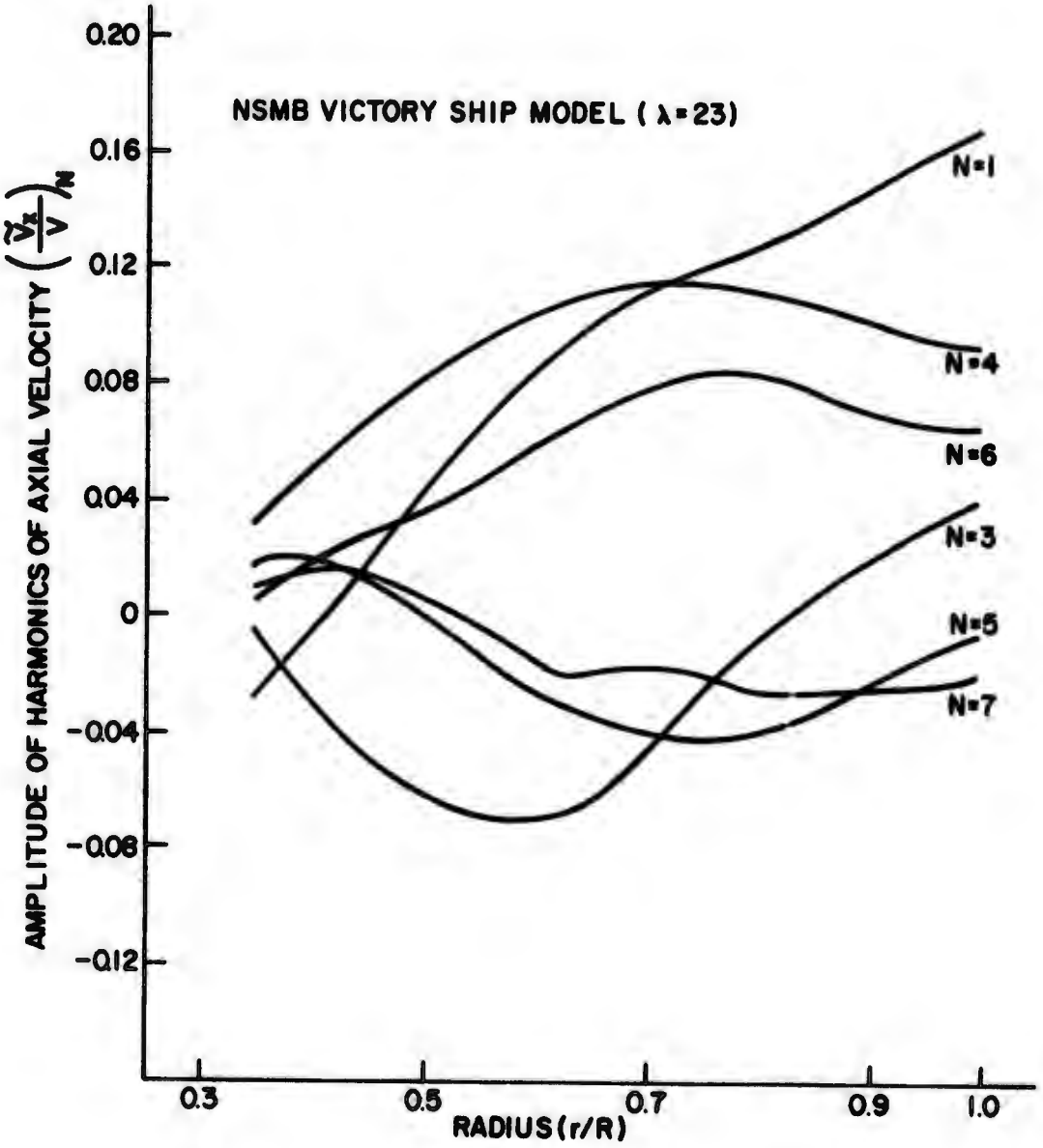

Figure 4 - Harmonic Content of the Axial Velocity Distribution in the Propeller Plane of a Single Screw Ship

Source: van Manen, J. D. and A. J. W. Lap, "Scale-Effect Experiments on Victory Ships and Models, Part II," Trans. Inst. Nav. Arch., 1958.

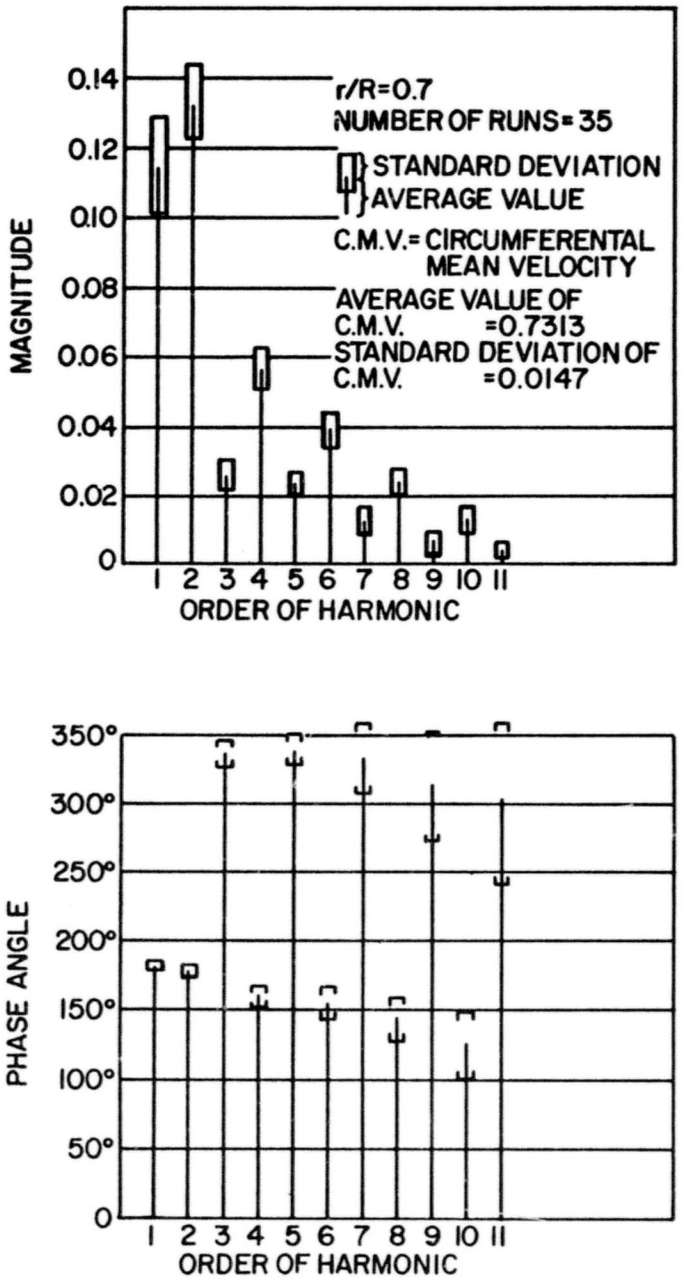

Figure 5 - Mean and Standard Deviation of Harmonic Content of the Axial Velocity Distribution in the Propeller Plane of a Single Screw Ship

Source: Tjoenneland, J. P., "An Investigation into the Repeatability of Wake Survey Data and the Effect of Small Yaw Angles on the Wake Velocities," MIT, Dept. of Naval Architecture and Marine Engineers, Report No. 67-5, January 1967.

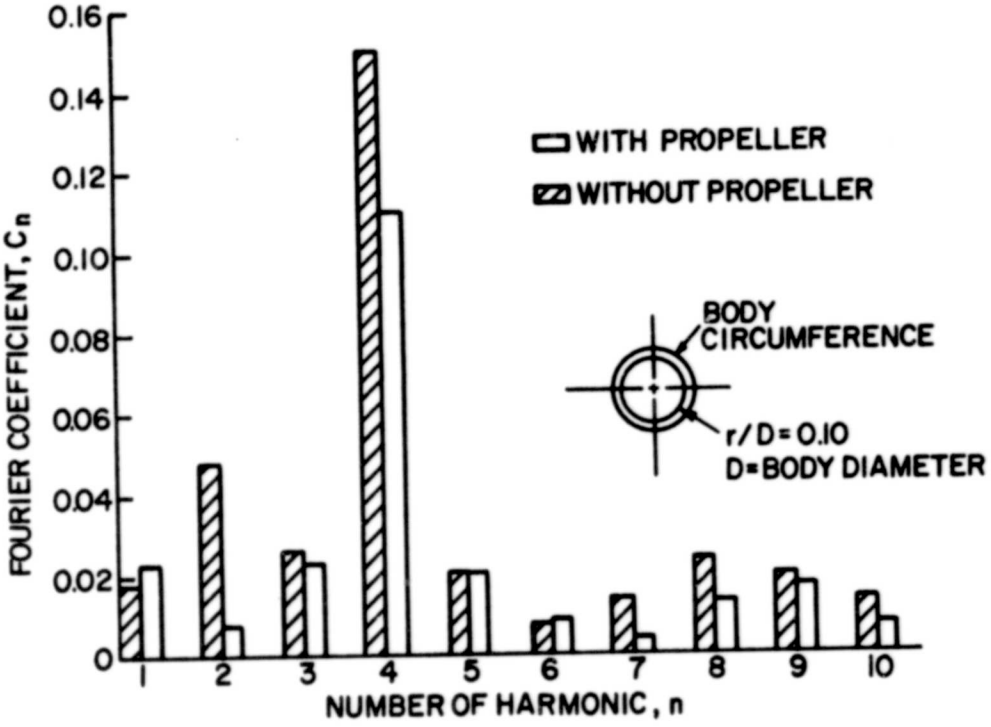

Figure 6 - Harmonic Content of the Axial Velocity Distribution With and Without a Propeller

Source: Burstein, N. M., "Boundary-Layer Investigation on a Body of Revolution with Fins," M. S. Thesis, The Pennsylvania State University, 1965.

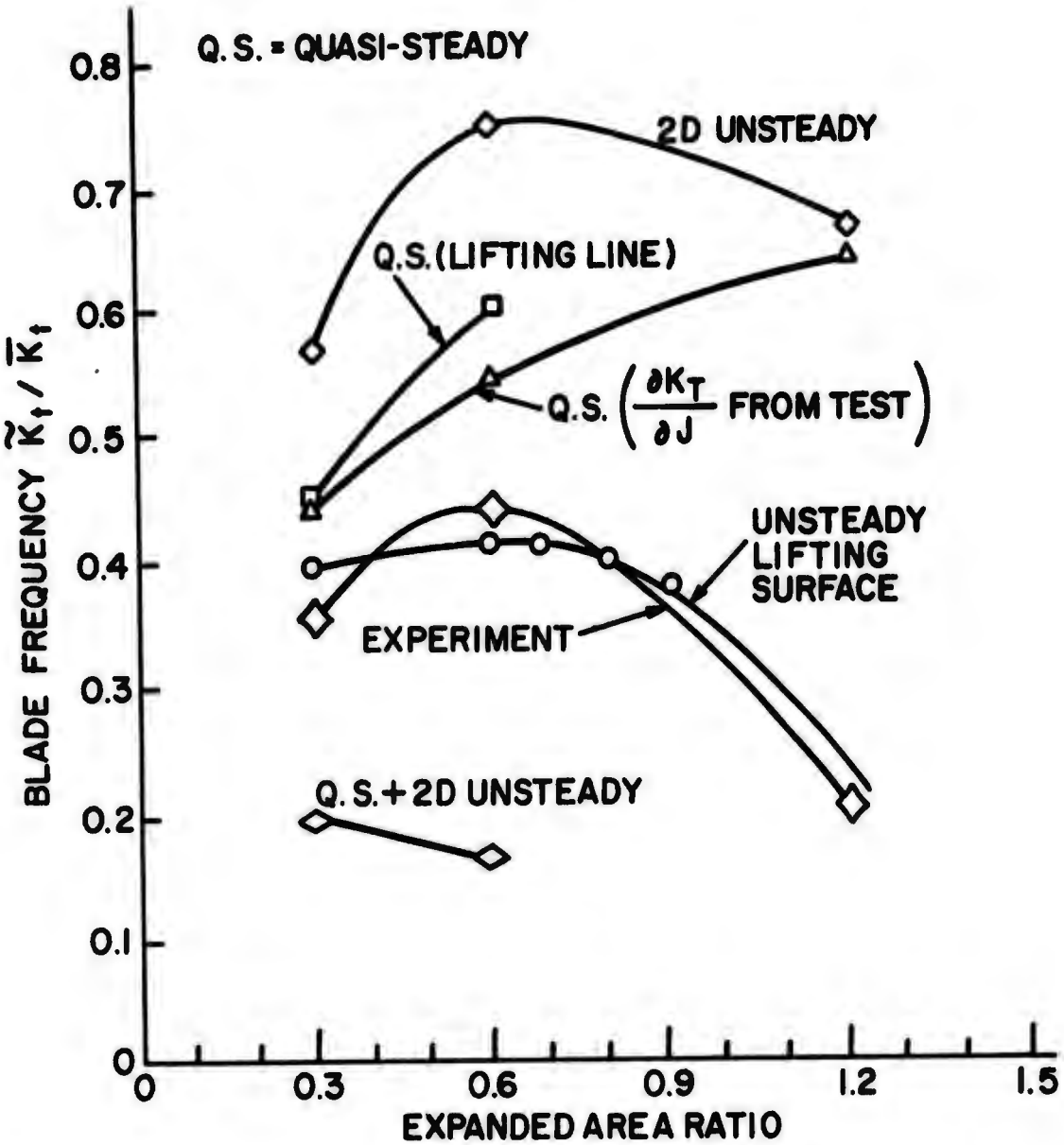

Figure 7 - Correlation of Blade Frequency Thrust Over Range of Expanded Area Ratio at Design $\bar{K}_t$

Source: Boswell, R. J., "Measurement, Correlation with Theory and Parametric Investigation of Unsteady Propeller Forces and Moments," M. S. Thesis, The Pennsylvania State University, August 1967.

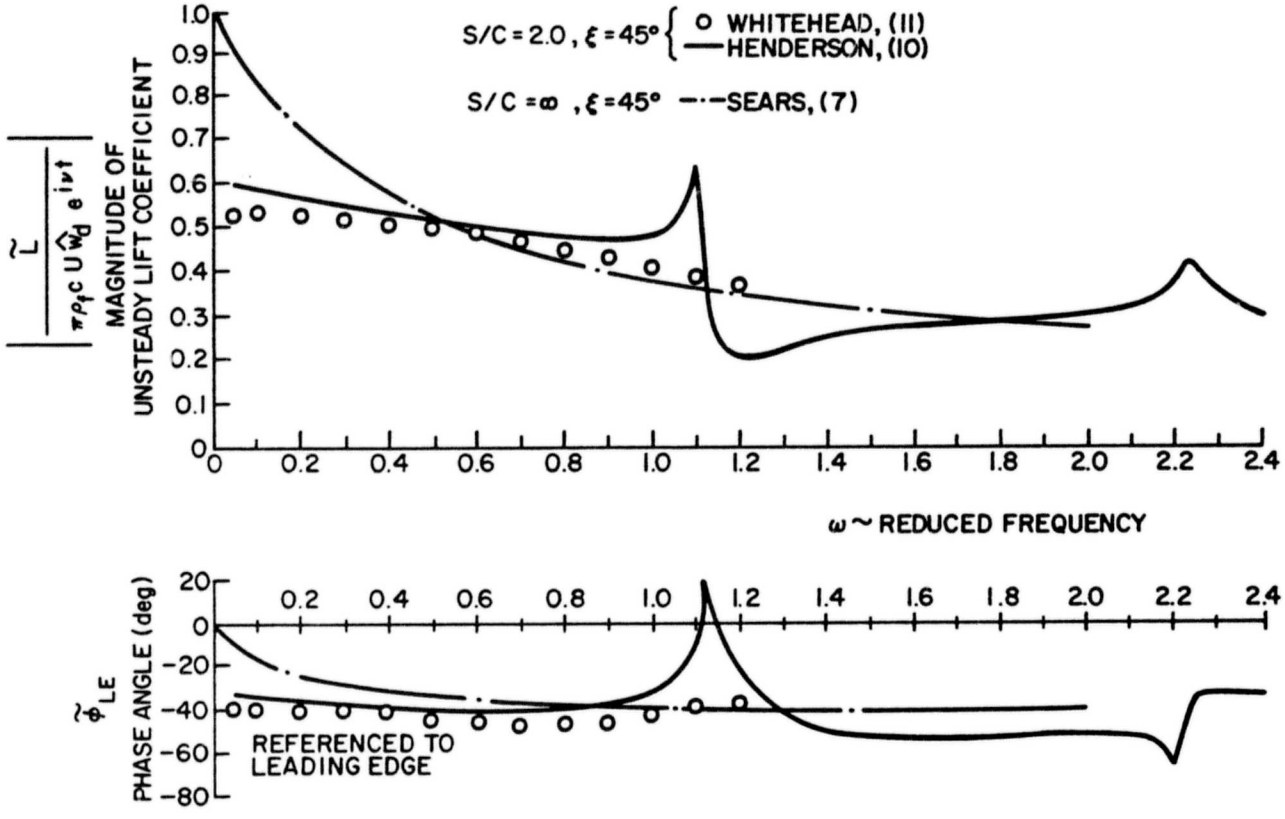

Figure 8 - Comparison of Predicted Unsteady Lift, s/c = 2.0, ξ = 45°

Source: Henderson, R. E., "Unsteady Response of an Axial Flow Turbomachine to an Upstream Disturbance," Ph. D. Thesis, Cambridge University, 1972.

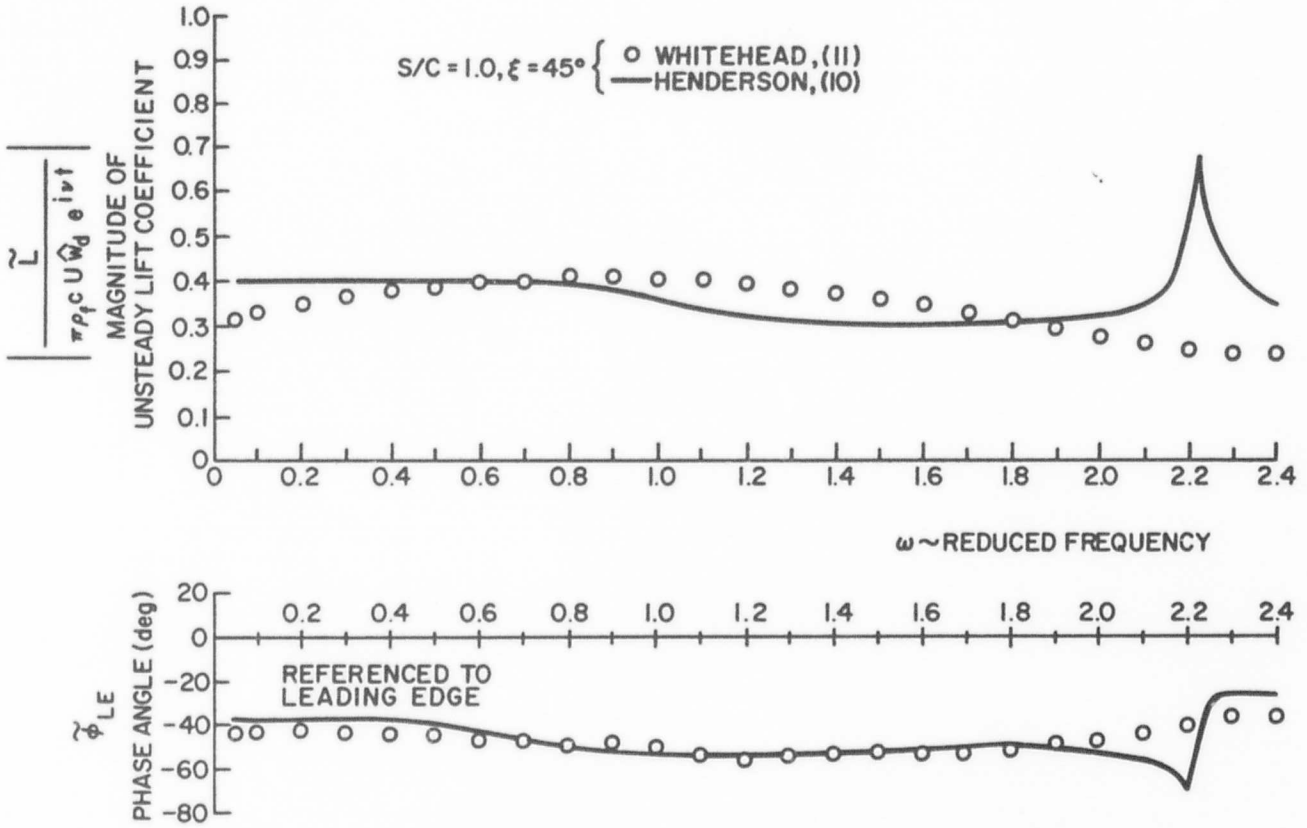

Figure 9 - Comparison of Predicted Unsteady Lift, s/c = 1.0, ξ = 45°

Source: Henderson, R. E., "Unsteady Response of an Axial Flow Turbomachine to an Upstream Disturbance," Ph. D. Thesis, Cambridge University, 1972.

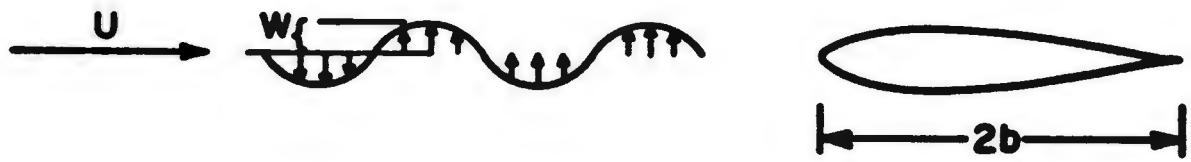

Figure 10 - Airfoil Operating in the Freestream with a Sinusoidal Gust Velocity Normal to the Airfoil's Surface

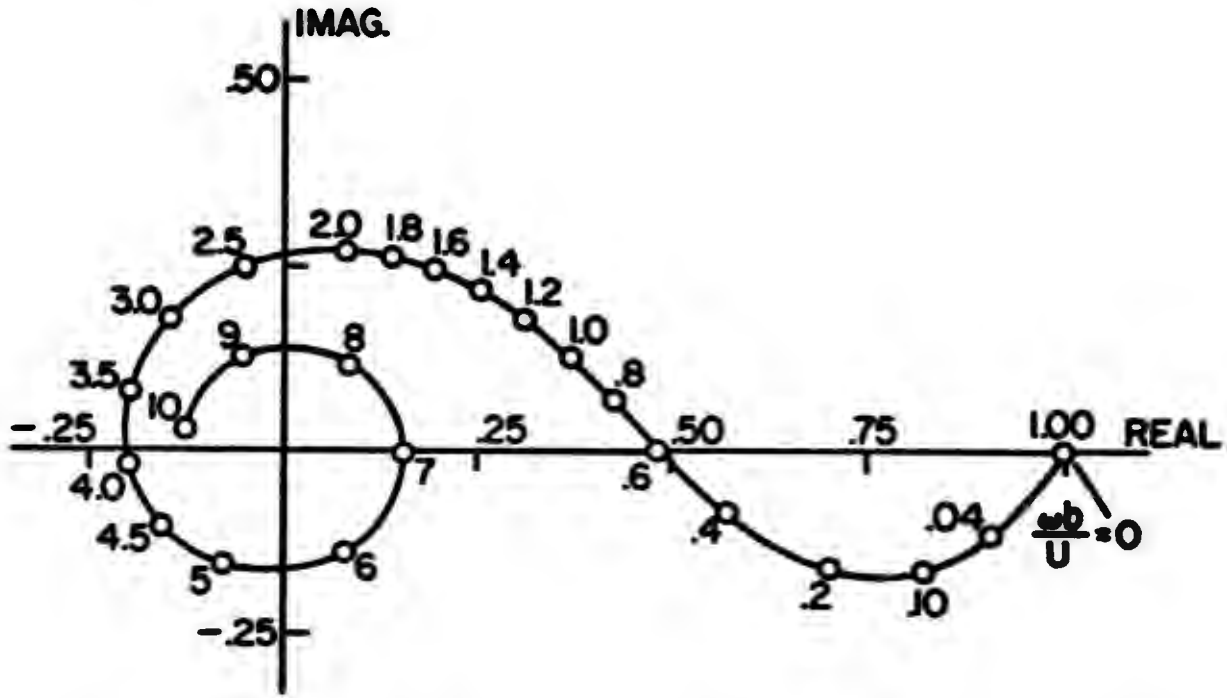

Figure 11 - Nondimensional Unsteady Lift Represented in the Complex Plane

Source: Sears, W. R., "Some Aspects of Non-Stationary Airfoil Theory and Its Practical Application," J. Aero. Sci., 1941.

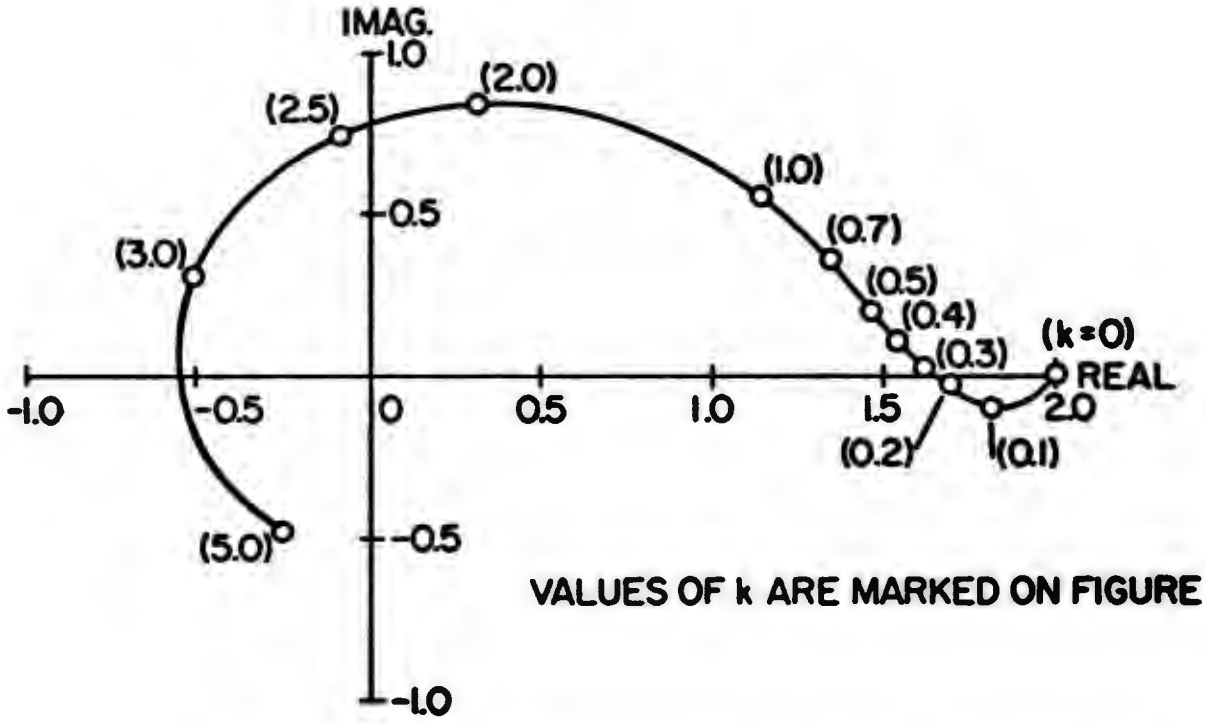

Figure 12 - Nondimensional Unsteady Lift Represented in the Complex Plane

Source: Horlock, J. H., "Fluctuating Lift Forces on Aerofoils Moving Through Transverse and Chordwise Gusts," Trans. ASME, J. Basic Eng., Paper No. 68-FE-28, 1968.

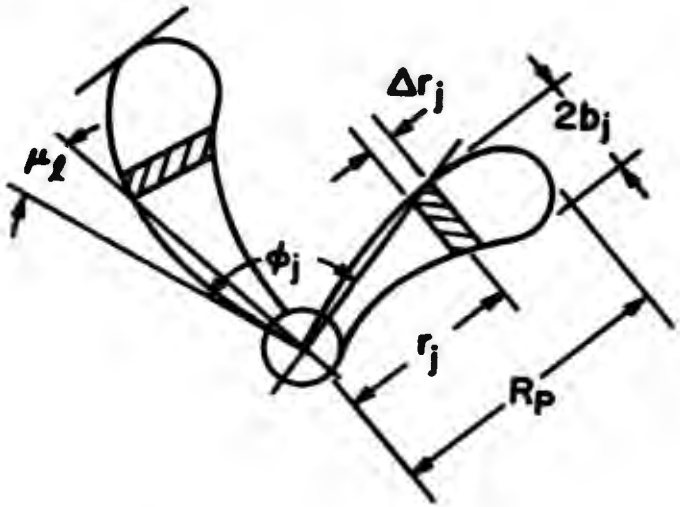

Figure 13a - Typical Propeller Blade

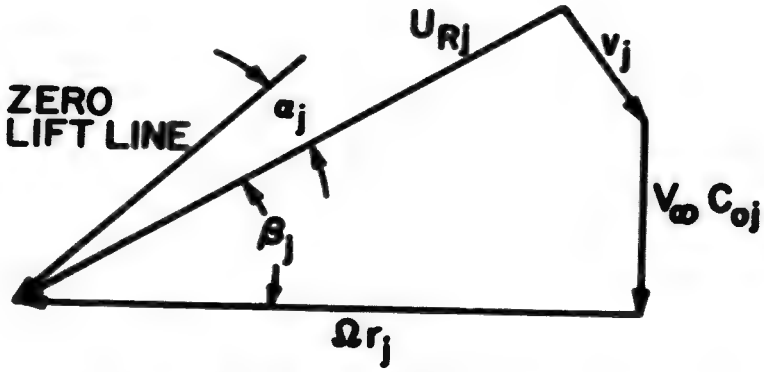

Figure 13b - Velocity Triangle Appropriate to the j^{th} Blade Section

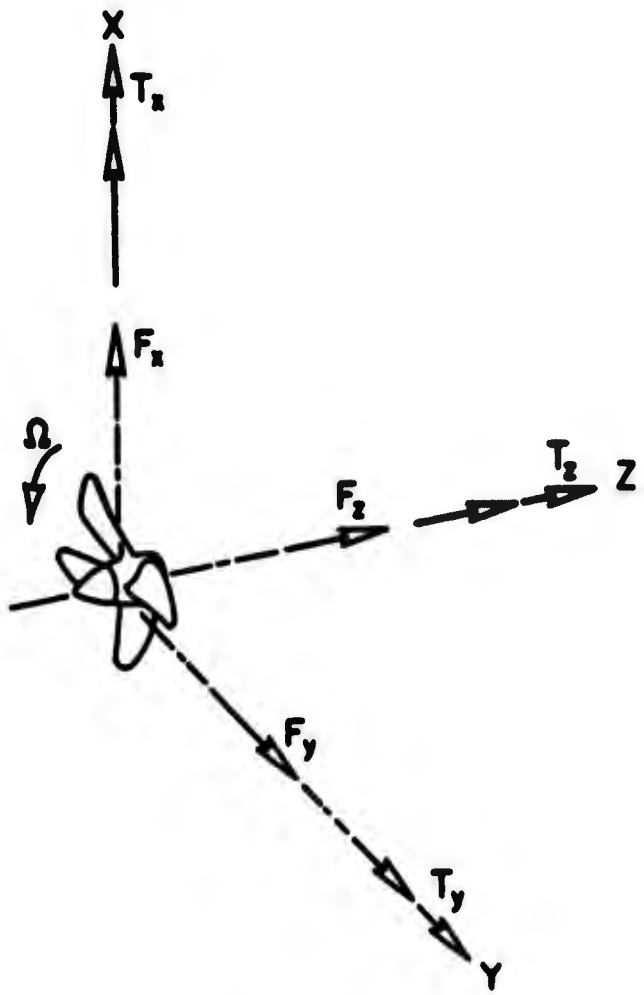

Figure 14 - Coordinate System Assumed for Calculation of Unsteady Forces and Moments

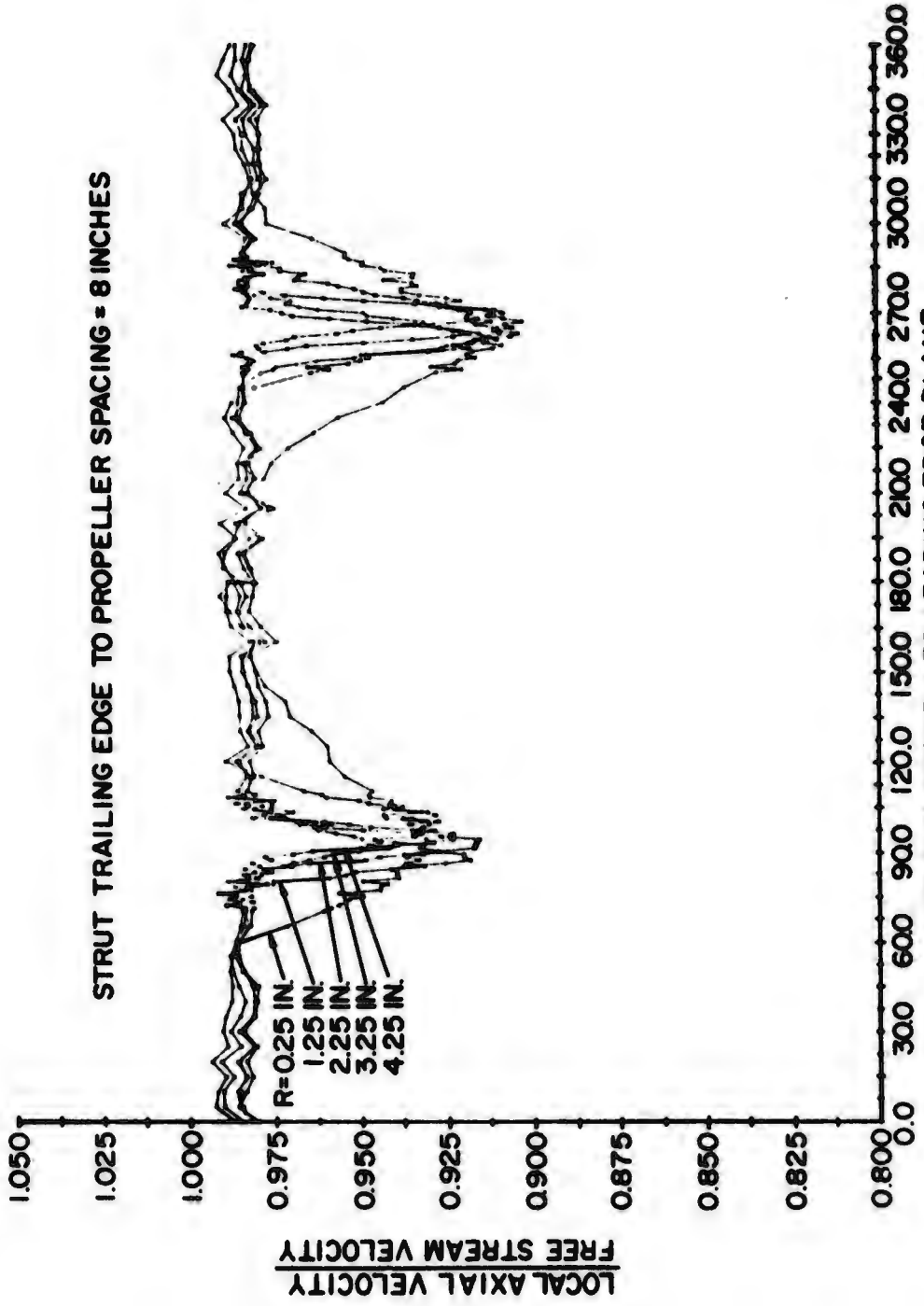

Figure 15 - Typical Circumferential Distributions at Various Radii of Axial Velocity Behind a Strut

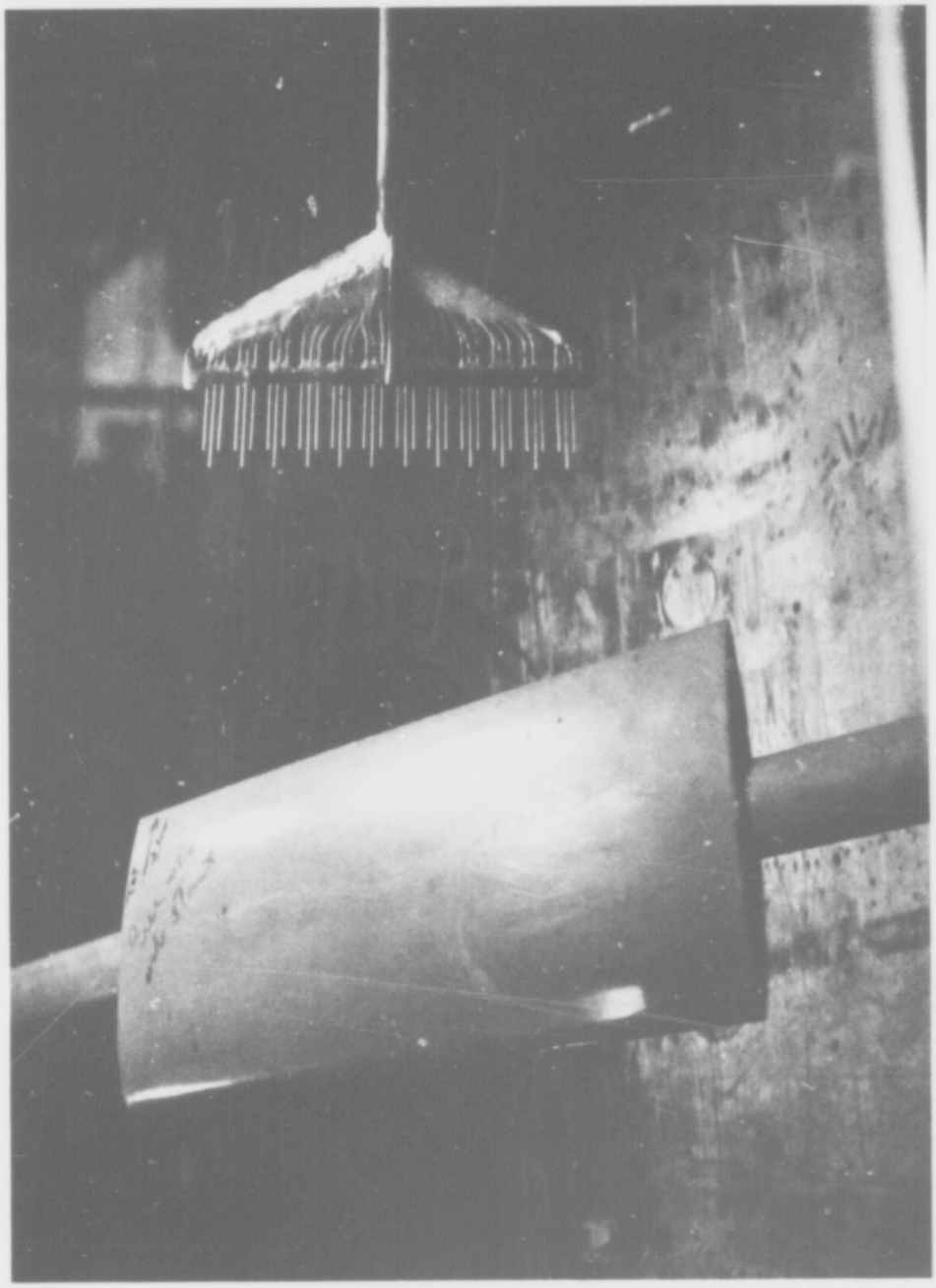

Figure 16 - Wake Rake Mounted Behind Strut

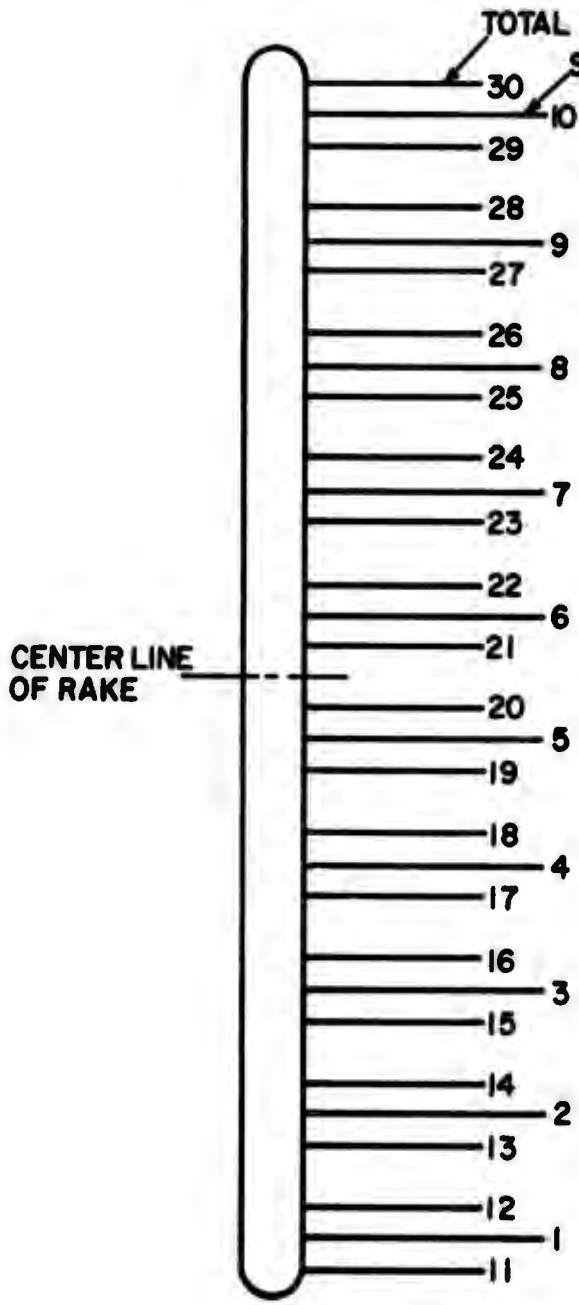

TUBE NO.	RADIUS (Inches)
1,10	4.5
2,9	3.5
3,8	2.5
4,7	1.5
5,6	0.5
11,30	4.75
12,29	4.25
13,28	3.75
14,27	3.25
15,26	2.75
16,25	2.25
17,24	1.75
18,23	1.25
19,22	0.75
20,21	0.25

Figure 17 - Schematic of Wake Rake

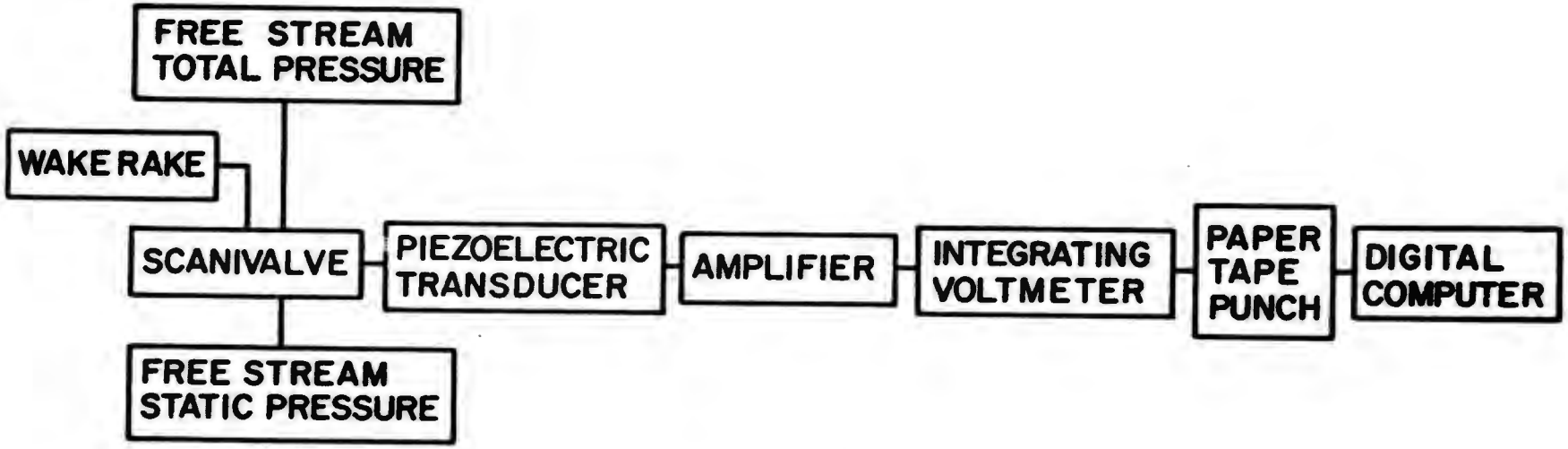

Figure 18 - Data Acquisition and Reduction System for Wake Surveys

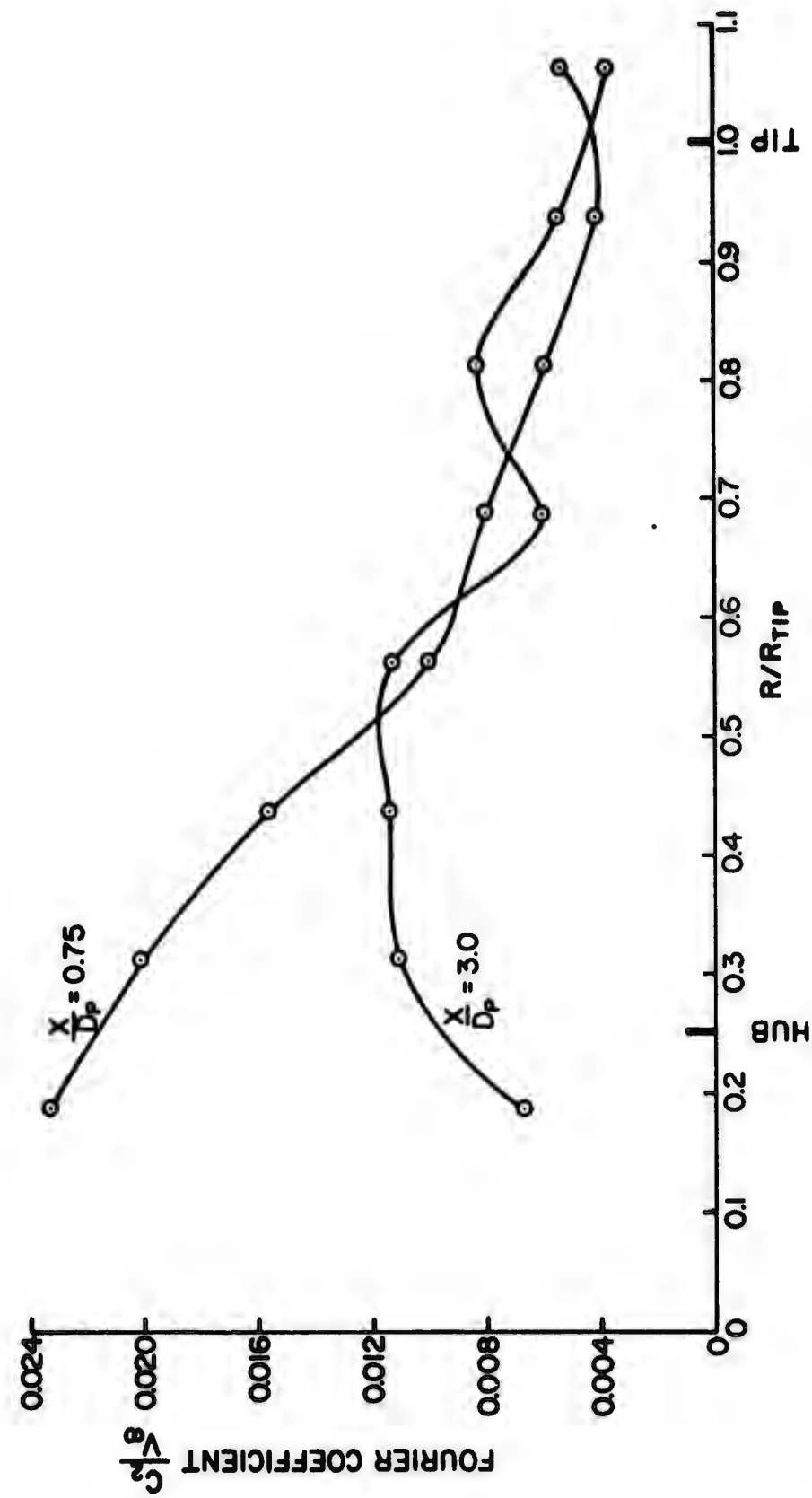

Figure 19 - Complex Fourier Coefficient C_2/V_∞ versus Nondimensional Radius for Two Strut-to-Propeller Spacings

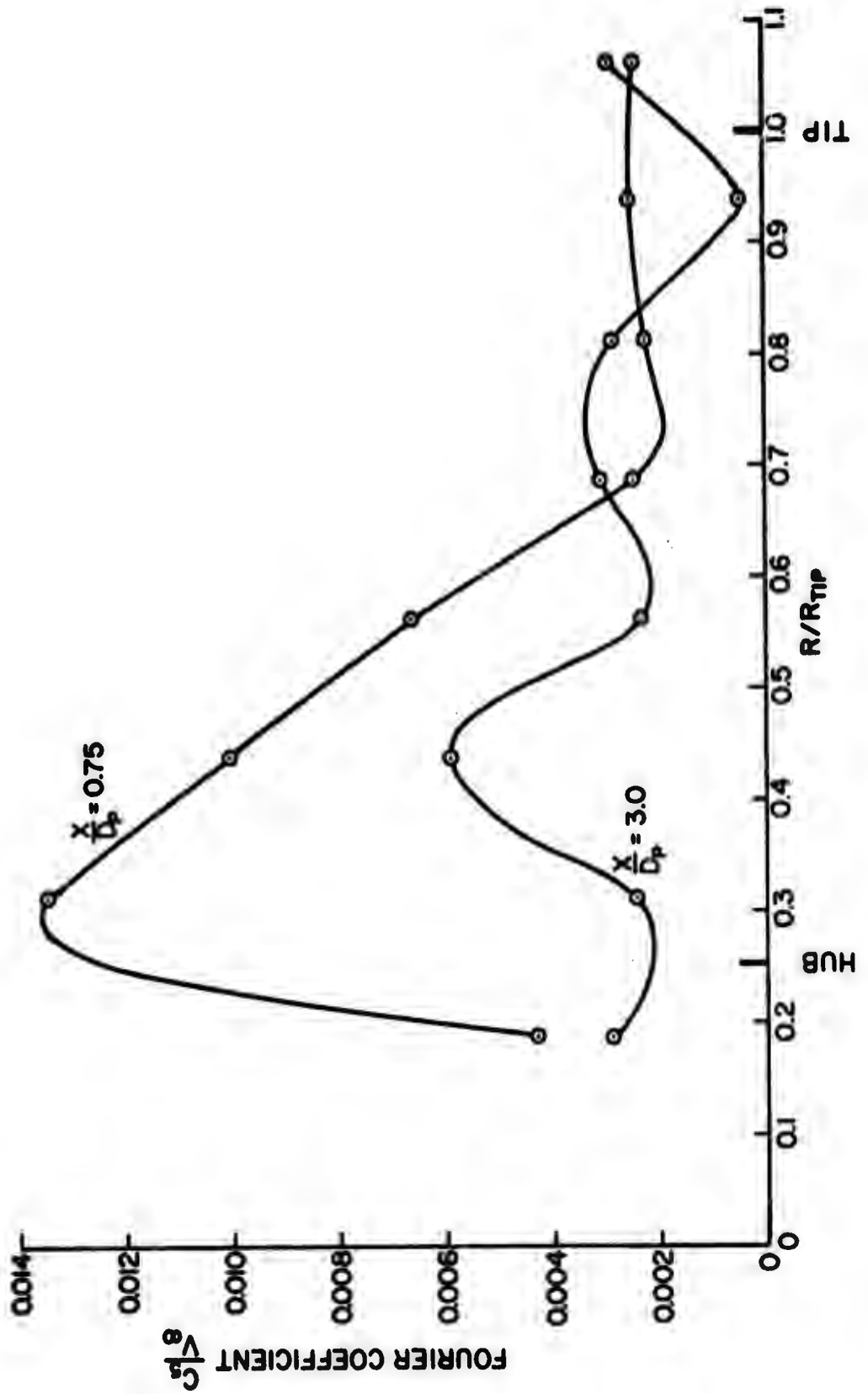

Figure 20 - Complex Fourier Coefficient C_5/V_∞ versus Nondimensional Radius for Two Strut-to-Propeller Spacings

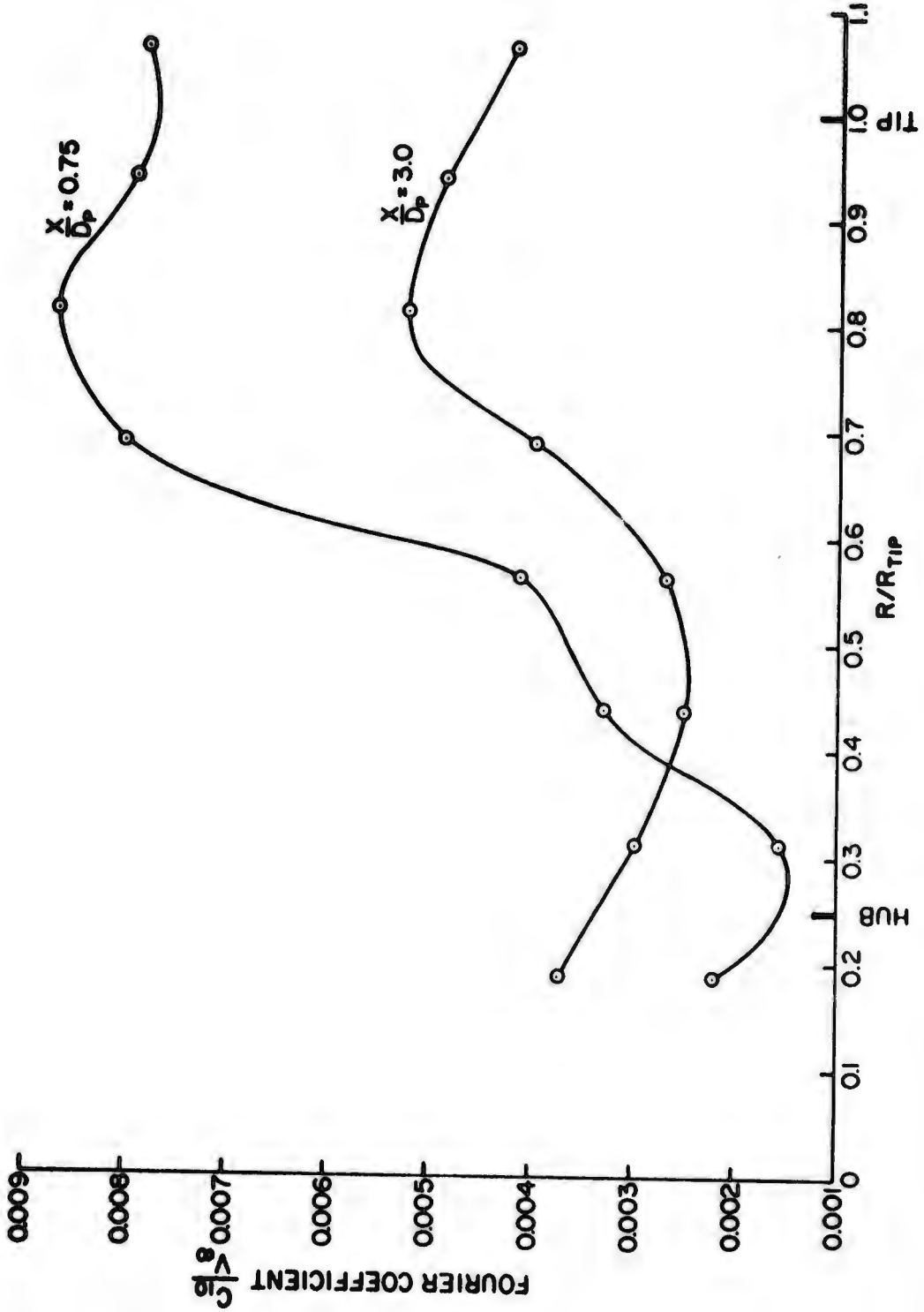

Figure 21 - Complex Fourier Coefficient C_{10}/V_∞ versus Nondimensional Radius for Two Strut-to-Propeller Spacings

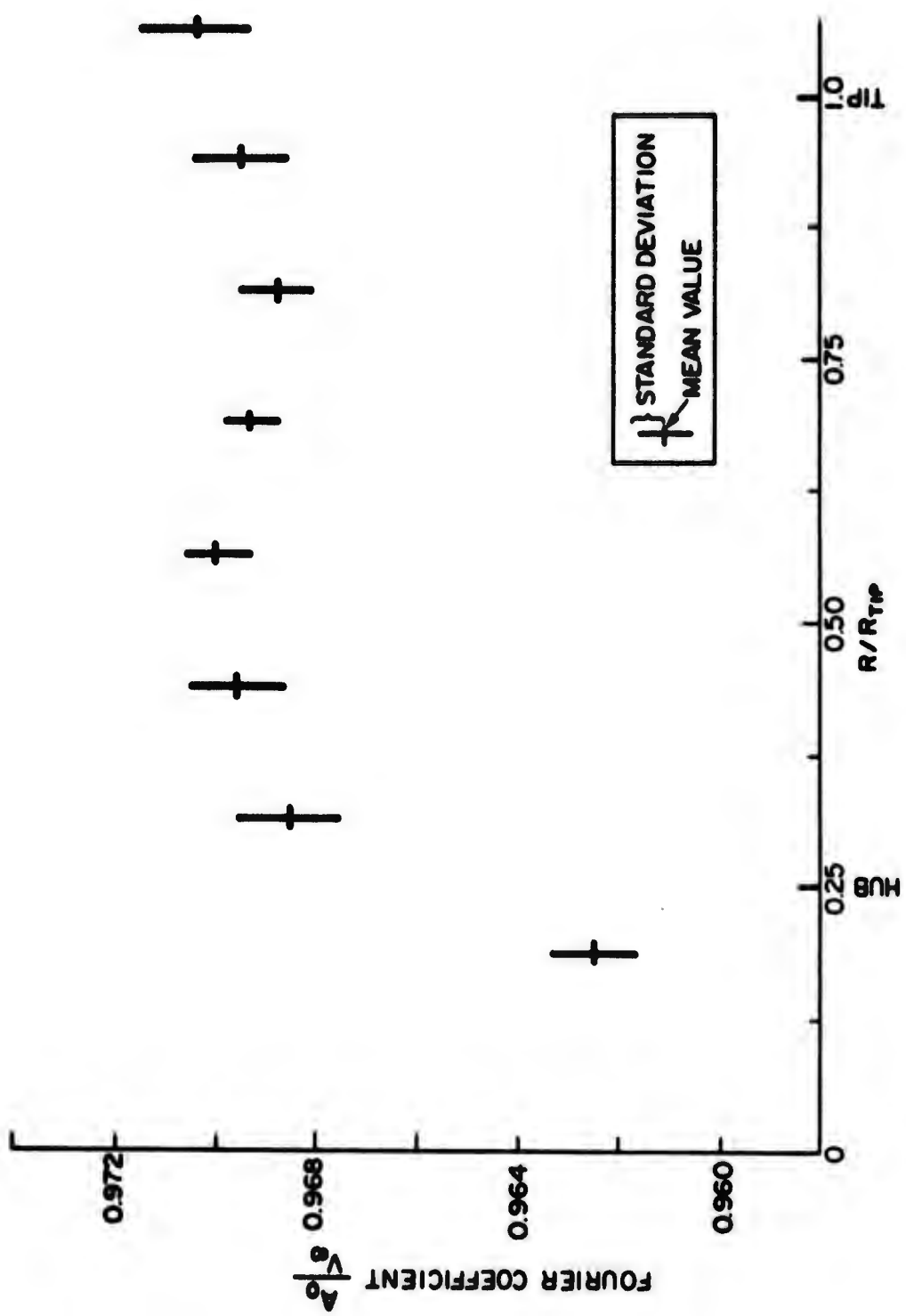

Figure 22 - Mean and Standard Deviation of Fourier Coefficient A_o/V_∞ versus Nondimensional Radius

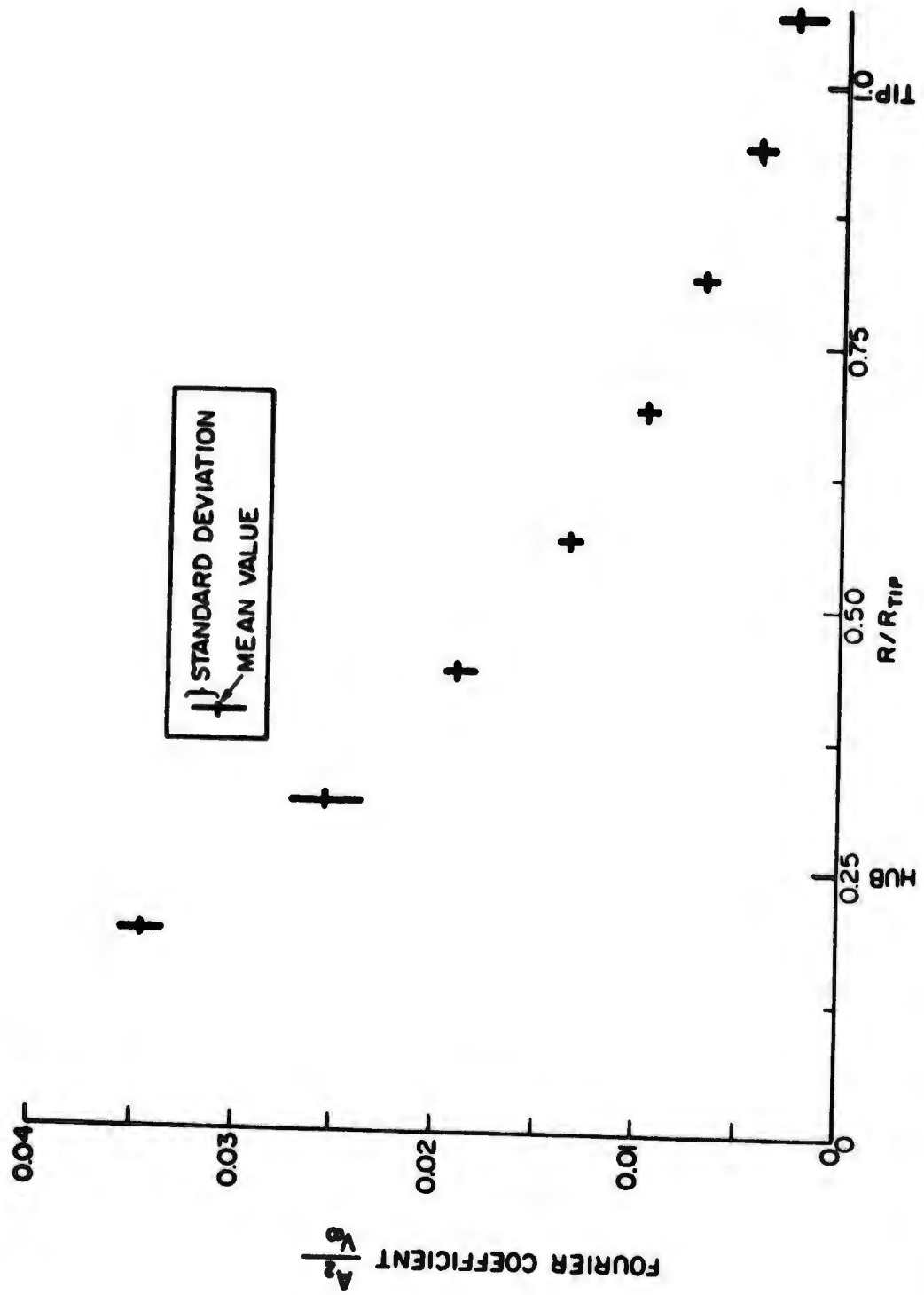

Figure 23 - Mean and Standard Deviation of Fourier Coefficient A_2/V_∞ versus Nondimensional Radius

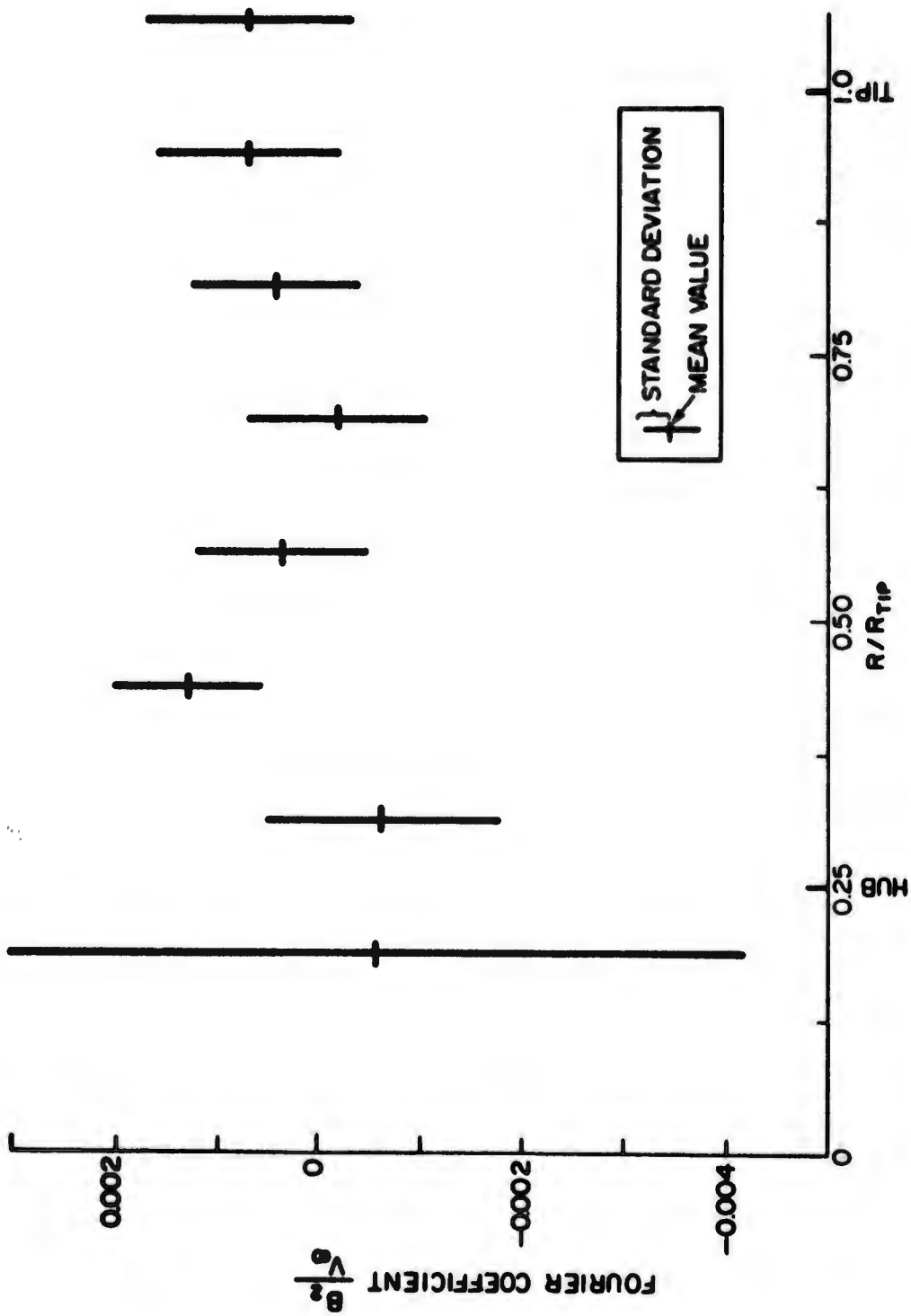

Figure 24 - Mean and Standard Deviation of Fourier Coefficient B_2/V_∞ versus Nondimensional Radius

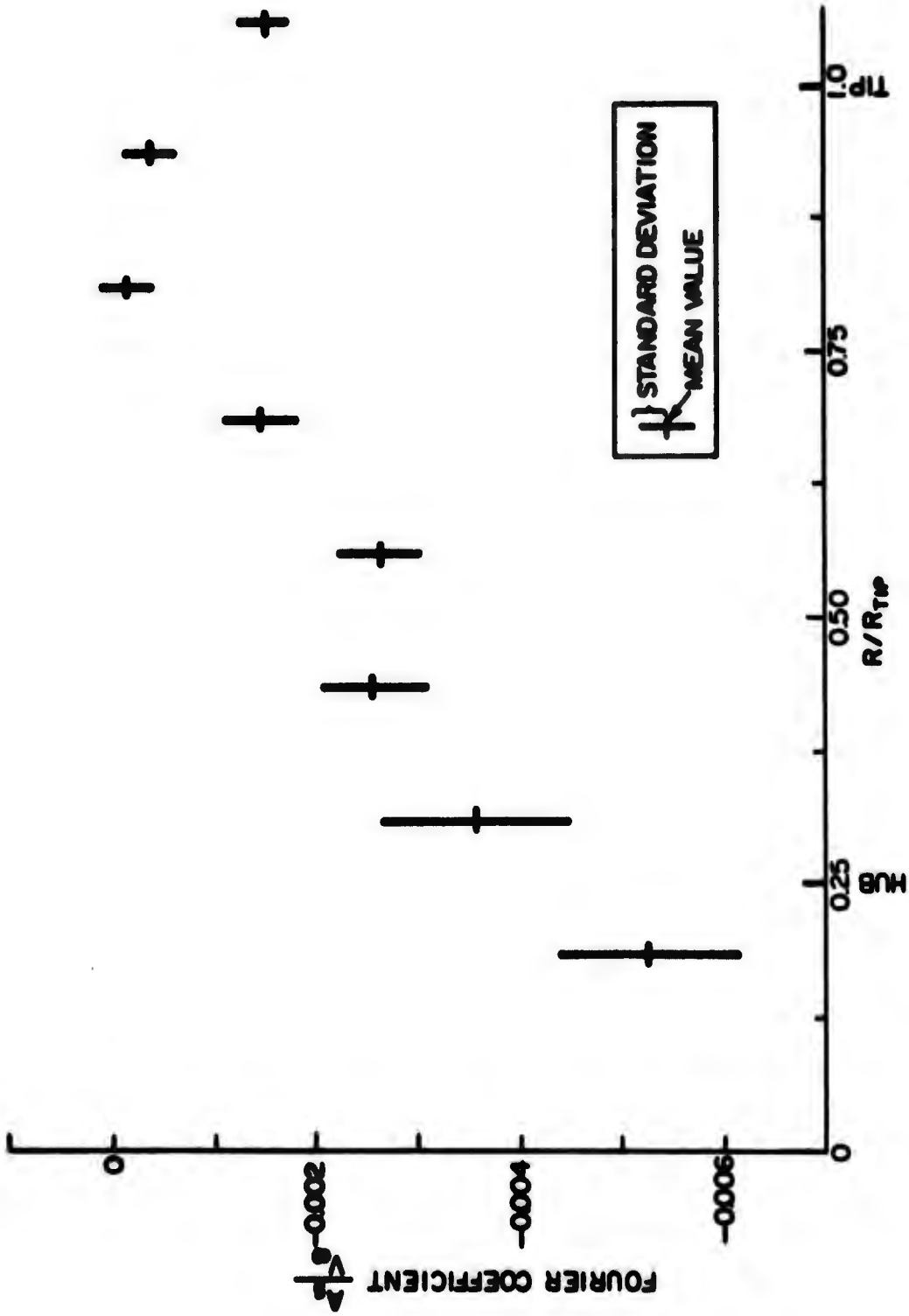

Figure 25 - Mean and Standard Deviation of Fourier Coefficient A_5/V_∞ versus Nondimensional Radius

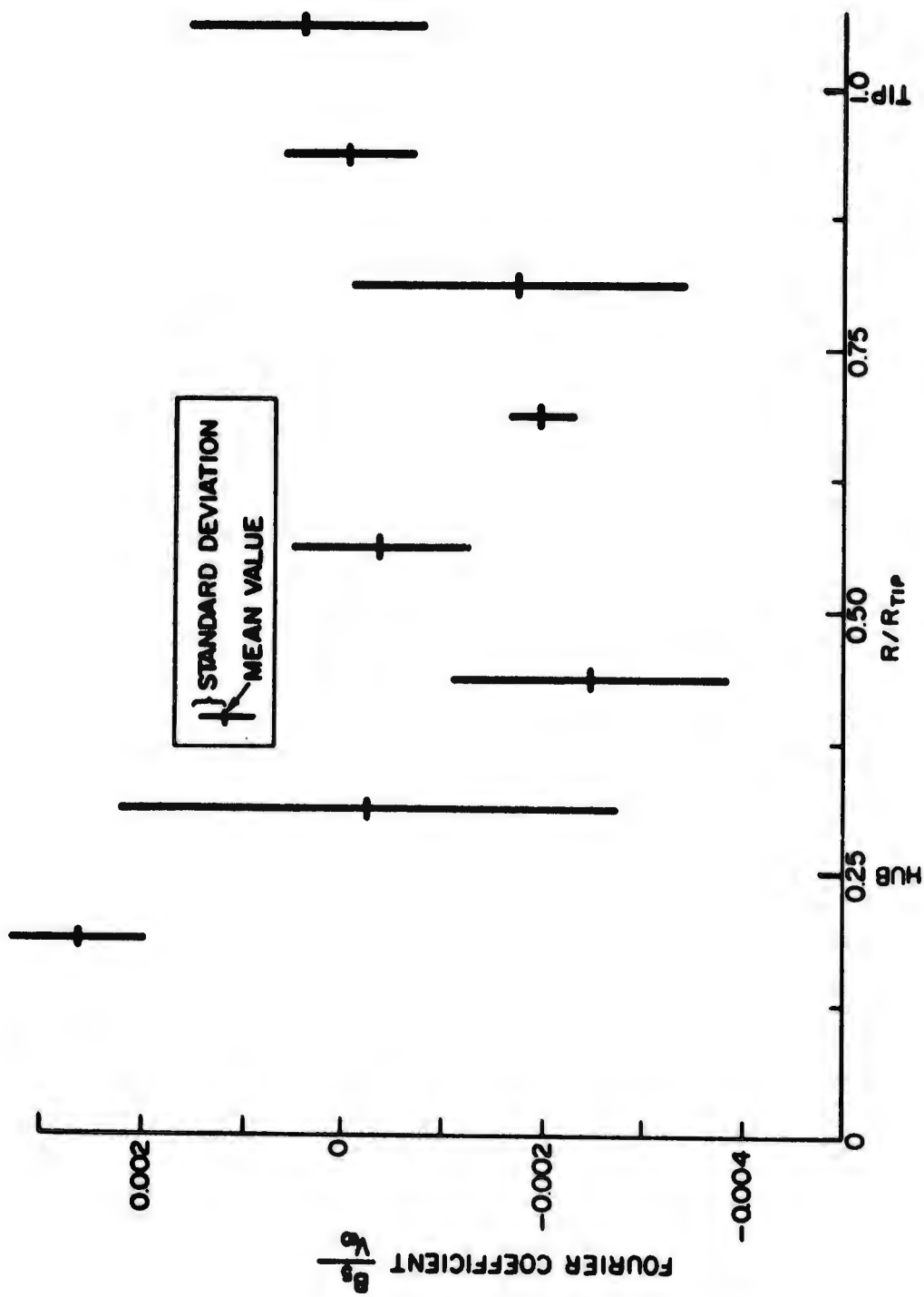

Figure 26 - Mean and Standard Deviation of Fourier Coefficient B_5/V_∞ versus Nondimensional Radius

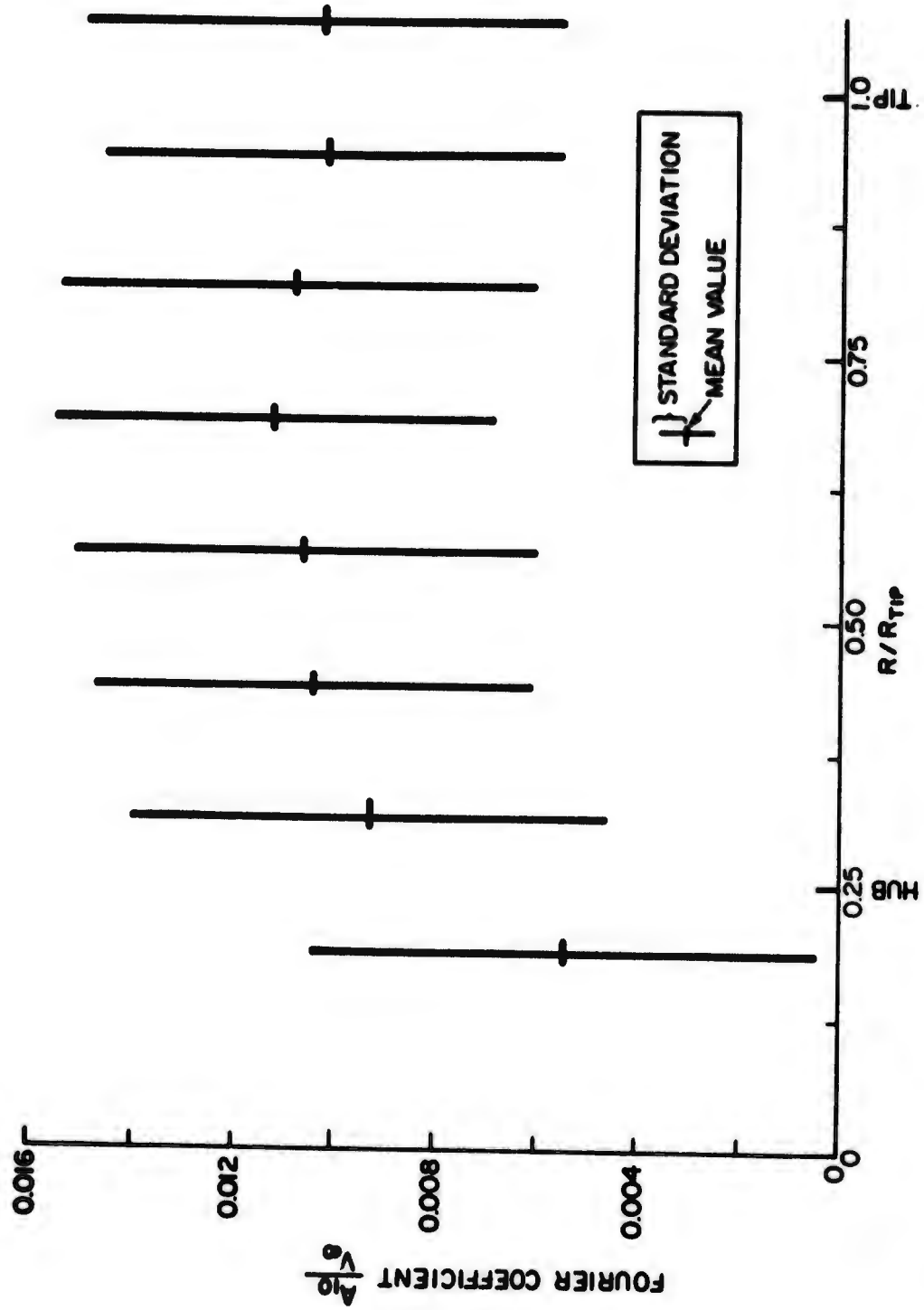

Figure 27 - Mean and Standard Deviation of Fourier Coefficient A_{10}/V_∞ versus Nondimensional Radius

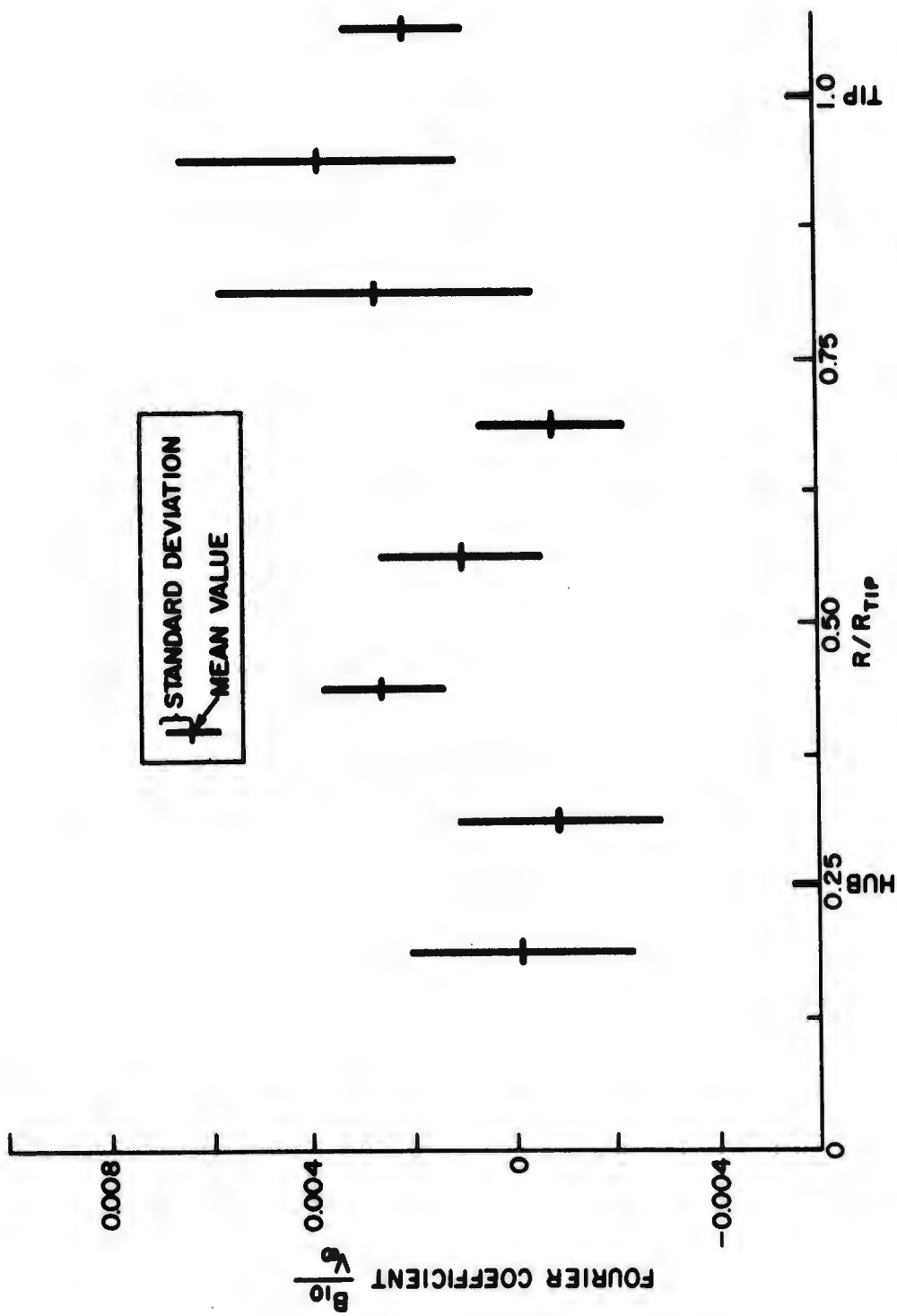

Figure 28 - Mean and Standard Deviation of Fourier Coefficient B_{10}/V_∞ versus Nondimensional Radius

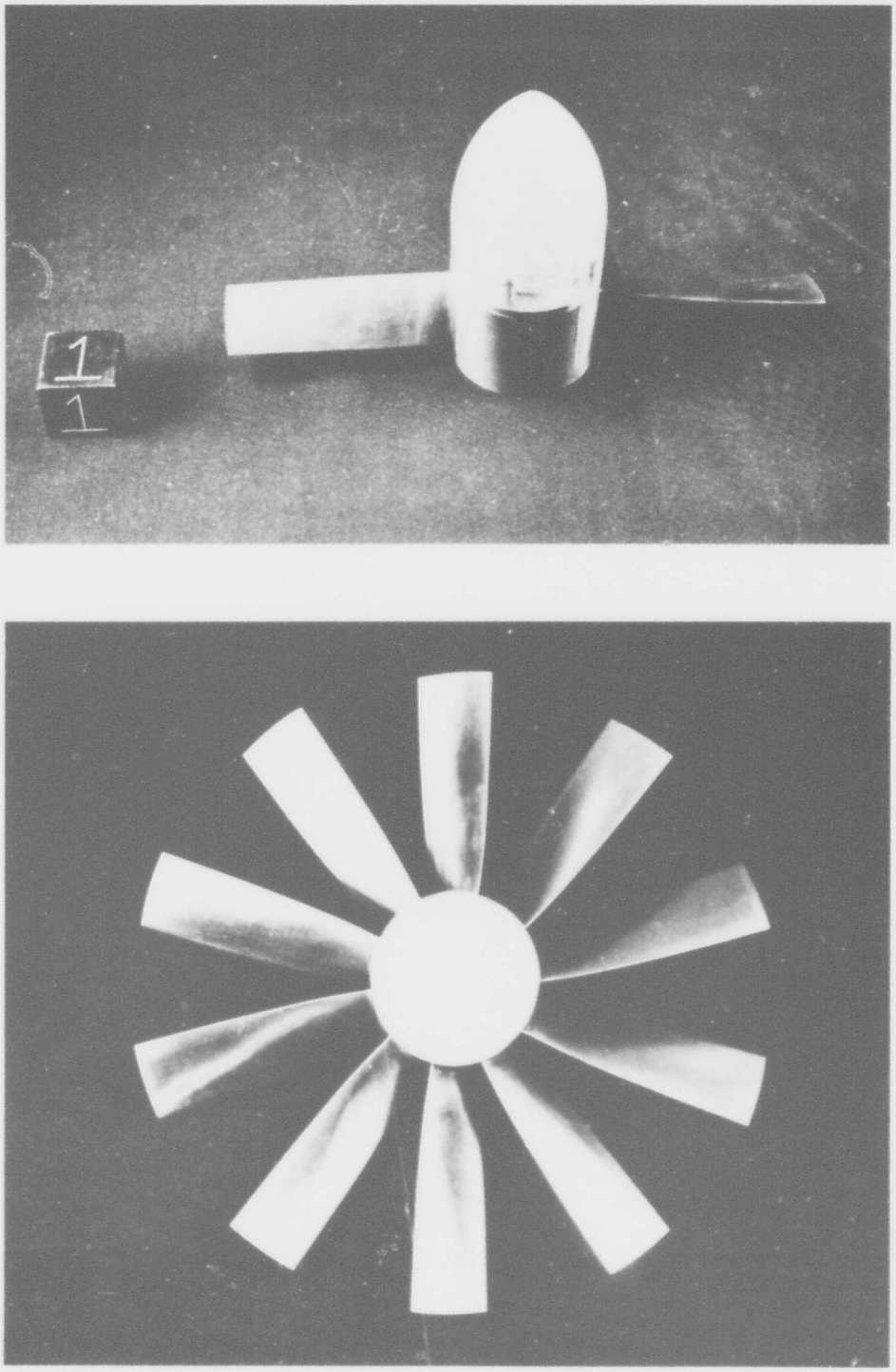

Figure 29 - Propellers Tested

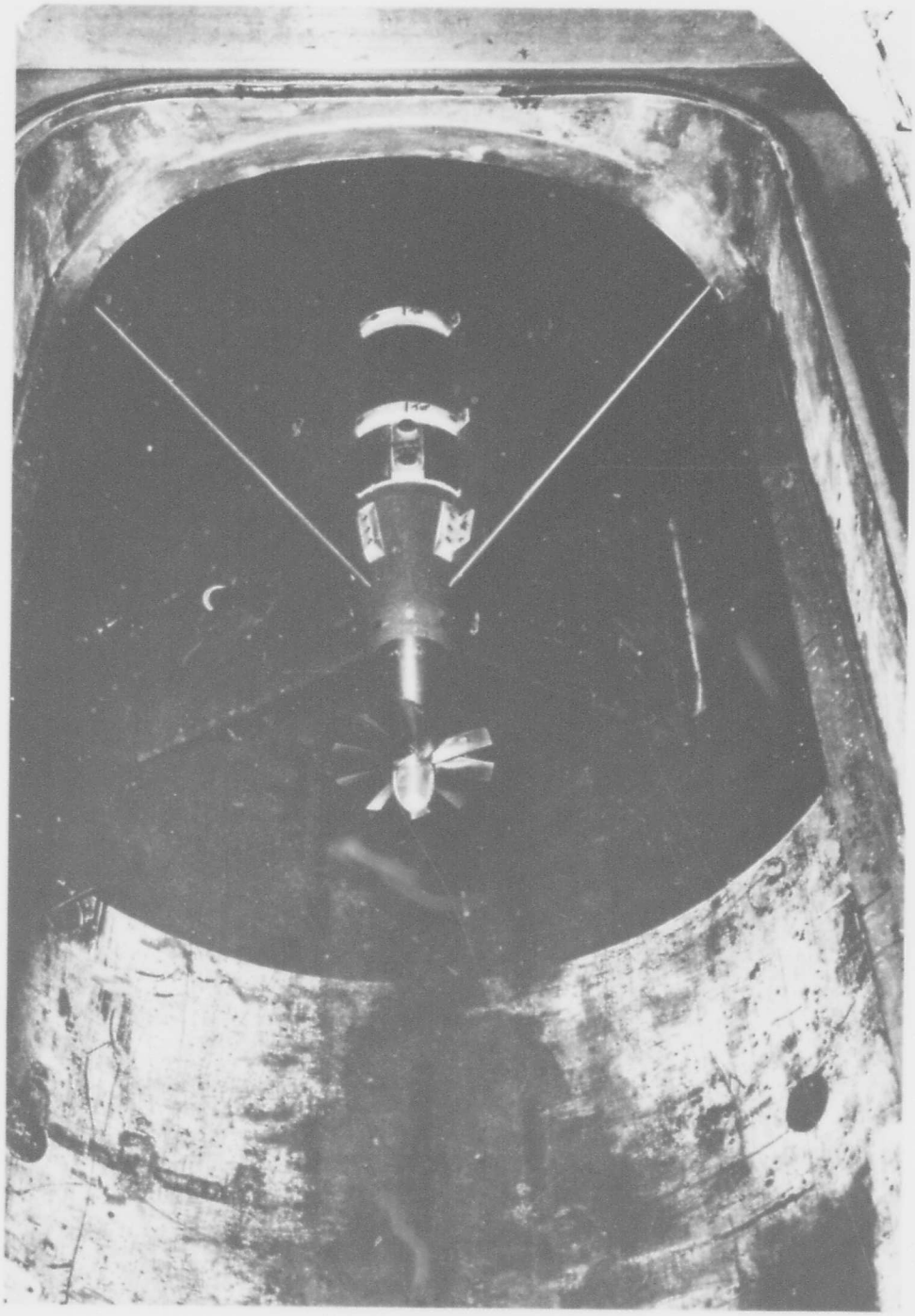

Figure 30 - External View of Dynamometer

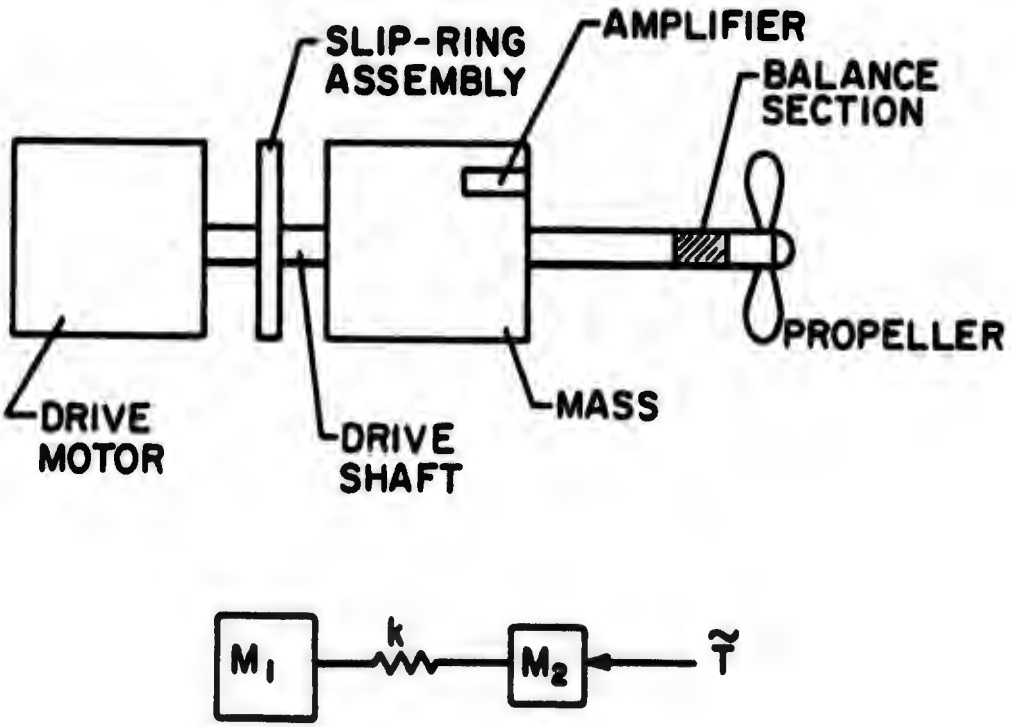

Figure 31 - Internal View of Dynamometer

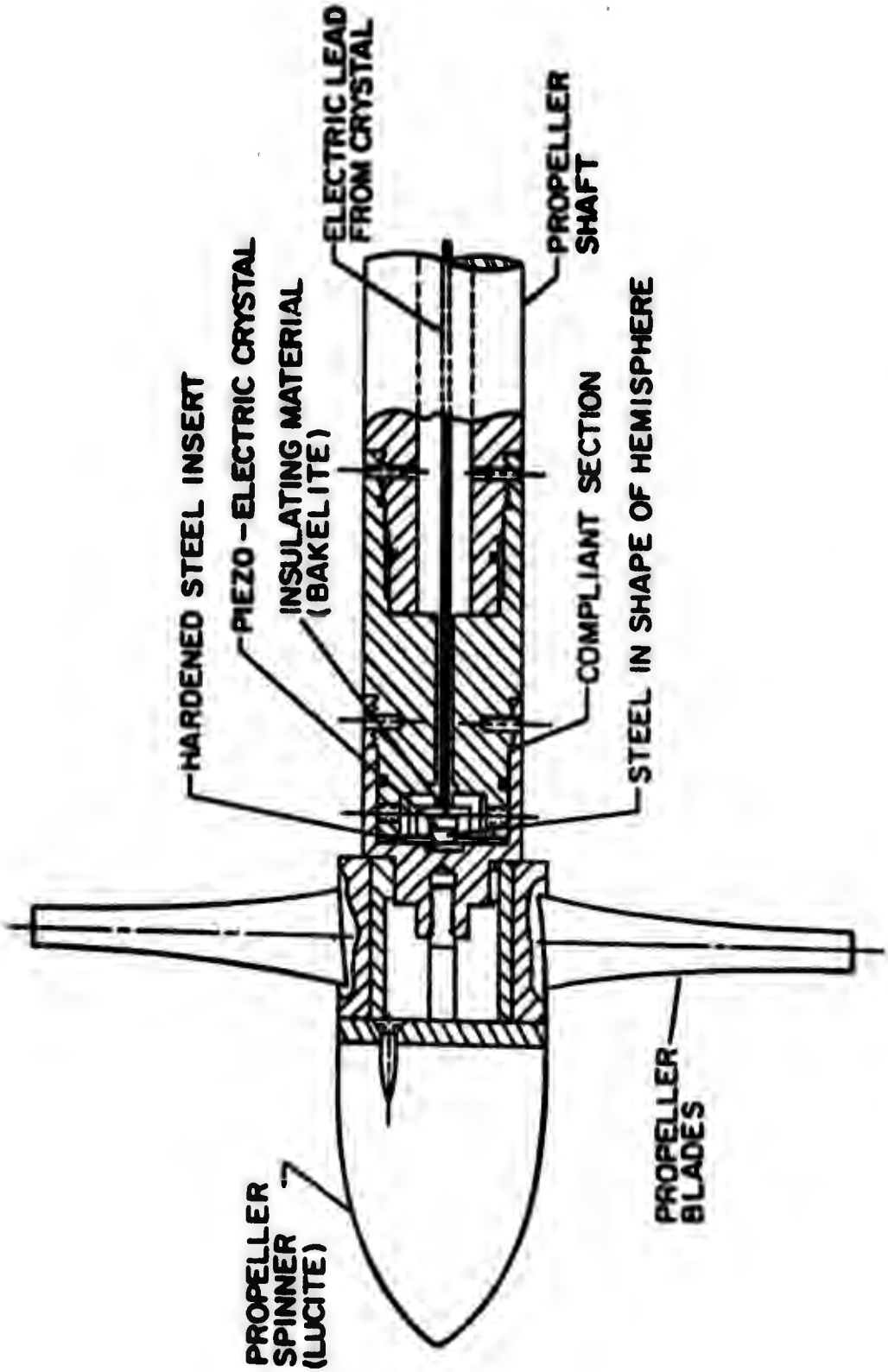

Figure 32 - Detailed Drawing of Time-Dependent Thrust Balance

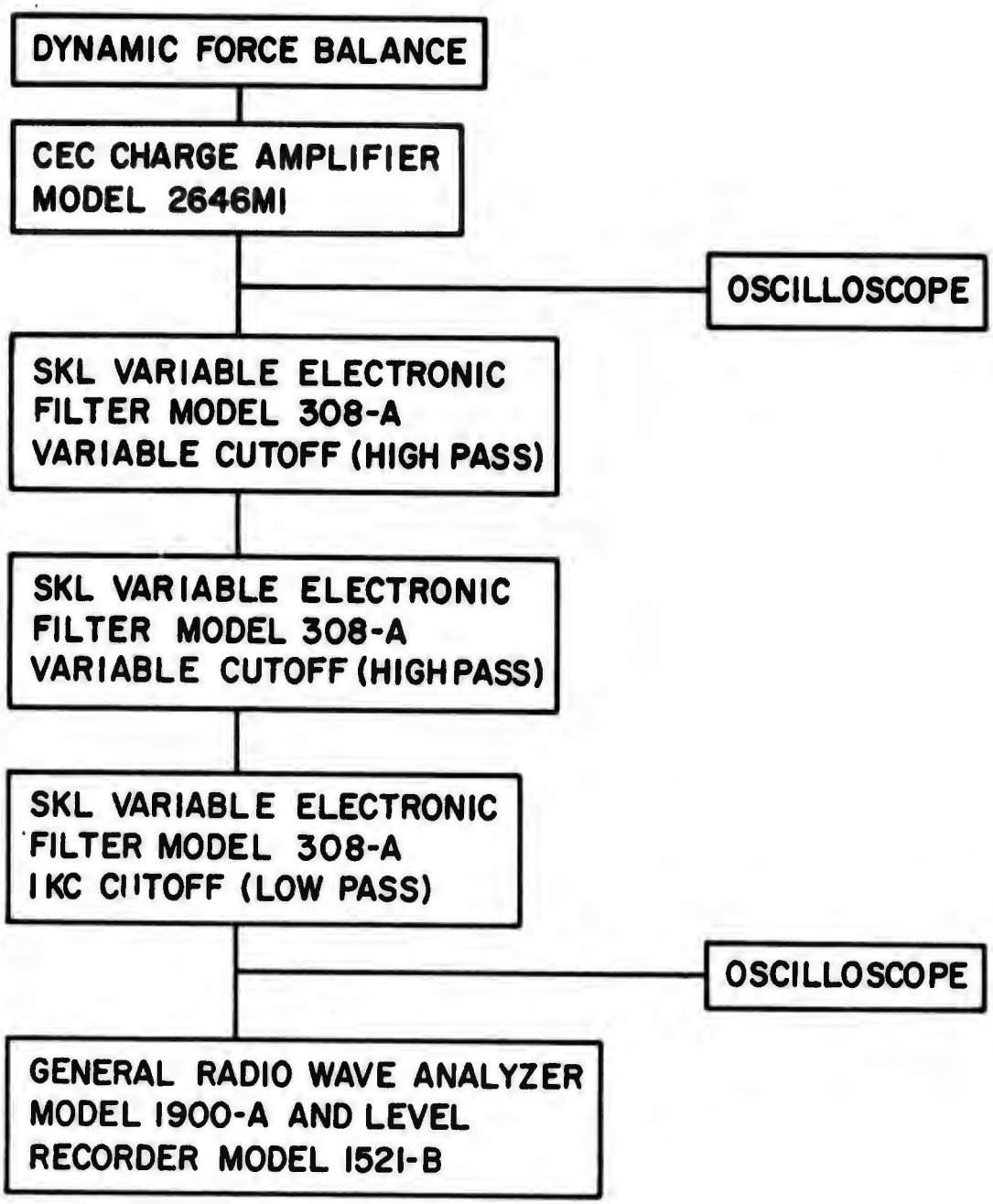

Figure 33 - Data Acquisition and Reduction System for Time-Dependent Thrust Measurement

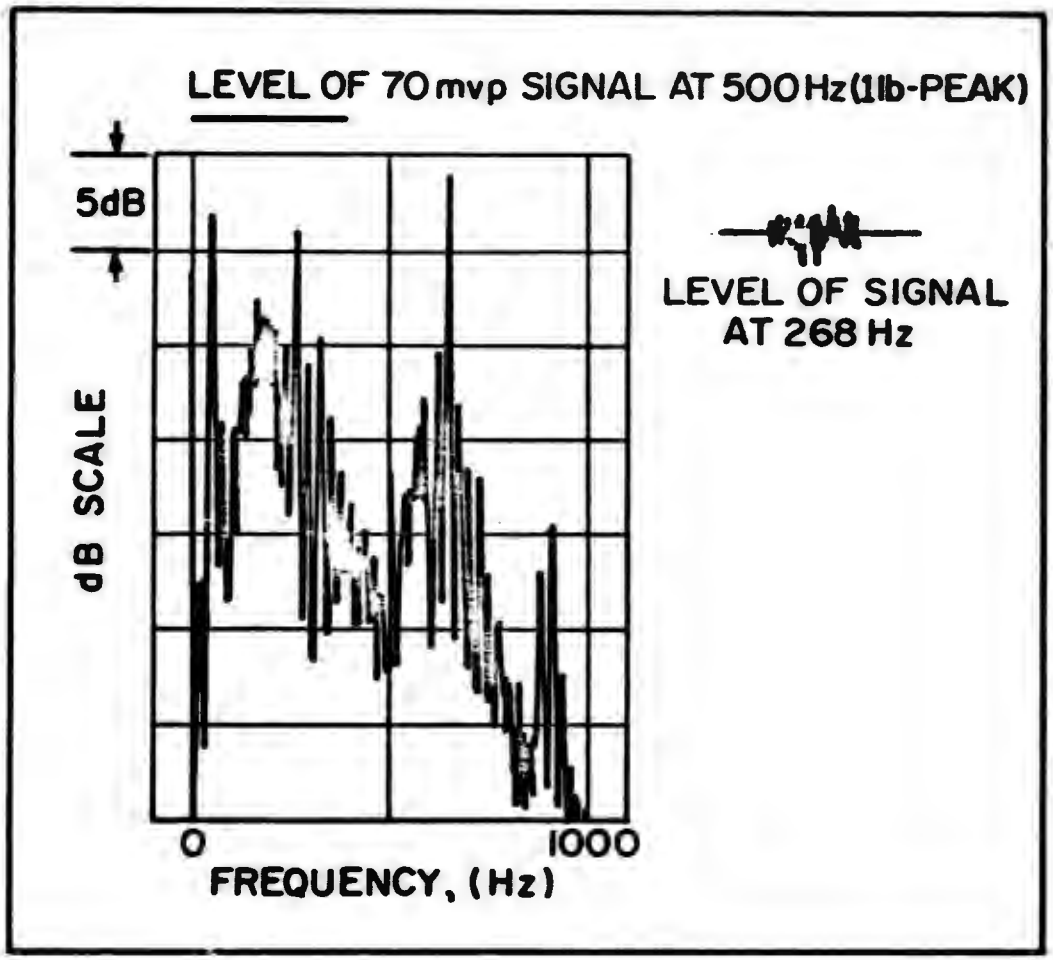

TEST CONDITIONS
10 BLADED PROPELLER
V_∞ = 21 ft/sec
J = 1.17
STRUT 6 inches FORWARD
OF PROPELLER

Figure 34 - Frequency Spectrum of Time-Dependent Thrust Signal, Blade-Rate Frequency Signal Level and Level of Calibration Signal

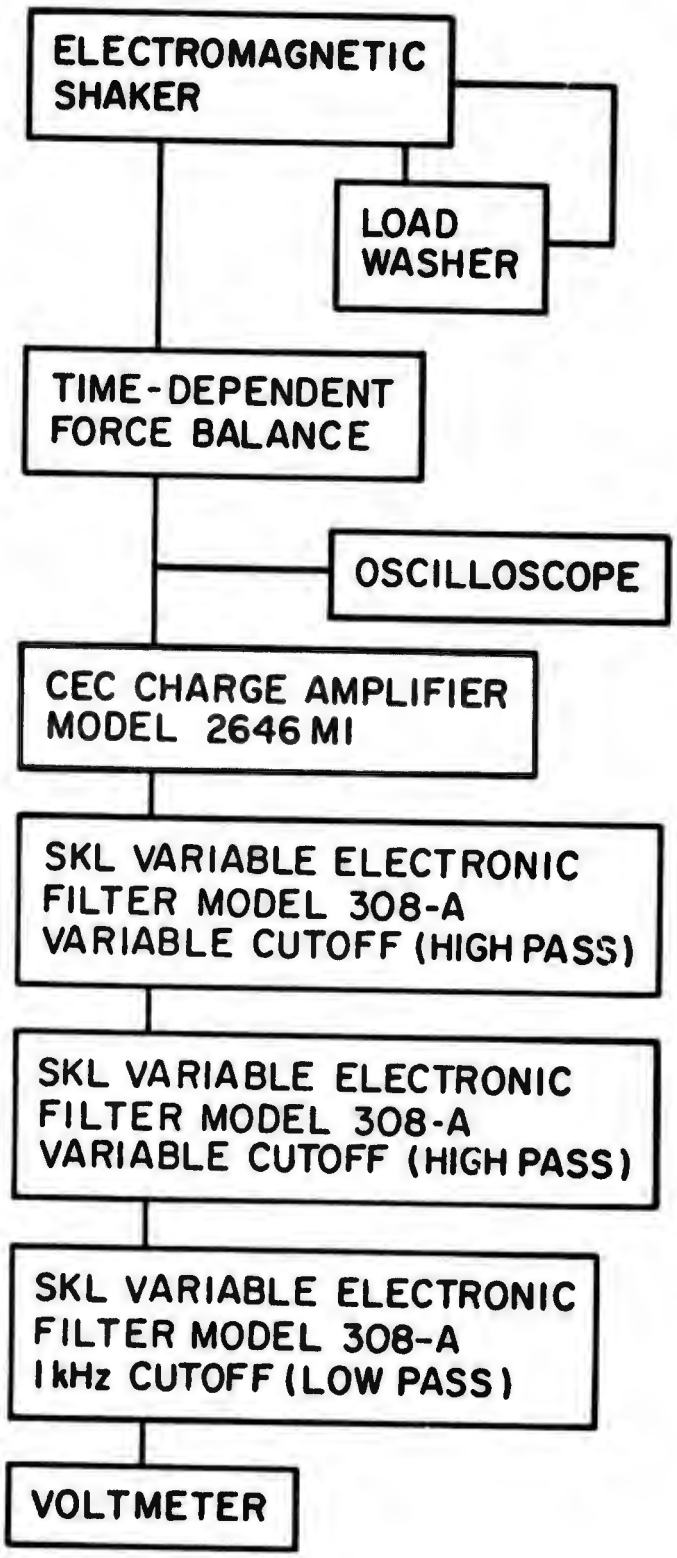

Figure 35 - Apparatus for Calibration of Time-Dependent Force Balance

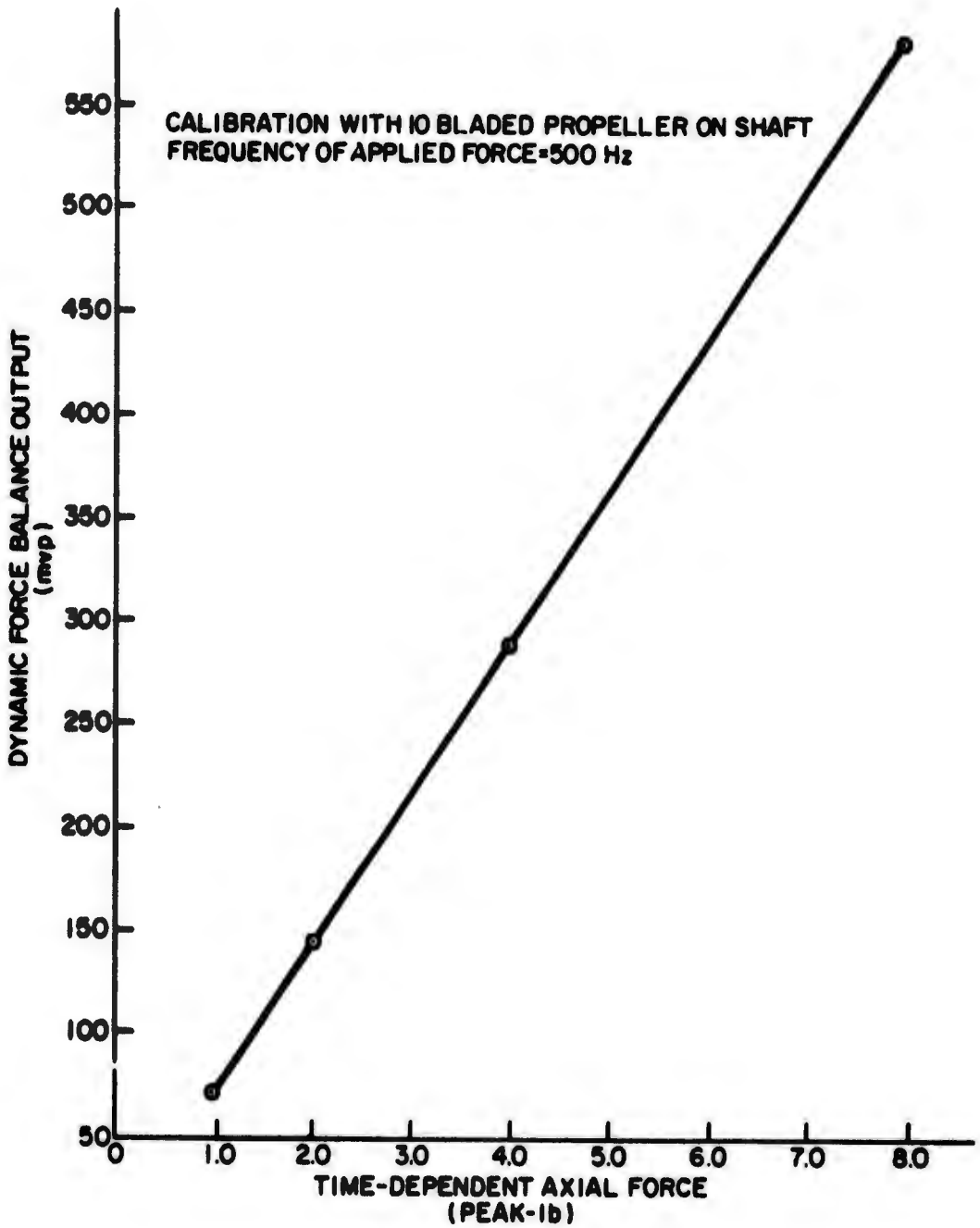

Figure 36 - Typical Calibration Curve

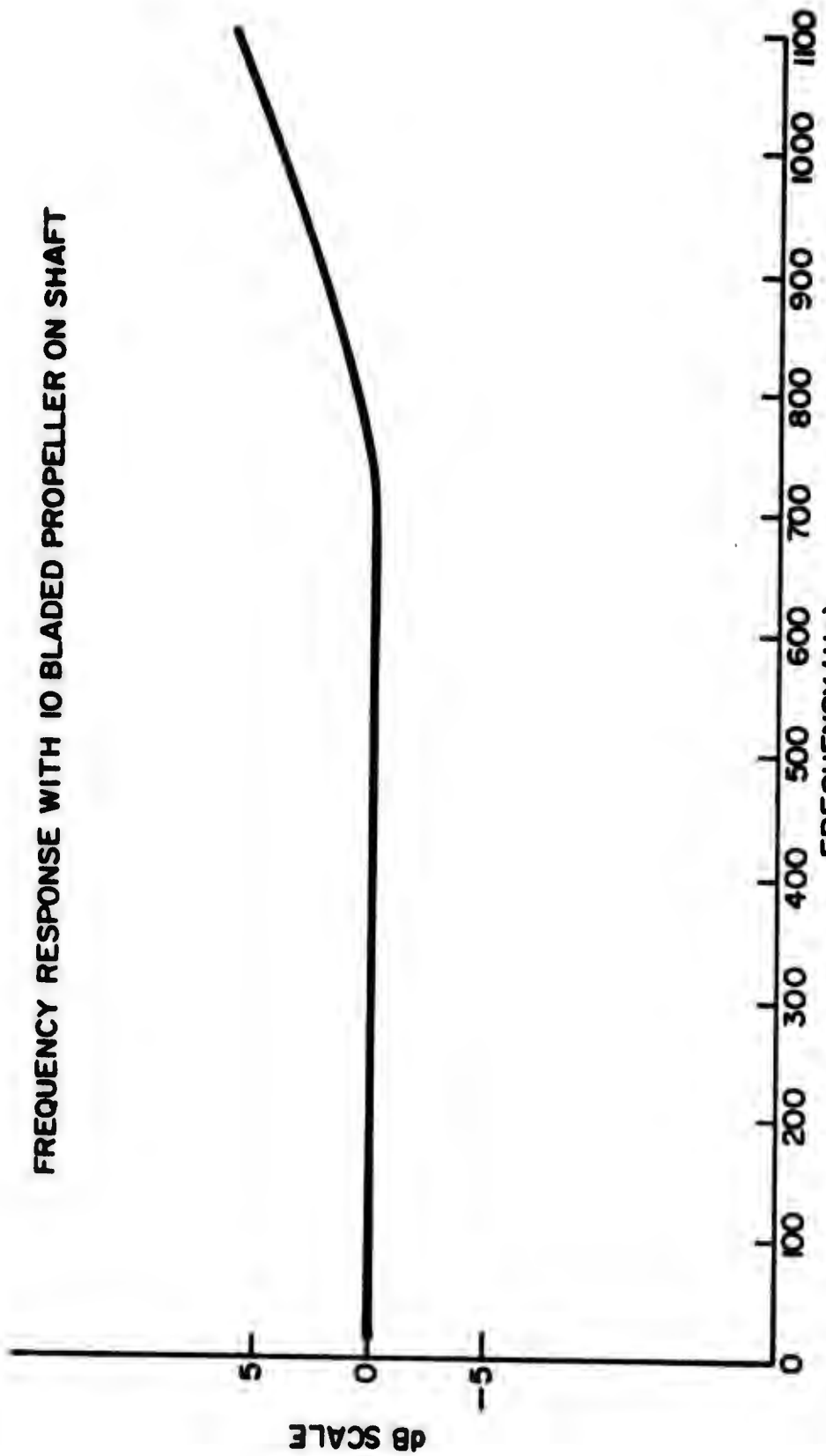

Figure 37 - Frequency Response of Time-Dependent Thrust Balance

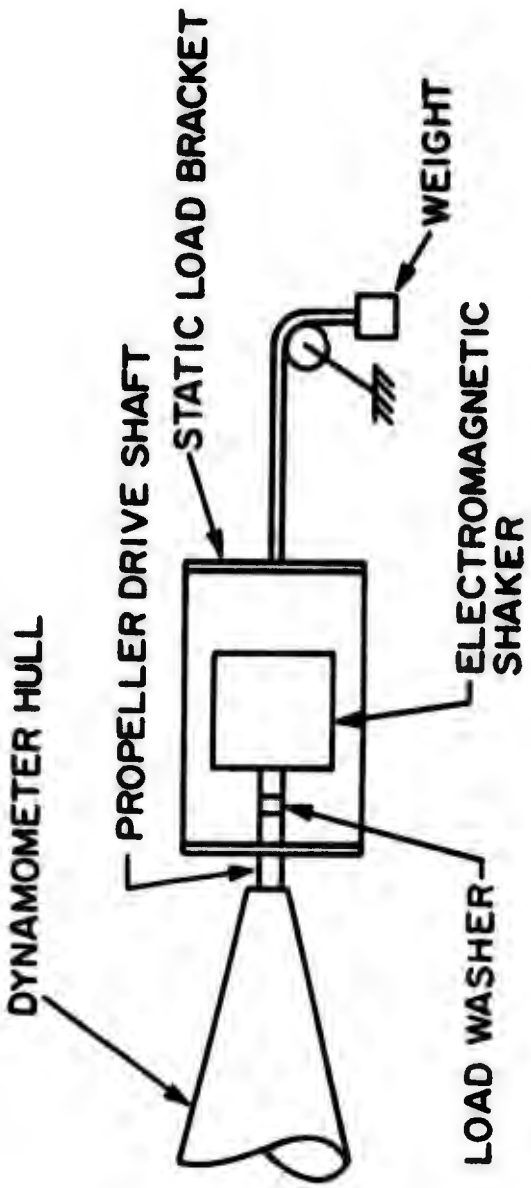

Figure 38 - Apparatus for Calibration of Time-Dependent Thrust Balance with Applied Steady Axial Force

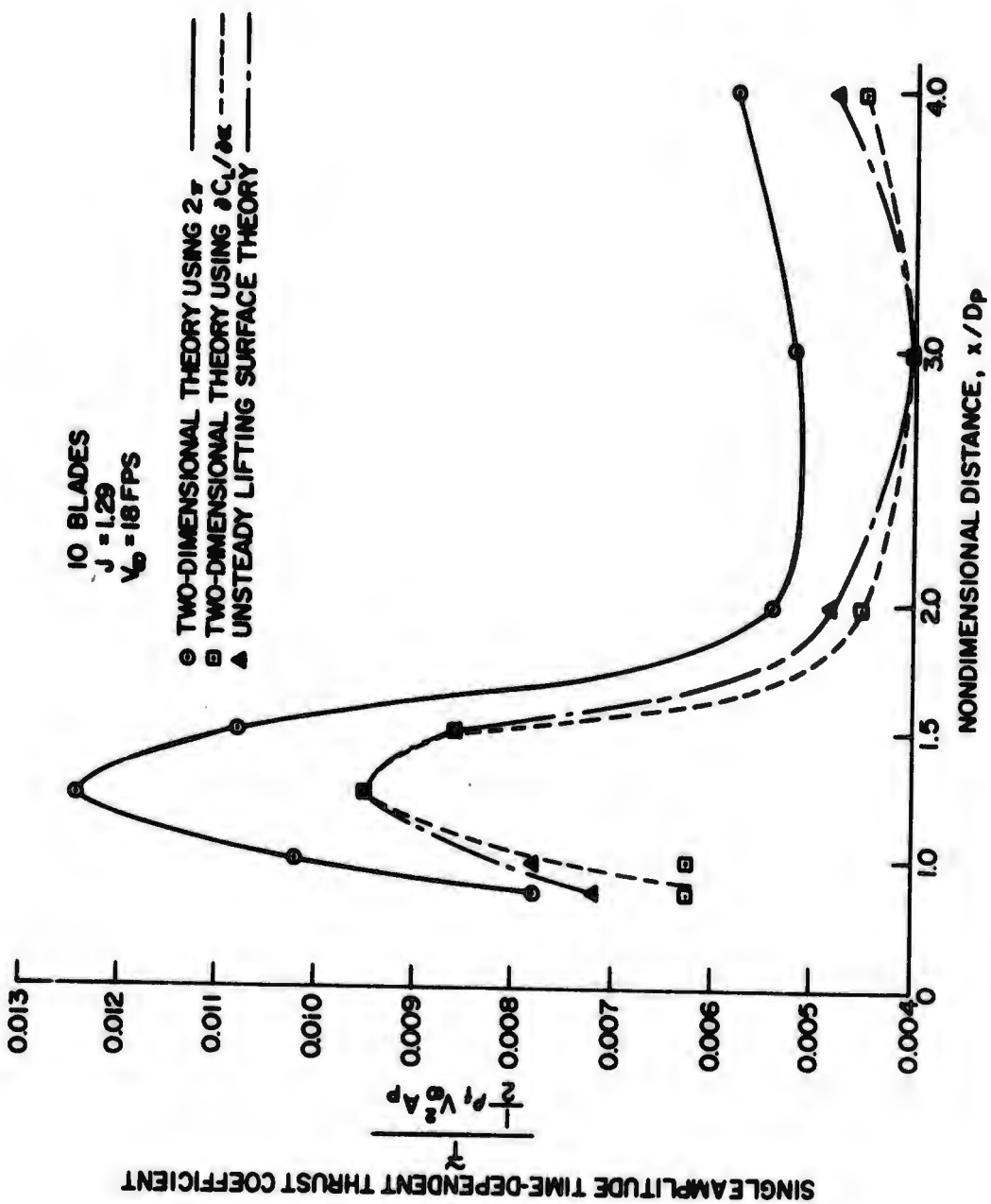

Figure 39 - Time-Dependent Thrust Coefficient versus Nondimensional Strut Distance (10 Blades, J=1.29)

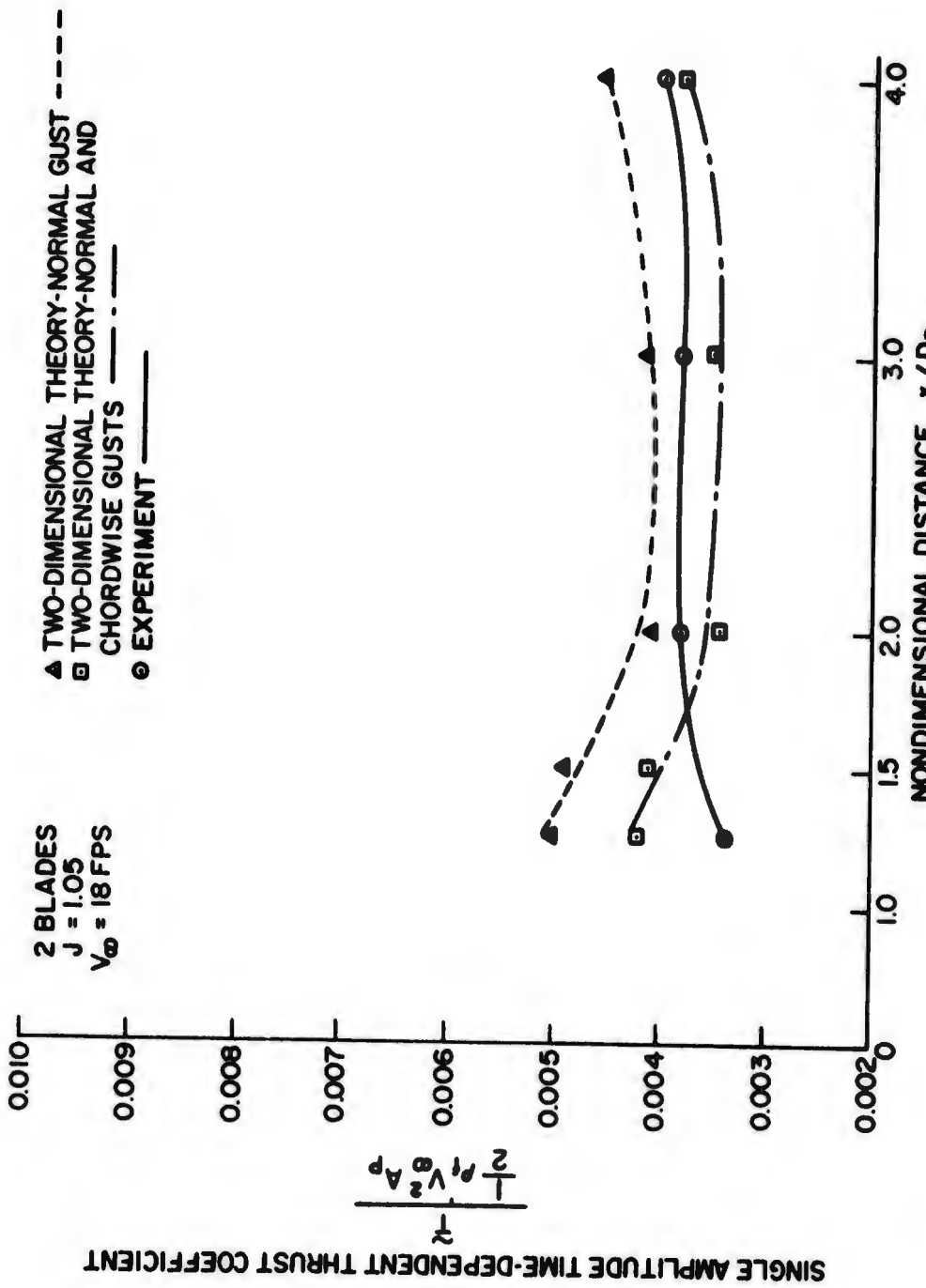

Figure 40 - Time-Dependent Thrust Coefficient versus Nondimensional Strut Distance (2 Blades, J=1.05)

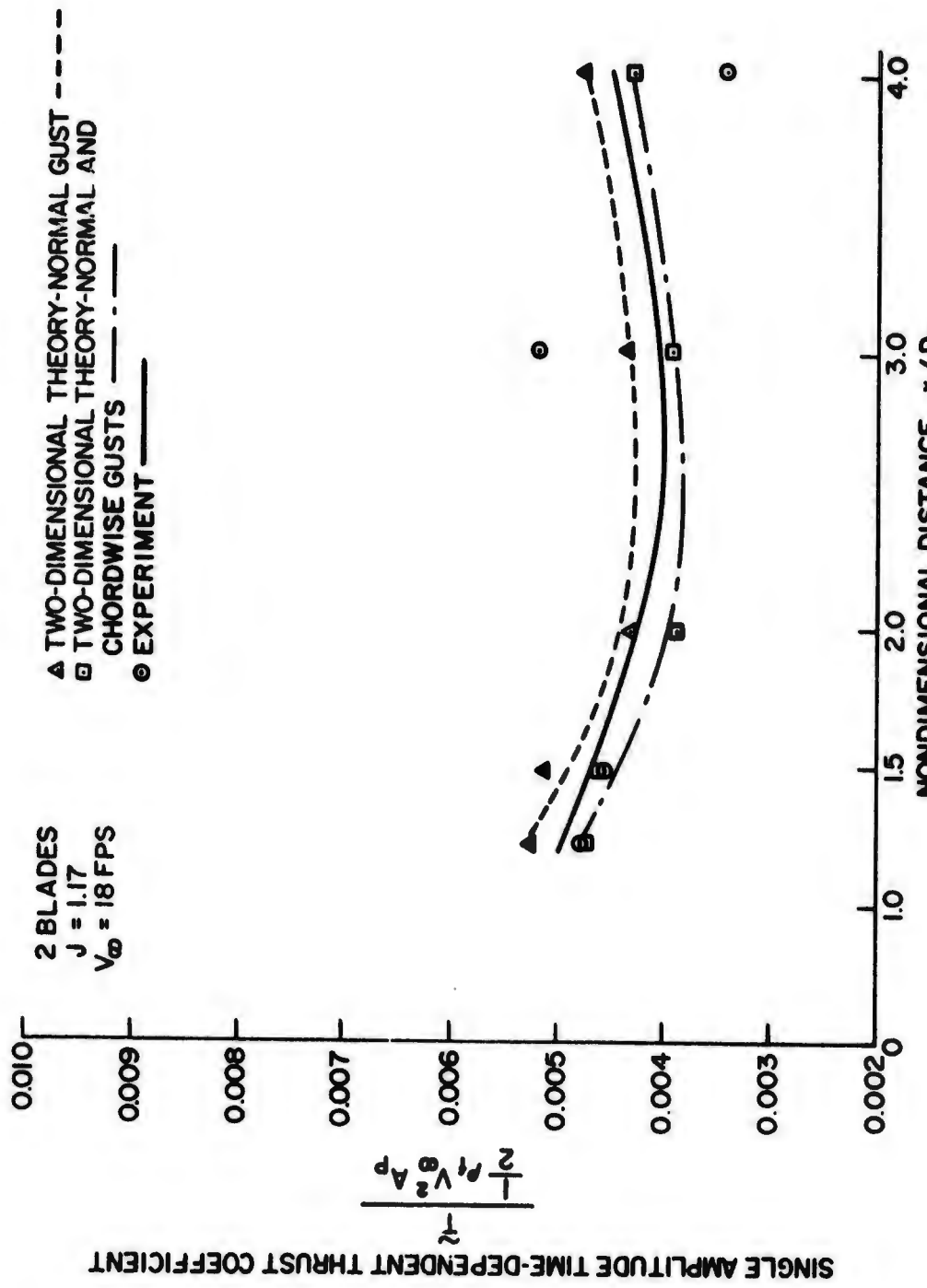

Figure 41 - Time-Dependent Thrust Coefficient versus Nondimensional Strut Distance (2 Blades, J=1.17)

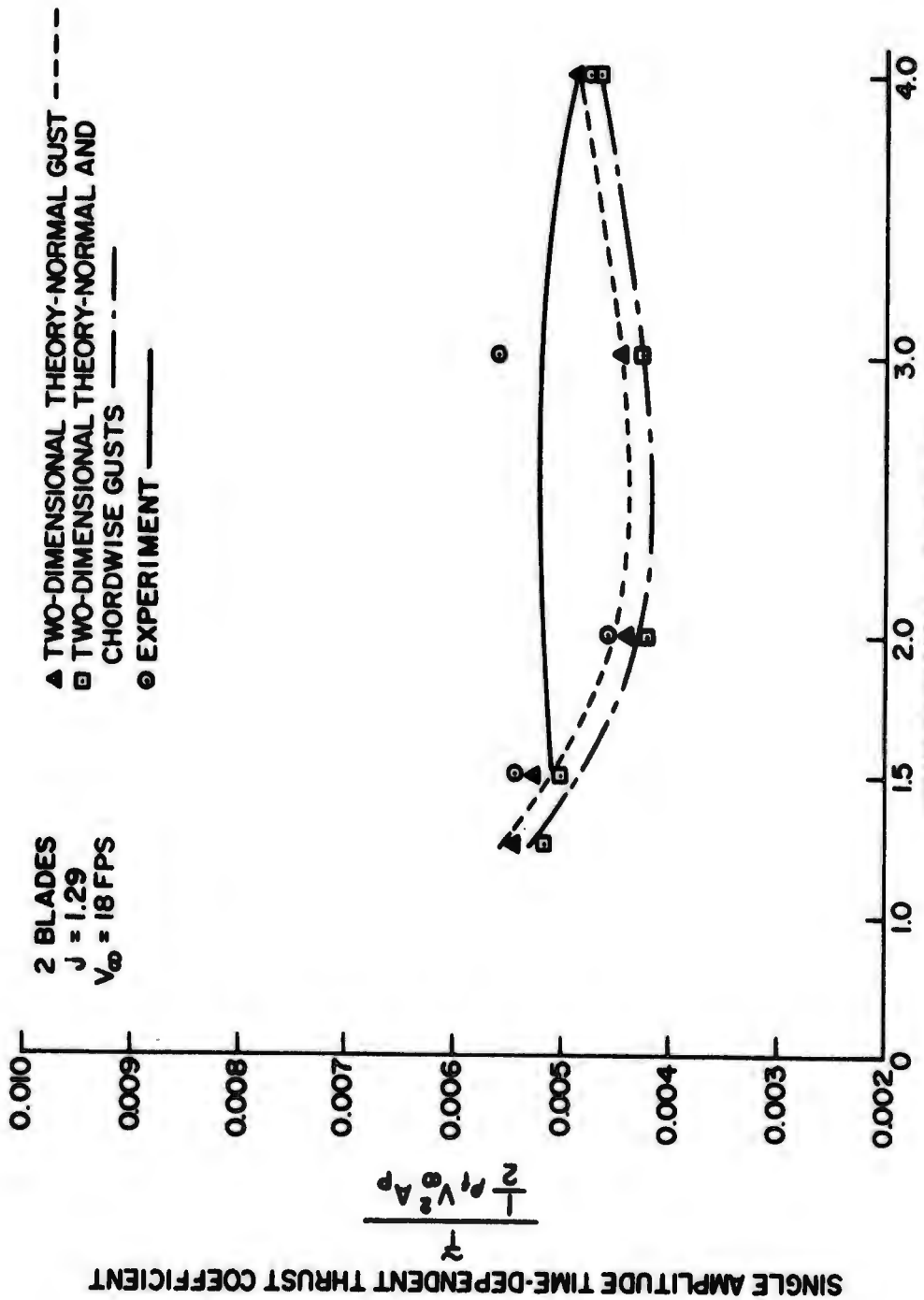

Figure 42 - Time-Dependent Thrust Coefficient versus Nondimensional Strut Distance (2 Blades, J=1.29)

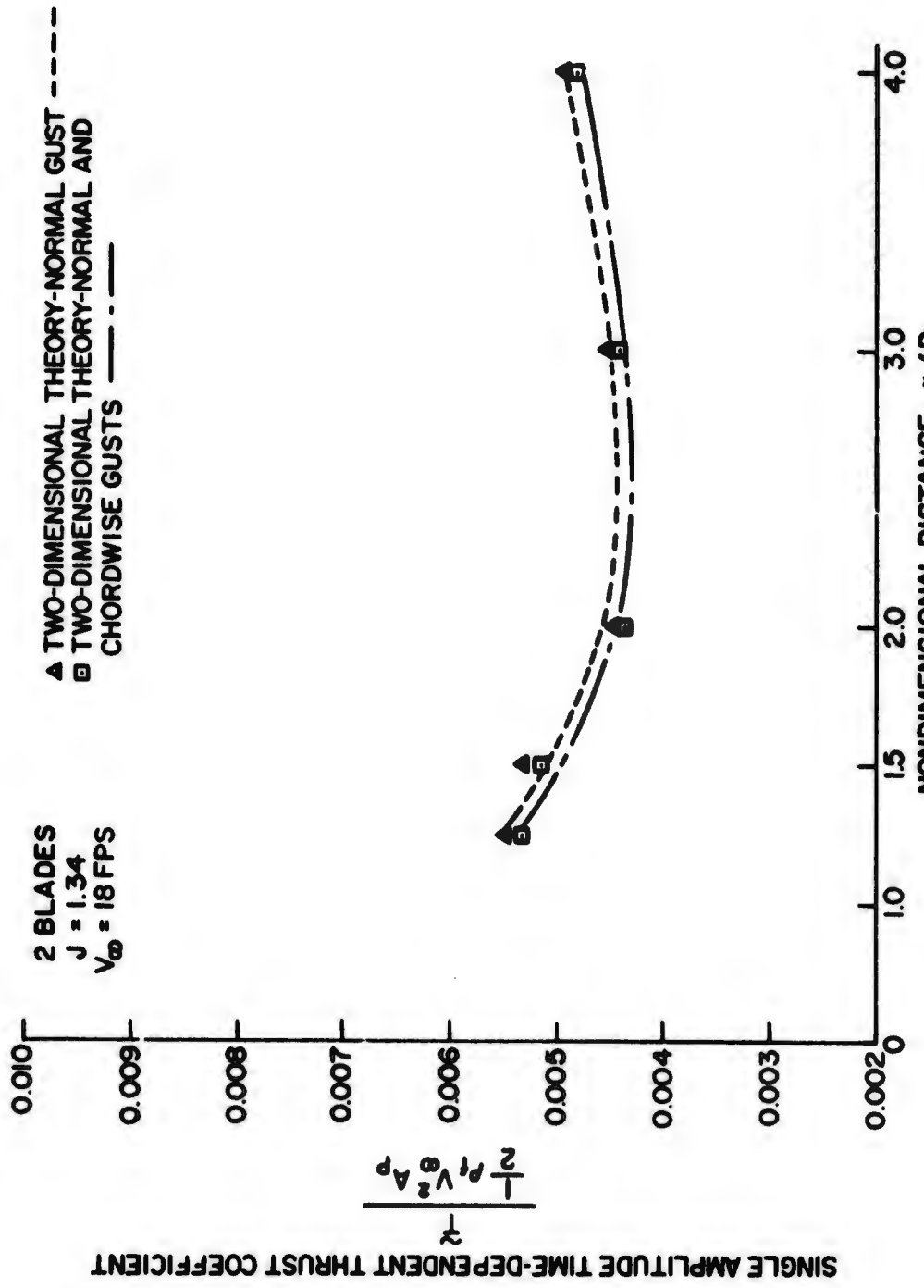

Figure 43 - Time-Dependent Thrust Coefficient versus Nondimensional Strut Distance (2 Blades, J=1.34)

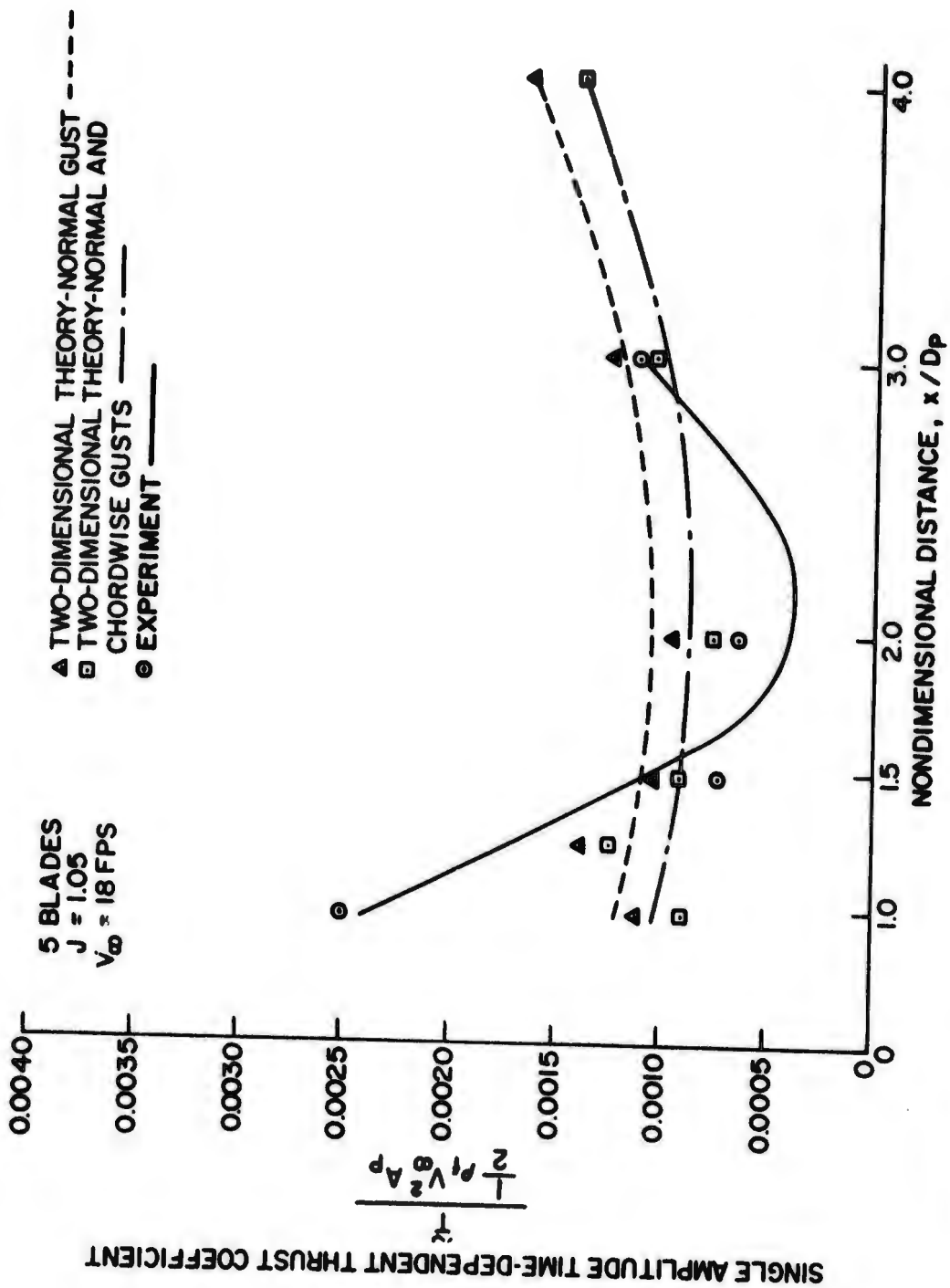

Figure 44 - Time-Dependent Thrust Coefficient versus Nondimensional Strut Distance (5 Blades, J=1.05)

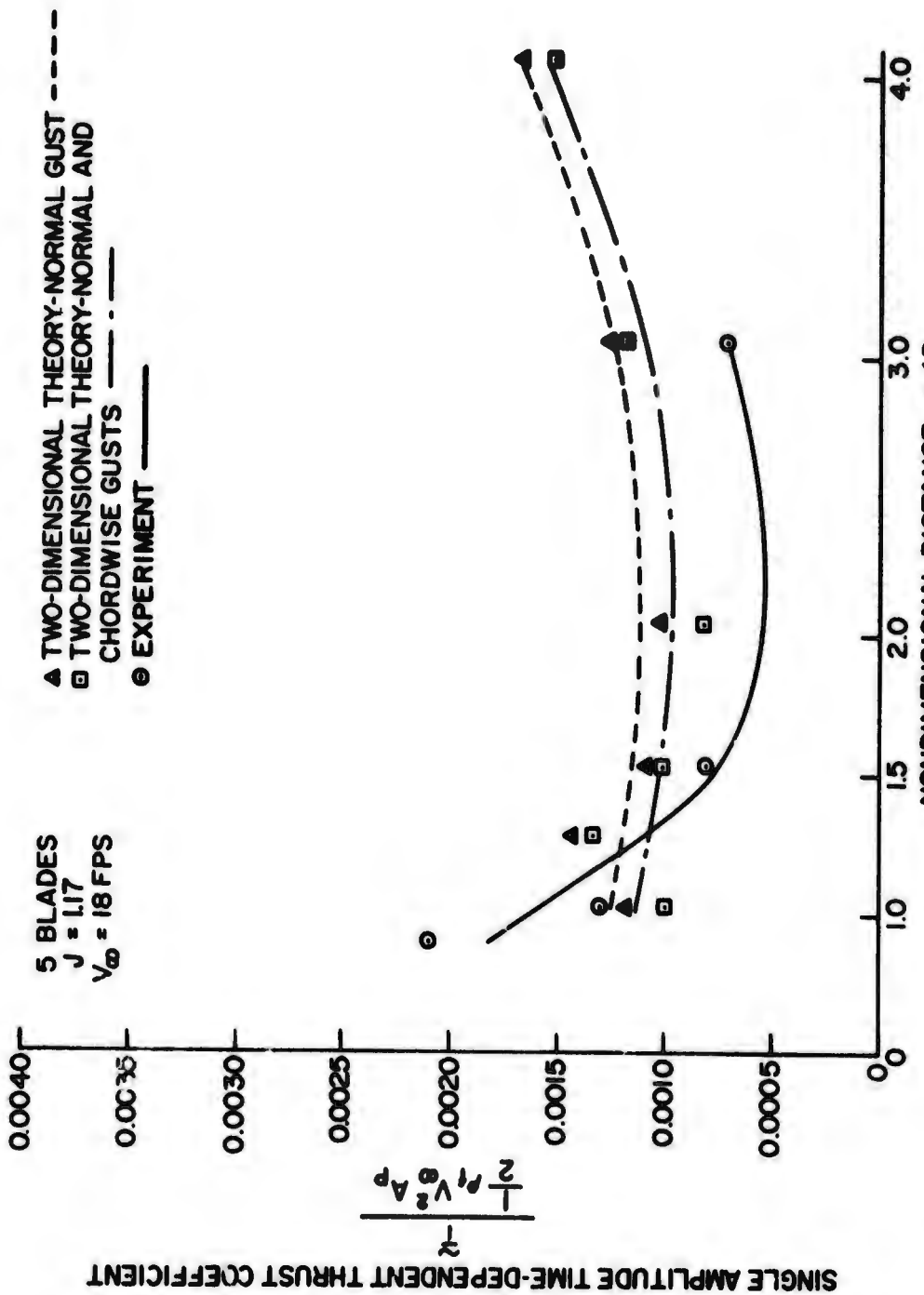

Figure 45 - Time-Dependent Thrust Coefficient versus Nondimensional Strut Distance (5 Blades, J=1.17)

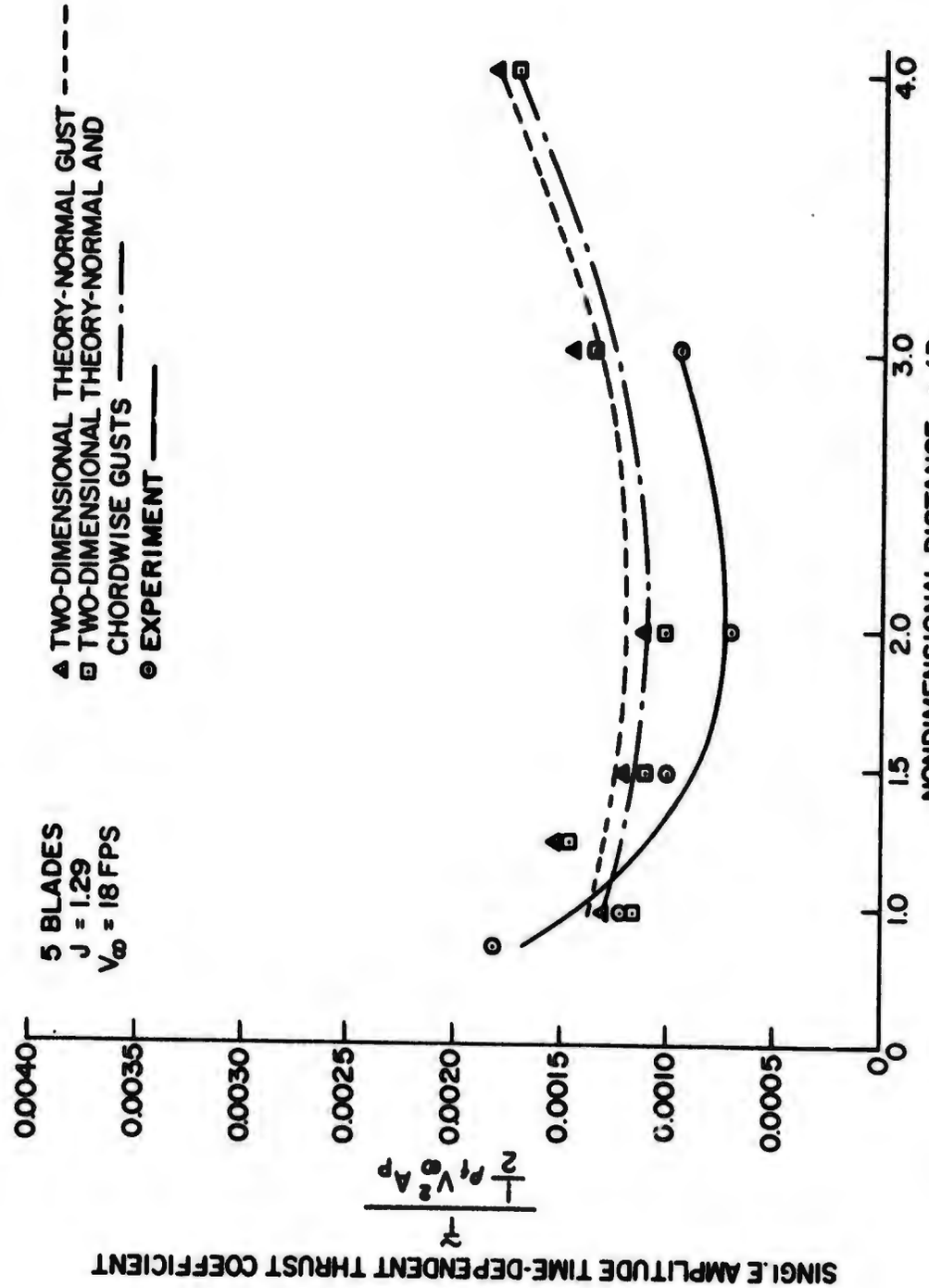

Figure 46 - Time-Dependent Thrust Coefficient versus Nondimensional Strut Distance (5 Blades, J=1.29)

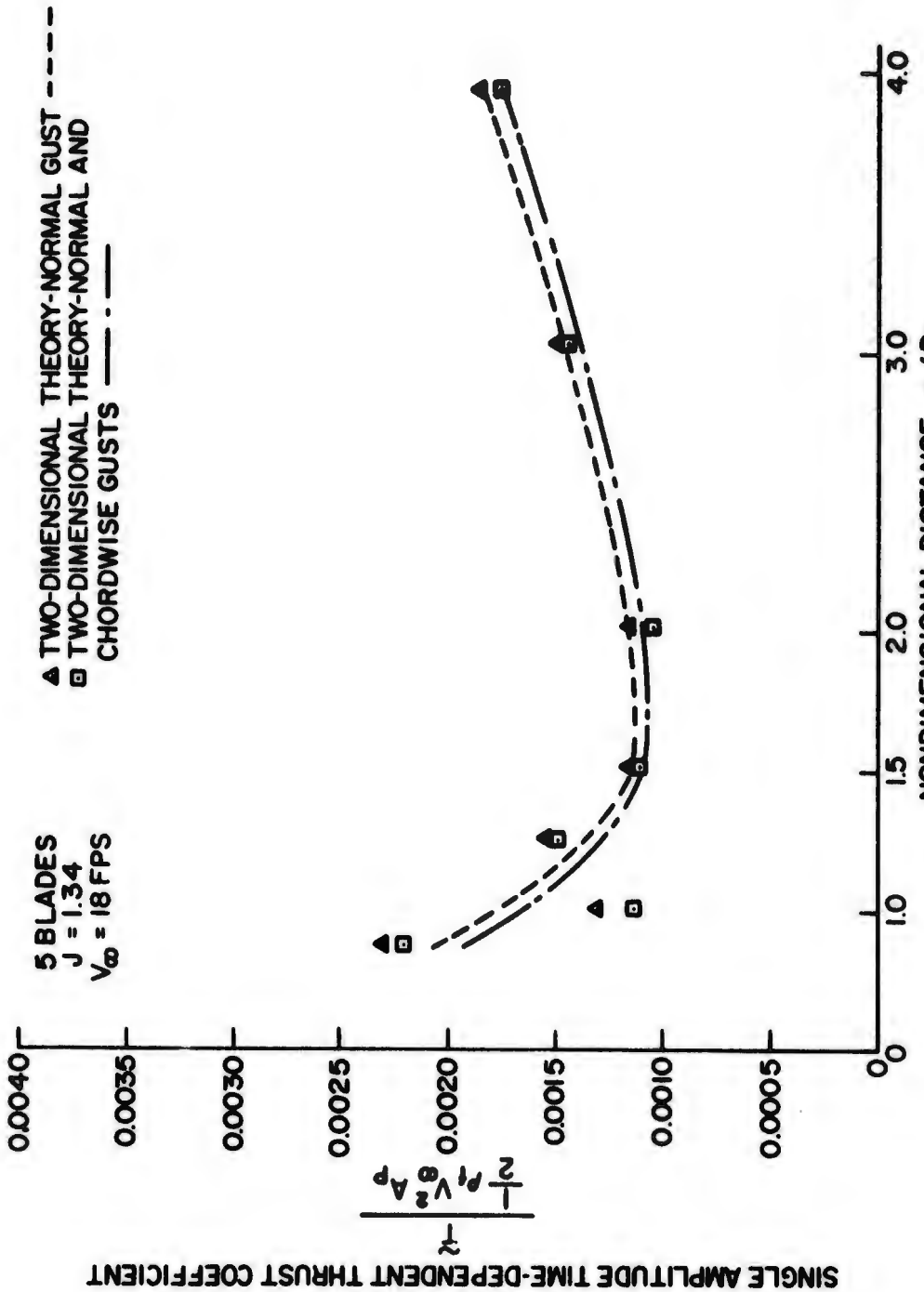

Figure 47 - Time-Dependent Thrust Coefficient versus Nondimensional Strut Distance (5 Blades, J=1.34)

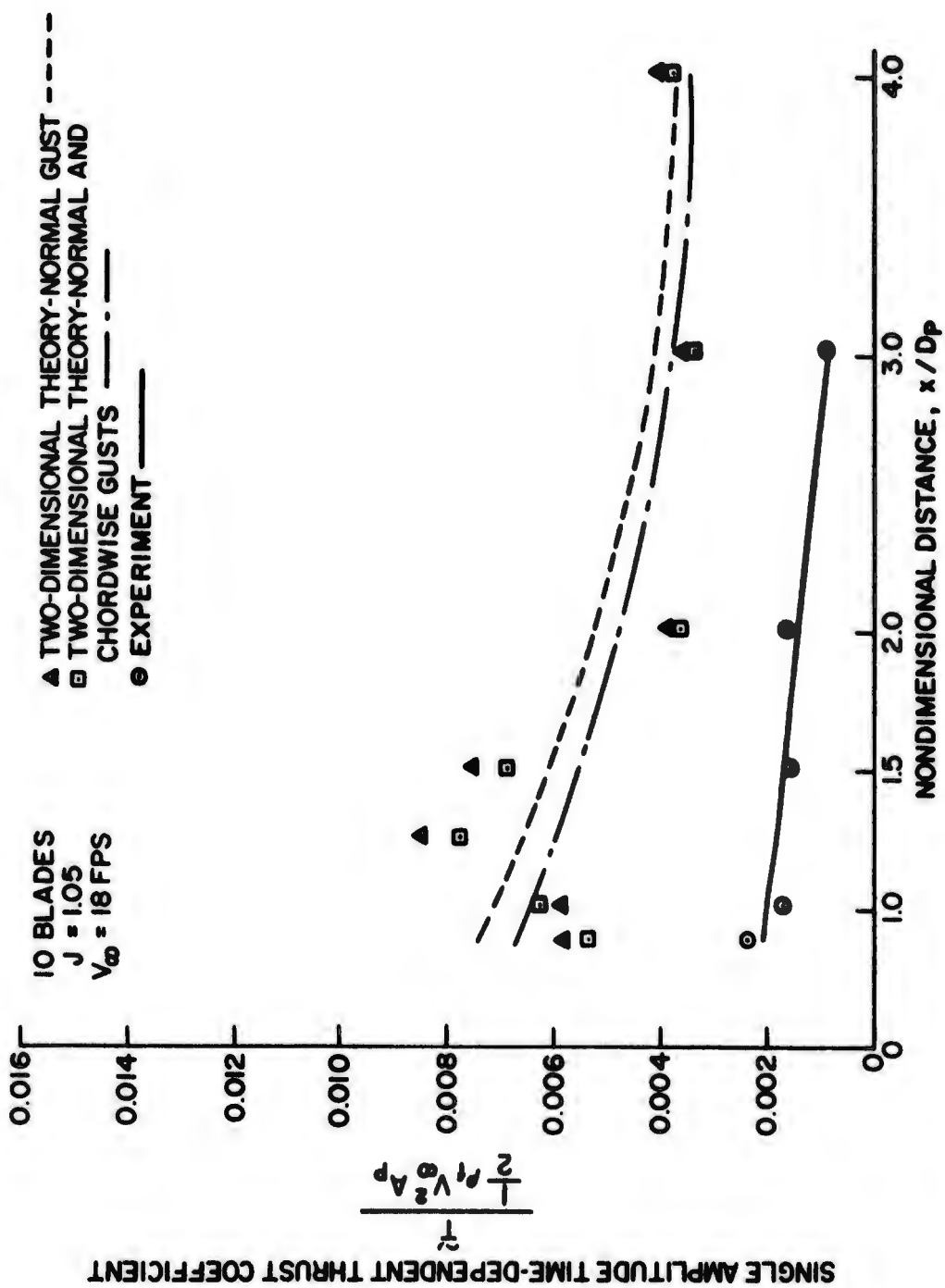

Figure 48 - Time-Dependent Thrust Coefficient versus Nondimensional Strut Distance (10 Blades, J=1.05)

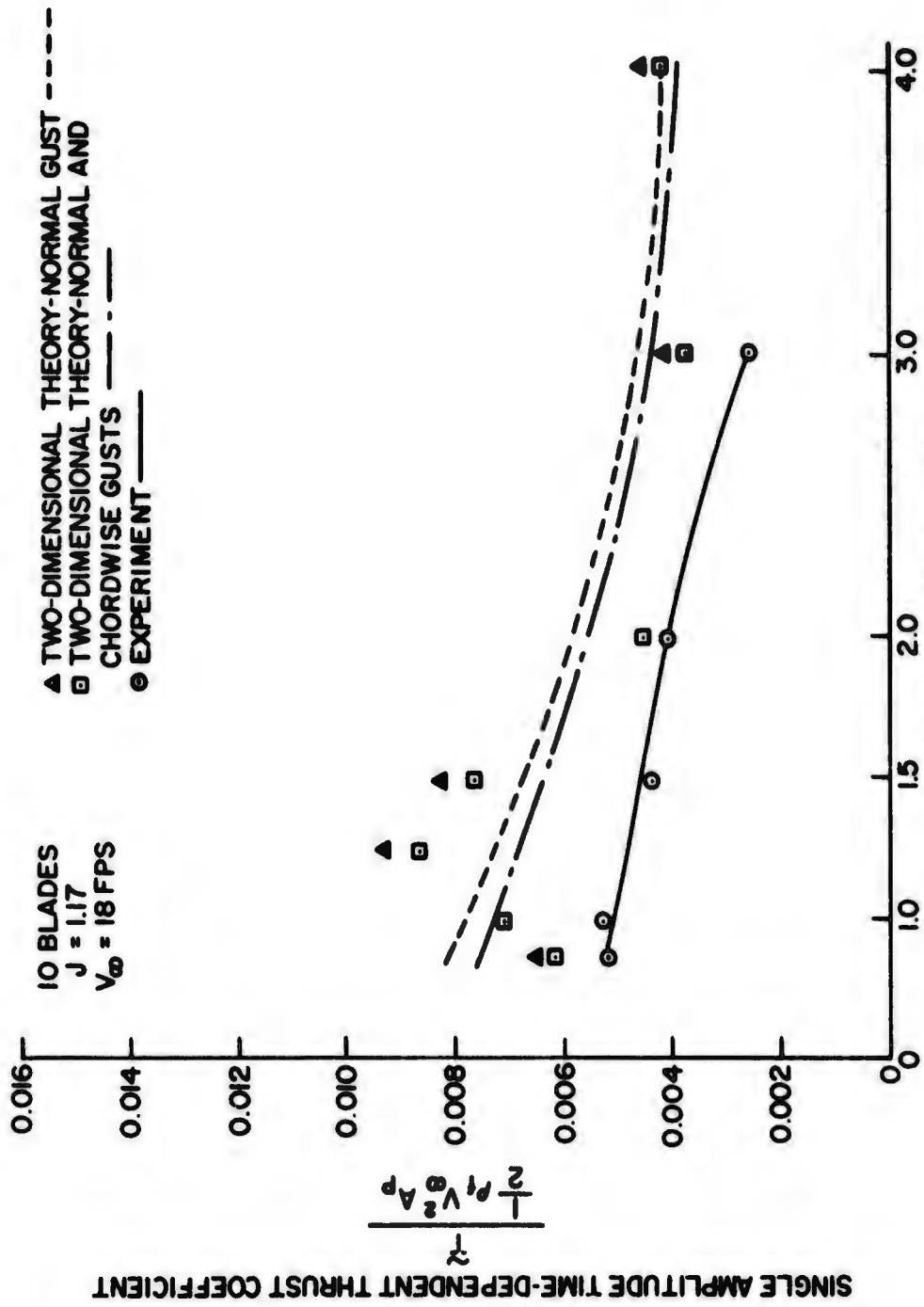

Figure 49 - Time-Dependent Thrust Coefficient versus Nondimensional Strut Distance (10 Blades, J=1.17)

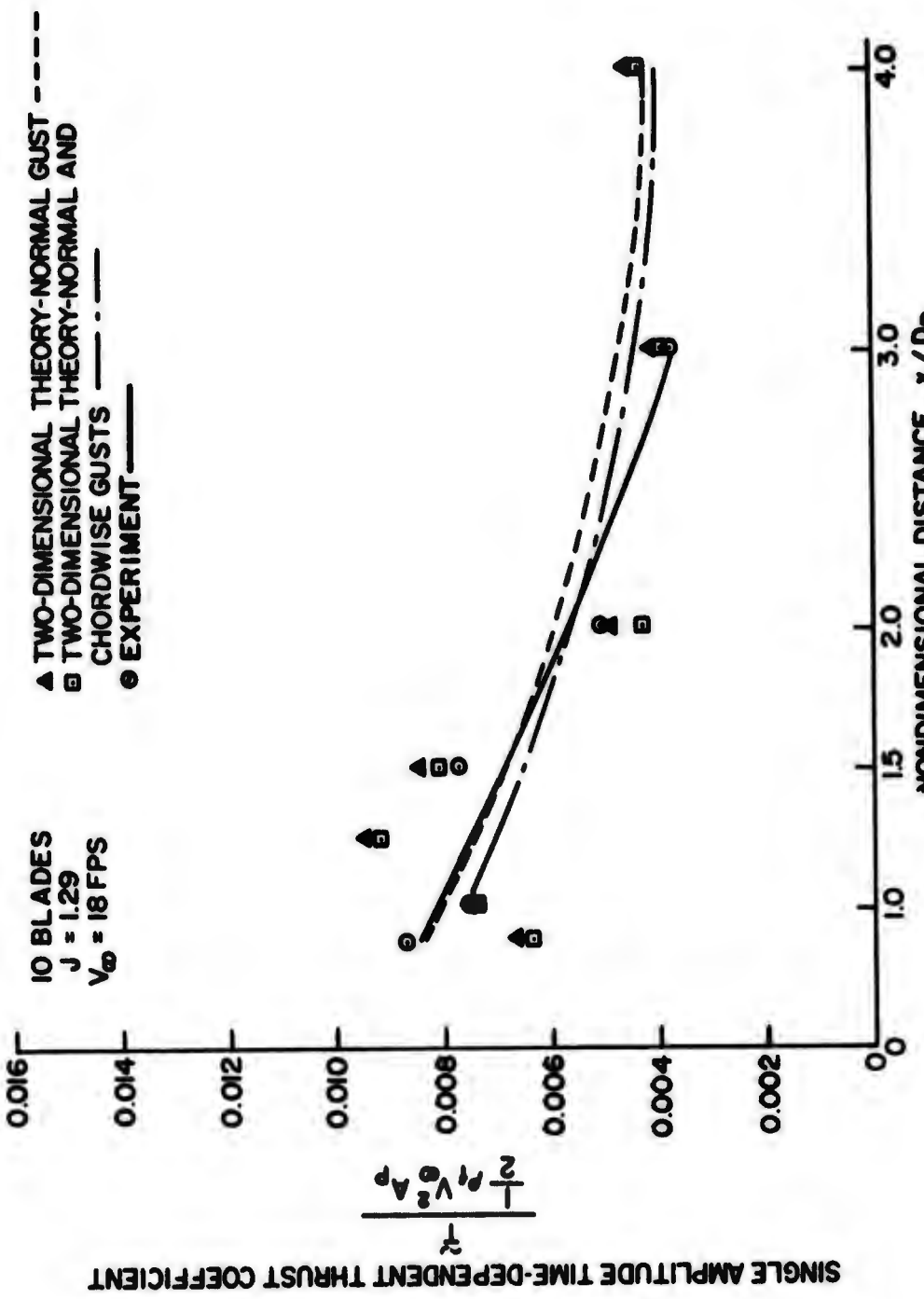

Figure 50 - Time-Dependent Thrust Coefficient versus Nondimensional Strut Distance (10 Blades, J=1.29)

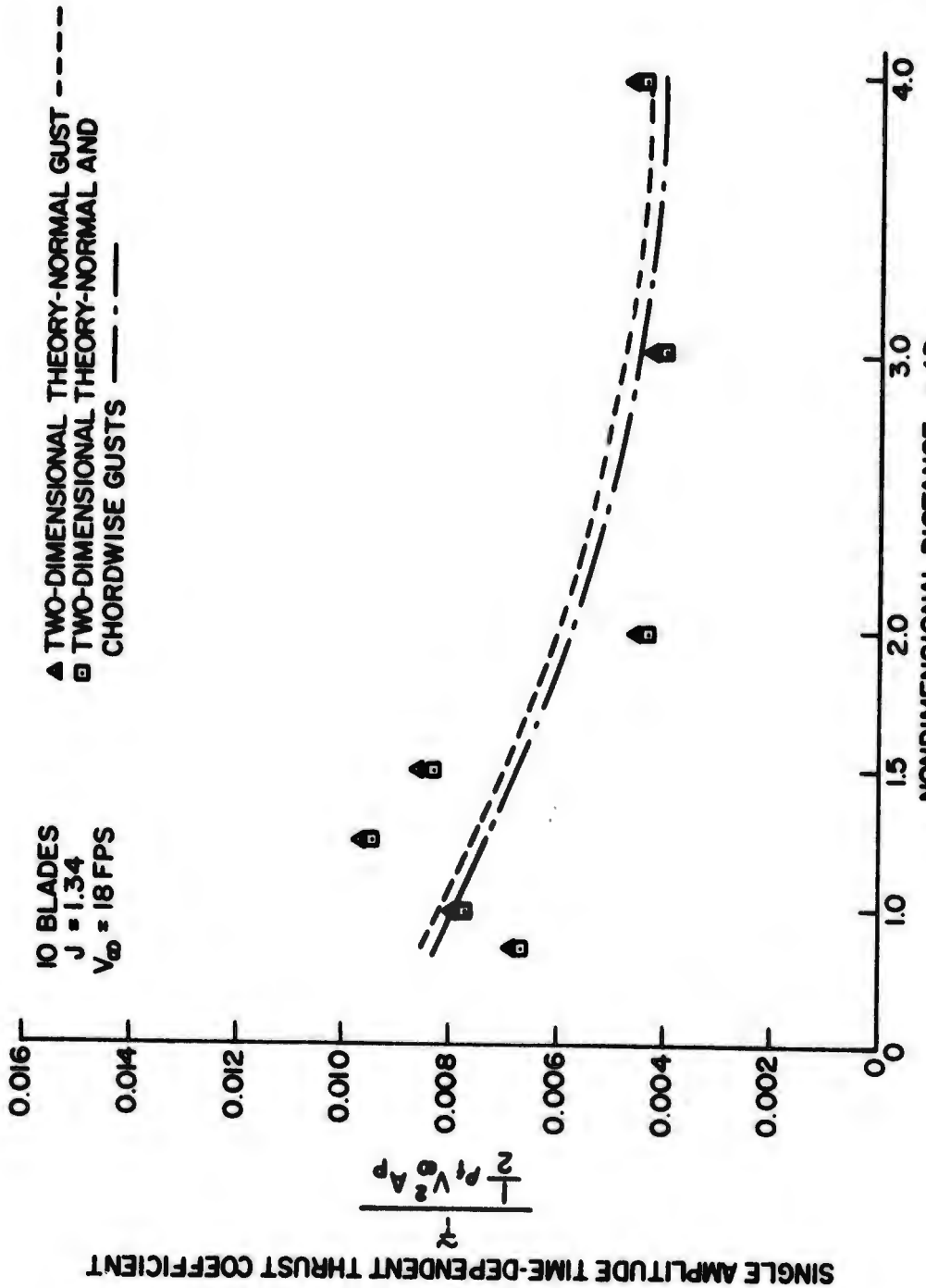

Figure 51 - Time-Dependent Thrust Coefficient versus Nondimensional Strut Distance (10 Blades, J=1.34)

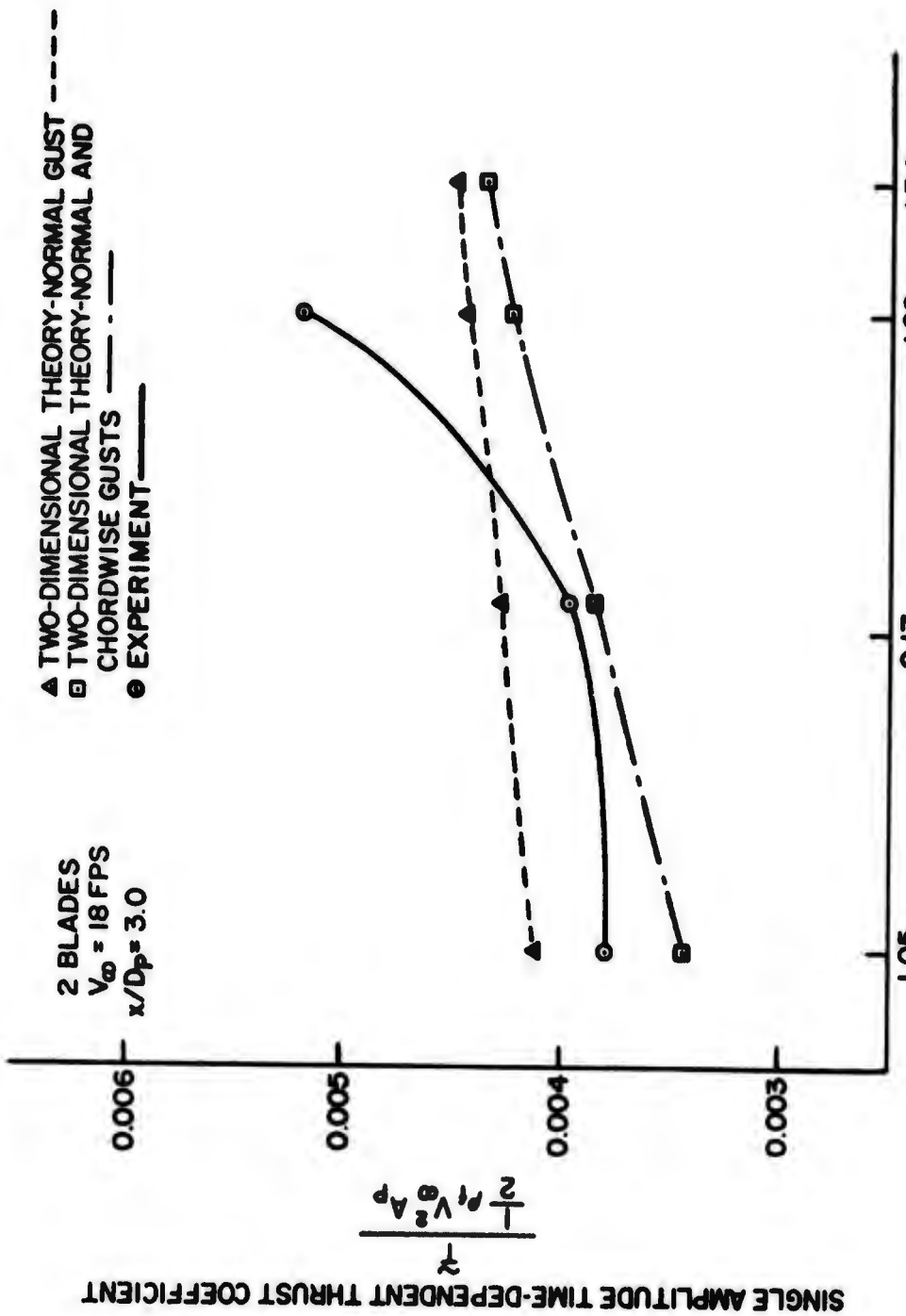

Figure 52 - Time-Dependent Thrust Coefficient versus Advance Ratio (2 Blades, $x/D_p = 3.0$)

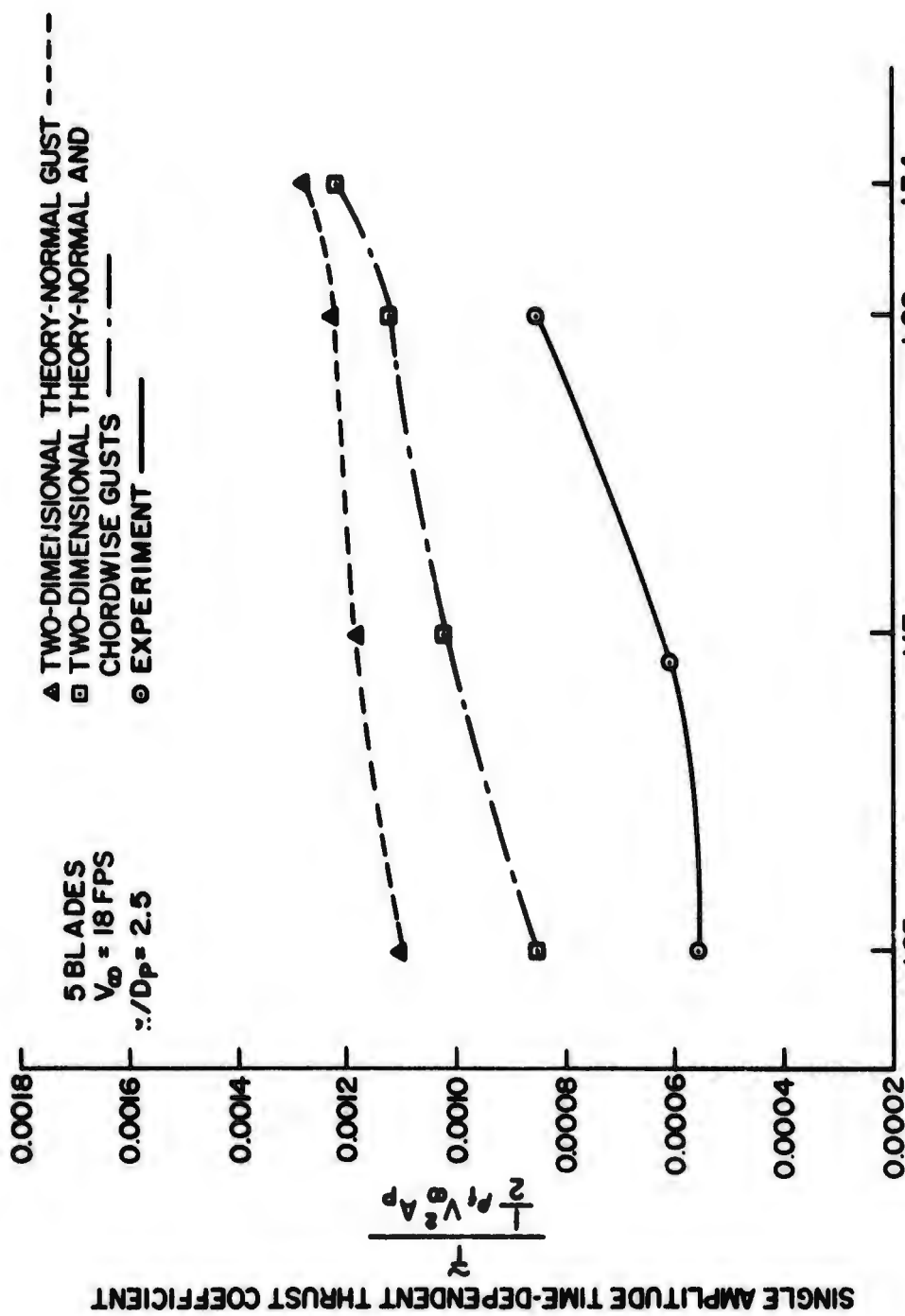

Figure 53 - Time-Dependent Thrust Coefficient versus Advance Ratio (5 Blades, x/D_p=2.5)

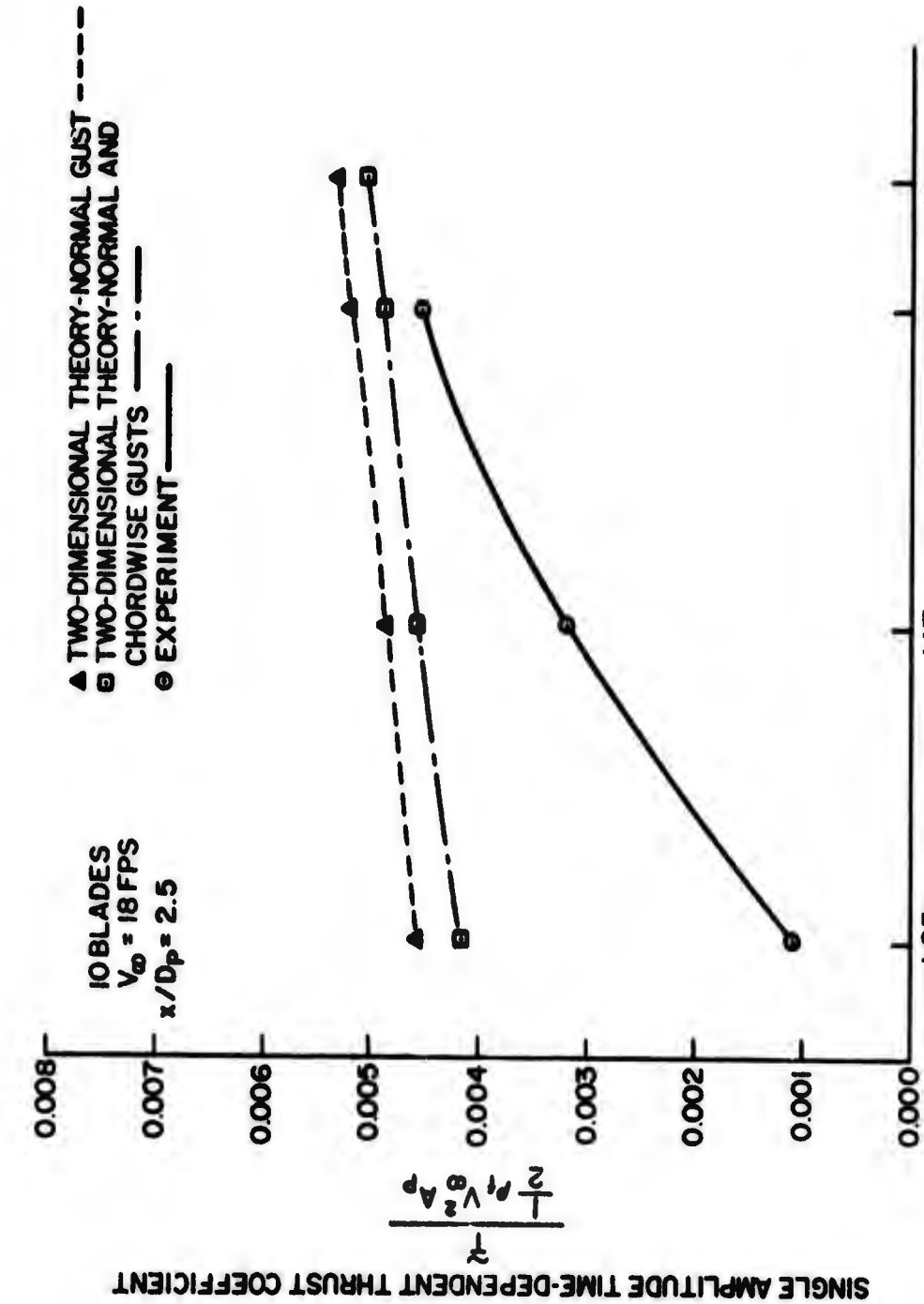

Figure 54 - Time-Dependent Thrust Coefficient versus Advance Ratio (10 Blades, x/D_p=2.5)

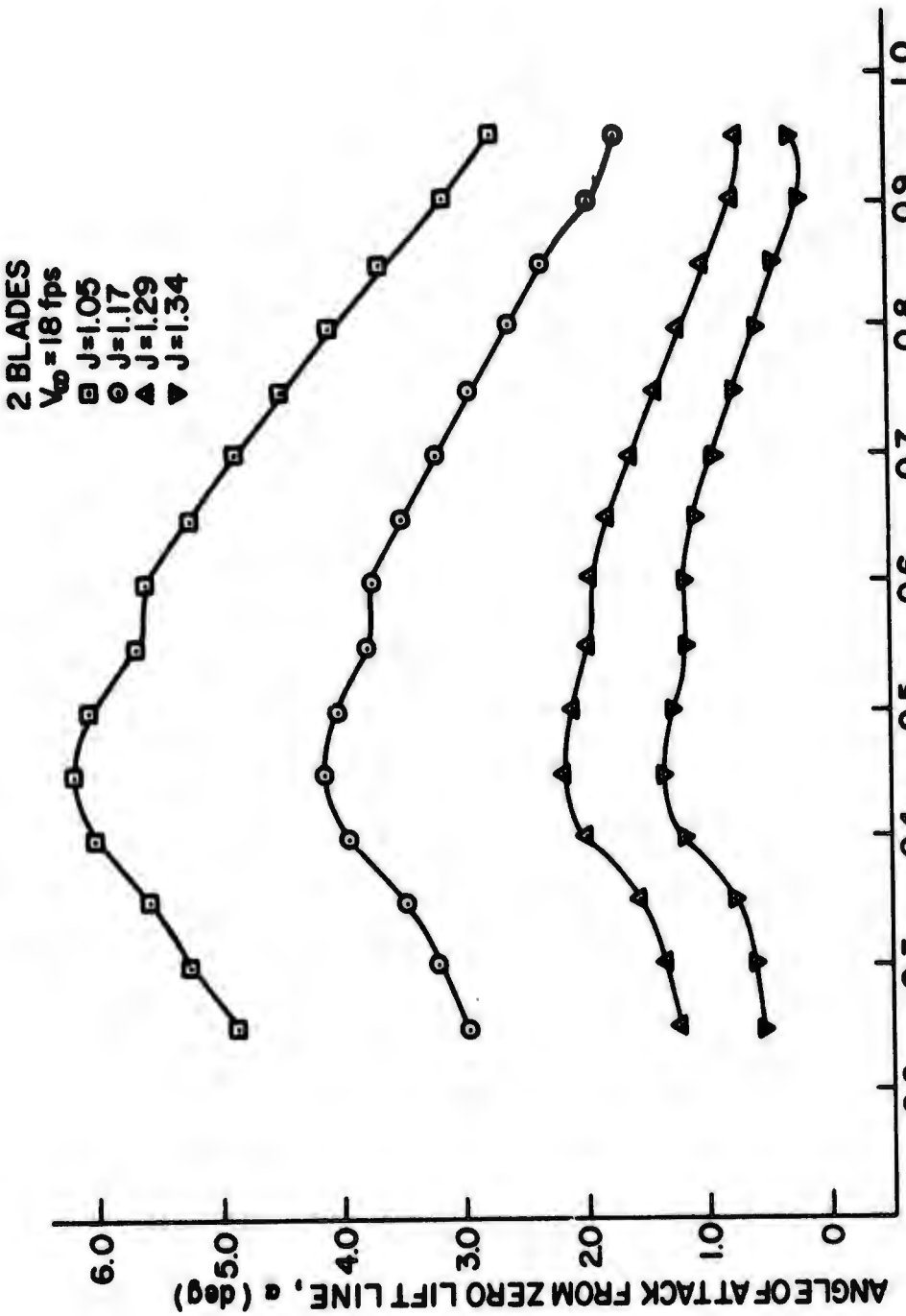

Figure 55 - Steady Angle of Attack, Measured from Zero Lift Line, versus Nondimensional Radius (2 Blades)

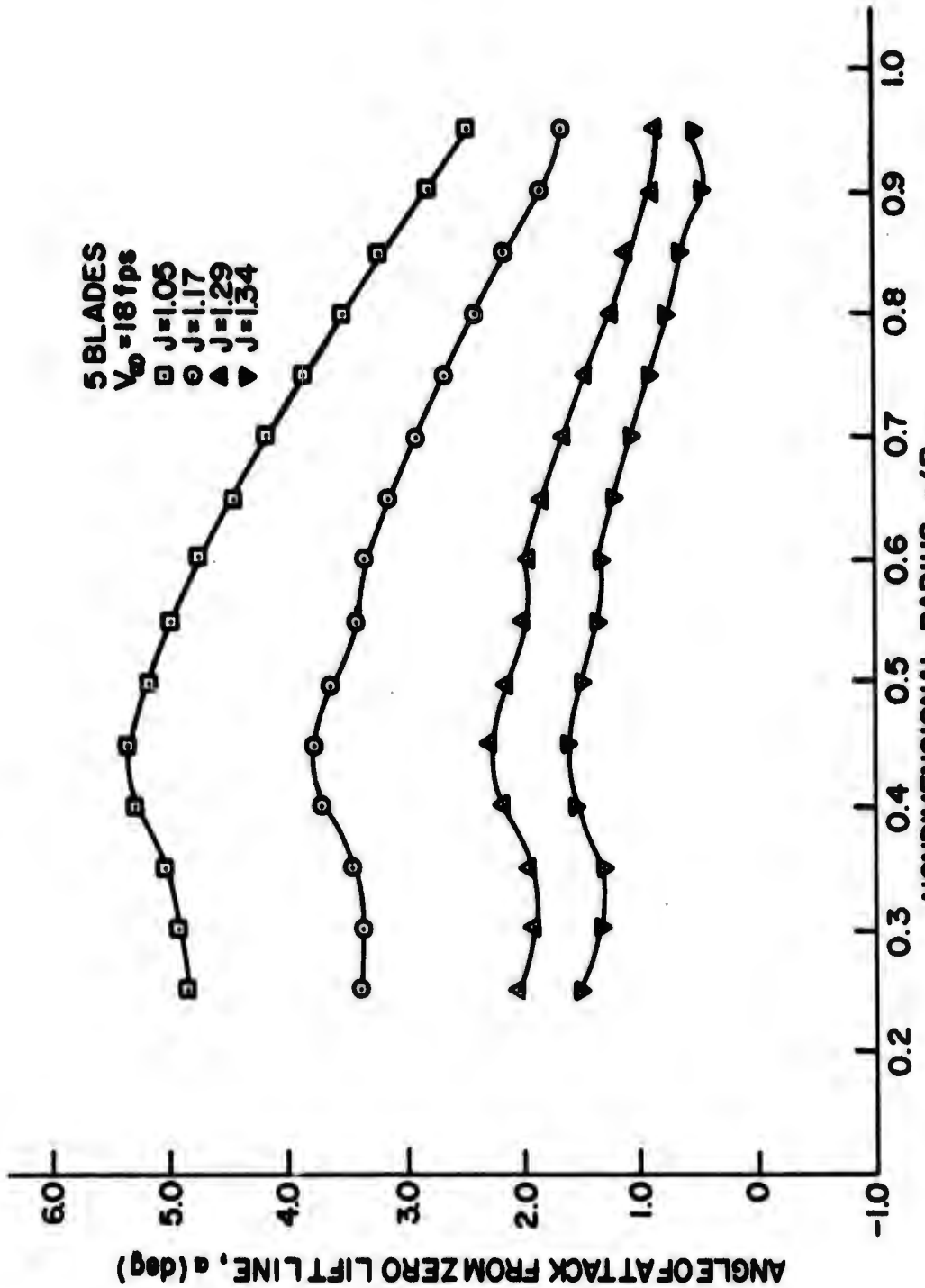

Figure 56 - Steady Angle of Attack, Measured from Zero Lift Line, versus Nondimensional Radius (5 Blades)

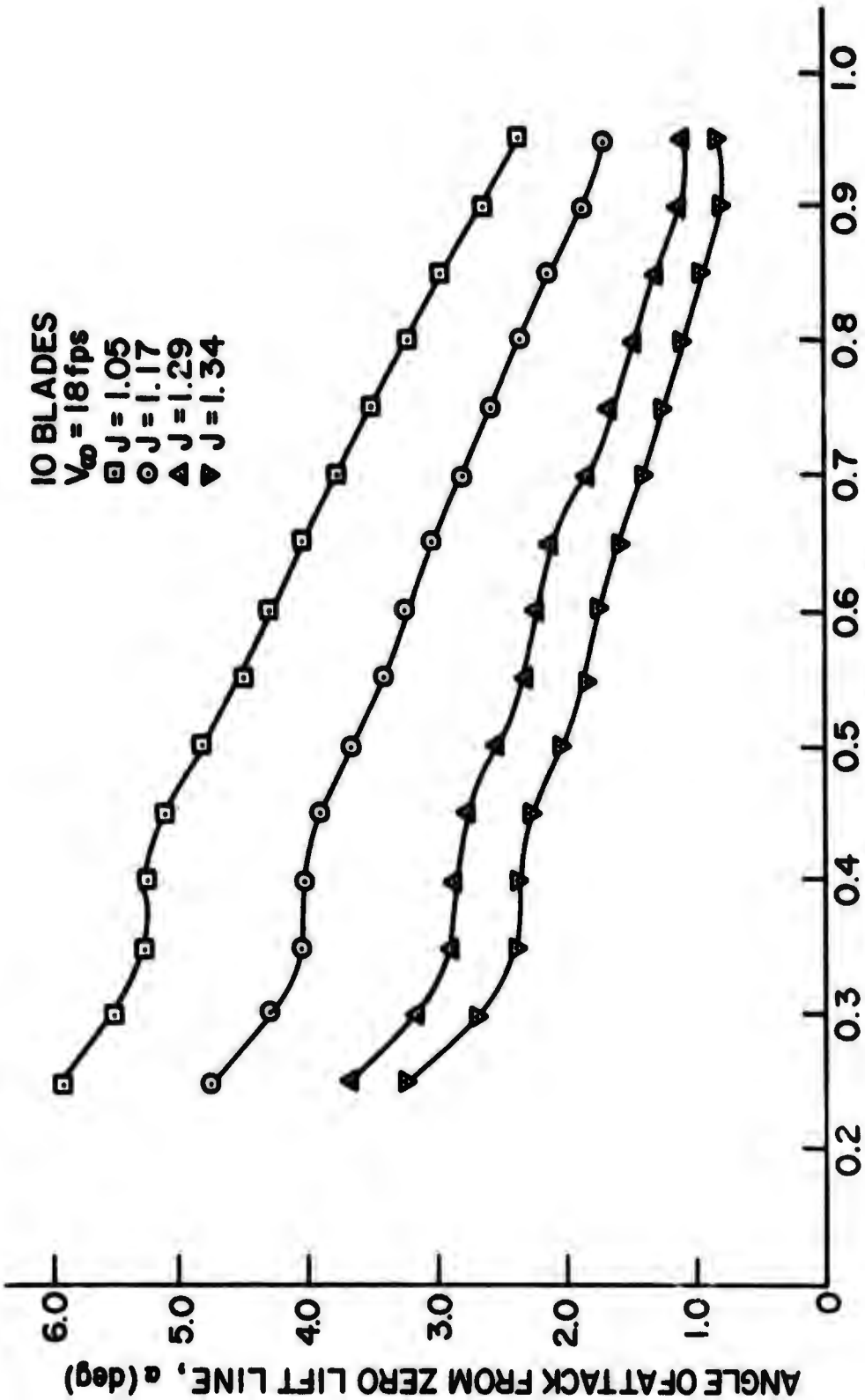

Figure 57 - Steady Angle of Attack, Measured from Zero Lift Line, versus Nondimensional Radius (10 Blades)

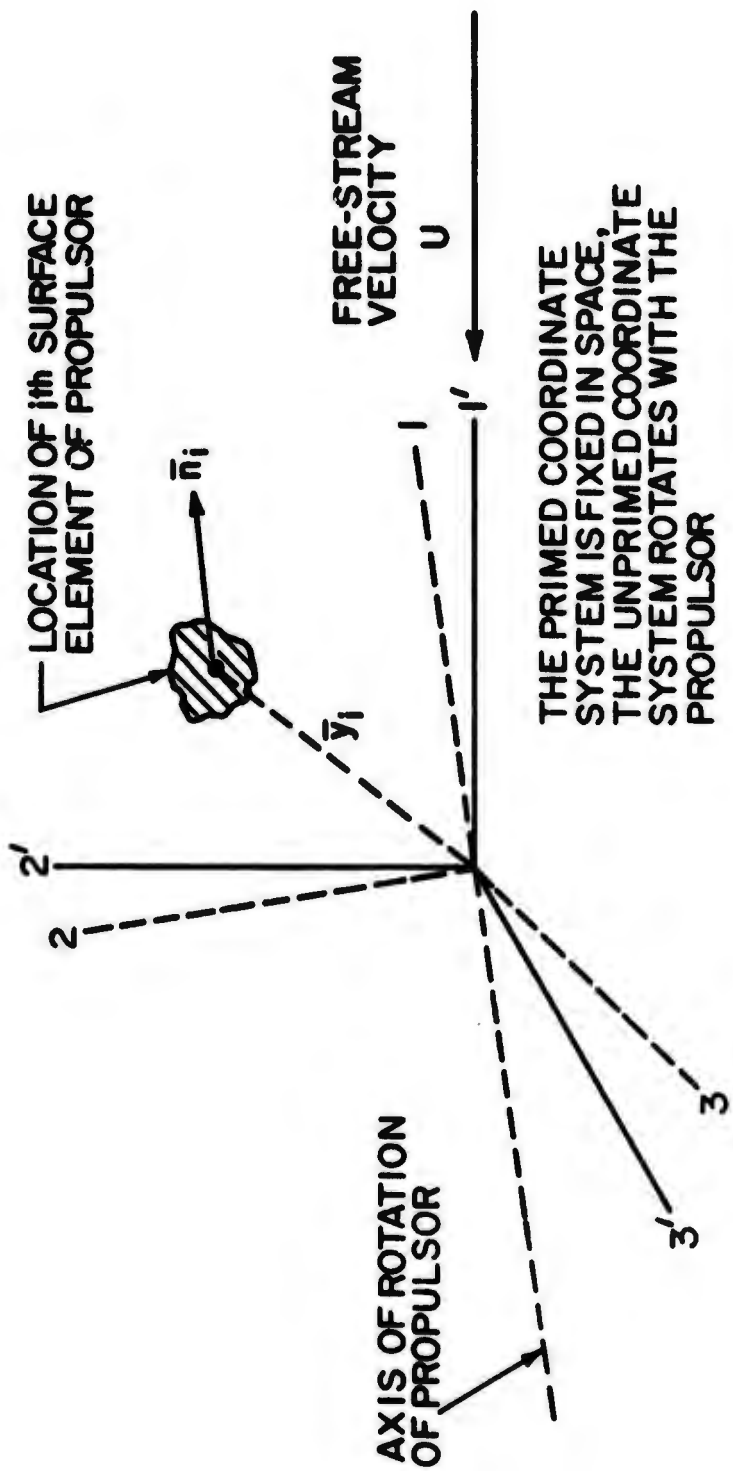

Figure 58 - Coordinate System Used for Calculation of Response to Turbulence

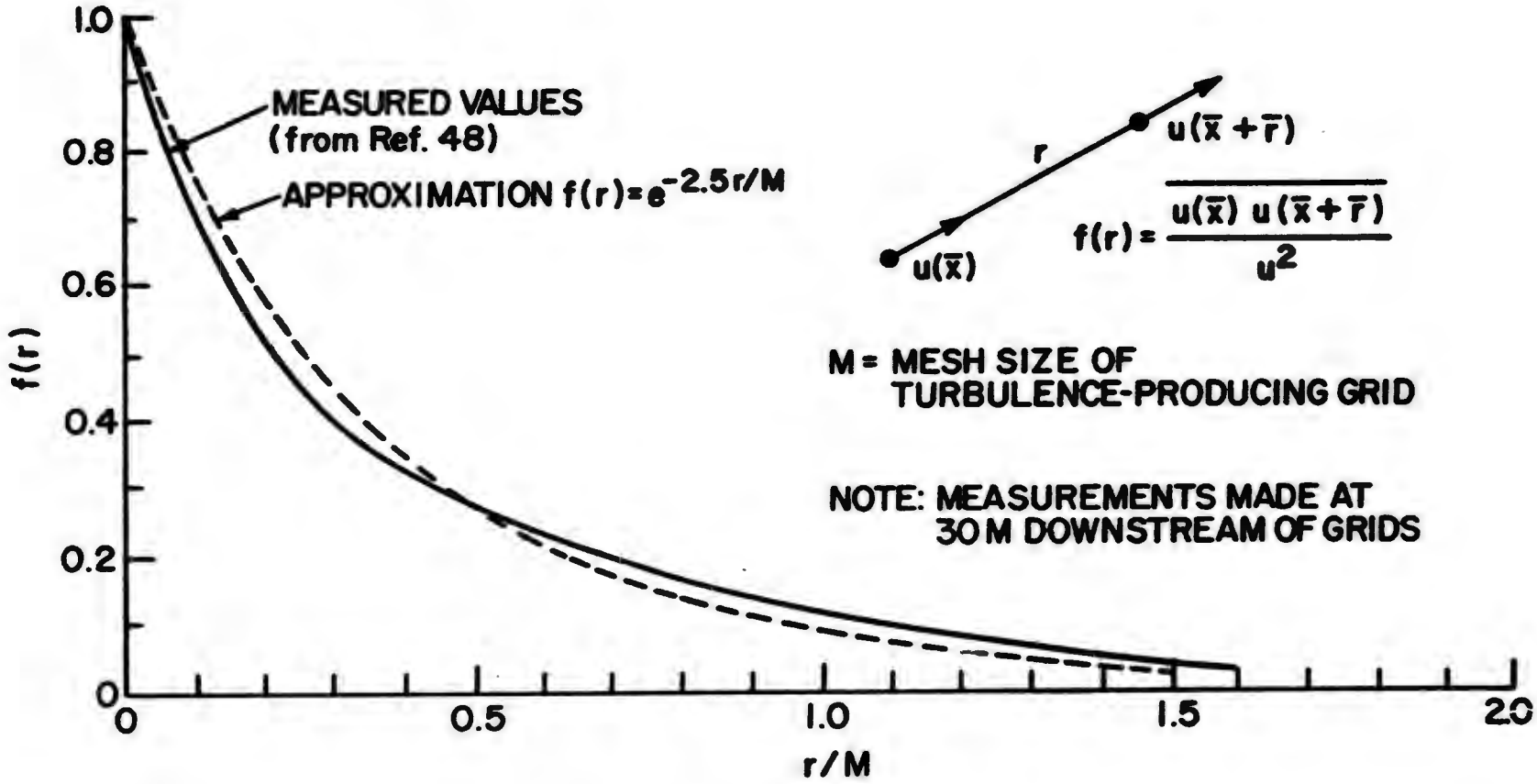

Figure 59 - Correlation Curve for Isotropic Turbulence

Source: Stewart, R. W., and Townsend, A. A. "Similarity and Self-Preservation in Isotropic Turbulence," Phil. Trans., Series A, Vol. 243, 1951, p. 359.

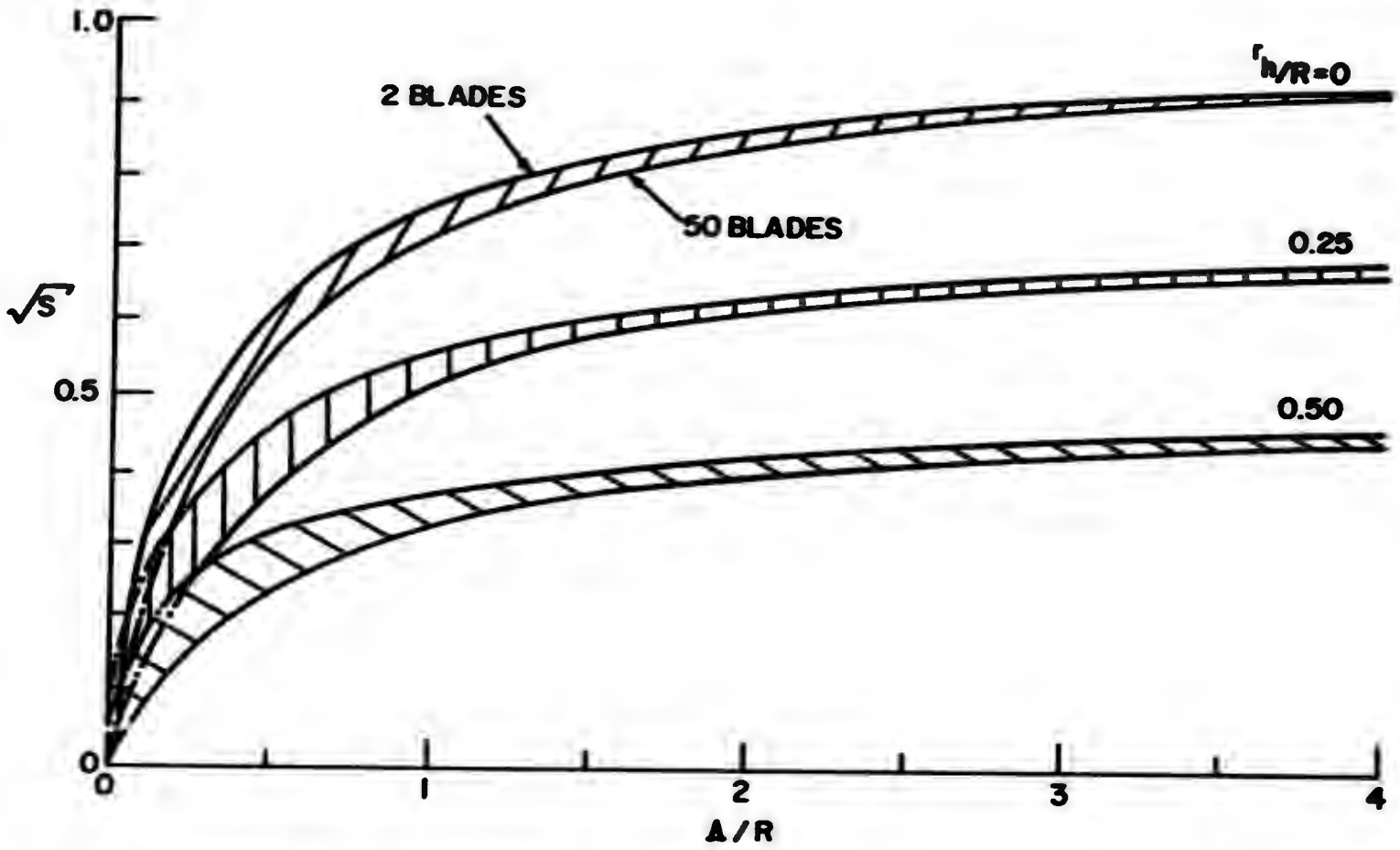

Figure 60 - The "Correlation Area" Function S(R/Λ) from Equation (47)

Source: Sevik, M. M., "The Response of a Propulsor to Random Velocity Fluctuations," ORL, Serial No. N00017-70-C-1407-2, April 30, 1970.

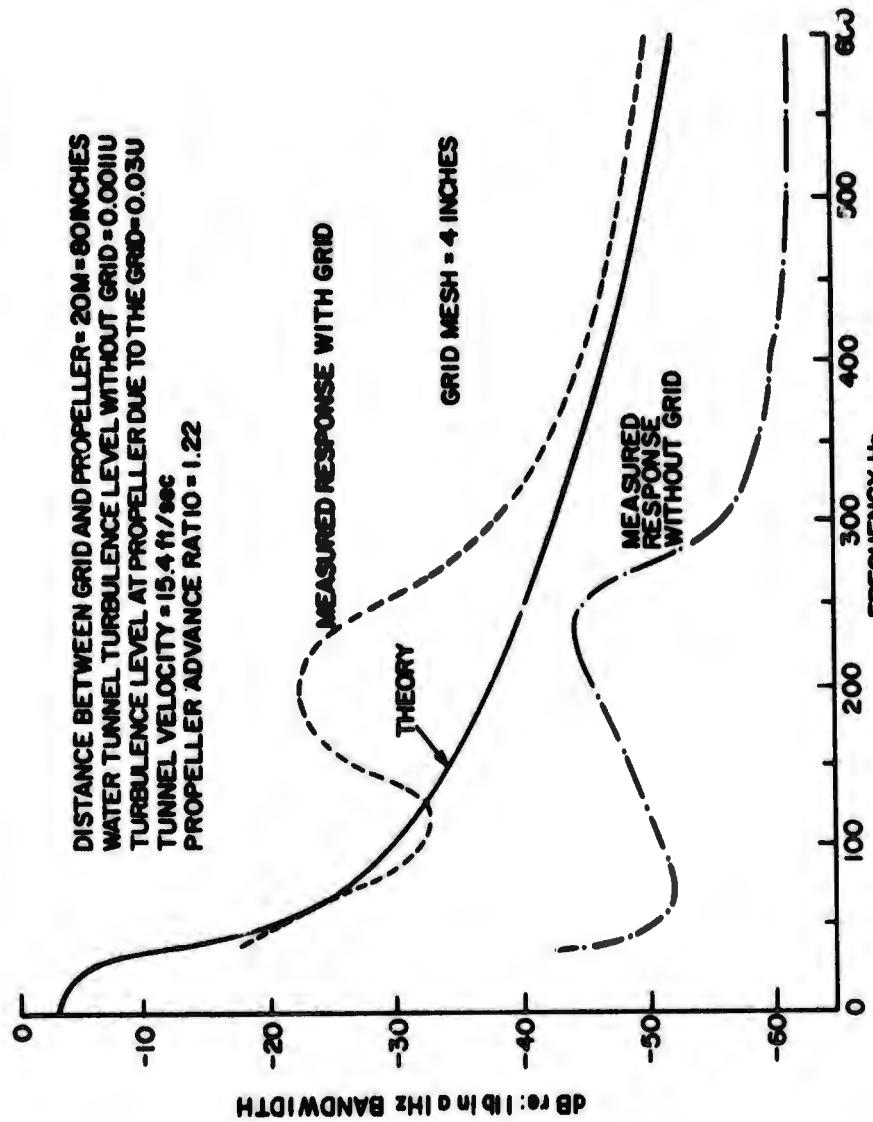

Figure 61 - Power Spectral Density of the Response of a Ten-Bladed Propeller to Turbulence Generated by a 4-inch Mesh Grid

Source: Sevik, M. M., "The Response of a Propulsor to Random Velocity Fluctuations," ORL, Serial No. N00017-70-C-1407-2, April 30, 1970.

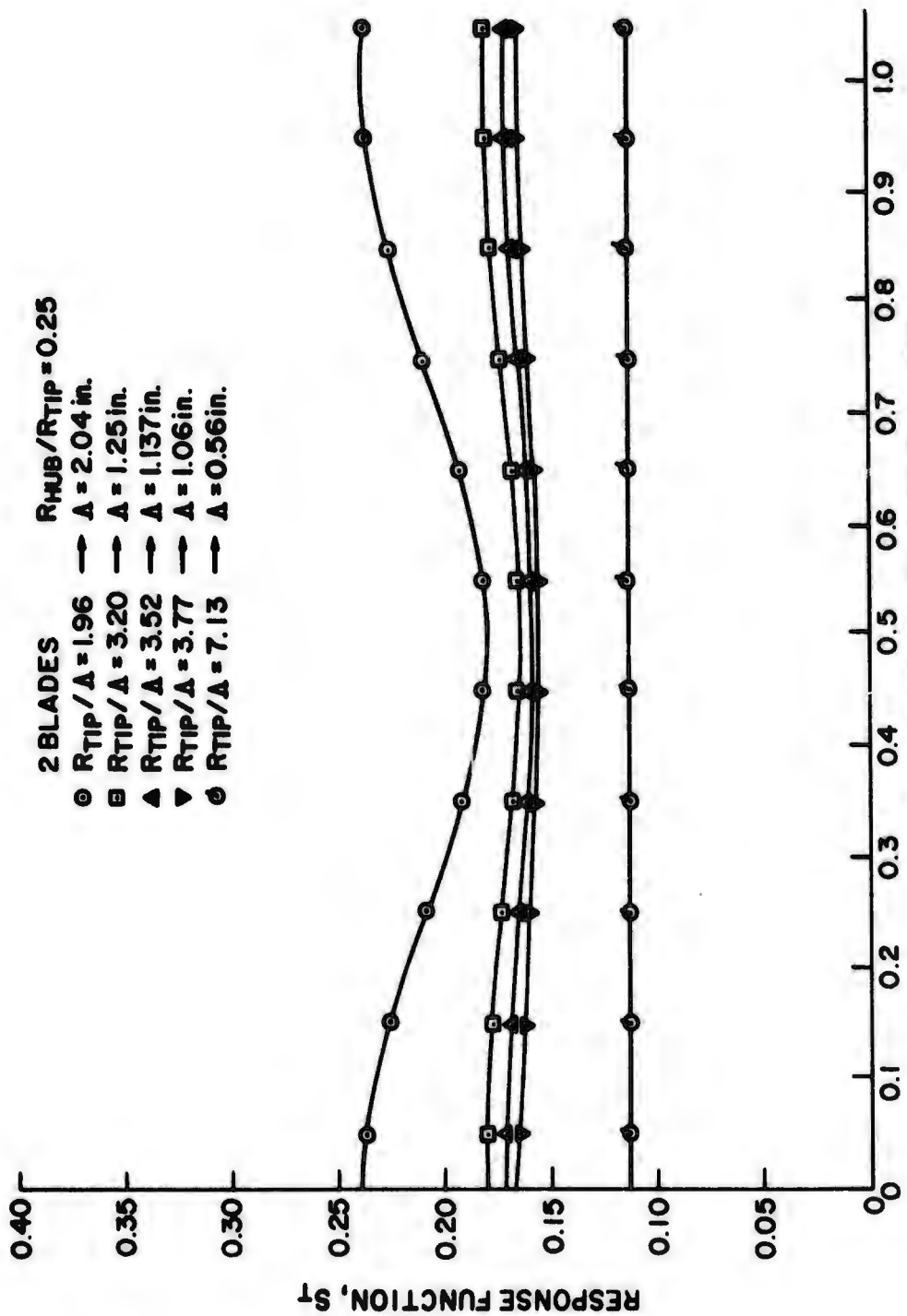

Figure 62 - Response Function S_T, Equation (53), versus Nondimensional Frequency (2 Blades, R_{HUB}/R_{TIP}=0.25)

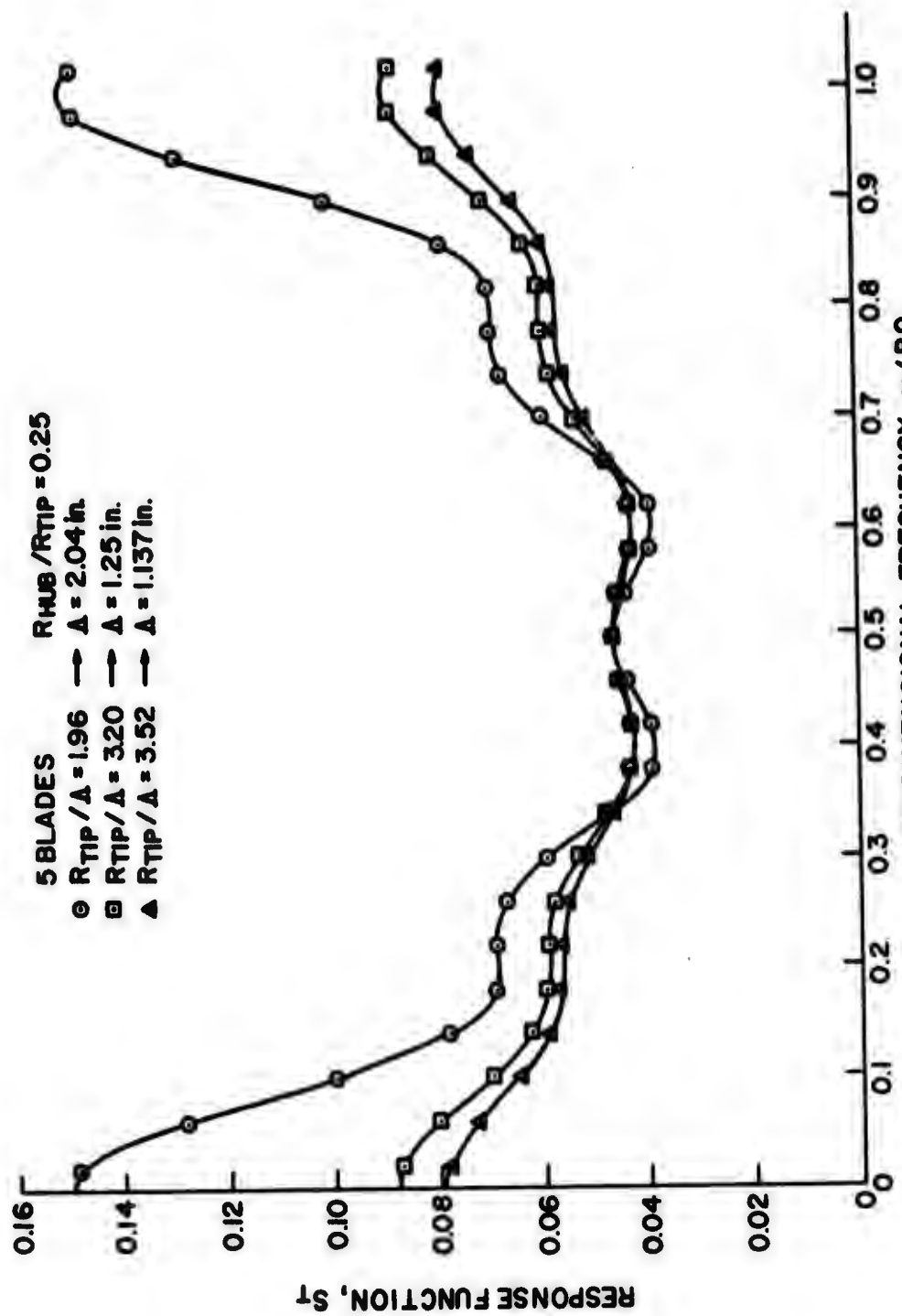

Figure 63 - Response Function S_T, Equation (53), versus Nondimensional Frequency (5 Blades, R_{HUB}/R_{TIP}=0.25)

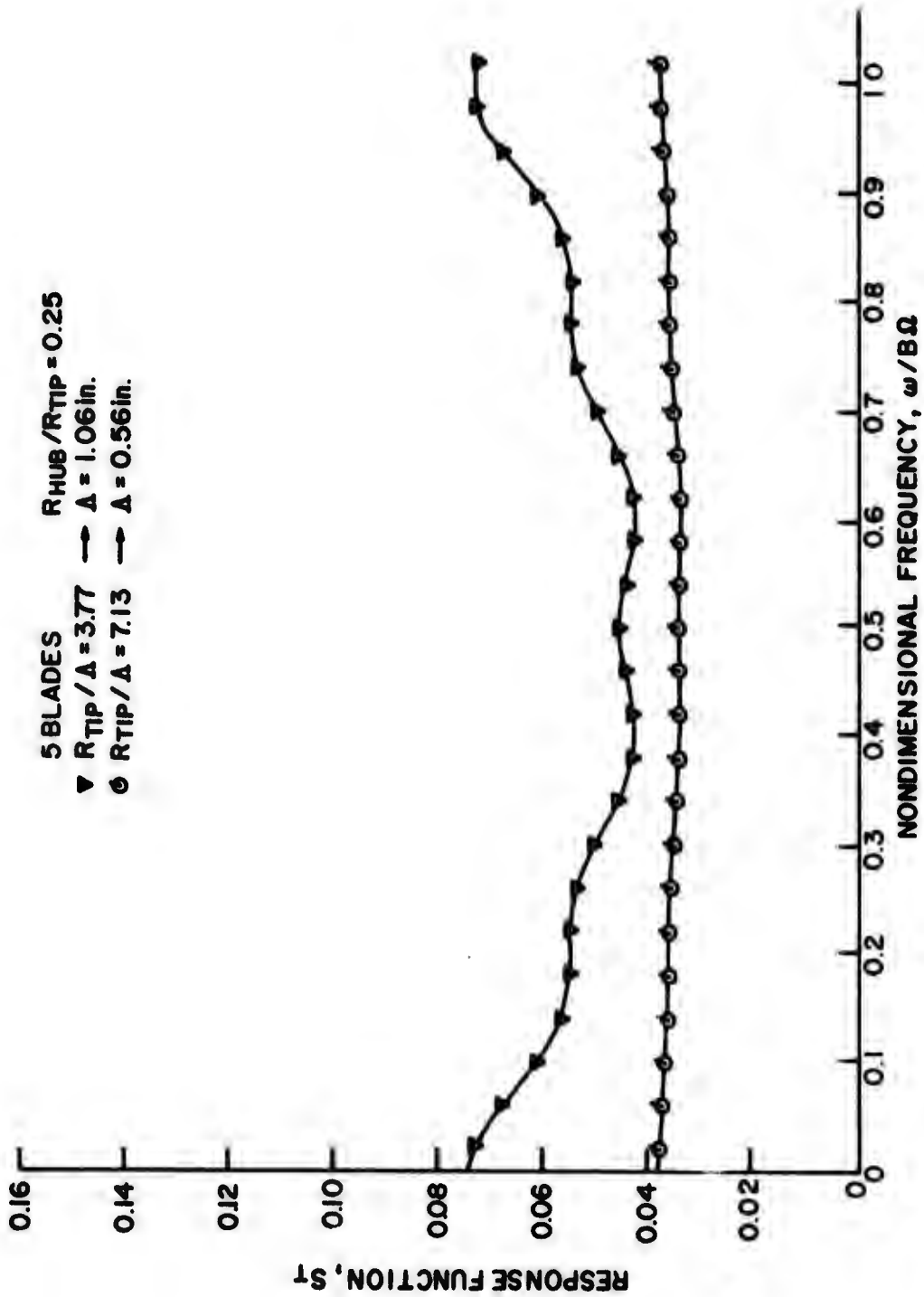

Figure 64 - Response Function S_T, Equation (53), versus Nondimensional Frequency (5 Blades, $R_{HUB}/R_{TIP}=0.25$)

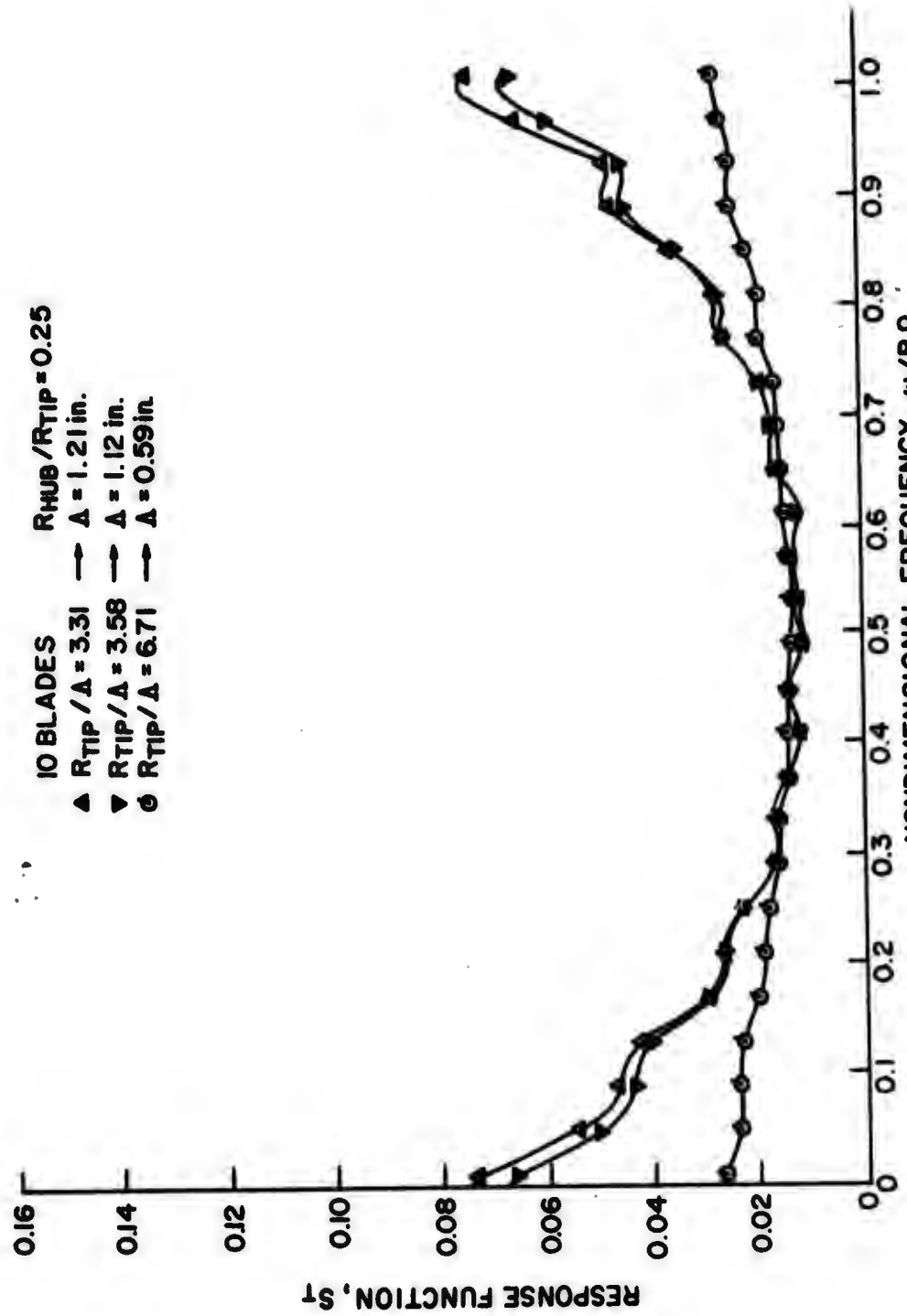

Figure 65 - Response Function S_T, Equation (53), versus Nondimensional Frequency (10 Blades, R_{HUB}/R_{TIP}=0.25)

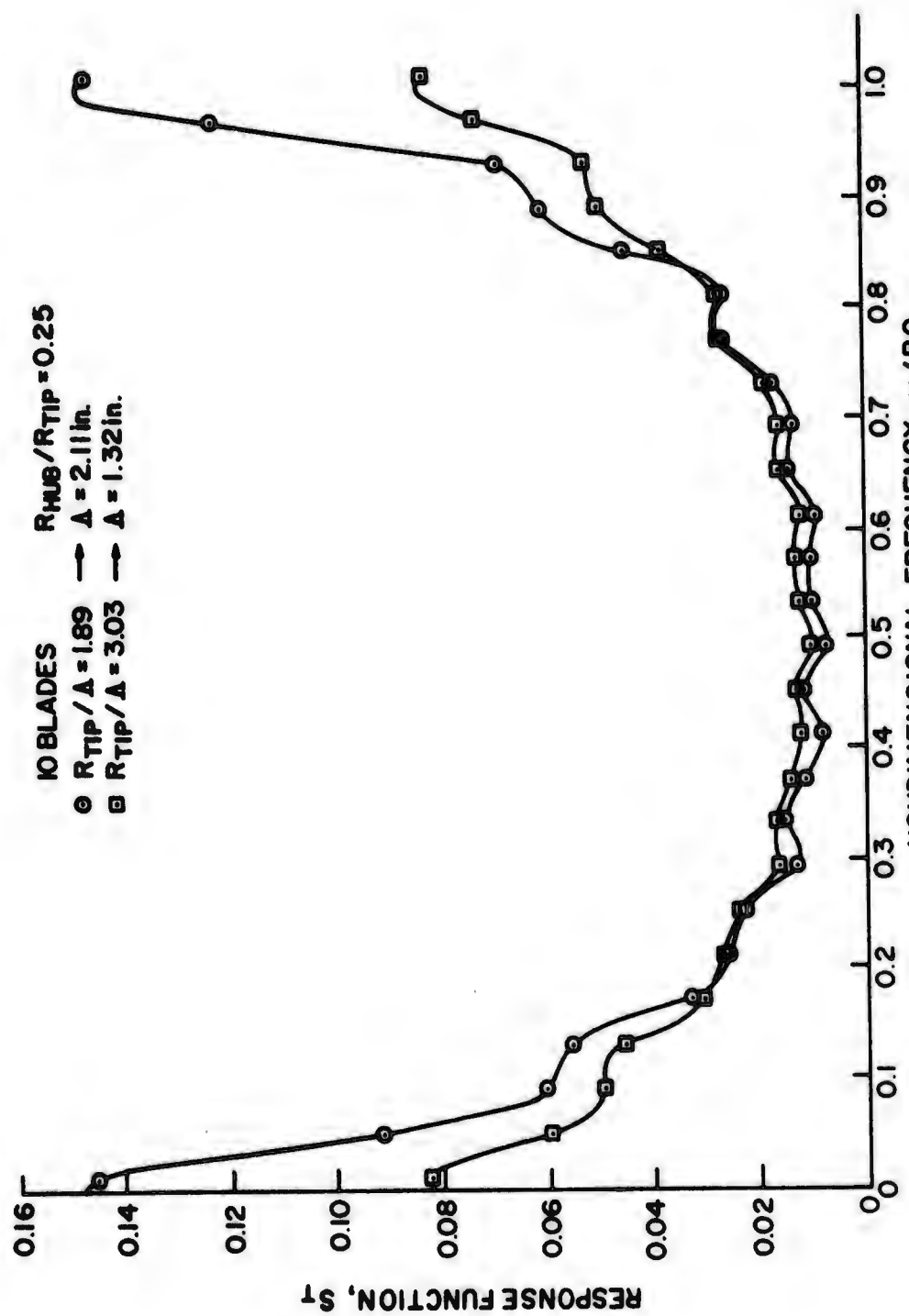

Figure 66 - Response Function S_T, Equation (53), versus Nondimensional Frequency (10 Blades, R_{HUB}/R_{TIP}=0.25)

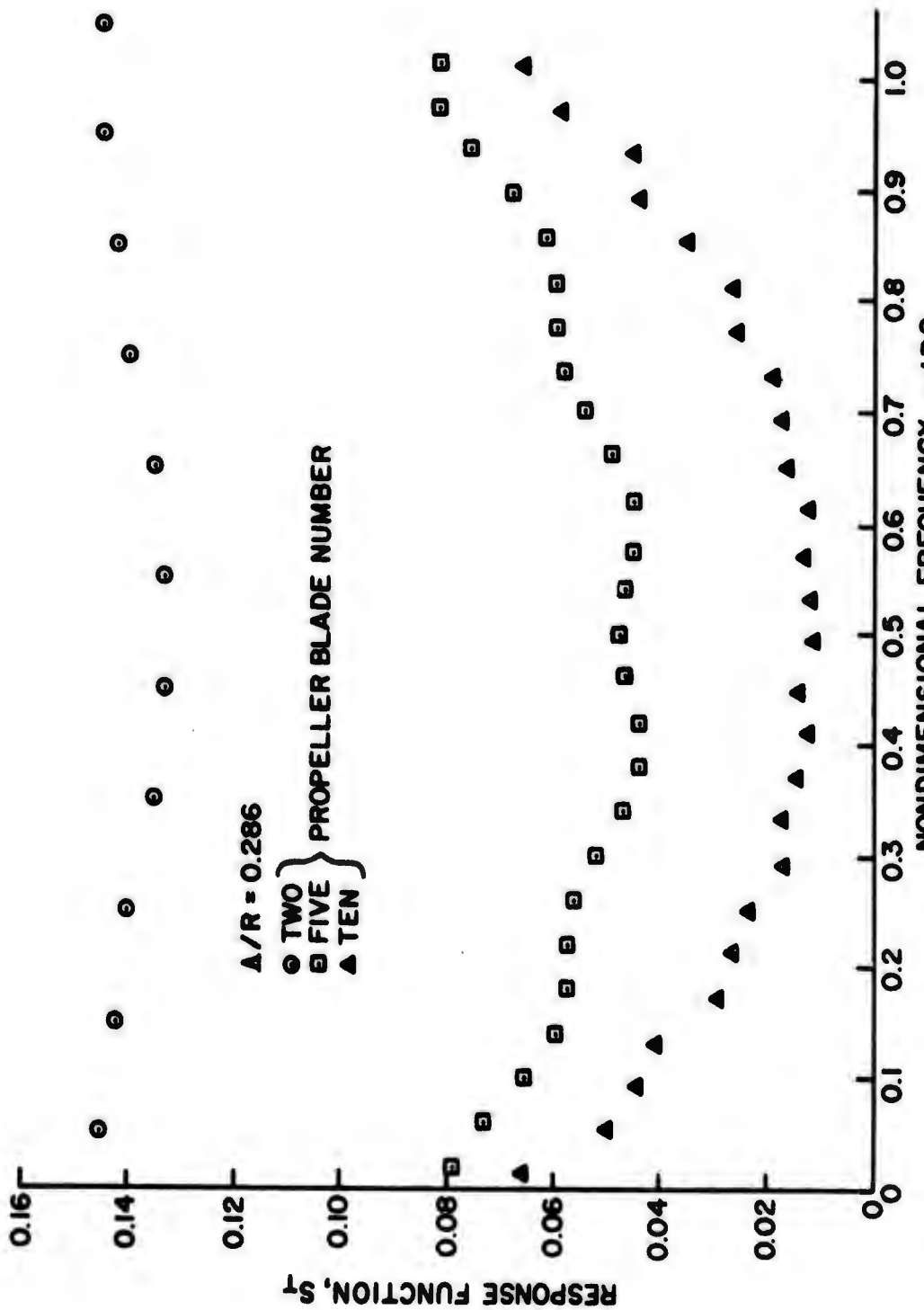

Figure 67 - Response Function S_T, Equation (53), versus Nondimensional Frequency (Λ/R=0.286, Various Blade Numbers)

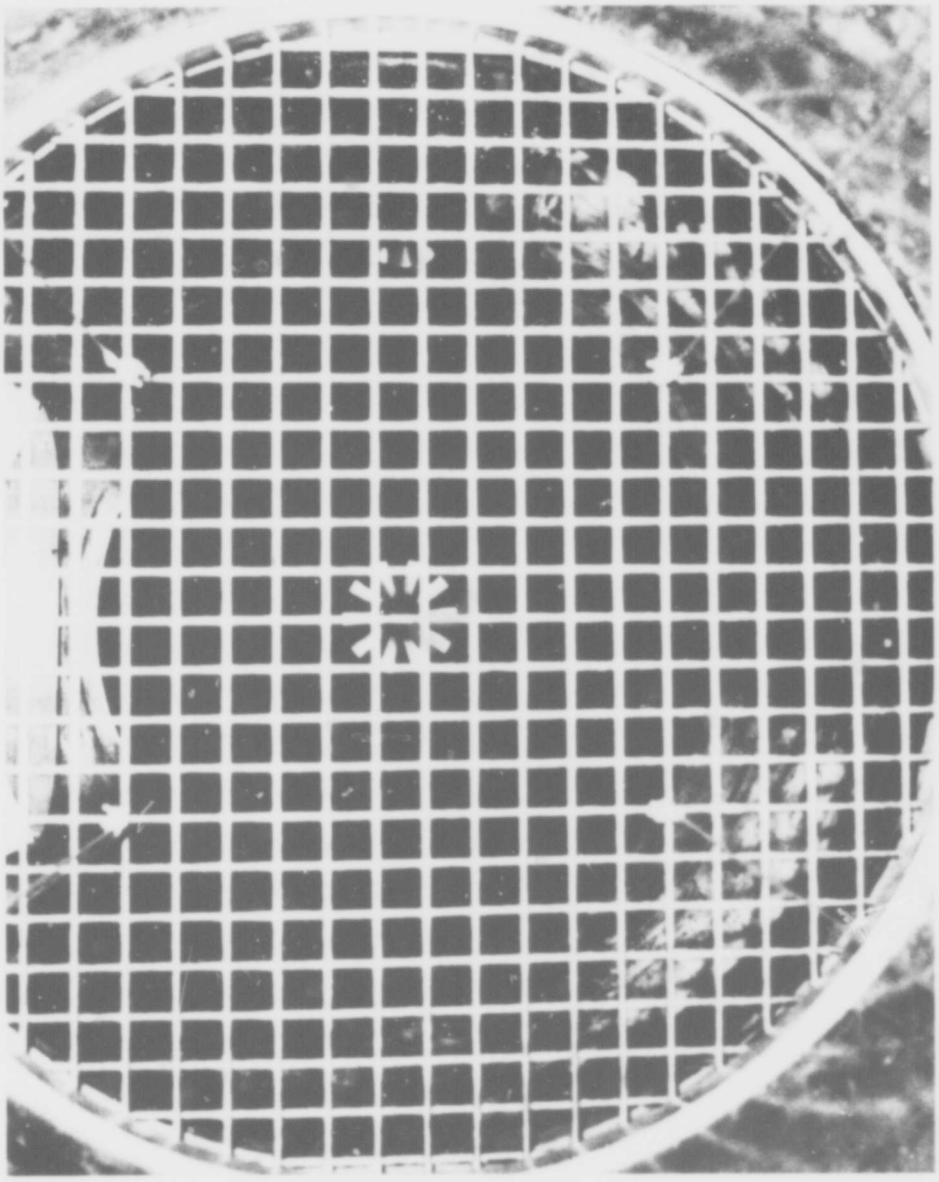

Figure 68 - Square Mesh Grid Mounted in Water Tunnel

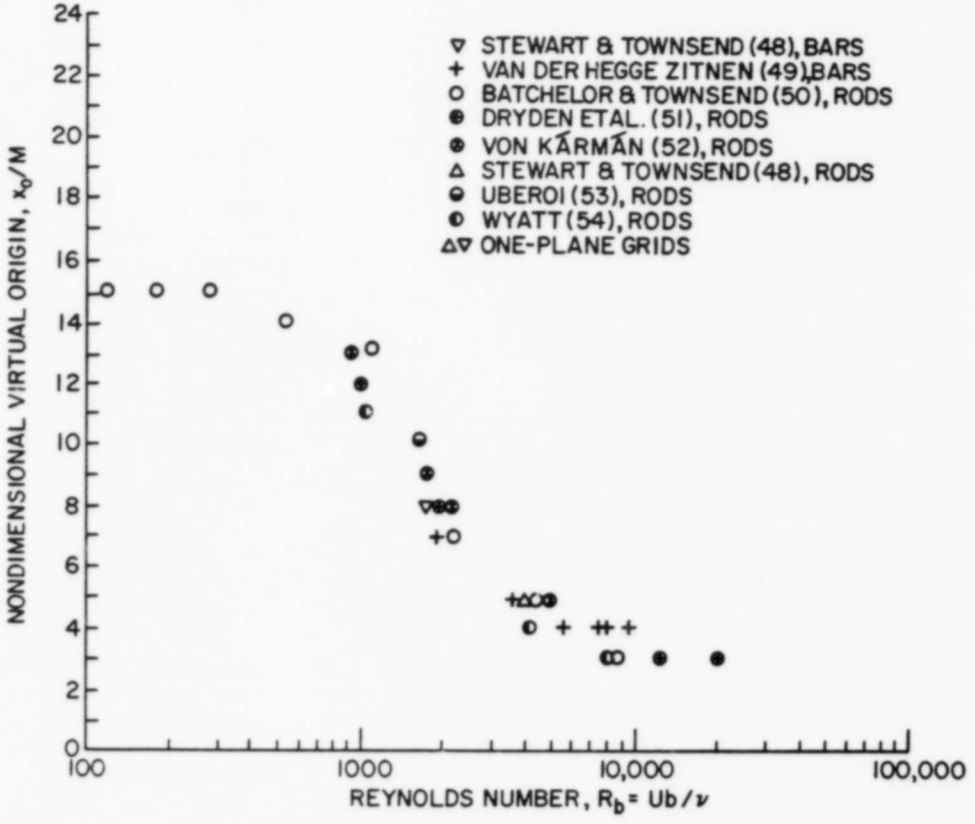

Figure 69 - Grid Turbulence Nondimensional Virtual Origin versus Reynolds Number

Source: Naudascher, E., and C. Farell, "Unified Analysis of Grid Turbulence," J. Eng. Mch. Div., Proc. ASCE, pp. 121-141, April 1970.

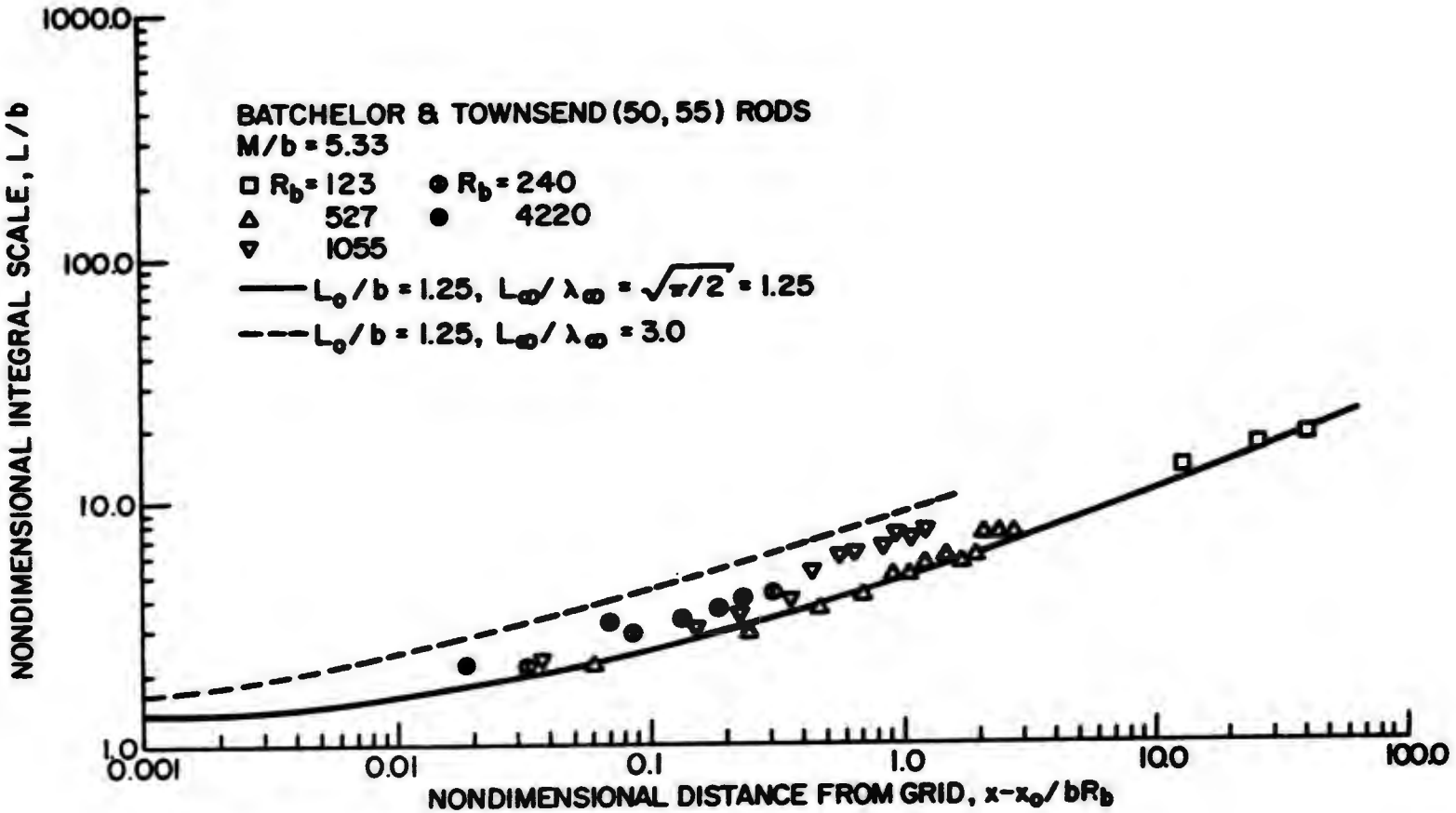

Figure 70 - Grid Turbulence Nondimensional Integral Scale versus Nondimensional Distance from Grid

Source: Naudascher, E., and C. Farell, "Unified Analysis of Grid Turbulence," J. Eng. Mch. Div., Proc. ASCE, pp. 121-141, April 1970.

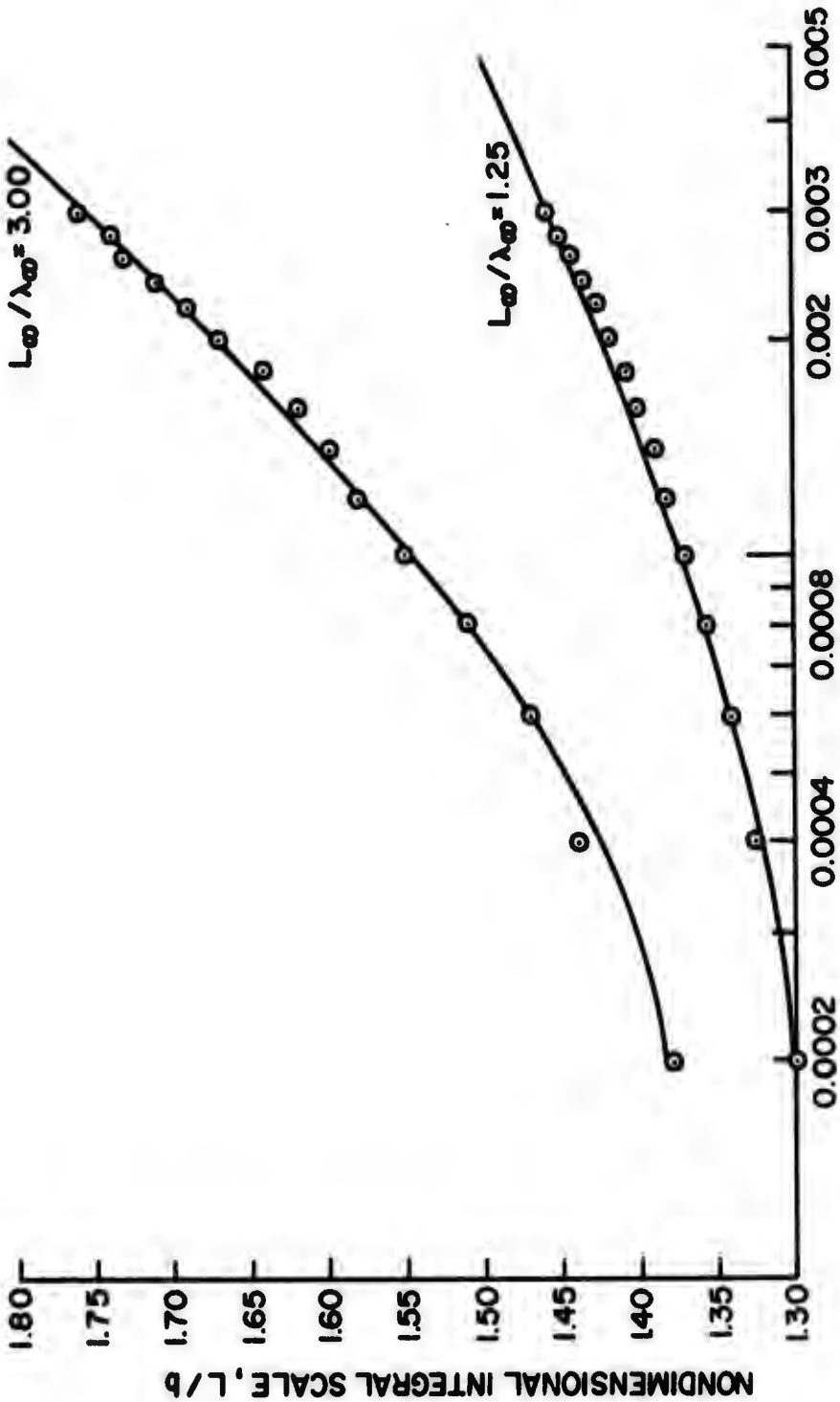

Figure 71 - Grid Turbulence Nondimensional Integrai Scale versus Nondimensional Distance from Grid

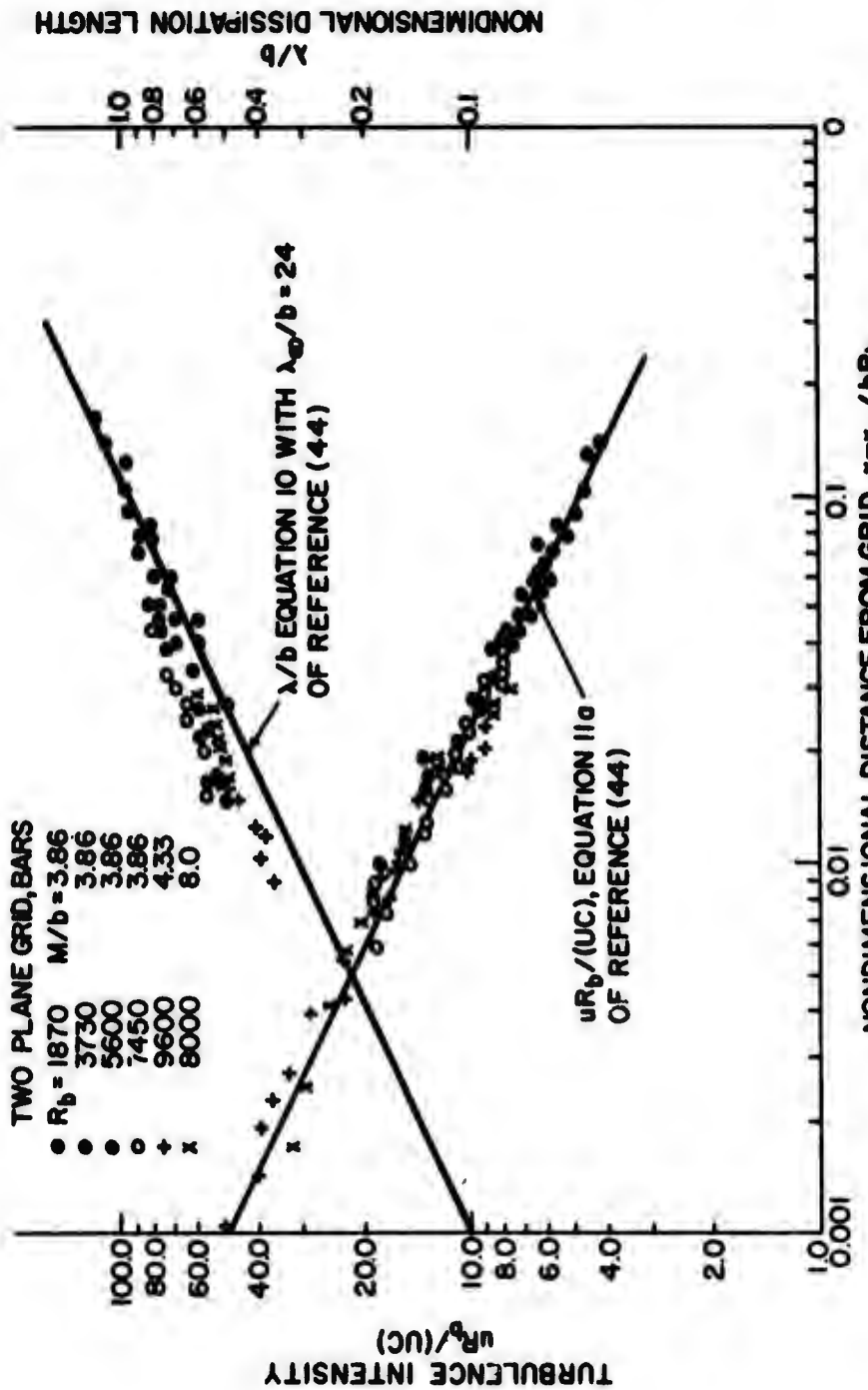

Figure 72 - Grid Turbulence Intensity versus Nondimensional Distance from Grid

Source: Naudascher, E., and C. Farell, "Unified Analysis of Grid Turbulence," J. Eng. Mch. Div., Proc. ASCE, pp. 121-141, April 1970.

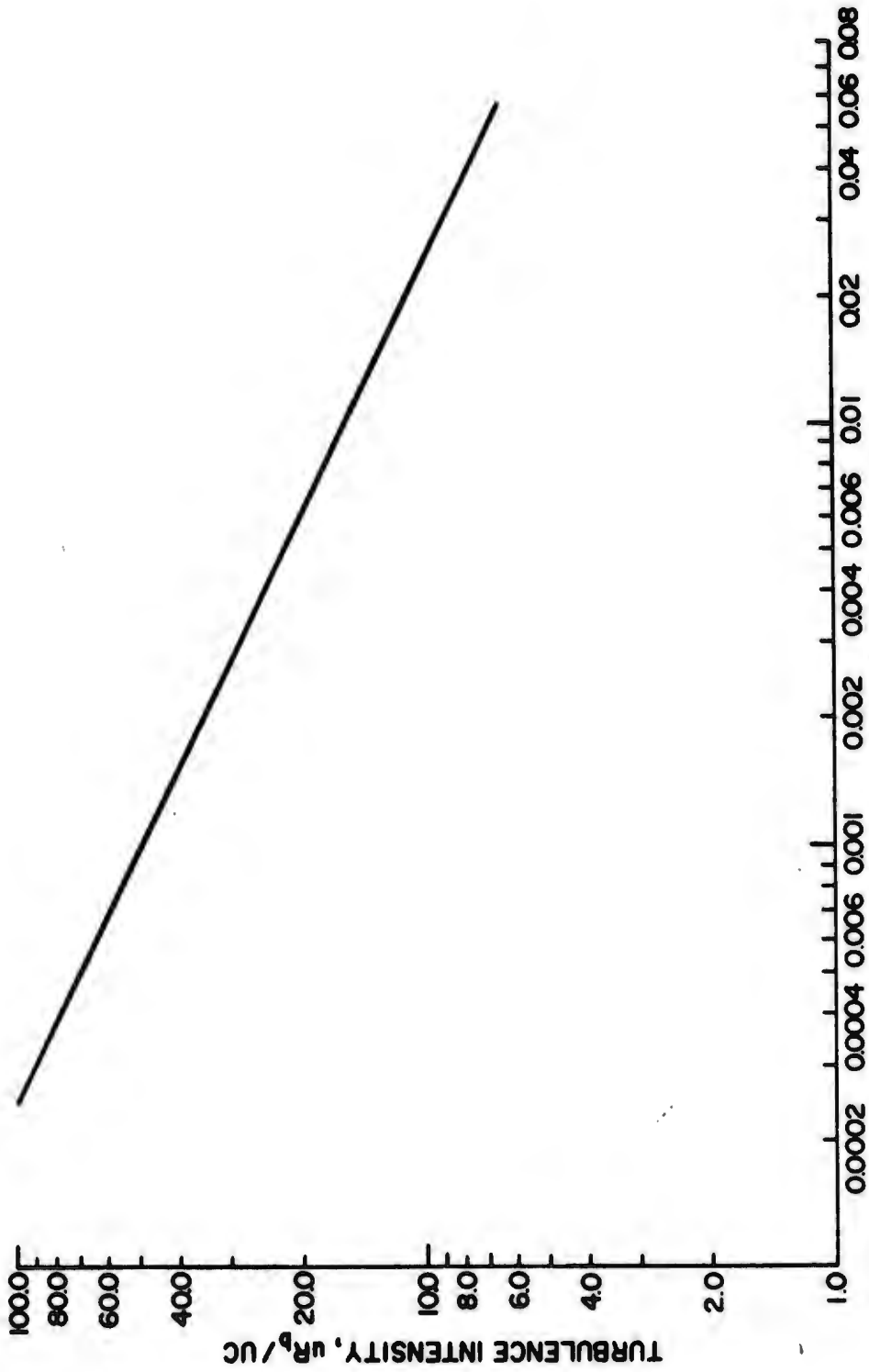

Figure 73 - Grid Turbulence Intensity versus Nondimensional Distance from Grid

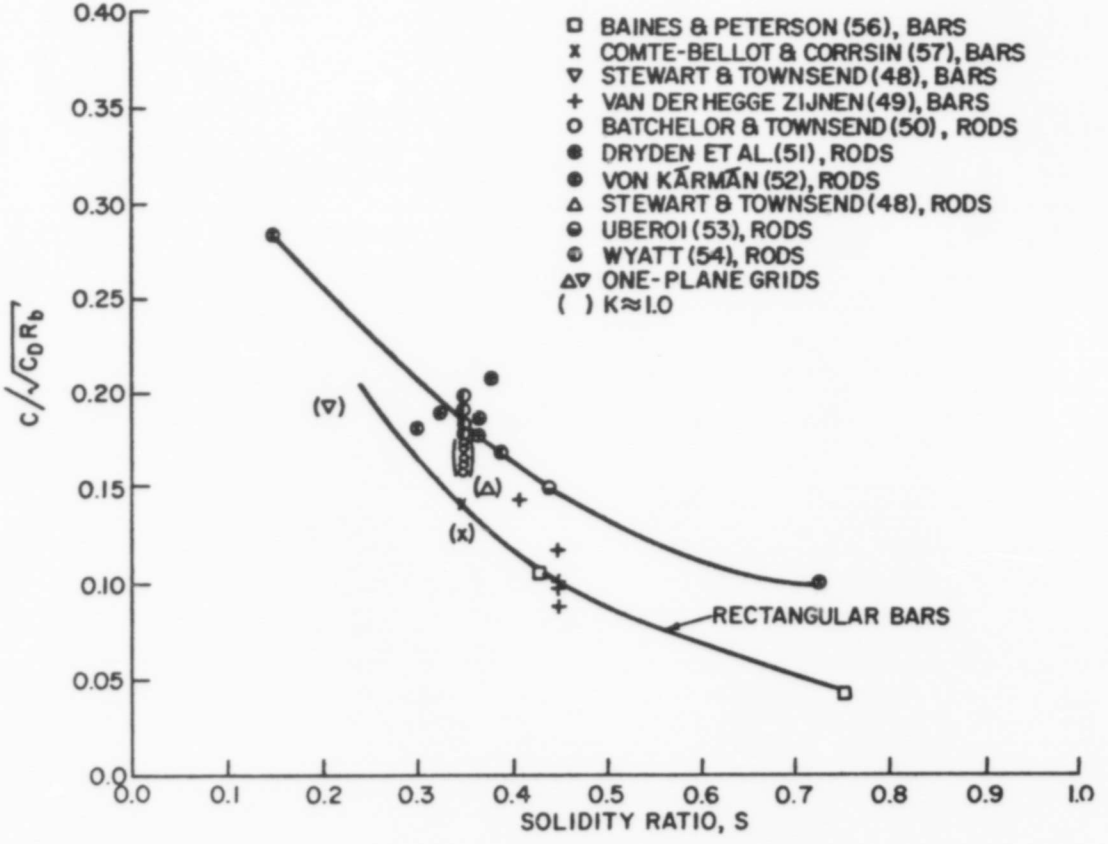

Figure 74 - The Grid Parameter $C/\sqrt{C_D R_b}$ versus Solidity Ratio

Source: Naudascher, E., and C. Farell, "Unified Analysis of Grid Turbulence," J. Eng. Mch. Div., Proc. ASCE, pp. 121-141, April 1970.

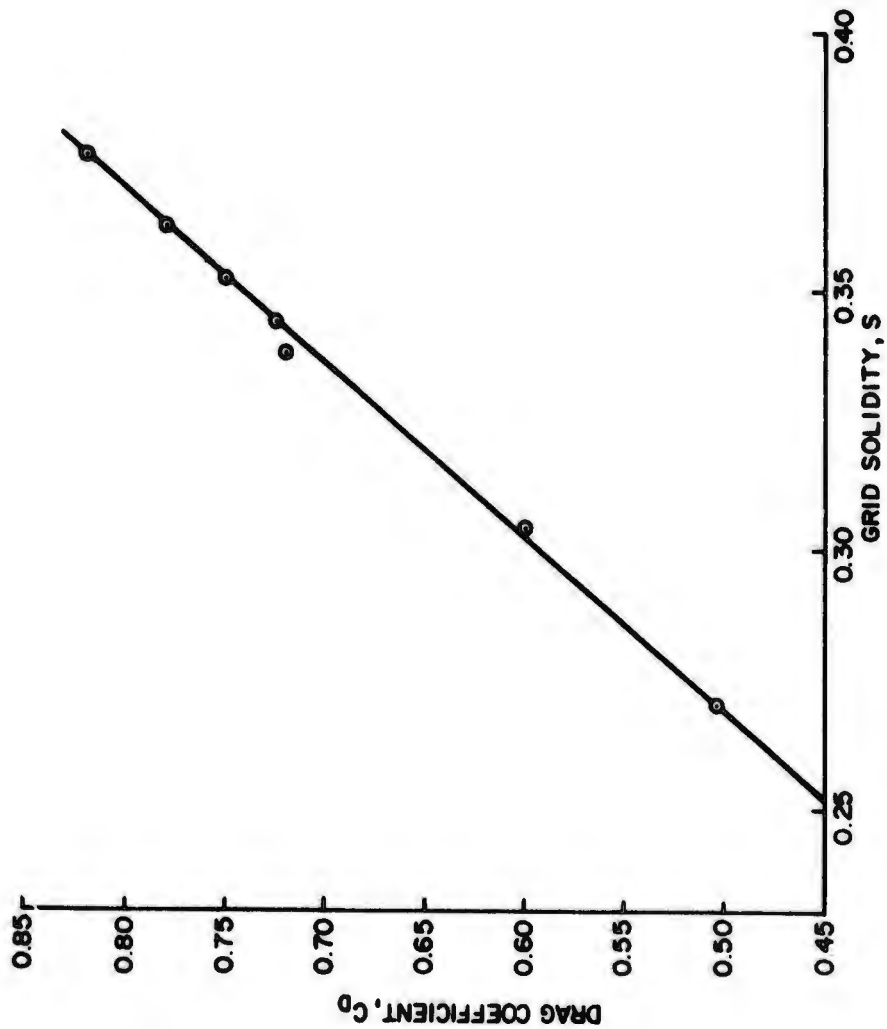

Figure 75 - Grid Drag Coefficient versus Grid Solidity

Source: Naudascher, E., and C. Farell, "Unified Analysis of Grid Turbulence," J. Eng. Mch. Div., Proc. ASCE, pp. 121-141, April 1970.

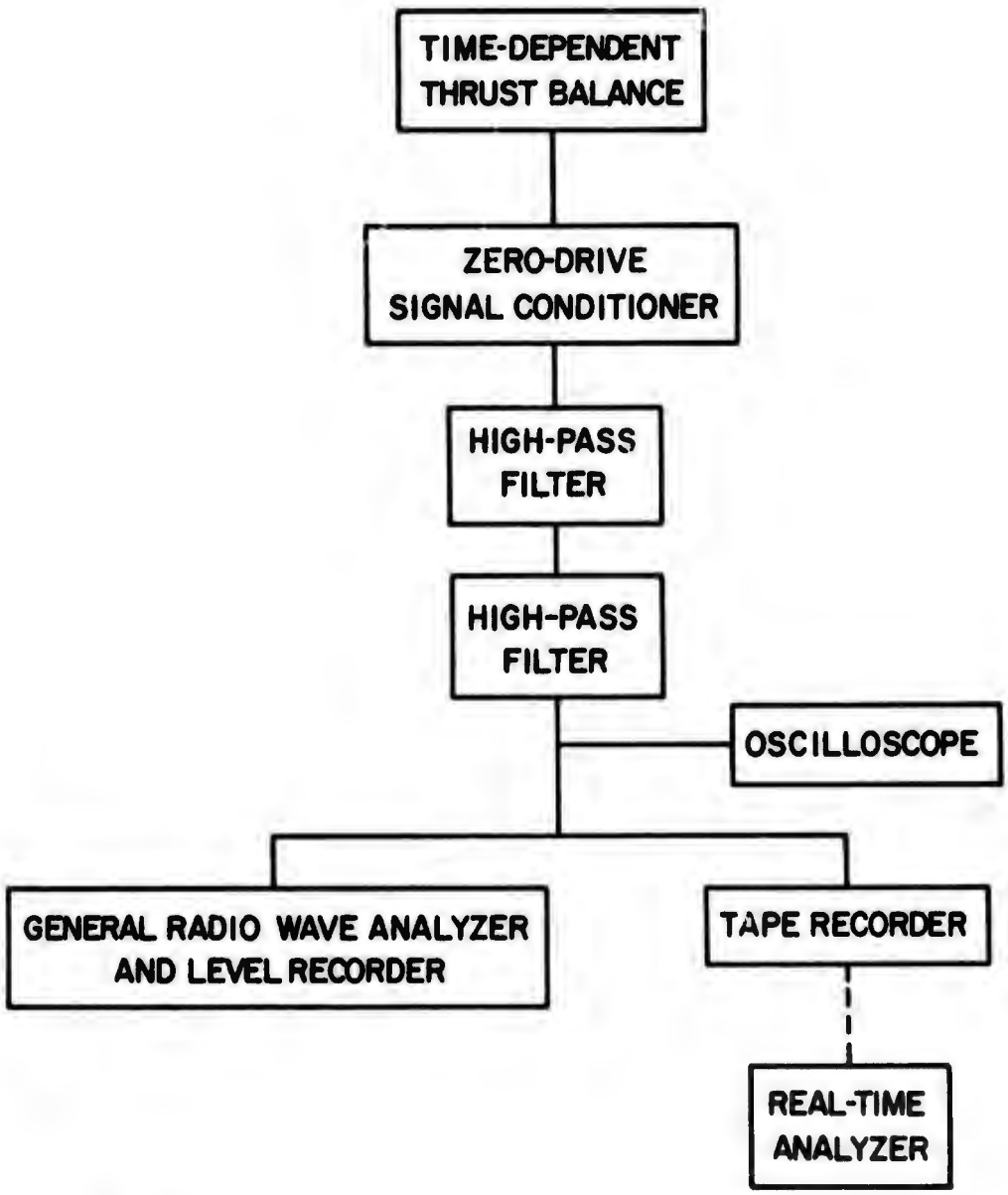

Figure 76 - Data Acquisition and Analysis System for Turbulence Response Measurements

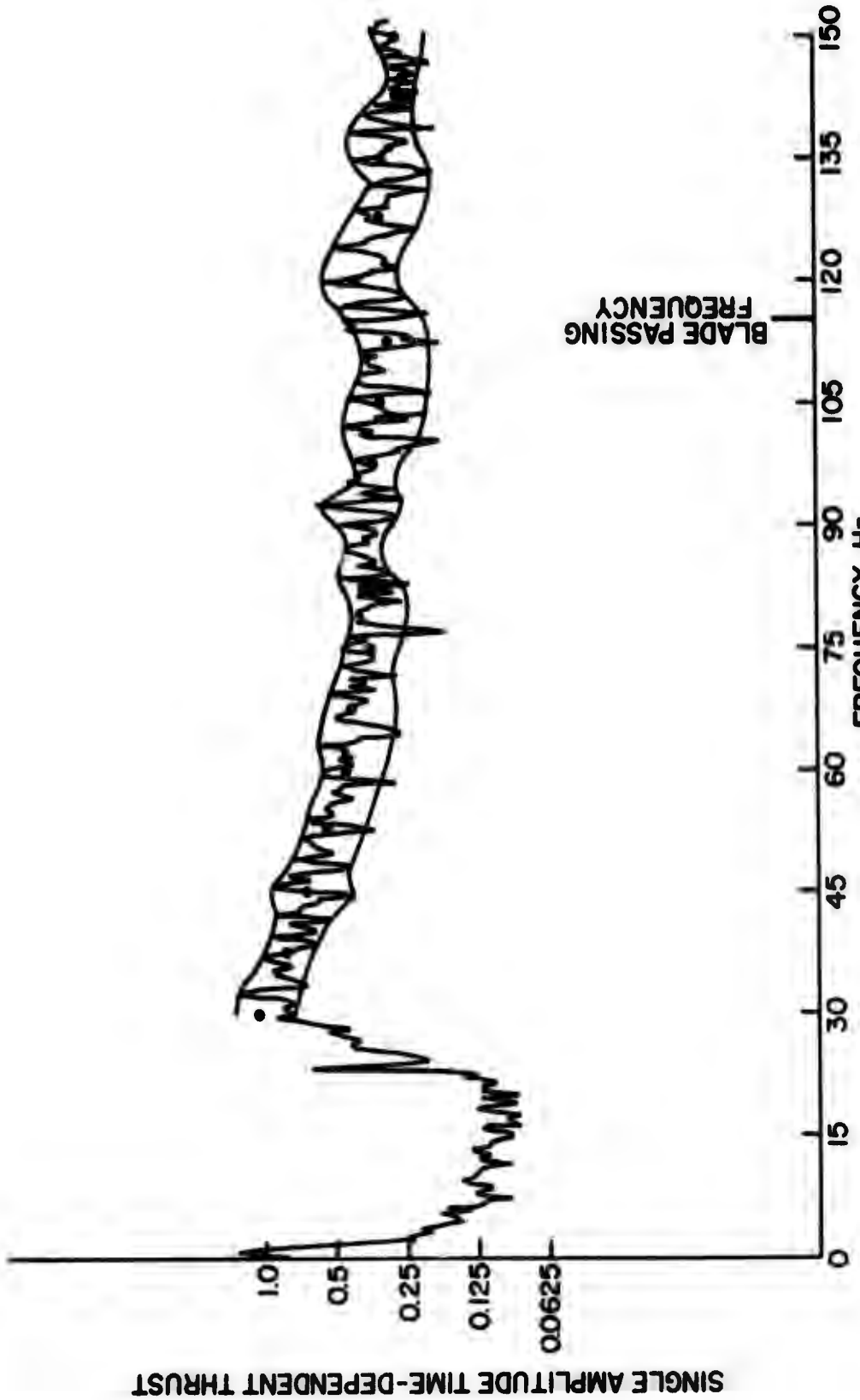

Figure 77 - Typical Time-Dependent Thrust Spectrum for Response to Turbulence

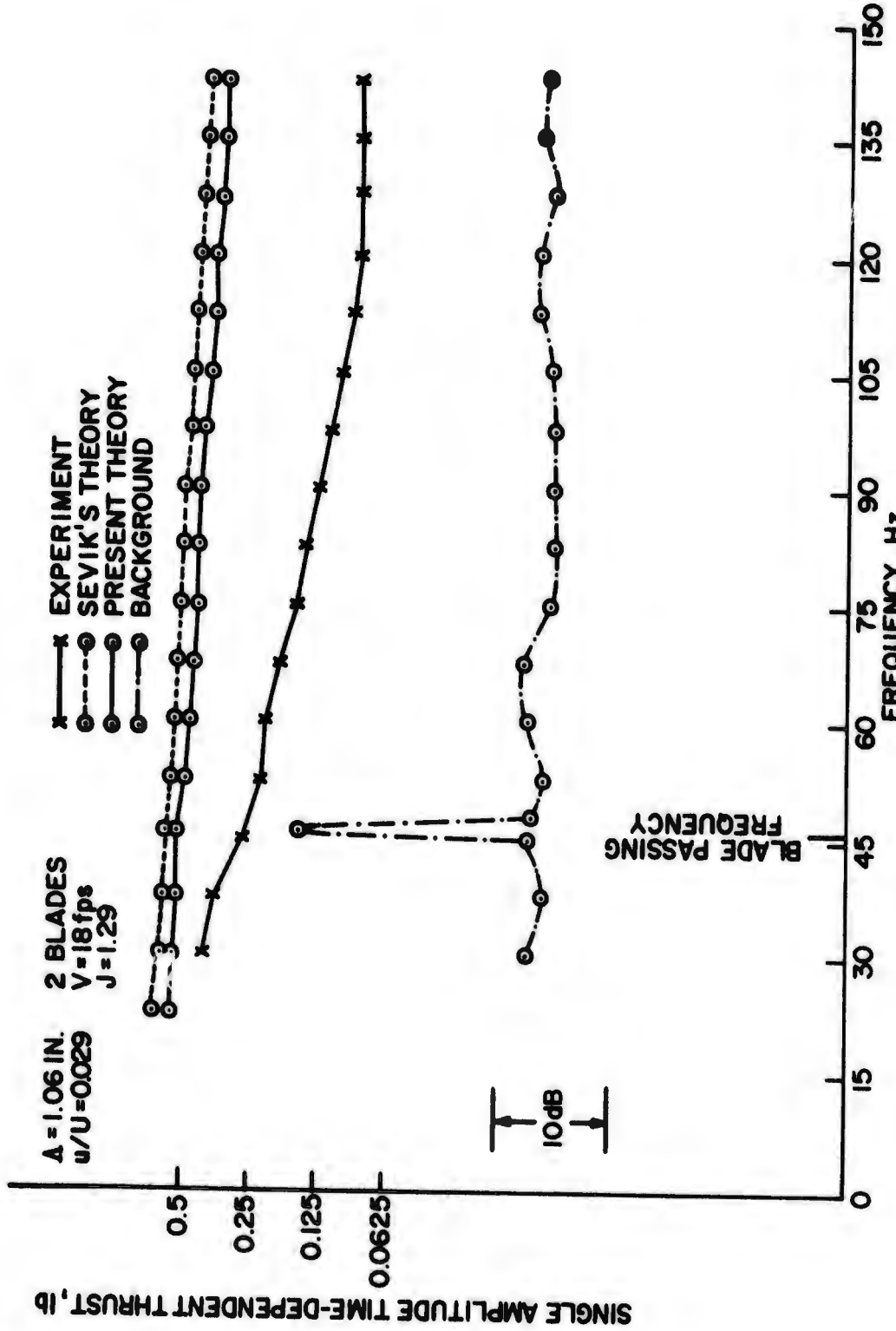

Figure 78 - Turbulence Generated Time-Dependent Thrust versus Frequency
(2 Blades, J=1.29, Λ=1.06 in., u/U=0.029)

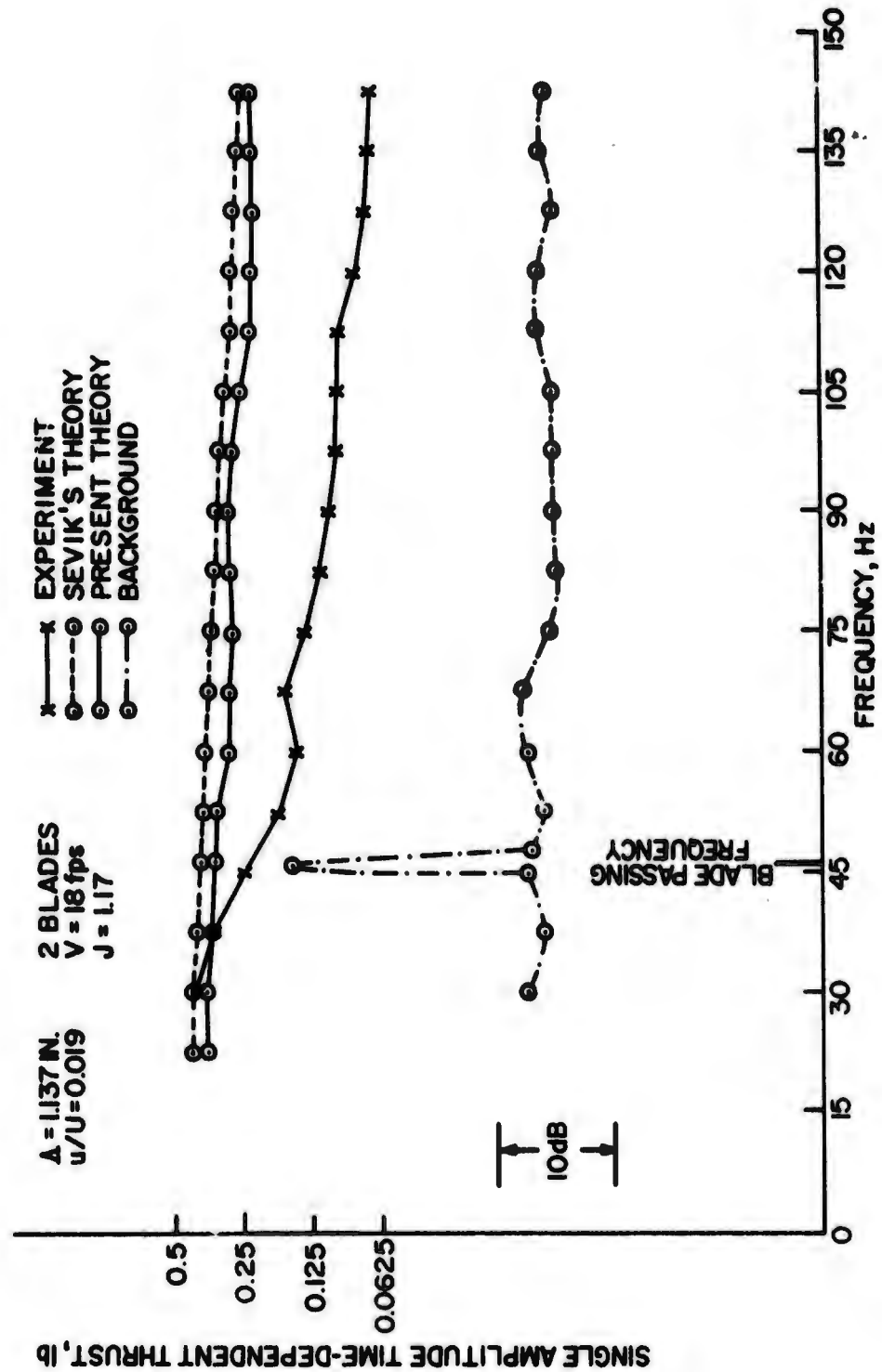

Figure 79 - Turbulence Generated Time-Dependent Thrust versus Frequency (2 Blades, J=1.17, Λ=1.137 in., u/U=0.019)

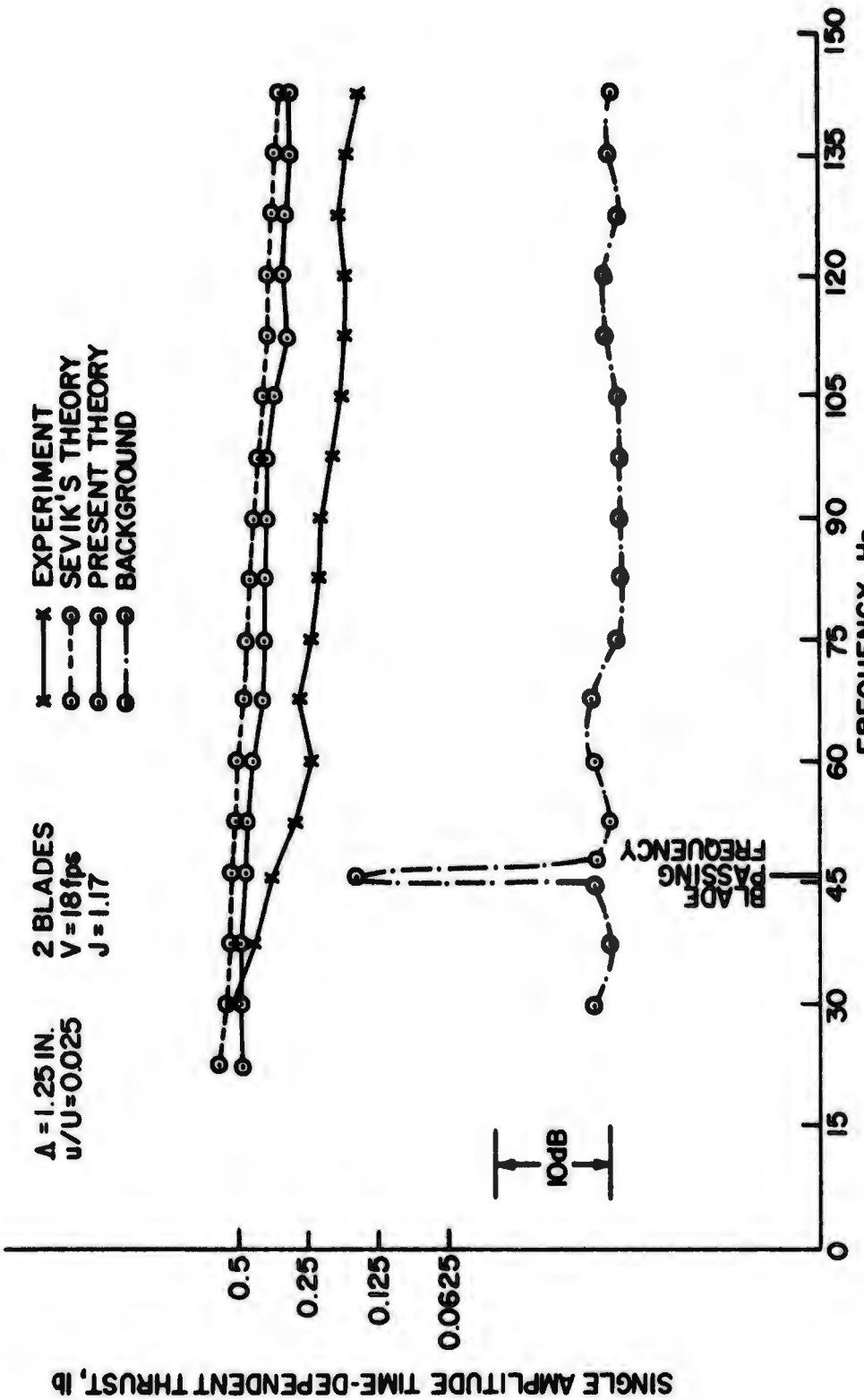

Figure 80 - Turbulence Generated Time-Dependent Thrust versus Frequency (2 Blades, J=1.17, Λ=1.25 in., u/U=0.025)

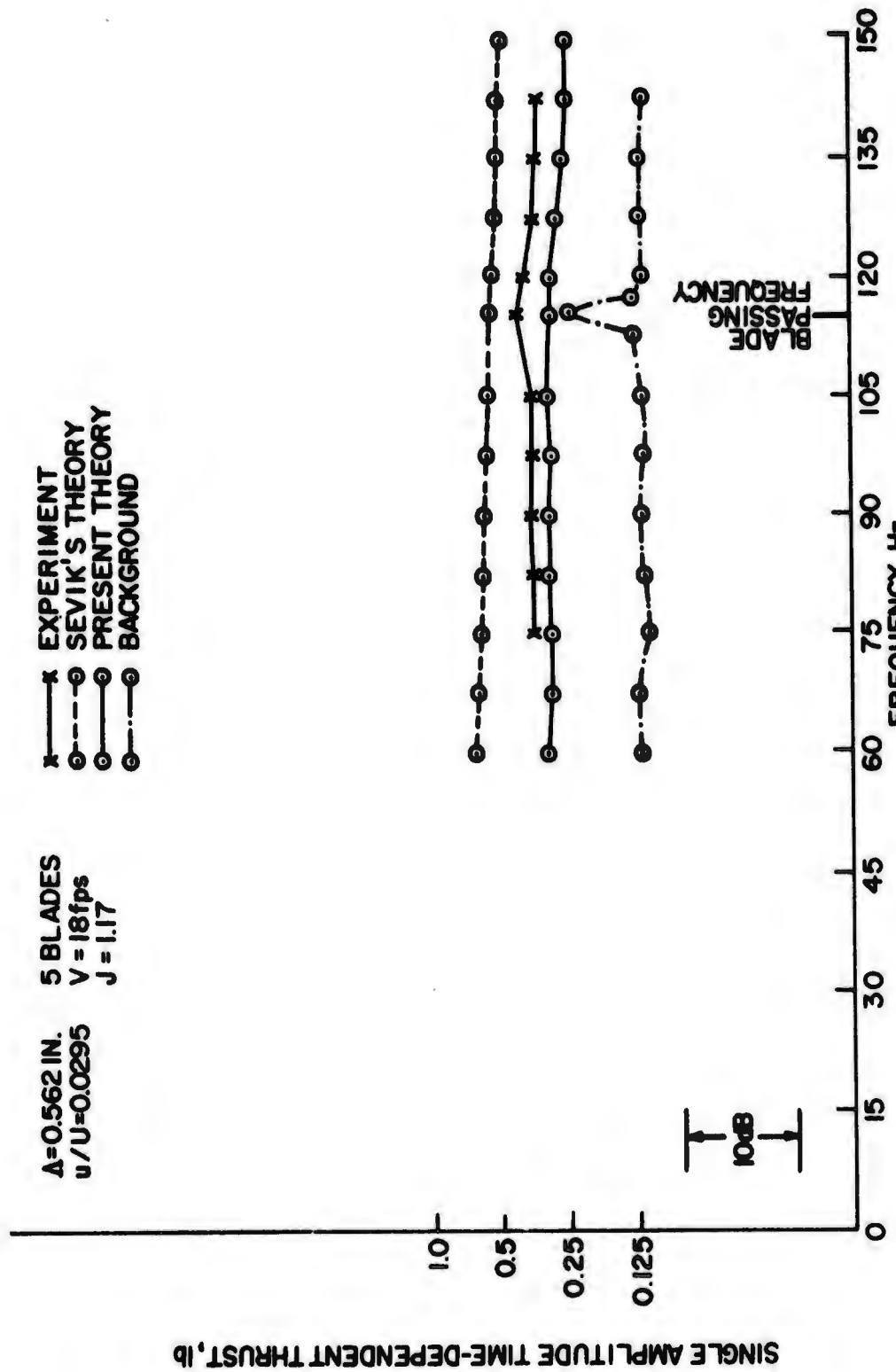

Figure 81 - Turbulence Generated Time-Dependent Thrust versus Frequency (5 Blades, J=1.17, Δ=0.562 in., u/U=0.0295)

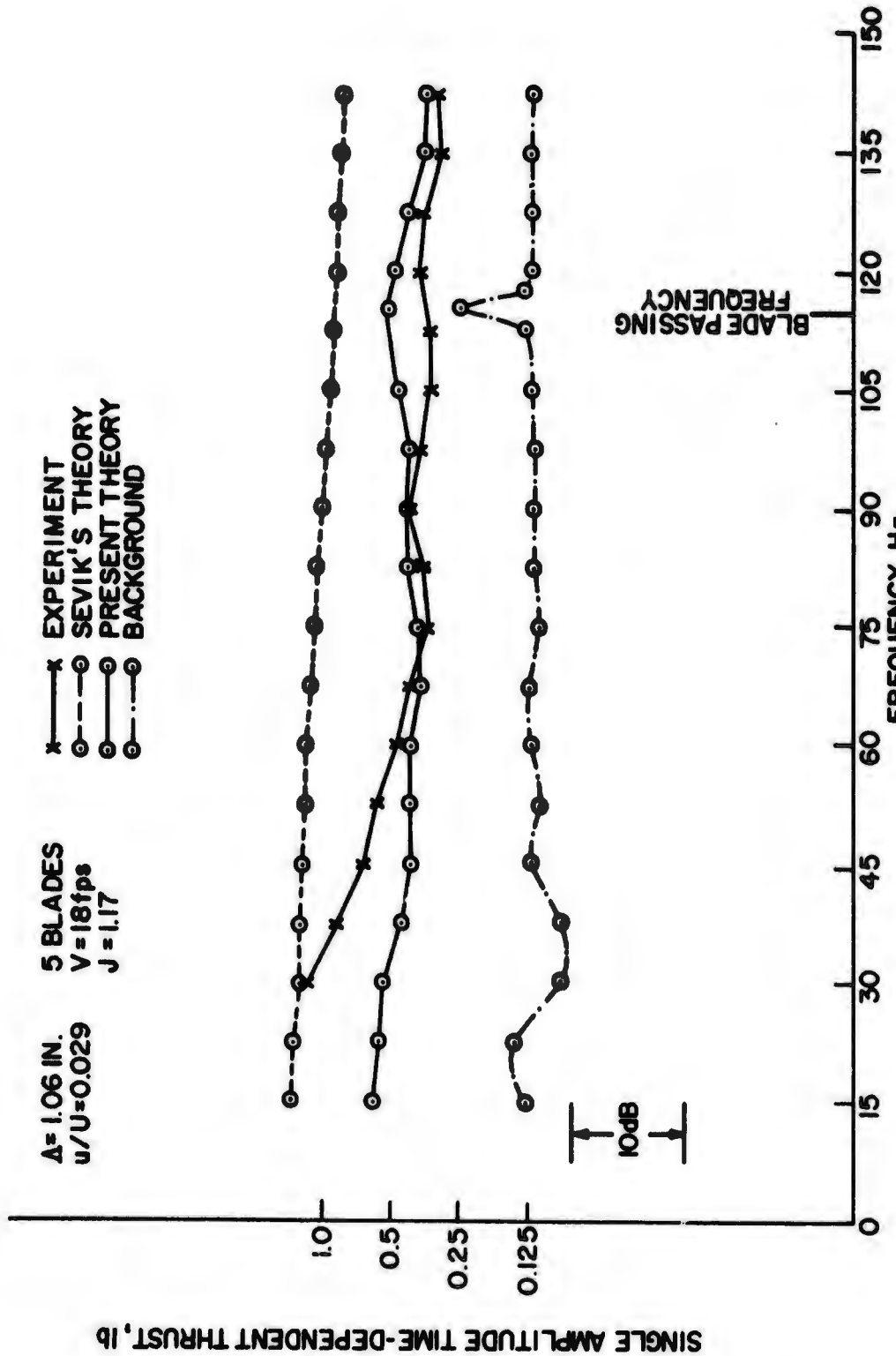

Figure 82 - Turbulence Generated Time-Dependent Thrust versus Frequency
(5 Blades, J=1.17, Δ=1.06 in., u/U=0.029)

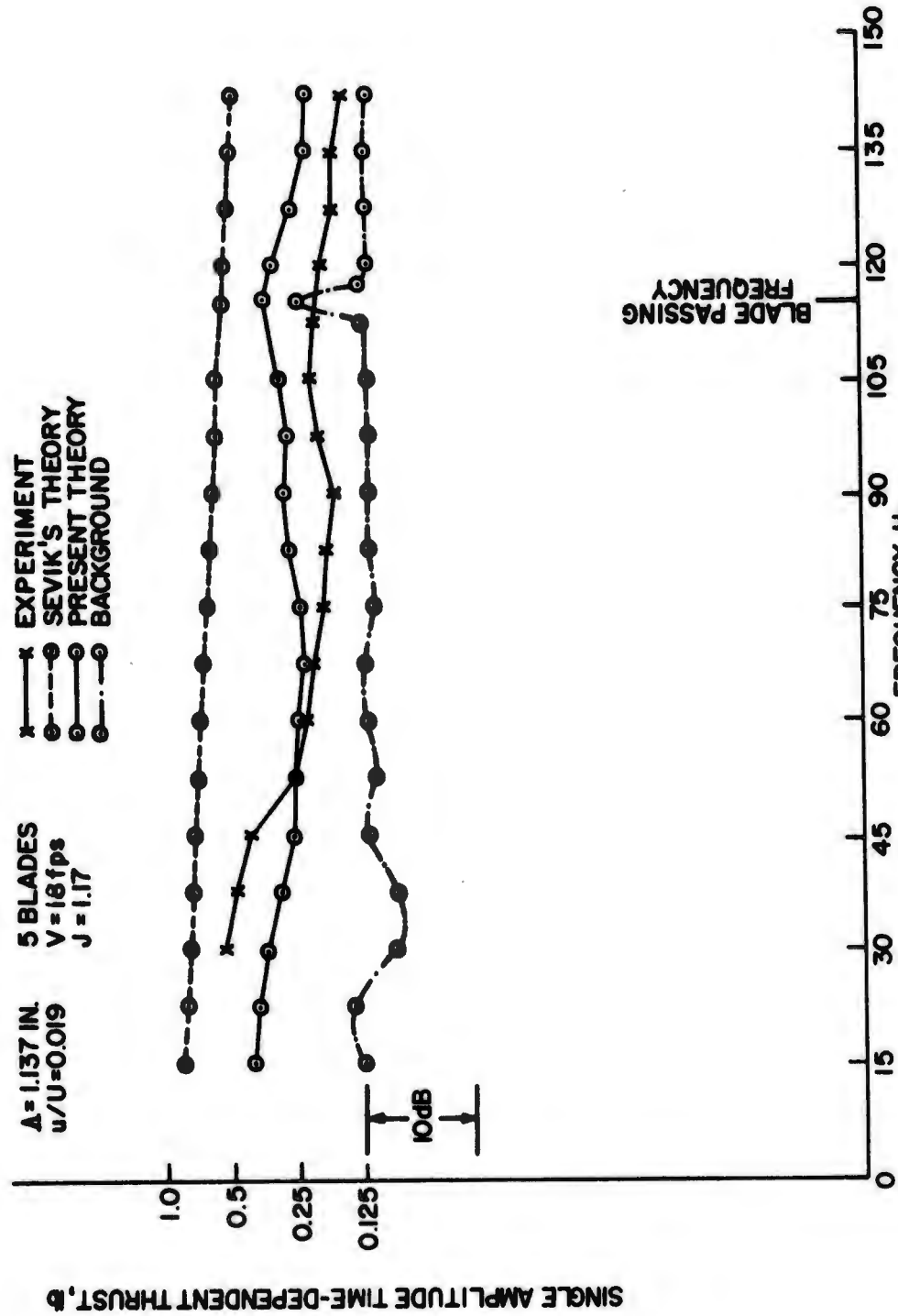

Figure 83 - Turbulence Generated Time-Dependent Thrust versus Frequency
(5 Blades, J=1.17, Λ=1.137 in., u/U=0.019)

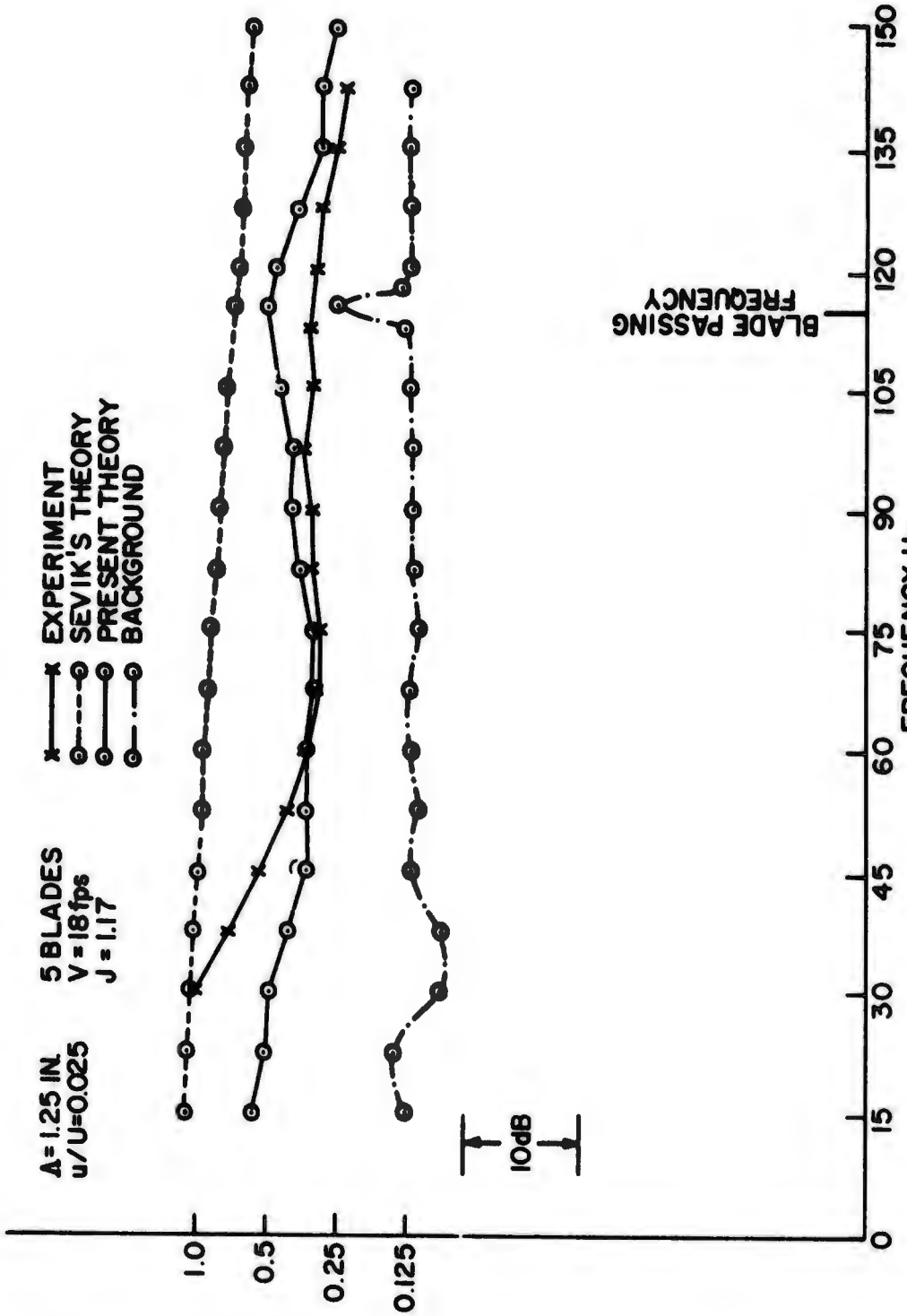

Figure 84 - Turbulence Generated Time-Dependent Thrust versus Frequency (5 Blades, J=1.17, Λ=1.25 in., u/U=0.025)

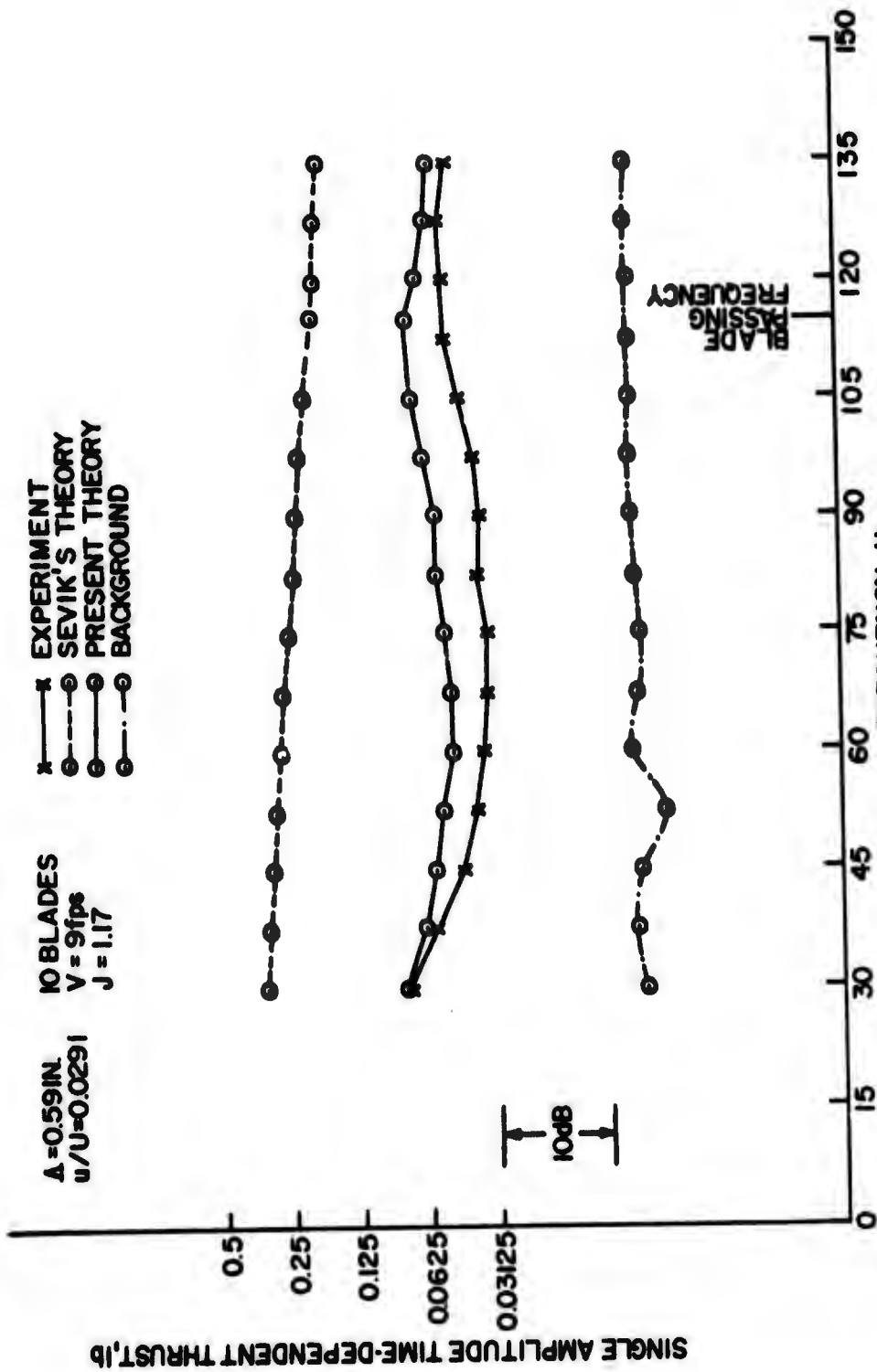

Figure 85 - Turbulence Generated Time-Dependent Thrust versus Frequency (10 Blades, J=1.17, Δ=0.59 in., u/U=0.0291)

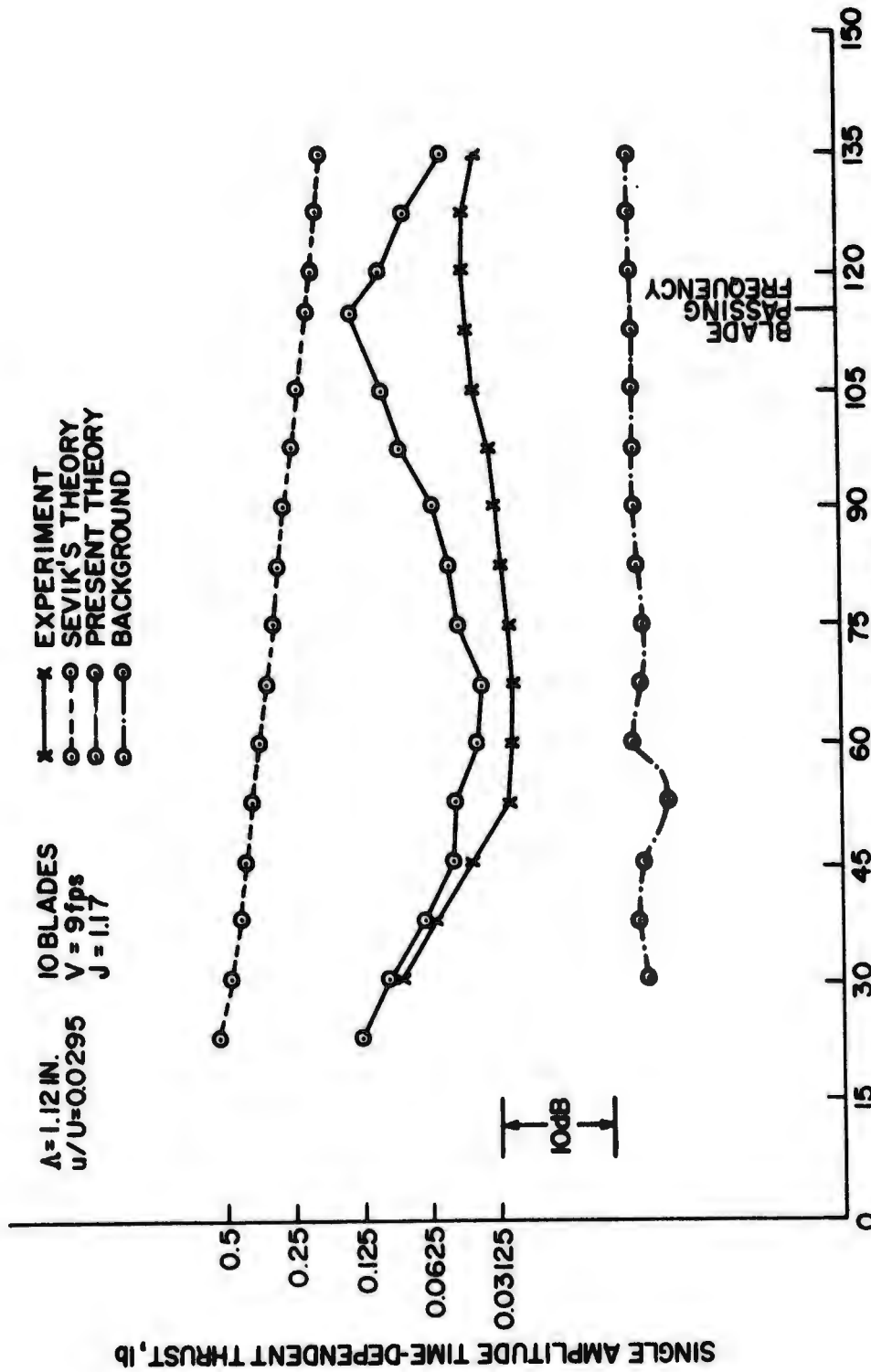

Figure 86 - Turbulence Generated Time-Dependent Thrust versus Frequency (10 Blades, J=1.17, Λ=1.12 in., u/U=0.0295)

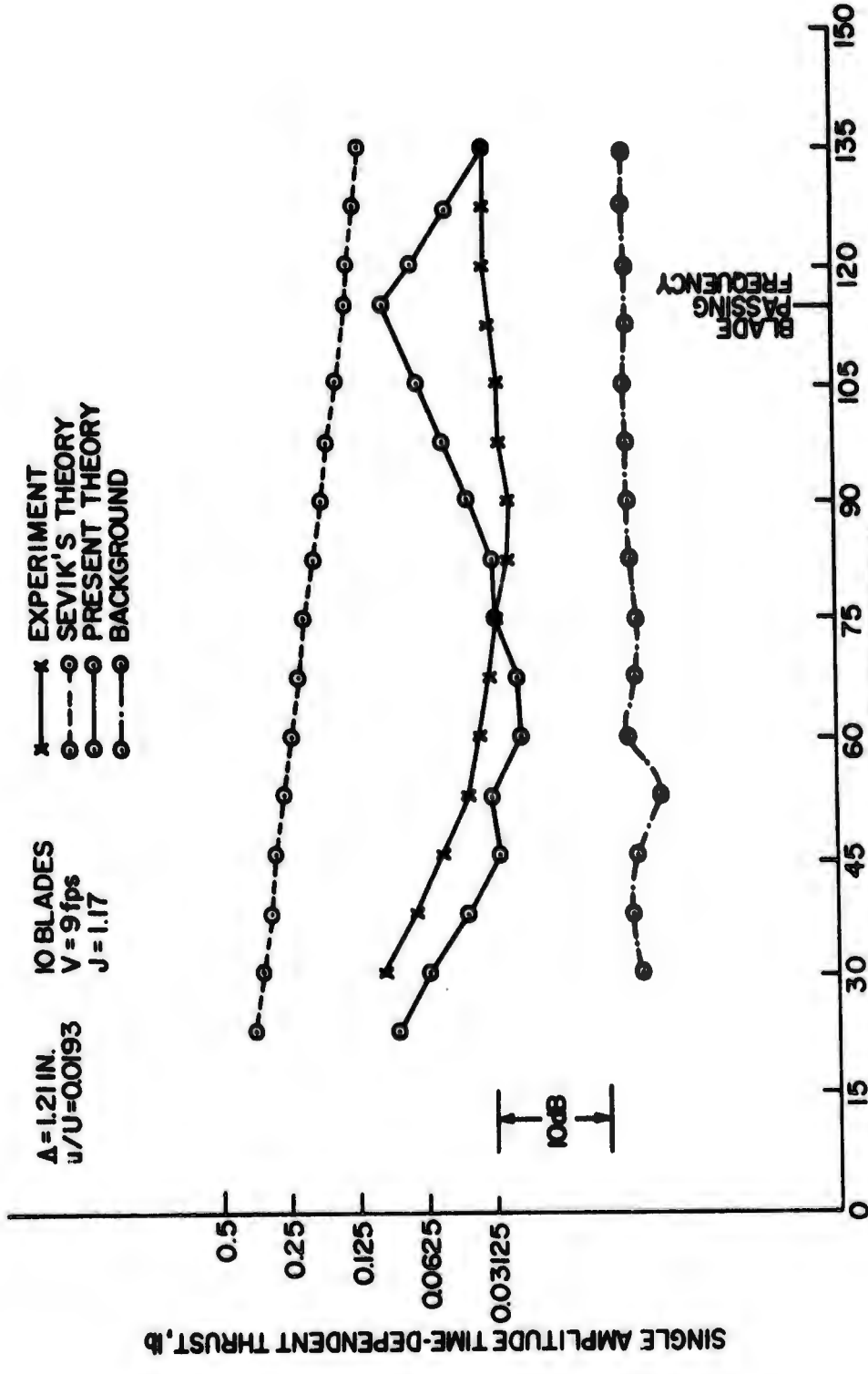

Figure 87 - Turbulence Generated Time-Dependent Thrust versus Frequency (10 Blades, J=1.17, Δ=1.21 in., u/U=0.0193)

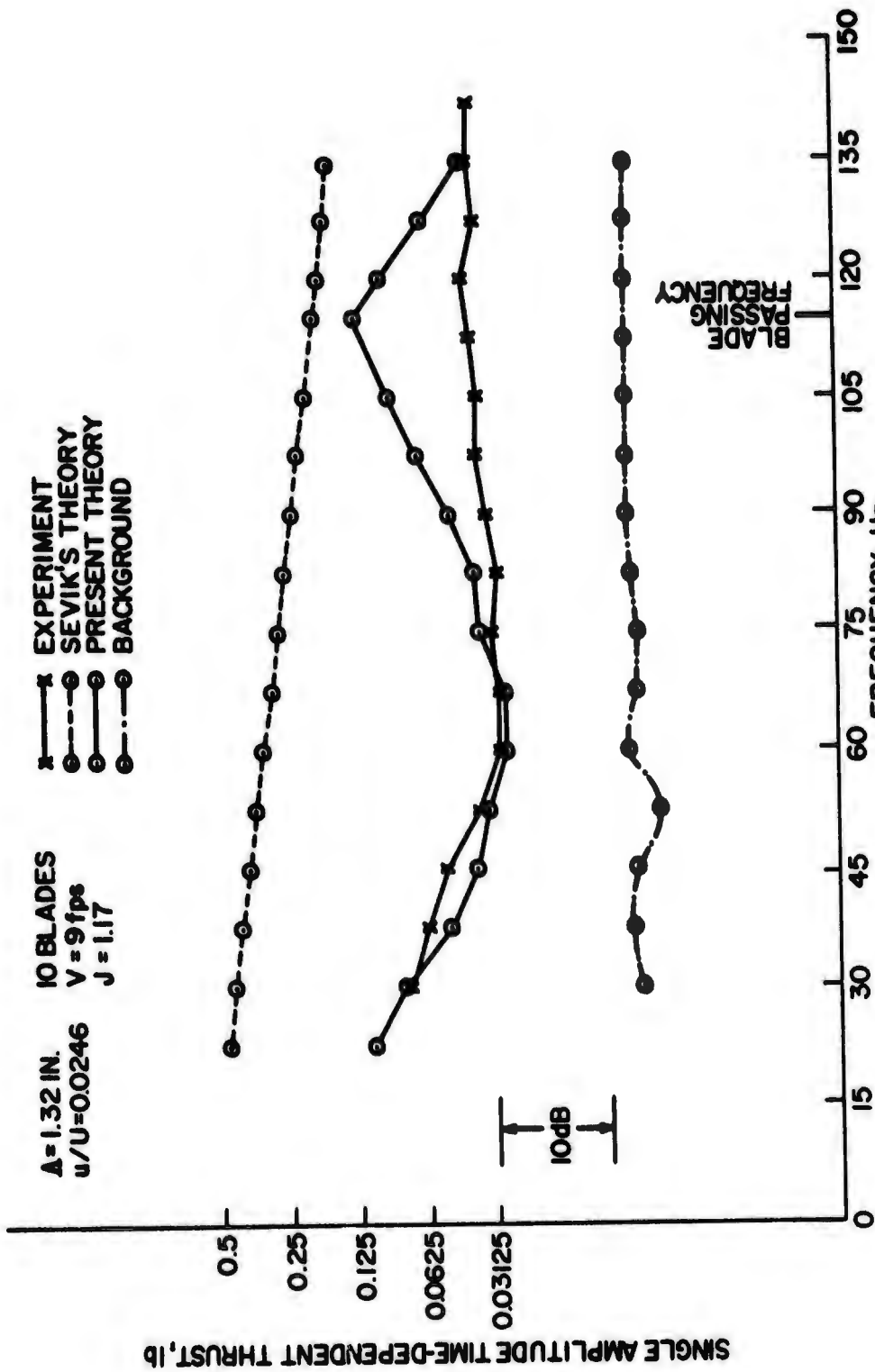

Figure 88 - Turbulence Generated Time-Dependent Thrust versus Frequency (10 Blades, J=1.17, Δ=1.32 in., u/U=0.0246)

VITA

Donald Edwin Thompson was born December 19, 1942, in Pottsville, Pennsylvania. He graduated from Spring Grove Joint High School in June 1960. In 1965, he received the B. A. degree in Physics from Gettsyburg College and the B. S. degree in Aerospace Engineering from The Pennsylvania State University. In 1967, he received the M. S. degree in Engineering Mechanics from The Pennsylvania State Univeristy. From 1967 to the present he has been a research assistant at the Applied Research Laboratory, The Pennsylvania State University concerned with basic and applied research in time-dependent forces generated by propulsors and the resulting hull vibrations and radiated sound. He has also conducted research in the radiated sound from cavitating flows.